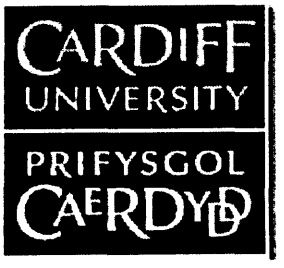
Nanoscale surface patterning as a means of controlling protein immobilisation

A thesis submitted to the University of Wales in accordance with the requirements for the degree of

DOCTOR OF PHILOSOPHY
BY EXAMINATION AND THESIS

By
Sophie Elizabeth Williams B.Sc.

Molecular Recognition Research Unit (MRRU)
Drug Delivery Department
Welsh School of Pharmacy
Cardiff University



March 2008

UMI Number: U584292

All rights reserved

INFORMATION TO ALL USERS
The quality of this reproduction is dependent upon the quality of the copy submitted.

In the unlikely event that the author did not send a complete manuscript
and there are missing pages, these will be noted. Also, if material had to be removed,
a note will indicate the deletion.



UMI U584292
Published by ProQuest LLC 2013. Copyright in the Dissertation held by the Author.
Microform Edition © ProQuest LLC.
All rights reserved. This work is protected against
unauthorized copying under Title 17, United States Code.



ProQuest LLC
789 East Eisenhower Parkway
P.O. Box 1346
Ann Arbor, MI 48106-1346

Acknowledgements

I would firstly like to thank my supervisor, Chris Allender, for giving me the opportunity to study for a PhD and for his wonderful help and advice.

A very special thank you to Andy, who has given me a tremendous amount of love, support and encouragement, and without whom this would not have been possible. Also, many thanks to Mum, Dad, Alice, Gran, Esme, Betty, Diana, Michael and David for their love and support.

Thank you to Dr Phil Davies for allowing me use of the AFM and for his enthusiasm, help and advice. I would also like to thank Federico for his invaluable help with AFM.

Thank you very much to Dr Albert Carley and Dr Dave Morgan for carrying out all of the XPS experiments presented in this thesis, and also to Dr Alex White for carrying out the molecular modeling studies. Thank you to Drs Arwen Jones, Mariam and Jin Jin, for their help and advice with using the fluorescence microscope.

To MRRU past and present: Dr Chris Allender, Dr Keith Brain, Chris Jeans, Pete, Betty, Ron, Anna, Chris Jones, Darren, Ollie, Jimmi, Jenna and Yvonne. Special thanks to Ron for his fantastic help in the lab, Ollie for help with contact angle studies, Pete for advice on TLC and HPLC and Betty for introducing me to organic chemistry and the beautiful language of Italian!

A huge thanks to Chris McGuigans lab, especially Marco Migliori for his wonderful help with NMR. I would also like to thank everyone who let me borrow their Rotovaps (Yousseff, Maria-Chiara, Stefan, Constantino, Rocco, Rina and many more).

Thank you very much to Wendy, Colin and Paul for their help and friendly chats.

For my Dad

Thank you to the Coffee Crew: Chris Jeans, El, Chris Thomas, Sion, Bec, Stu, Siti, Wing, Zoe, Rhys, Al and Rich for much fun, amusement and support. A huge thanks to my friends, Sian and Helena and my others friends in the WSOP.

Many thanks to all of the five-a-side footy guys for making Mondays the best day of the week!

And last but not least, a big thanks to my friends in London (Raynes Park massive) and Cardiff for all of the good times.

Summary

It would be desirable to synthesise a molecularly imprinted polymer with specific high-affinity protein recognition sites as a durable, cost-effective replacement for antibodies in biotechnology. A novel protein imprinting approach was proposed as an outline for these investigations. The focus of this project was consideration of fundamental aspects of surface nanometer-scale patterning and protein-surface interactions with the aim of preparing an ordered array of surface protein. This was in part achieved during the course of the work.

An equilibrium dialysis method was validated for the measurement of ligand-protein binding parameters. Human serum albumin (HSA) and ethacrynic acid (ETH) were chosen as the ligand-protein pair to be surface-immobilised. Molecular modelling suggested a good fit for ethacrynic acid in the covalent HSA binding 'cleft', however, the covalent HSA-ETH complex was not successfully isolated. A derivative of the ligand, ETH-glycine, was synthesised to a very high purity but a low yield. A gas-phase silanisation method was developed to deposit functional aminopropyletriethoxysilane (APS) groups onto silicon wafer surfaces. The dispersion of APS could not be sufficiently controlled, by changing the evaporative distance or the APS evaporation concentration, and hence it was not possible to bring about gold nanoparticle (AuNP) patterning at the nanometer scale using this approach. However AuNP patterning could be achieved by incubating APS monolayer surfaces with different dilutions of a commercially available AuNP solution. Subsequent development of a protein imprinting strategy would require that non-specifically adsorbed HSA can be removed from PNA silicon surfaces. This was found to be difficult to achieve using mild conditions.

Controlled gas-phase deposition of APS could not be used to directly facilitate dispersed ligand attachment. AuNP patterning can potentially be used as an indirect method for controlling surface dispersion of immobilised ligand. Controlled surface orientation and patterning of HSA, using the specific interaction with ETH, remains a significant challenge.

Contents

Chapter 1

Introduction 1

1.1 Molecular recognition 2

1.1.1 Introduction

1.1.2 Molecular recognition in biology

1.1.2.1 Introduction

1.1.2.2 Protein structure

1.1.2.3 Protein-ligand receptor interactions 3

- Covalent interactions 4
- Non-covalent interactions

1.1.3 Molecular recognition in biotechnology and bioengineering 5

1.1.3.1 Antibodies

1.1.3.2 Immunoassays 6

1.1.3.3 Affinity separation of proteins 7

1.1.3.4 Biosensors

1.1.3.5 Bioarrays 8

1.1.3.6 Non-specific binding

1.1.4 Synthetic molecular recognition 9

1.1.4.1 Artificial receptors

1.2 Surface immobilisation of proteins 10

1.2.1 Introduction

1.2.2 Surfaces for protein immobilisation 11

1.2.3 Non-specific protein immobilisation

1.2.3.1 Adsorption and entrapment 12

1.2.3.2 Covalent immobilisation via protein amino groups

1.2.4 Specific immobilisation

1.2.4.1 Covalent immobilisation of protein thiol groups to reactive surface groups

1.2.4.2 Specific affinity immobilisation 13

- Small molecule affinity immobilisation (Ligands, ligand-analogues, inhibitors and drugs)
- Carbohydrate / metal affinity immobilisation 14
- Site-specific labelling / tagging (genetic modification) for immobilisation

1.3 Controlling the surface distribution of proteins

1.3.1 Self-assembled monolayers

1.3.1.1 Mixed SAMs 15

1.3.1.2 Photolithography

1.3.1.3 Microcontact printing 16

1.4 Molecular imprinting 17

1.4.1 Introduction

1.4.2 Preparation of molecularly imprinted polymers 18

1.4.2.1 Covalent imprinting

1.4.2.2 Non-covalent imprinting

1.4.2.3 Semi-covalent imprinting 19

- Sacrificial spacer approach

1.4.3 Protein imprinting

1.4.3.1 Imprinting in aqueous solvents

1.4.3.2 Bulk Imprinting of protein templates 20

1.4.3.3 Alternative protein imprinting approaches 21

a. Protein adsorption onto flat surfaces

b. Microcontact printing of proteins onto flat surface polymer 22

c. Covalent immobilisation of proteins on a solid surface

d. Specific / Affinity interactions between protein and polymer 23

i. Boronate / metal-affinity interactions

ii. Enzyme-inhibitor / ligand analogue interactions 24

e. Epitope imprinting approach 25

1.4.3.3 Potential applications 26

1.4.3.4 Future of protein imprinting

1.5 A novel protein imprinting concept 27

1.6 Aims and objectives

1.6.1 Aim

1.6.2 Objectives 29

References 31

Chapter 2

Validation of an approach for determining ligand binding parameters using an HSA / SAL model 38

2.1 Introduction 39

2.1.1 Protein-ligand binding analysis

2.1.2 Equilibrium dialysis 40

2.1.2.1 Background

2.1.2.2 Previously described approaches 41

2.1.3 Chapter objectives 43

2.2 Methods 44

2.2.1 Equipment and materials

2.2.2 HSA and SAL analysis using UV spectroscopy 45

2.2.2.1 SAL and HSA UV absorbance spectra

2.2.2.2 SAL and HSA UV calibration graphs

a. SAL

b. HSA

2.2.2.3 Detection limits for SAL in the UVS 46

2.2.3 SAL analysis using fluorescence spectroscopy

2.2.3.1 SAL fluorescence spectra

2.2.3.3 SAL fluorescence calibration graphs

2.2.3.4 SAL detection limits by fluorescence 47
a. Lower concentration limit
b. Lower volume limit
2.2.4 Dialysis of HSA with SAL using diffusion cells
2.2.4.1 Diffusion cell equilibrium dialysis set-up
2.2.4.2 Equilibration time and mass balance controls 48
2.2.4.3 Protein control experiments 49
2.2.4.4 Ligand control experiments
2.2.4.5 HSA-SAL equilibrium dialysis binding experiments
2.2.5 Dialysis of HSA with SAL using Eppendorf tubes
2.2.5.1 Eppendorf dialysis set-up 50
2.2.5.2 Equilibration time and mass balance controls
2.2.5.3 Protein control experiments 51
2.2.5.4 Ligand control experiments
a. Fluorescence spectroscopy
b. UV spectroscopy
2.2.5.5 HSA-SAL equilibrium dialysis binding experiments
a. Fluorescence spectroscopy
b. UV spectroscopy 52

2.3 Results and discussion 53

2.3.1 HSA and SAL analysis using UV spectroscopy
2.3.1.1 SAL and HSA UV absorbance spectra
a. SAL
b. HSA
2.3.1.2. SAL and HSA UV calibration graphs 54
a. SAL
b. HSA
2.3.1.3 Detection limits for SAL by UVS 55
2.3.2 SAL analysis using fluorescence spectroscopy 56
2.3.2.1 SAL fluorescence spectra
2.3.2.2 SAL detection limits by fluorescence 57
a. Lower concentration limit
b. Lower volume limit

2.3.3 Dialysis of HSA with SAL using diffusion cells
2.3.3.1 Equilibration time and mass balance controls
2.3.3.2 Protein control experiments 58
2.3.3.3 Ligand control experiments
2.3.3.4 HSA-SAL equilibrium dialysis binding experiments 60
2.3.4 Dialysis of HSA with SAL using Eppendorf tubes 61
2.3.4.1 Equilibration time and mass balance controls
2.3.4.2 Protein control experiments
2.3.4.3 Ligand control experiments 62
a. Fluorescence spectroscopy
b. UV spectroscopy
2.3.4.4 HSA-SAL equilibrium dialysis binding experiments 64
a. Fluorescence spectroscopy
b. UV spectroscopy 65
2.3.5 Conclusions 66

References 68

Chapter 3

Selection and characterisation of a high-affinity protein-ligand interaction 70

3.1 Introduction 71

3.1.1 Selection of a high-affinity protein-ligand interaction
3.1.1.1 Criteria for choosing a high-affinity ligand and model protein
3.1.1.2 Selection of a model protein 72
3.1.1.3 Selection of a ligand 73
3.1.2 Chapter objectives 74

3.2 Methods 75

3.2.1 Equipment and materials
3.2.2 Identifying a high-affinity ligand
3.2.2.1 UV spectroscopic measurements of aromatic ligands

3.2.2.2 Fluorescence spectroscopic measurements of aromatic ligands

3.2.3 Evaluation of HSA-ETH binding 76

3.2.3.1 UV spectroscopic analysis of ETH

- ETH UV calibration graph

3.2.3.2 Equilibrium dialysis of HSA with ETH without pre-saturation of the covalent site (Cys-34)

a. Equilibrium control experiment and mass balance

b. Ligand control experiments

c. HSA-ETH binding graph

3.2.3.3 Pre-saturation of the covalent HSA sites (Cys-34) with ETH 77

a. Saturation

b. Freeze-drying

c. Removal of vast excess ETH by bulk dialysis

i. First method (M1)

ii. Second method (M2)

d. Removal of excess ETH using size exclusion chromatography (PD10 columns) 79

i. PD10 column 1 80

ii. PD10 column 2

iii. PD10 columns 3 and 4

iv. PD10 column 5 81

e. Equilibrium dialysis removal of ETH

3.3 Results and discussion 82

3.3.1 Identifying a high-affinity ligand

3.3.1.1 UV spectroscopic measurements of aromatic ligands

3.3.1.2 Fluorescence spectroscopic measurements of aromatic ligands

3.3.1.3 Ligand selection

3.3.2 Evaluation of HSA-ETH binding 85

3.3.2.1 UV spectroscopic analysis of ETH

- UV scan of ETH to find λ_{max}
- ETH UV calibration graph

3.3.2.2 Equilibrium dialysis of HSA with ETH without pre-saturation of the covalent site (Cys-34)

a. Equilibrium control experiment and mass balance
b. Ligand control experiments 86
c. HSA-ETH binding graph 87
3.3.2.3 Pre-saturation of the covalent HSA sites (Cys-34) with ETH 89
a. Removal of vast excess ETH by bulk dialysis
i. First method (M1)
ii. Second method (M2)
b. Removal of excess ETH using size exclusion chromatography (PD10 columns) 91
i. PD10 column 1 and 2
ii. PD10 column 3 and 4 93
iii. PD10 columns 5 94
c. Equilibrium dialysis removal of ETH 96
3.3.3 Conclusions 98

References 99

Chapter 4

Synthesis and purification of N-{[2,3-dichloro-4-(2-methylenebutyryl)-phenoxy]-acetyl}glycine (ETHGLY) 102

4.1 Introduction 103

4.1.1 Coupling of ETH to a spacer molecule to minimise HSA surface denaturation
4.1.2 Amide coupling of ETH to a spacer molecule 104
4.1.3 Glycine methylester as the spacer molecule
4.1.4 Amide coupling reactions 106
4.1.4 Chapter objectives 108

4.2 Methods 110

4.2.1 Equipment and Materials
4.2.2 TLC analysis
4.2.3 NMR analysis 111

4.2.4 Amide coupling of ETH and GLYOMe
4.2.4.1 CDI as coupling reagent
4.2.4.2 $SOCl_2$ as coupling reagent
4.2.4.3 EDC as a coupling reagent 112
4.2.2 Ester hydrolysis of ETHGLY
4.2.4.1 Base-catalysed ester hydrolysis using NaOH or LiOH
4.2.4.2 Base-catalysed ester hydrolysis using $NaHCO_3$
4.2.4.3 Base-catalysed ester hydrolysis using Na_2CO_3 113
4.2.5 HPLC purification of ETHGLY
4.2.6 Solid-phase extraction of ETHGLY 114

4.3 Results and discussion 115

4.3.1 Amide coupling of ETH and GLYOMe
4.3.1.1 CDI as coupling reagent
4.3.1.2 $SOCl_2$ as coupling reagent 122
4.3.1.3 EDC as a coupling reagent
4.3.2 Ester Hydrolysis 125
4.3.2.1 Base-catalysed ester hydrolysis using NaOH or LiOH
4.3.2.2 Base-catalysed ester hydrolysis using $NaHCO_3$
4.3.2.3 Base-catalysed ester hydrolysis using Na_2CO_3
4.3.3 HPLC purification of ETHGLY 127
4.3.4 Solid-phase extraction of ETHGLY 129
4.3.5 Conclusions 131

References 132

Chapter 5

Preparation and characterisation of aminosilanised silicon substrates 135

5.1 Introduction 136

5.1.1 The chemistry of silane deposition on silicon surfaces 137
5.1.1.1 The structure of silicon wafers

5.1.1.2 Methods for activating the silica surface on silicon wafer surfaces

5.1.1.3 Silanes and their condensation with activated silicon surfaces 138

5.1.2 Derivatising silica with APS 139

5.1.2.1 Solution-phase deposition 140

5.1.2.2 Gas-phase deposition

5.1.3 Techniques for 2D surface chemistry analysis 141

5.1.3.1 Ellipsometry

5.1.3.2 Contact angle measurements 142

5.1.3.3 Atomic force microscopy 143

- Contact-mode
- Tapping-mode
- Non-contact-mode 144

5.1.3.4 Electron microscopy

5.1.3.5 X-ray photon spectroscopy

5.1.4 Characterization of silanised silicon wafer substrates using colloidal AuNP 145

5.1.4.1 AuNP synthesis

5.1.4.2 Electrostatic interaction between APS and AuNPs

5.1.4.3 Analysis of AuNP binding on APS-derivatised silicon surfaces 146

5.1.5 Chapter objectives

5.2 Methods 147

5.2.1 Equipment and materials

5.2.2 Development of a method for the cleaning, activation and silanisation of silicon surfaces

5.2.2.1 Solution-phase silanisation 149

a. Pre-cleaning silicon surfaces using a series of different solvents

b. Surfaces activated in PNA solution prior to silanisation

c. Surfaces activated in hot PNA solution and silanised in extra-dry solvent

d. An optimised method for surface cleaning, activation and solution-phase silanisation 150

5.2.2.2 Derivatisation of silicon with APS from gas-phase and treatment with AuNPs

a. Evaporation of silane from a Petri dish lid

b. Evaporation of silane from an Eppendorf tube lid 151

5.2.2.3 An optimised method of surface cleaning, activation and gas-phase silanisation

1. Cleaning
2. Activation
3. Silanisation 152

5.2.2.4 Gas-phase silanisation of surfaces with an increasing exposure time to APS/PO, followed by a sonication step

5.2.2.5 Contact angle measurement

5.2.3 Analytical methods 153

5.2.3.1 Atomic force microscopy

- Scan settings
  - Contact-mode AFM settings
  - Tapping-mode AFM settings
- Image processing 154
  - Applying filters to remove image artefacts
  - Image analysis 157

5.2.3.2 X-ray photon spectroscopy 158

5.2.3.3 Contact angle measurements 160

5.3 Results and discussion 162

5.3.1 Development of a method for the cleaning, activation and silanisation of silicon surfaces

5.3.1.1 Solution-phase silanisation

a. Pre-cleaning silicon surfaces using a series of different solvents

b. Surfaces activated in PNA solution prior to silanisation

c. Surfaces activated in hot PNA solution and silanised in extra-dry solvent 163

d. An optimised method for surface cleaning, activation and solution-phase silanisation 164

5.3.1.2 Gas-phase silanisation 166

a. Evaporation of silane from a Petri dish lid

b. Evaporation of silane from an Eppendorf tube lid 175

5.3.1.3 Gas-phase silanisation of surfaces with an increasing exposure time to APS/PO, followed by a sonication step 177

5.3.1.4 Contact angle measurements 178

5.3.2 Conclusions 179

References 181

Chapter 6

Controlling APS deposition and the nano-scale patterning of AuNPs on silicon surfaces 185

6.1 Introduction 186

6.1.1 Patterning of flat surfaces at the nanometer scale

6.1.1.1 Scanning tunnelling microscopy

6.1.1.2 Patterning of AuNPs on flat surfaces 187

- Atomic force microscope nanolithography
- Mixed SAMs 188
- Gravure printing

6.1.2 Creating silane gradients on flat surfaces

6.1.3 The preparation of AuNP density gradients using gas-phase deposition of APS on silicon surfaces 189

6.1.4 Nanoparticles binding on functionalised silicon surfaces 190

6.1.4.1 The kinetics of AuNP binding to APS-derivatised silicon wafer

6.1.4.2 The effect of solution concentration on AuNP binding to APS-derivatised silicon surfaces

6.1.4.3 The effect of the ionic strength on AuNP binding to APS-derivatised silicon surfaces 191

6.1.4.4 The effect of solution pH upon AuNP binding to APS-derivatised silicon wafer 193

6.1.5 Chapter objectives

6.2 Methods 194

6.2.1 Equipment and materials

6.2.2 Controlling the spatial distribution of molecules on silicon at the nanometer scale

6.2.2.1. Creating AuNP number density gradients on silicon surfaces derivatised by evaporation and gradient deposition of APS

a. Distance gradient method 1, using diluted AuNP solution

b. Distance gradient method 2, using diluted AuNP solution 195

c. Distance gradient method 3, using diluted AuNP solution

d. Distance gradient method 4, using undiluted AuNP solution

6.2.2.2 Determination of the effect of AuNP dilution on electrostatic binding to APS films 197

a. Dilution of 10nm AuNP solution with dH_2O

b. Dilution of 20nm AuNP solution with dH_2O

c. The stability of the APS-AuNP interaction on silicon surfaces in dH_2O 198

d. Kinetics of AuNP binding to an APS layer on silicon surfaces

e. The stability of APS on silicon surfaces in dH_2O, as viewed by AuNP binding

6.2.2.3 Non-specific binding of undiluted AuNP solution to underivatised silicon surfaces 199

6.2.2.4 Changing the concentration of APS in the evaporation medium 200

a. APS concentration gradient experiment 1

b. APS concentration gradient experiment 2

c. APS concentration gradient experiment 3

d. APS concentration gradient experiment 4

6.3 Results and discussion 201

6.3.1 Controlling the spatial distribution of molecules on silicon at the nanometer scale

6.3.1.1. Creating AuNP number density gradients on silicon surfaces derivatised by evaporation and gradient deposition of APS

a. Distance gradient method 1, using diluted AuNP solution

b. Distance gradient method 2, using diluted AuNP

solution 202

c. Distance gradient method 3, using diluted AuNP solution 206

d. Distance gradient method 4, using undiluted AuNP solution 207

6.3.1.2. Determination of the effect of AuNP dilution on electrostatic binding to APS films 209

a. Dilution of 10nm AuNP solution with dH_2O 210

b. Dilution of 20nm AuNP solution with dH_2O

c. The stability of the APS-AuNP interaction on silicon surfaces in dH_2O 213

d. Kinetics of AuNP binding to an APS layer on silicon surfaces

e. The stability of APS on silicon surfaces in dH_2O, as viewed by AuNP binding

6.3.1.3 Non-specific binding of undiluted AuNP solution to underivatised silicon surfaces 219

6.3.1.4 Changing the concentration of APS in the evaporation medium

a. APS concentration gradient experiments 1 and 2

b. APS concentration gradient experiments 3 and 4 221

6.3.2 Conclusions 225

References 226

Chapter 7

Chemical attachment of ETH to APS-derivatised silicon surfaces 229

7.1 Introduction 230

7.1.1 Amide coupling on surfaces

7.1.2 Chapter objectives 231

7.2 Methods 232

7.2.1 Equipment and materials

7.2.2 XPS analysis of ETH-treated silicon surfaces

7.2.3 XPS analysis of APS-derivatised silicon surfaces

incubated with ETH and EDC

7.2.4 Deprotonation of surface amines using NaOH to improve amide coupling to ETH 233

7.2.5 Amide coupling of ETH to APS surfaces

7.3 Results and discussion 234

7.3.1 XPS analysis of ETH-treated silicon surfaces

7.3.2 XPS analysis of APS-derivatised silicon surfaces incubated with ETH and EDC 237

7.3.3 Deprotonation of surface amines using NaOH to improve amide coupling to ETH 239

7.3.4 Amide coupling of ETH to APS surfaces

7.3.5 Conclusions 241

References 242

Chapter 8

Adsorption and desorption of HSA and FITC-BSA on underivatised and APS-derivatised silicon surfaces 243

8.1 Introduction 244

8.1.1 Protein adsorption on surfaces

8.1.1.1 Protein structural stability upon surface adsorption

8.1.1.2 The effect of surface composition upon protein adsorption 245

- Hydrophobic surfaces
- Hydrophilic surfaces
- Charged surfaces

8.1.1.3 Techniques for measuring protein adsorption 246

8.1.2 Serum albumin adsorption on silicon and glass surfaces 247

8.1.2.1 The effect of solvent upon serum albumin adsorption

8.1.2.2 The effect of pH upon serum albumin adsorption 248

8.1.2.3 Effect of protein concentration upon serum albumin adsorption

8.1.2.4 The effect of the surface upon serum albumin adsorption 249
8.1.2.5 Specific orientation of serum albumins adsorbed to silica
8.1.3 Protein desorption from surfaces 250
8.1.4 Chapter objectives 251

8.2 Methods 252

8.2.1 Equipment and materials
8.2.2 Fluorescence microscopy for analysis of FITC-BSA adsorption onto silicon surfaces 253
8.2.3 The adsorption of HSA and FITC-BSA on silicon and glass surfaces
8.2.3.1 HSA (30μM) adsorption on silicon surfaces in water
8.2.3.2 HSA (20μM) adsorption on silicon surfaces in NaPB 254
8.2.3.3 Calibration of FITC-BSA (1nM-10^4nM) adsorption from NaPB on glass surfaces using AFM and fluorescence microscopy
8.2.3.4 FITC-BSA (0.1-10^2nM) adsorption on glass surfaces in NaPB 255
8.2.3.5 FITC-BSA (10nM) desorption from glass and silicon surfaces 256
8.2.3.6 A comparison between AuNP, FITC-BSA (10nM) and HSA (10nM) adsorption on glass and silicon surfaces
8.2.3.7 HSA (10^2nM) adsorption on a silicon surface in NaPB 257

8.3 Results and discussion 258

8.3.1 Fluorescence microscopy for analysis of FITC-BSA adsorption onto silicon surfaces
8.3.2 The adsorption of HSA and FITC-BSA on silicon and glass surfaces
8.3.2.1 HSA (30μM) adsorption on silicon surfaces in water 259
8.3.2.2 HSA (20μM) adsorption on silicon surfaces in NaPB 261
8.3.2.3 Calibration of FITC-BSA (1nM-10^4nM) adsorption from NaPB on glass surfaces using AFM and fluorescence microscopy 265
a. Theoretical HSA or FITC-BSA concentration required for monolayer coverage of 1x1cm^2 glass or silicon surfaces in glass vials

b. Experimental results for FITC-BSA binding to surfaces 269

8.3.2.4 FITC-BSA (0.1-10^2nM) adsorption on glass surfaces in NaPB 271

8.3.2.5 FITC-BSA (10nM) desorption from glass and silicon surfaces 273

8.3.2.6 A comparison between AuNP, FITC-BSA (10nM) and HSA (10nM) adsorption on glass and silicon surfaces 275

8.3.2.7 HSA (10^2nM) adsorption on a silicon surface in NaPB 276

8.3.3 Conclusions

References 278

Chapter 9

General discussion and future work 281

9.1 Discussion 282

9.2 Future work 288

9.2.1 Specific immobilisation and orientation of HSA on ETH-derivatised silicon surfaces

9.2.2 Creating a molecular imprint 291

9.3 Conclusions 293

References 294

List of figures

Fig. 1.1	Connolly surface representation of HSA.	3
Fig. 1.2	Protein assays using specific antibody recognition.	6
Fig. 1.3	General components of a biosensor.	8
Fig. 1.4	Different protein immobilisation strategies lead to different surface orientations.	11
Fig. 1.5.	Mixed SAM for controlled protein density	15
Fig. 1.6	Photolithography.	16
Fig. 1.7	General schematic of molecular imprinting.	17
Fig. 1.8	Flat surface imprinting of proteins using molecular self-assembly.	22
Fig. 1.9	Boronate-affinity molecular imprinting of RNAse B.	24
Fig. 1.10	Metal-affinity molecular recognition for lysosyme imprinting.	24
Fig. 1.11	Molecular imprinting of Trypsin using enzyme-affinity interactions	25
Fig. 1.12	Scheme for creating a specific protein imprint on a flat surface.	28
Fig. 2.1	Structure of SAL	42
Fig. 2.2	Diffusion cell equilibrium dialysis set–up	48
Fig. 2.3	Eppendorf tube set up for equilibrium dialysis	50
Fig. 2.4	UV absorbance spectra of SAL and HSA	53
Fig. 2.5	UV calibration graphs for SAL	55
Fig. 2.6	UV calibration graph for HSA	55
Fig. 2.7	Fluorescence spectra of SAL	56
Fig. 2.8	Equilibrium control experiment for diffusion cell dialysis using UV analysis	58
Fig. 2.9	Ligand control experiment for diffusion cell dialysis using fluorescence analysis	59
Fig. 2.10	HSA-SAL binding curve measured from diffusion cell dialysis	60
Fig. 2.11	Equilibrium control experiment for Eppendorf tube dialysis	62
Fig. 2.12	Ligand control experiment for diffusion cell dialysis using UV analysis	63
Fig. 2.13	HSA-SAL binding curve using Eppendorf tube dialysis and fluorescence analysis	64
Fig. 2.14	HSA-SAL binding curve measured after Eppendorf tube dialysis and UV analysis	66
Fig. 3.1	The requirements of a high-affinity ligand for specific protein surface orientation	71
Fig. 3.2	Bulk dialysis removal of excess ligand	78
Fig. 3.3	PD10 separation column	79
Fig. 3.4	Covalent binding of ETH to HSA	83
Fig. 3.5	UV scan of ETH	85
Fig. 3.6	Equilibrium control graph	86
Fig. 3.7	Apparent [ETH] lost with increasing starting [ETH]	87
Fig. 3.8	HSA-ETH two-site binding curve measured after Eppendorf tube dialysis and UV analysis	88

Fig. 3.9	UV spectrum of HSA-ETH after bulk dialysis removal of excess ETH	89
Fig. 3.10	Gradual removal of free ETH from HSA-ETH after bulk dialysis (M2), measured by equilibrium dialysis experiments	91
Fig. 3.11	Consistency of HSA-ETH and ETH Elution in PBS and dH_2O	92
Fig. 3.12	Comparison of PBS and NaPB as PD10 mobile phases	93
Fig. 3.13	Effect of varying pH of the mobile phase on UV absorbance elution profiles of ETH from PD10 column 4	93
Fig. 3.14	Separation of Free ETH from HSA-ETH using three PD10 runs	95
Fig. 3.15	A comparison of HSA and HSA-ETH UV scans	95
Fig. 3.16	Gradual removal of free ETH from HSA-ETH by equilibrium dialysis	97
Fig. 3.17	UV scans of free ETH removal by equilibrium dialysis	97
Fig. 3.18	Shift in λmax of ETH after extensive equilibrium dialysis	98
Fig. 4.1	Structure of ETH	103
Fig. 4.2	Spacer Length Affects Protein Binding	104
Fig. 4.3	Structures of amine spacer molecules	105
Fig. 4.4	Selective ester hydrolysis of ETHGLYOMe	105
Fig. 4.5	Base hydrolysis	106
Fig. 4.6	EDC structure and mechanism	109
Fig. 4.7	Solid phase extraction of ETHGLY	114
Fig. 4.8	H^1 NMR spectra and structures of starting products and reaction product from CDI synthesis	119
Fig. 4.9	CDI Synthesis	119
Fig. 4.10	Michael addition of imidazole to an α,β-unsaturated ketone	120
Fig. 4.11	H^1 NMR of ETH(Iz)	
Fig. 4.12	Proton coupling at the ethyl end of ETH(Iz)GlyOMe	121
Fig. 4.13	H^1 NMR spectra of EDC coupling reagent and ETHGLYOMe product	123
Fig. 4.14	EDC coupling of ETH to GLYOMe	124
Fig. 4.15	Ester hydrolysis products	126
Fig. 4.16	The instability of ETH in mildly basic conditions	127
Fig. 4.17	UV spectrum of the product mixture after ester hydrolysis of ETHGLYOMe	128
Fig. 4.18	Analytical HPLC spectrum showing separation of four predicted products from ester hydrolysis	129
Fig. 4.19	H^1 NMR spectrum of final product: ETHGLY	130
Fig. 4.20	HPLC purity of ETHGLY	130
Fig. 5.1	Step one of a novel protein imprinting approach	136
Fig. 5.2	Types of silica on the surface of silicon wafer substrates	137
Fig. 5.3	Structure of silanes	139
Fig. 5.4	The condensation of APS with activated silicon surface groups	139
Fig. 5.5	Contact angle measurements used to determine the hydrophilicity of a surface	142

Fig. 5.6	Atomic force microscopy	144
Fig. 5.7	Structure of the citrate anion that stabilises AuNPs	148
Fig. 5.8	Evaporation of APS onto PNA-activated silicon surface	152
Fig. 5.9	Images produced from a single AFM scan	154
Fig. 5.10	Removal of 'bow' from AFM images using 2nd order and flattening processes	155
Fig. 5.11	The AFM 'flattening' process	156
Fig. 5.12	Processing of selected AFM scan lines	156
Fig. 5.13	Using WSXM flooding analysis to count AuNP number density	157
Fig. 5.14	Kratos Axis Ultra DLD x-ray photoelectron spectrometer	159
Fig. 5.15	Experimental set-up used for contact angle measurements	160
Fig. 5.16	Technique used to obtain contact angle measurements	161
Fig. 5.17	Contact angle measurements on silicon surfaces with different hydrophilicities	161
Fig. 5.18	The interaction of AuNPs with APS-derivatised (left) and underivatised (right) silicon surfaces (after pre-cleaning and activation steps)	162
Fig. 5.19	Contact-mode AFM images of surfaces from solution-phase silanisation experiments	165
Fig. 5.20	AFM profiles of surfaces from solution-phase silanisation experiments	165
Fig. 5.21	Tapping-mode AFM scans of surfaces from solution-phase silanisation experiments	165
Fig. 5.22	XPS spectra of surfaces from gas-phase and solution-phase silanisation experiments	171
Fig. 5.23	Attenuation of Si2p and N1s XPS surface signals for gas-phase and solution-phase silanisation experiments	173
Fig. 5.24	XPS spectra with curve fits for gas-phase and solution-phase silanisation experiments	174
Fig. 5.25	Contact-mode AFM images of surfaces from solution-phase silanisation experiments	176
Fig. 5.26	AFM profiles of surfaces from gas-phase silanisation experiments	176
Fig. 5.27	Tapping-mode AFM images of surfaces from gas-phase silanisation experiments	176
Fig. 5.28	Mol% composition of surface elements for increasing APS silanisation times	178
Fig. 6.1	Representation of an ordered array of single AuNPs developed using AFM nanolithography	187
Fig. 6.2	A AuNP number density gradient generated along an APS gradient	190
Fig. 6.3	The random deposition of AuNPs onto functionalised silicon surfaces from solution	192
Fig. 6.4	A regular lattice of AuNP formed on a silicon surface	192
Fig. 6.5	Experimental set ups for preparing AuNP number density gradients on silicon surfaces	197
Fig. 6.6	Arrangement of surfaces around an Eppendorf lid during gas-phase silanization	199

Fig. 6.7	AuNP distance gradient graph (method 1)	203
Fig. 6.8	A 'shadow effect' observed during APS silanisation	203
Fig. 6.9	AuNP distance gradient graph- method 2	204
Fig. 6.10	APS concentration along a distance gradient (Method 2) measured by XPS	205
Fig. 6.11	Correlation between AFM and XPS data for distance gradient method 2	205
Fig. 6.12	AuNP distance gradient graph (method 3)	206
Fig. 6.13	AuNP distance gradient graph (method 4)	207
Fig. 6.14	Mol% compositions of elements for surfaces prepared in 'distance gradient method 4'	209
Fig. 6.15	AuNP dilution gradient graph (10nm AuNPs)	211
Fig. 6.16	AuNP dilution gradient graph (20nm AuNPs)	212
Fig. 6.17	Stability of the APS-Au interaction	213
Fig. 6.18	Binding kinetics of diluted AuNPs	214
Fig. 6.19	APS stability in dH_2O	215
Fig. 6.20	A schematic showing surface areas occupied by closely packed 10nm and 20nm AuNPs.	218
Fig. 6.21	A comparison between AuNP density gradient plots for AuNP dilution experiments a and b	218
Fig. 6.22	Non-specific binding of 10nm AuNPs on PNA Au surfaces	219
Fig. 6.23	APS concentration gradient graph (experiment 1)	220
Fig. 6.24	APS concentration gradient graph (experiment 2)	221
Fig. 6.25	AFM images of APS concentration gradient (experiment 3) surfaces	223
Fig. 6.26	APS concentration gradient graph (experiment 4)	223
Fig. 6.27	XPS analysis of surfaces silanised with varying APS concentrations (experiments 3 and 4)	224
Fig. 6.28	AuNP adsorption onto silicon surfaces derivatised with various densities of APS	224
Fig. 7.1	Step two of a novel protein imprinting approach	230
Fig. 7.2	Montage of XPS Cl2p spectra for the detection of non-specific ETH binding on PNA and APS surfaces	235
Fig. 7.3	Silicon satellite peaks for APS surfaces incubated with and without ETH	235
Fig. 7.4	XPS Cl2s spectra of ETH-incubated surfaces	236
Fig. 7.5	XPS Cl2p spectra for the EDC- mediated coupling of ETH to APS surfaces	238
Fig. 7.6	XPS N1s spectra for the EDC- mediated coupling of ETH to APS surfaces	238
Fig. 7.7	The effect of NaOH and DMF incubation on the AuNP number density of APS Au surfaces	240
Fig. 7.8	Tapping-mode AFM scans of surfaces incubated with EDC	241
Fig. 8.1	Step three of a novel imprinting approach	244
Fig. 8.2	Structure of FITC	246
Fig. 8.3	Structures of HSA	247

Fig. 8.4	Highly schematic representation of the possible orientation of protein molecules adsorbed to a surface	249
Fig. 8.5	Measurement of RMSR	252
Fig. 8.6	AFM RMSr measurements of PNA silicon surfaces incubated with various HSA solutions in water	259
Fig. 8.7	AFM scans of HSA adsorbed to PNA silicon surfaces in water	260
Fig. 8.8	AFM RMSr measurements of PNA and APS silicon surfaces incubated with various HSA solutions in NaPB or water	263
Fig. 8.9	AFM scans of PNA and APS silicon surfaces incubated with various HSA solutions in NaPB or water	265
Fig. 8.10	AFM RMSr measurements of PNA and APS silicon surfaces incubated with an increasing FITC-BSA concentration in NaPB	270
Fig. 8.11	AFM image of apparent 'holes' in a surface FITC-BSA film	270
Fig. 8.12	Fluorescence microscopy of PNA and APS silicon surfaces incubated with an increasing FITC-BSA concentration in NaPB	271
Fig. 8.13	AFM RMSr measurements of PNA and APS silicon surfaces incubated with an increasing FITC-BSA concentration in NaPB	272
Fig. 8.14	Fluorescence measurements of PNA and APS silicon surfaces incubated with an increasing FITC-BSA concentration in NaPB	273
Fig. 8.15	Various washing treatments to remove FITC-BSA adsorbed to APS surfaces	274
Fig. 8.16	Two images of an APS FITC-BSA surface washed in NaCl (0.1M) and dH_2O	274
Fig. 8.17	A comparison of AuNP binding to glass and silicon APS surfaces	275
Fig. 8.18	AFM RMSr measurements of HSA and FITC-BSA (0.01μM) adsorbed on APS / PNA, glass / silicon surfaces	276
Fig. 8.19	HSA binding to APS silicon surfaces from different solution concentrations	277
Fig. 9.1	The effect of derivatisation of ETH on the binding of HSA.	286
Fig. 9.2	Schematic for creating nanometer-scale patterned APS groups on silicon surfaces	290

List of tables

Table 2.1	Volume detection limit of the fluorescence plate-reader for SAL	57
Table 5.1	Four standard surface treatments carried out for each silicon derivatisation experiment	148
Table 5.2	Surface treatments for solution-phase APS silanisation on silicon wafers	149
Table 5.3	Surface treatments for solution- and gas-phase APS silanisation on silicon wafers	151
Table 5.4	Surface treatments measured by contact angle analysis	152
Table 5.5	XPS correction factors for a selection of elements	159
Table 5.6	XPS surface atomic composition data for gas-phase and solution-phase silanisation experiments	172
Table 5.7	Contact angles of gas-phase and solution-phase silanised surfaces	179
Table 6.1	Molar % compositions and ratios for each surface treatment prepared in distance gradient experiment 2	206
Table 6.2	Mol% compositions of each element for surfaces prepared in 'distance gradient method 4'	209
Table 7.1	ETH / EDC surface treatments using different solvents	232
Table 7.2	Control surface treatments	233
Table 7.3	ETH / EDC surface treatments	233
Table 8.1	Surfaces prepared in experiment 8.2.2.1.	254
Table 8.2	Surfaces prepared in experiment 8.2.3.2.	254
Table 8.3	Surfaces prepared in experiment 8.2.2.3	255
Table 8.4	Surfaces prepared in experiment 8.2.2.4	255
Table 8.5	Surfaces prepared in experiment 8.2.2.5.	256
Table 8.6	Surfaces prepared in experiment 8.2.2.4.	257
Table 8.7	HSA adsorption processes on PNA and APS surfaces at pH 7.4 and 2.7	263
Table 8.8	Predicted concentration of HSA or FITC-BSA required for monolayer coverage of APS glass and silicon surfaces	268
Table 9.1	Equilibrium dialysis experiments outlined to characterise covalent and non-covalent binding of HSA with ETH.	284

Abbreviations

[X]	concentration of 'X'
ε	molar absorptivity
λ_{em}	maximum fluorescence emission wavelength
λ_{ex}	maximum fluorescence emission wavelength
λ_{max}	maximum UV absorbance wavelength
A	absorbance
aa	amino acids
Ab	antibody
AFM	atomic force microscopy
Ag	antigen
APBA	aminophenylboronic acid
APS	aminopropyltriethoxysilane
Arg	arginine
ASA	5-aminosalicylic acid
Asp	aspartic acid
ASP	amplitude set-point
AuNP	gold nanoparticle
BE	binding energy
B_{max}	maximum number of binding sites
BSA	bovine serum albumin
CDI	carbonyldiimidazole
CD	circular dichroism
CVD	chemical vapour deposition
Cys	cysteine
Cyt. C	cytochrome C
DCM	dichloromethane
DCS	decylchlorosilane
dH_2O	de-ionised water
DIF	diclofenac
DNA	deoxyribonucleic acid
DLVO	Deyagin-Landau and Verwy-Overbeek
EDC	1-ethyl-3-(3-dimethylaminopropyl) carbodiimide
ESCA	electron spectroscopy for chemical analysis

ELISA	enzyme-linked immunoassays
ETH	ethacrynic acid
ETHGLY	ethacrynic acid-glycine
ETHGLYOMe)	ethacrynic acid-glycine methylester
EtOH	ethanol
FA	fatty acid
FITC	fluorescein isothiocyanate
FITC-BSA	fluorescein isothiocyanate-BSA
Gly	glycine
GlyOMe	glycine methylester hydrochloride
H-bond	hydrogen bond
His	histidine
HPLC	high-performance liquid chromatography
HSA	human serum albumin
HCl	hydrochloric acid
IBU	ibuprofen
IDA	iminodiacetic acid
IEP	isoelectric point
Ig	immunoglobulin
IPA	isopropyl alcohol
K_a	association constant
K_c	equilibrium constant
K_d	dissociation constant
KE	kinetic energy
KPB	potassium phosphate buffer
L compartment	ligand compartment
Lys	lysine
Lyz	lysozyme
MIP	molecularly imprinted polymer
MOE	molecular operating environment
mol%	molar percentage composition
MP	melting point
MS (ES-)	electro-spray mass spectroscopy (negative mode)
MWCO	molecular weight cut-off
NAP	naproxen

NaPB	sodium phosphate buffer
NHS	N-hydroxysuccinimide
NIP	non-imprinted polymer
NMR	nuclear magnetic resonance
ODS	octadecyltrichlorosilane
OEt	ethoxy
P compartment	protein compartment
P5P	pyridoxal 5'-phosphate
pATP	aminothiophenol
PABA	N-acryloyl para-aminobenzamidine
PBS	phosphate buffered silane
PDB	protein data bank
PEG	polyethylene glycol
PEO	polyethylene oxide
Phe	phenylalanine
PNA	piranha
PO	paraffin oil
QCM	quartz crystal microbalance
RMSr	route mean squared roughness
RNH_2	basic amine
RNH_3^+	quaternary amine
RCONHR	amide
RSA	random sequential adsorption
RS-SR	disulfide bond
RT	retention time
SAL	salicylic acid
SAM	self-assembled monolayer
SH	sulfhydryl / thiol
SPE	solid-phase extraction
SPR	surface plasmon resonance
STM	scanning tunneling microscopy
THF	tetrahydrofuran
TFA	trifluoroacetic acid
TLC	thin-layer chromatography
Trp	trypsin

Tyr	tyrosine
UV	ultra-violet
UVO	ultra-violet ozone
UVS	ultra-violet spectrophotometer
VAC	vanillic acid
VAN	vanillin
VdW	Van der Waals
XPS	x-ray photon spectroscopy
Y	maximum binding capacity

Chapter 1

Introduction

1.1 Molecular recognition

1.1.1 Introduction

Biological systems use the process of *specific molecular recognition* to drive all essential bio-processes including cell signalling, metabolism and deoxyribonucleic acid (DNA) replication. Such systems have evolved to display delicate control over molecular recognition and molecular association through manipulation of orientation, assembly and surface order (Ratner and Shi 1999). Biotechnology has utilised the effectiveness of biological molecular recognition systems (e.g. protein-ligand interactions) to develop a wide range of experimental techniques. Largely based on biologically derived antibodies and enzymes, techniques such as biosensing, bioassays, and affinity chromatography are standard procedures across a wide range of laboratories and are of major commercial importance to large number of manufacturing and research orientated companies. However, despite the efficacy and breadth of application of biomacromolecules, their use is hampered by issues of cost, reproducibility, stability and ethical considerations, and as such a major scientific goal is the development of fully synthetic mimics for biomolecules such as antibodies and enzymes.

1.1.2 Molecular recognition in biology

1.1.2.1 Introduction

The majority of fundamentally important cellular biological processes rely on specific protein-ligand interactions (Ratner and Shi 1999). Proteins (e.g. enzymes, membrane receptors) can possess the ability to reversibly recognise a ligand with high specificity and have evolved to recognise small molecules, lipids (e.g. fatty acid transport) and even other proteins (e.g. DNA translation complexes) (Stryer 1999).

1.1.2.2 Protein structure

There are thousands of proteins in the human body, each with its own unique amino acid sequence, specifically bonded and folded into secondary

(α-helix, β-sheet), tertiary (monomeric protein) and quaternary (multimeric protein) structures (Stryer 1999). Proteins can consist of between ~50-2000 amino acid residues (Stryer 1999). A typical protein surface will mainly be occupied by hydrophilic amino acid residues with the hydrophobic amino acids folded away inside to maintain the protein structure in aqueous environments (Stryer 1999). This is illustrated using a Molecular Operating Environment (MOE, Chemical Computing Group, W. Montreal, Quebec, Canada) space-fill model of human serum albumin (HSA) (Fig. 1.1), where hydrophilic residues are depicted as red and hydrophobic residues as green (See Appendix III for further modelling details).

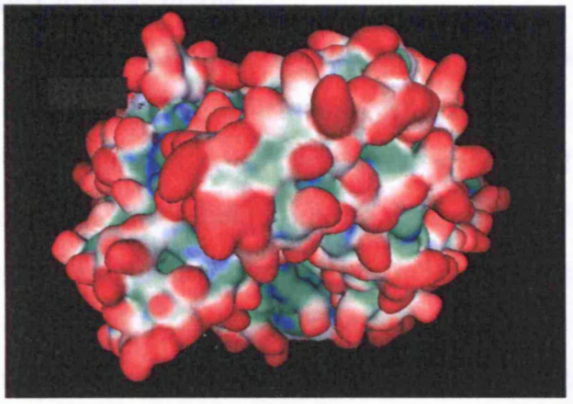


Fig. 1.1 Connolly surface representation of HSA. Hydrophilic amino acid residues are shown in red, hydrophobic residues in green and other residues in blue (Appendix III).

1.1.2.3 Protein-ligand receptor interactions

Receptor sites must be geometrically and chemically defined for recognition of a specific molecule (Ratner and Shi 1999). Pockets and domains on the protein surface are complementary in shape and functionality to bring about association with specific ligands. Rather than a rigid lock-and-key binding mechanism where the pockets are pre-formed, the flexibility of many protein structures can allow 'induced fit' of a ligand inside a binding pocket i.e. the protein will change its conformation to accommodate the ligand (Stryer 1999). Receptors occasionally contain covalent interaction points or spatially positioned amino acids for non-covalent interactions (Peters 1992; Banner 2003)

- **Covalent interactions**

Reversible covalent interactions are sometimes formed between protein and ligand. These can be very short lived, e.g. during the enzymatic catalysis of peptides by chymostrypsin, a 'transient tetrahedral intermediate' is formed in the active site (Stryer 1999). More stable interactions, however still reversible, can be formed between some amino acid residues of human serum albumin (HSA) and small ligands (e.g. the single free cysteine (Cys-34) forms disulfide bonds (RS-SR) with other sulfhydryl (SH)-containing compounds (Peters 1992, Section 3.3.1.3)).

- **Non-covalent interactions**

A protein and ligand are brought together by non-covalent interactions which generally fall into one of three groups: ionic, electrostatic or hydrophobic. Tight protein-ligand binding requires the interaction of complementary polar and lipophilic regions at the protein-ligand interface, without any repulsive interactions (Bohm and Schneider 2003). In chymotrypsin for example, there is a pocket close to the active site that binds the hydrophobic side-chains of aromatic amino acids tyrosine (Tyr), tryptophan (Trp) and phenylalanine (Phe), for specific recognition prior to peptide cleavage (Stryer 1999). Hydrogen bonding (H-bonding) and ionic interactions give specific geometry to a protein-ligand interaction (Williams and Ladbury 2003).

The ligand-protein binding interaction must be energetically favourable, and can be enthalpy- (heat energy required for the interaction to take place, ΔH (joules) or entropy- (disorder, ΔS, Joules $Kelvin^{-1}$) driven (Bohm 2003). Gibb's Free Energy (ΔG) must be a negative value for binding to occur spontaneously (Raffa 2003, Fig. 1). T equals temperature (Kelvin).

Eq. 1 $$\Delta G = \Delta H - T\Delta S$$

The enthalpic contribution is partly due to the breaking and forming of H-bonds (Bohm 2003). Water molecules within binding pockets solvate lipophilic groups (no H-bonding) and polar groups (H-bonding). Upon ligand binding and 'desolvation', the relative number of H-bonds broken between

the confined water molecules and protein groups (increase ΔH) and formed between released water and bulk water molecules (decrease ΔH) will contribute to an overall change in ΔH. However, it is also important to consider the relative strengths of the H-bonds being broken and formed (Williams and Ladbury 2003). The binding interaction will require Van der Waals forces (VdW) to be overcome, to facilitate the rearrangement of some amino acids in and around the binding pocket (Williams and Ladbury 2003). Breaking VdW contributes to a positive ΔH (therefore ΔG will increase). The better the 'fit' between a protein and its ligand, the lower the ΔH will be (Williams and Ladbury 2003).

The entropic contribution is often known as the 'hydrophobic effect'. Polar solvents do not interact favourably with apolar regions of a given ligand, and a hydrophobic binding pocket provides a more energetically favourable environment (Williams and Ladbury 2003). Solvent (water) will H-bond to the free protein and ligand in solution. Upon protein-ligand binding, the release of ordered water molecules will lead to an increase in ΔS (and therefore a decrease in ΔG). If the protein and ligand lose flexibility upon complexation, there will be a decrease in ΔS.

1.1.3 Molecular recognition in biotechnology and bioengineering

1.1.3.1 Antibody structure

Protein recognition systems in biotechnology commonly rely on the use of antibodies (Ab, also known as immunoglobulins (Ig)), to bring about strong, stable, specific molecular recognition. Abs are produced naturally by the immune system to help protect against potentially harmful foreign bodies (Hermanson et al. 1992).

Ab have a common structure composed of four protein chains bound together by flexible disulfide linkages. The variable region contains specific antigen (Ag)-binding sites. Ags posses an epitope that is recognised by this part of the Ab (Stryer 1999). The constant region contains sites for carbohydrate modification (Ab are glycoproteins). Five classes of antibody

(Ab) are produced by the human body: IgA, IgD, IgE, IgG and IgM (Hermanson et al. 1992). IgG have the widest range of interaction and specific IgG can be raised to a desired Ag that is injected into a host animal. Antiserum from the blood of the animal can be purified to isolate the specific polyclonal antibodies i.e. many Ab raised to the same antigen (Stryer 1999). Alternatively cells from the antiserum can be fused with mutant proliferating cells. Selected hybrid cells produce only specific Ab to the antigens injected into the host (monoclonal) (Lodish 2000). The high affinity of mono / polyclonal antibodies towards specific targets allows them to be exploited in a number of applications.

1.1.3.2 Immunoassays

Enzyme-linked immunoassays (ELISA) and radioimmunoassays use Ab for the specific detection of molecular targets. The most common method is the 'sandwich' assay, where a specific Ab is immobilised to a surface (e.g. microtitre plate), incubated with Ag and with a second specific Ab added. Binding of the latter can be detected directly (e.g. using a beta-galactosidase label) or indirectly using a secondary, labelled Ab (Stryer 1999) (Fig. 1.2).

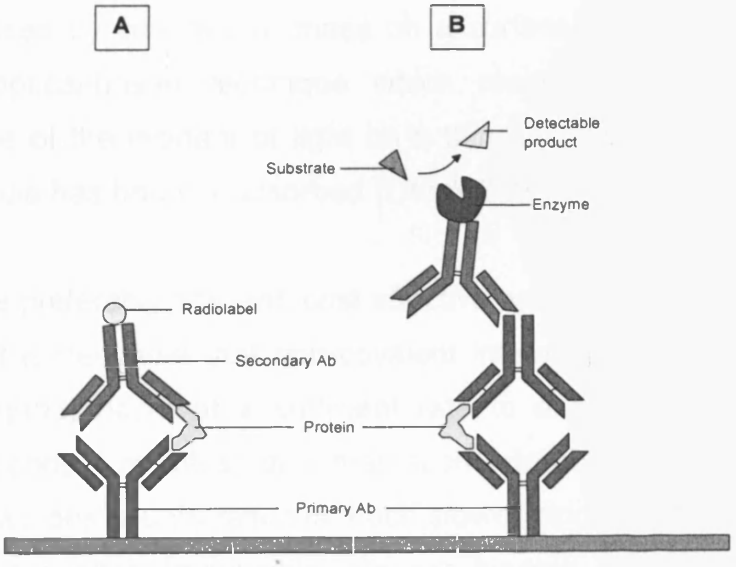


Fig. 1.2 Protein assays using specific antibody recognition. a) Radioimmunoassay **b)** ELISA 'sandwich' assay. *Adapted from Stryer 1999.*

1.1.3.3 Affinity separation of proteins

Protein separation systems require the selective recognition of a single protein from within a mixture. Metal-affinity (immobilised metal-ion affinity chromatography (Sharma and Agarwal 2001)), immuno-affinity (Ab-Ag) and bioaffinity (enzyme-ligand) interactions have been utilised in separation columns, as well as non-covalent ionic interactions (ion-exchange chromatography), hydrophobic interactions (reverse-phase chromatography) and size difference (size-exclusion chromatography / gel filtration).

1.1.3.4 Biosensors

Many types of biosensor have been described, and all rely on the same principle, that a specific biological interaction causes a change in the surface to which it is immobilised. (Hermanson et al. 1992). Two common biosensor formats for studying and detecting biomolecular interactions are the quartz crystal microbalance (QCM, qsense (Goteborg, Sweden)) and surface plasmon resonance (SPR, BiaCore (GE Healthcare, Chalfont St. Giles, Bucks, UK)). QCM works by detecting the change in resonance frequency caused by changes of mass on a surface (Pavey et al. 2001). SPR is an optical-based technique which measures changes in the reflection angle of the incident of light on a thin gold / silver surface, onto which a molecule has bound / adsorbed (Litvak 2003).

Biosensors are preferably efficient, cost effective and re-usable (Hermanson et al. 1992). It is desirable that non-covalent interactions (e.g. between a protein and ligand) occur at a sufficient rate to elicit a quick biosensor response (seconds / minutes) and that such interactions are reversible. Covalent interactions usually result in much slower binding kinetics (minutes / hours) and are often irreversible. Sensor binding capacities vary, for instance, flat biosensor surfaces require a high density of ligands for efficient recognition (Ahluwalia et al. 1992). Most sensors focus on single-molecule immobilisation whilst biosensor interfaces with biologically relevant architectures (e.g. lipid bilayers) have been shown to increase the range of possible interactions and resulting sensor effectiveness (Sergi et al. 2004).

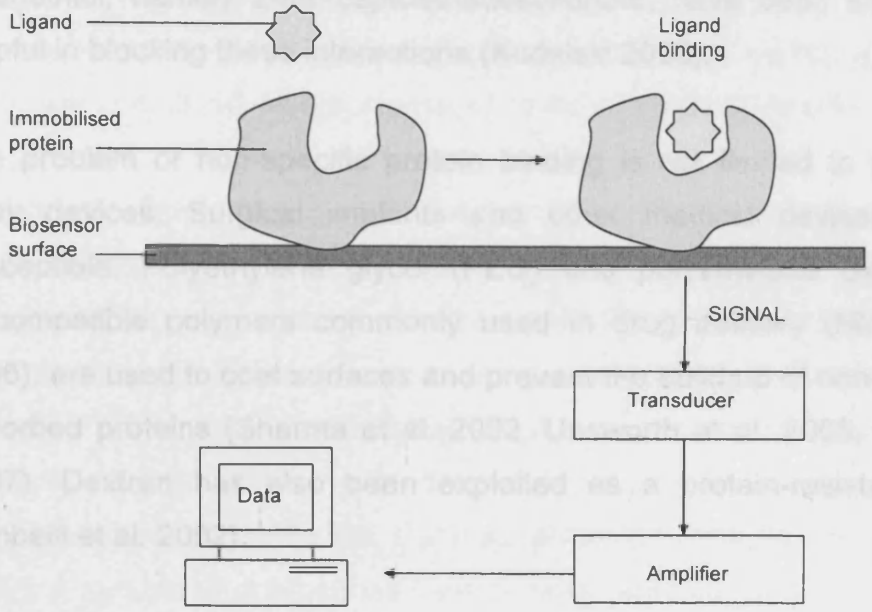


Fig. 1.3 General components of a biosensor. A protein-ligand interaction is used as an example. *Adapted from Hermanson 1992.*

1.1.3.5 Bioarrays

Bioarrays are useful tools for studying various biological interactions at high-throughput (Schneider 2003). Biomolecules e.g. DNA, protein, Ab or carbohydrates are immobilised onto solid supports (e.g. glass) in parallel arrays, in order to probe interactions with target ligands (Taussig 2003). Proteins can be 'spotted' in microdrops onto the surfaces. Conversely, an array of potential ligands can be covalently immobilised for binding to a single target protein (Schneider 2003). Protein-ligand binding is often detected by labelled probe methods (Cretich et al. 2006).

1.1.3.6 Non-specific protein binding to surfaces

Non-specific adsorption and aggregation of proteins on surfaces has had a limiting effect on sensor and array commercialisation (Meyer et al. 2006). Non-specific binding can irreversibly block binding sites, thus reducing the number of uses and the binding efficiency, leading to false signals with a wide distribution of binding energies (Johnson and Arnold 1995). Gold surfaces are widely used in SPR and QCM biosensors. However, proteins are especially susceptible to denaturing on gold surfaces, as inter-chain disulfide bonds can break and interact with surface thiols (Mrksich and Whitesides 1996). Self-assembled monolayers (SAMs, Section 1.3.1) of an

alkanethiol, namely 2-mercaptoethanesulfonate, have been shown to be helpful in blocking these interactions (Kudelski 2003).

The problem of non-specific protein binding is not limited to sensor and array devices. Surgical implants and other medical devices are also susceptible. Polyethylene glycol (PEG) and polyethylene oxide (PEO), biocompatible polymers commonly used in drug delivery (Nicolas et al. 2006), are used to coat surfaces and prevent the build up of non-specifically adsorbed proteins (Sharma et al. 2002, Unsworth et al. 2005, Zhou et al. 2007). Dextran has also been exploited as a protein-resistant coating (Ombelli et al. 2002).

These strategies have also been used to prevent non-specific binding in other techniques such as microarrays (Soultani-Vigneron et al. 2005). Serum albumin proteins have been used to block unreacted surface binding sites, but have also been shown to mask small ligands and to provide sites of interaction itself (Guo and Zhu 2006).

1.1.4 Synthetic molecular recognition

1.1.4.1 Artificial receptors

The creation of artificial receptors is desirable for the replacement of naturally occurring biomolecules in a number of biotechnology systems (Section 1.1.3). Although techniques such as ELISA are well established, the cost of producing specifically-labelled Ab is very high and the technique is sensitive to temperature, pH and solvent due to instability of the biological component (Nicholls and Rosengren 2002). Replacing antibody technology would also reduce the need for using laboratory animals (Nicholls and Rosengren 2002).

Host-guest chemistry (e.g. crown ethers) has been described to create receptors for small ligand 'templates' (Cram 1988 in Turner et al 2006). The shape of the receptor site is recreated by designing and synthesising a mimicking host structure. Each template requires the synthesis of a specific host. Although elegant and moderately effective this approach can be

extremely time-consuming and expensive. Naturally occurring molecules (e.g. cyclodextrins) have been used in a similar way, relying on design and synthesis or inefficient 'coincidental fit' of the template. (Allender et al. 1999).

Molecularly imprinted polymers (MIPs) are synthetic polymers that have been engineered in such a way as to introduce sites of target- or template-specific molecular recognition (Vulfsen et al. 1997). This approach uses the self-assembly of functional monomer units around a desired template molecule rather than pre-designed positioning of functional groups. The versatility of this approach provides an opportunity for imprinting of large, complicated macromolecules such as proteins (Nicholls and Rosengren 2002). A number of approaches for imprinting proteins have previously been described. These will be more fully discussed in Section 1.4.3.

1.2 Techniques for protein surface immobilisation

1.2.1 Introduction

There a number of different strategies for immobilising peptides, proteins, Abs and enzymes onto surfaces (Sections 1.2.3 and 1.2.4). Immobilisation can be specific or non-specific, reversible or irreversible and covalent or non-covalent (Brena and Batista-Viera 2006). Covalent modification can sometimes lead to denaturation and deactivation of a protein or enzyme (Brena and Batista-Viera 2006). More often than not, covalent immobilisation forms irreversible links which require harsh washing protocols for surface regeneration. Individual proteins frequently have pockets or domains for reversible, non-covalent binding to specific ligands (Section 1.1.2.3). Theoretically, if attachment is mono-valent, all molecules would have the same surface orientation thus giving rise to a homogenous surface (Carbajal et al. 2003). This would improve both the kinetics and the molecular specificity of surfaces designed for use in sensor and array applications (Sections 1.1.3.4 and 1.1.3.5). Surface orientation is fundamentally linked to the immobilisation strategy (Fig. 1.4).

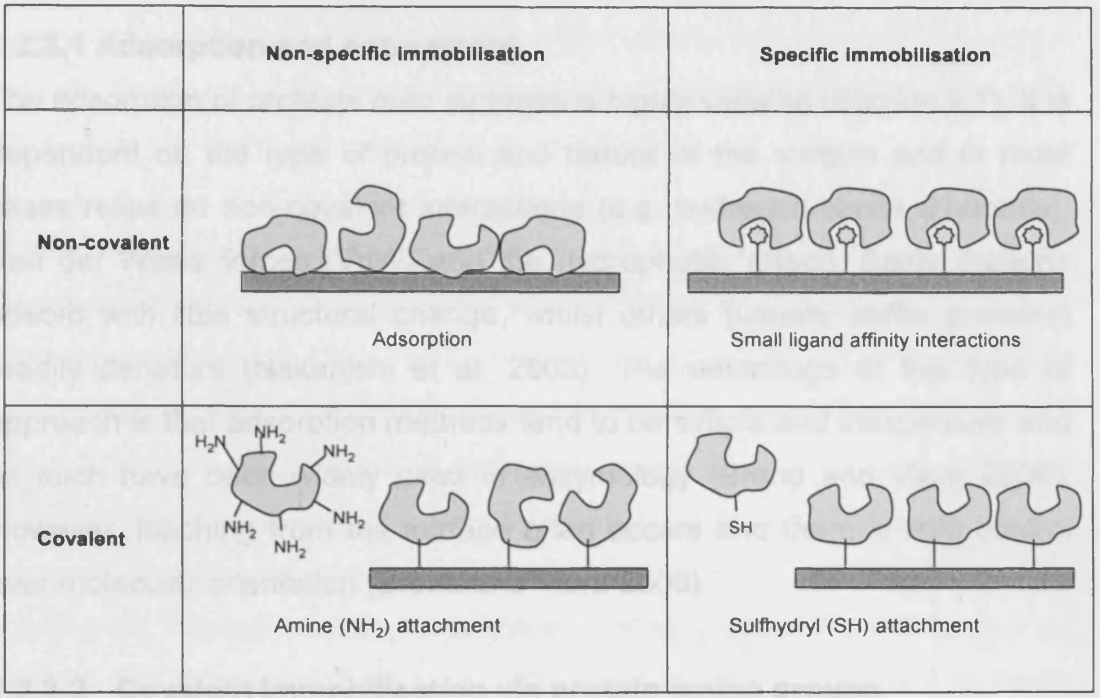


Fig. 1.4 Different protein immobilisation strategies lead to different surface orientations.

1.2.2 Choice of surface for protein immobilisation

The physical / chemical nature of the support is important to minimise conformational changes and retain the natural micro-environment of the protein upon immobilisation (Abad et al 2006). Surfaces possessing free hydroxyl groups are commonly used, since they can readily be derivatised in order to attach more reactive functionality to the surface (Hermanson et al. 1992). Silica, in its various forms, is particularly amenable to surface modification and is commonly used in a wide range of techniques, including chromatography, biosensors and arrays (Soultani-Vigneron et al. 2005, Lakhiari and Muller 2004, Liao et al. 2004) It comes in many forms such as porous gels or as thin layers on the surface of glass or silicon wafer. Silica forms strong covalent interactions with silane molecules which condense with surface hydroxyls in the presence of water (Section 5.1.2.3) (Dugas and Chavalier 2003).

1.2.3 Non-specific protein immobilisation

Non-specific immobilisation can be used as a general method for almost all proteins.

1.2.3.1 Adsorption and entrapment

The adsorption of proteins onto surfaces is highly variable (Section 8.1). It is dependent on the type of protein and nature of the surface and in most cases relies on non-covalent interactions (e.g. hydrogen-bonds (H-bonds), Van der Waals forces (VdW) and the hydrophobic effect). Some proteins adsorb with little structural change, whilst others (usually *softer* proteins) readily denature (Nakanishi et al. 2003). The advantage of this type of approach is that adsorption methods tend to be simple and inexpensive and as such have been widely used in enzymology (Brena and Viera 2006). However, leaching from the surface often occurs and there is little control over molecular orientation (Brena and Viera 2006).

1.2.3.2 Covalent immobilisation via protein amino groups

Amine / guanidine groups are abundant on protein surfaces (lysine and argenine amino acid residues respectively) and provide points for surface attachment. However, control of protein orientation is not usually possible using non-specific amine-coupling (Lee et al. 1993). Many protocols have been described for attaching proteins to amine-reactive surfaces. These include epoxy supports (Mateo et al 2006), zero-length coupling reagents (e.g. carbonyldiimidazole (CDI, Ong et al. 1994), 1-ethyl-3-(3-dimethylaminopropyl) carbodiimide (EDC (Section 4.1.4.3), Tyagi et al. 1998)) and spacers (Section 4.1.1, e.g. N-hydroxy succinimide (NHS) esters (Hermanson et al 1992), gluteraldehyde (Liu et al. 2004)). Gluteraldehyde is a useful spacer for silicon-silane surface chemistry (Liu et al. 2004). However, the reagent is quite toxic and poorly biocompatible.

1.2.4 Specific protein immobilisation

1.2.4.1 Covalent immobilisation via protein thiol groups

Protein surface thiol groups (i.e. SH on Cys residues) are much less common than amines and carboxylic acid groups, and often are completely absent (Wade 2006). Thiols have a nucleophilic chemistry similar to amines, and similar covalent immobilisation protocols are used e.g. EDC, epoxy and also iodoacetyl chemistry and maleimide esters (Ong et al. 1994;

Hermanson et al. 1992). Some proteins have a single free thiol group allowing for potentially homogenous surface attachment (e.g. HSA). Laminin peptide fragment was immobilised via its N-terminus Cys residue onto specific halide-SAMs on glass (Lee et al. 1993).

Protein thiols can form reversible covalent linkages (RS-SR) with surface-immobilised thiols e.g. thiosulfinate (Batista-Viera et al. 2006) or TNB-thiol agarose (Hermanson et al. 1992). It may be required to denature a protein slightly (break disulfide bridges) to provide reactive sites (Hermanson et al. 1992). This can be done using reducing agents such as dithiothreitol and beta-mercaptothiol. Abs can be cleaved at specific points using the enzymes pepsin and papain, and then reduced to provide sulfhydryls for specific Ab fragment binding (Hermanson et al. 1992). A more controlled method has been described using localised ultra-violet (UV) light to break intramolecular disulfide bonds. Surface immobilisation of proteins (Ab fragments and hydrolases) with specific orientation was thus achieved (Neves-Petersen 2005).

1.2.4.2 Specific affinity immobilisation

- **Small molecule affinity immobilisation (Ligands, ligand-analogues, inhibitors and drugs)**

Small molecules are easier to couple to surfaces with specific orientation as they have much fewer reactive groups. A free amine is particularly useful as there are many types of attachment chemistry that can be used (Section 1.2.3.2). N-acetylglucosamine (a natural ligand of insulin) was coupled in this way to silica beads for HPLC, and was able to purify the protein from pancreatic extract (Lakhairi and Muller 2004). For enzyme immobilisation, substrate analogues or inhibitors are often immobilised rather than the natural substrate, which may be cleaved or modified in the active site and released (Hermanson et al. 1992). p-Aminobenzamidine is a competitive inhibitor of trypsin (Hermanson et al. 1992). The interaction is tight in neutral buffer but easily reversed in mild acid buffer

Drugs with known protein binding can be immobilised to analyse the nature of the drug-protein interaction. Drugs of unknown protein binding capacity can be immobilised as probes, e.g. a gold-coated QCM electrode was derivatised with epoxy functionality to immobilise amine-terminated sulfa-drugs (Liu et al 2003). IgG was found to be a relatively strong binder from a selection of proteins with unknown affinities.

- **Carbohydrate / metal affinity immobilisation**

Some proteins (e.g. Ab, lectins) are post-translationally modified with carbohydrate chains in a process called glycosylation (Lakhiari and Muller 2004). For orientated protein immobilisation, specific sugar groups can be activated and coupled to complementary surface functionality (Section 1.4.3.2a (i)). Histidine (HIS)-containing proteins can be immobilised using common metal-affinity ligands (e.g. iminodiacetic acid (IDA), Section 1.4.3.2a (ii)).

- **Site-specific labelling / tagging (genetic modification) for immobilisation**

If a protein does not contain a specific site of attachment (e.g. His, Cys or carbohydrate) for affinity immobilisation it can be genetically engineered to do so. The N or C terminus of a protein is the ideal position, as it is often exposed, and located away from sites of post-translational modification (Nishino et al. 2006). Cys and His groups have been site-specifically tagged to proteins for orientated immobilisation (Ong et al. 1994; Liu et al 2006; Wade et al. 2006; Ahmed et al. 2006; Carjabal et al. 2003). Alternatively a protein can be genetically fused to one with binding capabilities by site-directed mutagenesis (Roy and Gupta 2006).

1.3 Controlling the surface distribution of proteins

1.3.1 Self-assembled monolayers

Self-assembled monolayers (SAMs) have been defined as a 'spontaneous organisation of molecules under thermodynamic equilibrium conditions into structurally well-defined and rather stable arrangements through a number

of non-covalent interactions' (Zhang 2002). Common SAMs include alkanethiol assembly on metal electrode surfaces (e.g. gold) and silane assembly on silicon oxide surfaces (Abad et al. 2006). The patterning of SAMs can be controlled at the micrometre and nanometre scale, and can subsequently be used to create specific protein-binding domains (Borini et al. 2007). Patterning of nanoparticles is discussed in Section 6.1. A number of patterning techniques have been utilised in biosensor and bioarray technology (Section 1.1.3.5, Borini et al. 2007).

1.3.1.1 Mixed SAMs

SAMs have been fabricated on silver surfaces using mixed alkanethiols (Liu et al. 2006). One short-chain alkanethiol was deposited with a longer-chain alkanethiol containing a derivatisable group (Fig. 1.5). The latter was used to specifically orientate the protein, RNase A, whilst controlling its surface density.

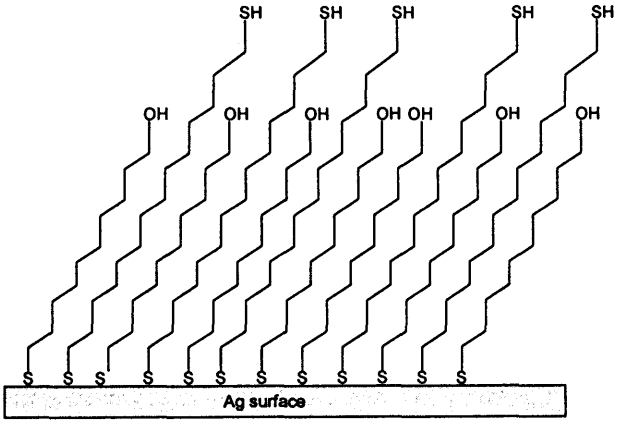


Fig. 1.5. Mixed SAM for controlled protein density.
Diagram adapted from Liu et al 2006.

1.3.1.2 Photolithography

Photolithography is a microfabrication technique used to create surface pattern, usually using UV light to selectively irradiate surfaces through a patterned mask (Mrksich and Whitesides 1996). A silicon surface is covered with a layer of photoresist (Sorribas et al. 2001; Mooney et al. 1996). A positive resist is damaged by UV and removed by a developing solution from areas not covered by the mask, whilst a negative resist becomes resistant to the developer upon UV irradiation and unexposed areas are selectively removed (Mrksich and Whitesides 1996) (Fig. 1.6). This creates

areas of silicon oxide which allows the selective patterning of functional SAMs. SAMs of silanes on silicon have been patterned using photolithography for antibody, protein or cell attachment (Mooney et al. 1996; Sorribas et al. 2001; Veiseh et al. 2004).

Nanolithographic techniques have recently been use to control the patterning of single protein molecules on surfaces for use in nanoarrays (Borini et al. 2007). These techniques utilise the nanoscale dimensions of an atomic force microscopy (AFM, Section 5.1.3.3)) tip, either to etch a protective layer as in photolithography (anodic oxidation, (Section 6.1.1.2), create electric fields (charge writing) or deposit molecules directly (dip-pen nanolithography) on selected areas (Naujoks and Stemmer 2004; Smith et al. 2003; Lee et al. 2006).

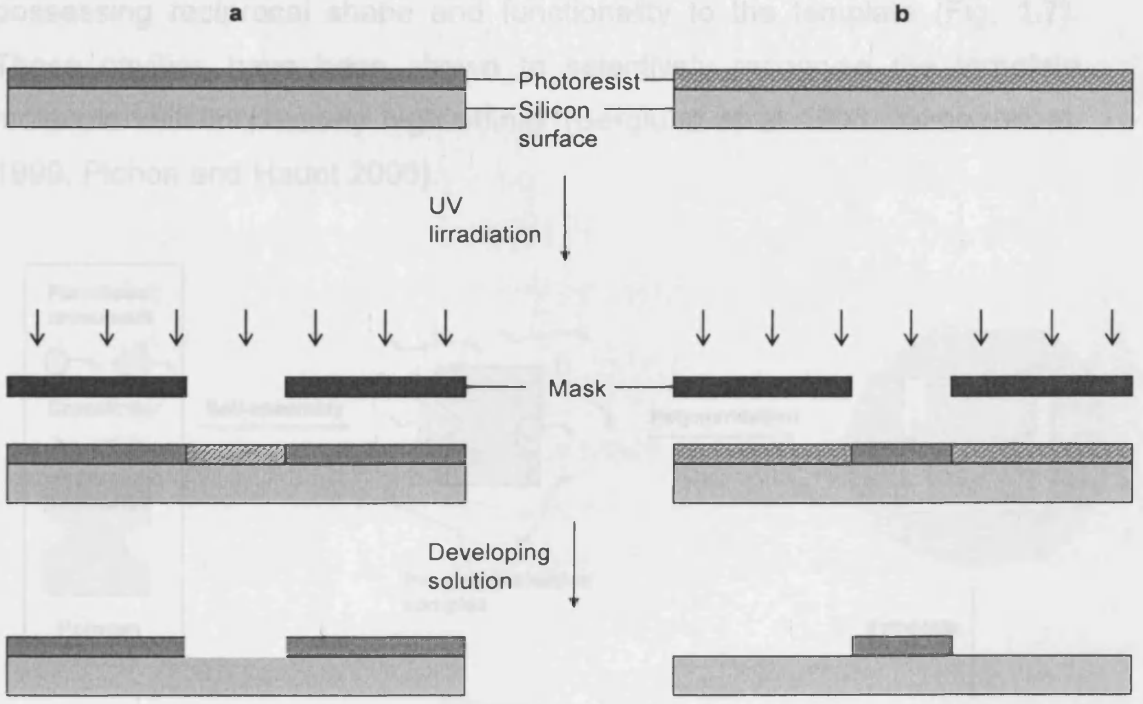


Fig. 1.6 Photolithography. A photoresist is irradiated with UV light through a patterned mask. **a**) Using a positive resist, UV-exposed areas are weakened and removed by developing solution. **b**) Using a negative resist, UV-exposed areas are strengthened and resistant to developing solution. The patterned surfaces can be used as made, or used to pattern other SAMs on the silicon surface. *Diagram adapted from Sorribas et al. 2002.*

1.3.1.3 Microcontact printing

Microcontact printing is a technique used to micropattern protein onto surfaces (Ruiz et al. 2006). Photolithography is used to prepare a 3D 'master' template (Mrksich and Whitesides 1996). The negative pattern is

cast in a polymer stamp, which is subsequently 'inked' with molecules (silanes, alkanethiols or proteins themselves) and used to 'print' a patterned SAM onto a flat surface (Lu et al. 2001; Shim et al. 2004).

1.4 Molecular imprinting

1.4.1 Introduction

Molecular imprinting uses template-directed polymerisation to prepare molecularly selective synthetic receptors. The process relies on the formation of a solution-phase complex between a template molecule and a number of polymerisable units. Polymerisation, in the presence of an excess of cross-linkable monomer, results in the permanent entrapment of the complex. Subsequent template removal gives rise to cavities possessing reciprocal shape and functionality to the template (Fig. 1.7). These cavities have been shown to selectively recognise the template molecule with moderately high affinity (Berglund et al 1998. Yilmaz et al. 1999. Pichon and Haupt 2006).

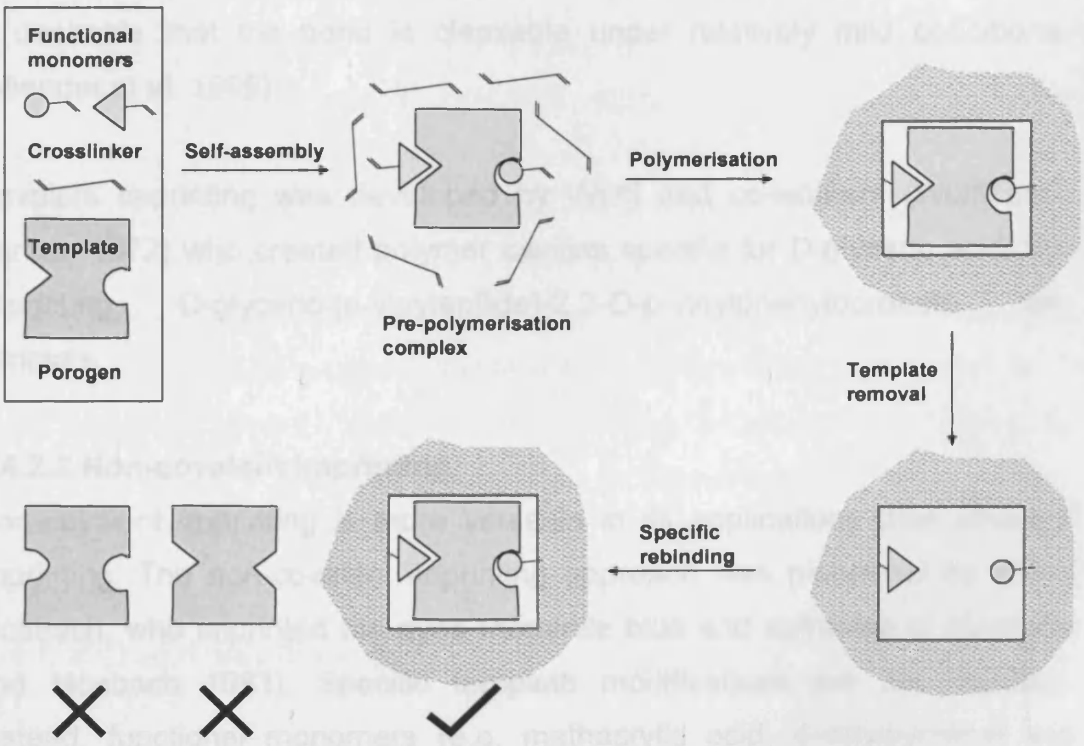


Fig. 1.7 General schematic of molecular imprinting.

Molecularly imprinted polymers (MIPs) are readily prepared, durable and potentially cost effective alternatives to biological recognition systems such as antibodies and enzymes (Rathbone 1995; Hjerten et al. 1997).

1.4.2 Preparation of molecularly imprinted polymers

One of key steps in the preparation of a molecularly imprinted polymer is the formation of a stable, solution phase, pre-polymerisation complex. In general this has been achieved either covalently or non-covalently.

1.4.2.1 Covalent imprinting

Covalent imprinting involves the formation of a reversible, covalent bond between the template and monomer (pre-polymerisation complex). Polymerisation results in template entrapment and the formation of a rigid imprint within the polymer (Vulfson et al. 1997). This approach is restricted by the types of bond that can be formed (e.g. ketals, aldehydes and boronate esters) and so certain functional groups must be present on the monomer and the template (Vulfson et al. 1997). Template removal requires that the covalent link between template and polymer is cleaved. Therefore it is desirable that the bond is cleavable under relatively mild conditions (Allender et al. 1999).

Covalent imprinting was developed by Wulff and co-workers (Wulff and Sarhan 1972) who created polymer cavities specific for D-glyceric acid, by imprinting D-glyceric-(p-vinylanilide)-2,3-O-p-vinylphenylboronate as template.

1.4.2.2 Non-covalent imprinting

Non-covalent imprinting is more versatile in its applications than covalent imprinting. The non-covalent imprinting approach was pioneered by Klaus Mosbach, who imprinted the dyes rhodanile blue and safranine O (Arshady and Mosbach 1981). Specific template modifications are not required. Instead, functional monomers (e.g. methacrylic acid, 4-vinylpyridine) are chosen to form a number of different interactions with the template such as hydrogen bonds (H-bonds), ionic bonds, electrostatic interaction (e.g. π-π

interactions between aromatic groups) and dispersive forces (e.g. Van der Waals) (Allender et al. 1999). There are a large number of possible monomer–template interactions and orientations and this has proven difficult to model and predict. Directional bonds (e.g. H- bonds, ionic) are favourable for specific template rebinding, as specific orientation is required. H-bonds are also distance-dependent and predominate in molecular imprinting (Komiyama et al. 2003). Due to the relatively weak interactions between the template and monomer, allowing the polymer more conformational flexibility, populations of non-covalent imprinted polymer sites tend to be less homogeneous than those generated using the covalent approach. In addition non-specific binding can be problematic due to the large excess of functional monomer needed to ensure formation of adducts (Komiyama et al. 2003). However, rebinding kinetics are much faster therefore non-covalent materials can be used in formats such as high performance liquid chromatography (HPLC) (Kempe and Mosbach 1995).

1.4.2.3 Semi-covalent imprinting

- **Sacrificial spacer approach**

To take advantage of the rigidity and stability of covalent imprints and the fast rebinding kinetics of non-covalent imprinting, a 'sacrificial spacer' method was developed (Whitcombe et al. 1995). Monomers were linked covalently to the template (cholesterol) via spacer molecules prior to the polymerisation step. These spacers were cleaved from the site along with the template leaving an imprint with a phenolic moeity for non-covalent template rebinding. Importantly the template removal step also releases a small 'sacrificial spacer' molecule thus providing addition space within the cavity for efficient template rebinding. A single binding affinity was observed, characteristic of biological receptors (Whitcombe et al. 1995).

1.4.3 Protein imprinting

1.4.3.1 Imprinting in aqueous solvents

In general, imprinting in water has been shown to be less efficient than imprinting in organic solvents. In general, protein imprinting has been

carried out in aqueous solvents with the aim of retaining physiological conformation and function (Turner et al 2006). However, proteins may also retain their stability in some dry organic solvents (e.g. ethylacetate) (Braco et al 1990). This has been utilised in 'bio-imprinting' to imprint proteins themselves with small ligand molecules (Braco et al 1990, Yu et al. 2002). The possibility of imprinting in organic solvents should not be ruled out. In aqueous environments, low complementarity between hydrophilic protein surfaces and the hydrophobic polymer leads to less favourable rebinding interactions (Allender et al. 1999). Water molecules compete for hydrogen bonds, and effectively solvate charged template and monomer species, disfavouring assembly of the pre-polymerisation complex. Instead other non-covalent interactions such as π-π stacking, ionic bonds and hydrophobic bonding must be relied upon to bring about complex formation and template binding (Ramstrom and Ansell 1998). The binding pockets of proteins often use entropically favourable hydrophobic interactions for specific ligand binding (Section 1.1.2.3), which could be used as an advantage of carrying out imprinting in aqueous solvents (Dauwe and Sellergren 1995).

1.4.3.2 Bulk imprinting of protein templates

Conventional bulk molecular imprinting is generally perceived as being inappropriate for large molecules such as proteins. Imprinting requires a certain polymer rigidity to maintain the shape of imprinted sites but also enough flexibility for the induced fit (Stryer 1999) of template rebinding and porosity for diffusion of protein through the matrix (Tong et al 2001). Protein is often removed using denturants such as urea, Tween or SDS (Kempe and Mosbach 1995; Shi and Ratner 2000; Tong et al 2001). During the imprinting process protein may become permanently entrapped inside the cross-linked polymer network and covalent modification of the protein during free-radical polymerisation can also be a problem (Jeans 2004). Subsequently during rebinding the mass transfer is poor (Nicholls and Rosengren 2002). Heterogeneity of the binding sites can arise from damage during polymer processing, imprinting of denatured protein conformations, protein aggregates (incompatibility with hydrophobic polymer, Section

8.1.1.2) and different protein conformations (as appear in solution) (Turner et al. 2006). This decreases the rebinding efficiency of the template.

Despite the drawbacks of bulk imprinting, selective protein recognition has been demonstrated in bulk polyacrylamides (Liao et al. 1996; Hjerten et al 1997). Selectivity was shown for cytochrome C (Cyt. C), haemoglobin and transferrin for their respective imprints (Liao et al. 1996). A reduced proportion of crosslinking was shown to improve diffusion of the proteins within imprinted gels. The mechanism of recognition was proposed to be multiple, weak, electrostatic interaction between the proteins and polymers.

1.4.3.3 Alternative protein imprinting approaches

A wide variety of imprinting techniques have been used to overcome the difficulties of bulk protein imprinting (Turner et al. 2006; Bossi et al. 2006; Hansen 2007). Surface imprinting of thin polymer films, has been shown to give rise to improved mass transfer and greater binding site homogeneity (Nicholls and Rosengren 2002). This approach has been applied to the surface of beads as well as flat surfaces and a range of template proteins and polymers have been reported (Shi et al. 1999; Tong et al. 2001; Hayden et al. 2003; Lin et al 2004; Rick and Chou 2005; Guo et al. 2005; Pang et al. 2006; Bonini et al. 2007).

a. Protein adsorption onto flat surfaces

A novel flat surface protein imprinting approach was described by Shi et al. 1999 (Fig. 1.8). Radiolabelled protein was adsorbed onto a hydrophilic mica surface and coated with sugar to prevent denaturation or degradation of the protein. A thin fluoropolymer film was then deposited onto the surface using radio frequency glow-discharge plasma deposition. The protein template and mica surface were removed leaving specific nanocavities. 'Soft' proteins such as α-lactalbumin did not work as well as 'harder' proteins, such as lysozyme (Lyz), due to conformational changes upon adsorption to the mica (Shi and Ratner 2000).

b. Microcontact printing of proteins onto flat surface polymer

An alternative flat surface technique, microcontact printing, was used to imprint cells, viruses and enzymes (Hayden et al. 2003). Lyz crystal layers on quartz glass were stamped onto polymer-coated quartz crystals. A specific QCM sensor signal was observed for template rebinding to the Lyz-imprinted polymer. Using a similar approach, thin polymer films of aminophenylboronic acid (APBA) were imprinted with Lyz and Cyt. C, and grafted onto glass slide supports (Rick and Chou 2005a). The imprints were selective but the film quickly became unstable in air and in buffer. Bacterial degradation of trapped protein in the polymer was suggested to be responsible. This research was expanded to look at the imprinting of the two proteins together, and polymer layers were formed on gold-coated quartz crystals (Rick and Chou 2005b). The individual proteins did not bind to the dual-template imprinted polymer and it was concluded that MIP QCM sensors could potentially be used for looking at protein-protein interactions. Repeated measurements with the electrode indicated site degradation due to instability. The poor stability of soft polymers, especially thin films, leads to a heterogeneous population of binding sites and poor re-usability (Bossi et al. 2006). Fixing the polymer to a solid surface improves stability.

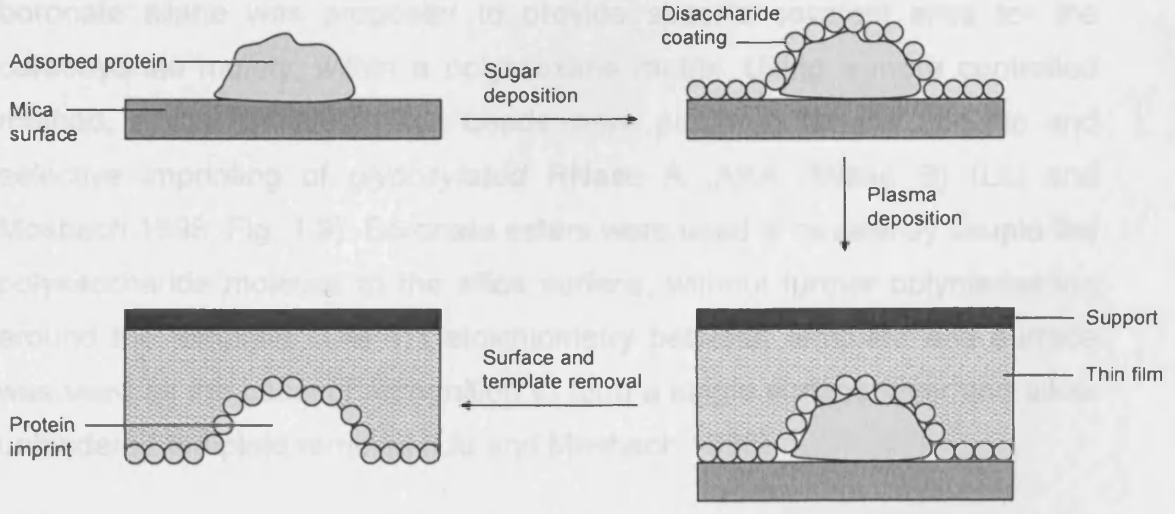


Fig. 1.8 Flat surface imprinting of proteins using molecular self-assembly. *Adapted from Shi and Ratner 1999.*

c. Covalent immobilisation of proteins on a solid surface

The 2-dimensional nature of thin films improves issues of protein entrapment but can lead to partial imprints, heterogenous sites and reduced capacity

(Bossi et al 2001, Rick and Chou 2005). Covalent immobilisation of proteins to a surface before polymerisation improves homogeneity by imparting greater control over the organisation of proteins to be imprinted (Section 1.2). This has been demonstrated using reversible aldehyde chemistry to fix proteins onto beads (Bonini et al, Shiomi et al 2005) and nanowires (Li 2006)

d. Specific / Affinity interactions between protein and polymer

Protein recognition relies upon the formation of multipoint interactions (electrostatic/hydrophobic) between the protein and polymer. Although some template re-binding specificity has been shown with these imprints, improved efficiency is required (Nicholls and Rosengren 2002). The most promising approaches have used affinity-based recognition of the protein template and its imprint (Liu and Mosbach 1998, Vaidya et al. 2000). Affinity-based recognition has been used previously in boronate affinity, immobilised metal affinity and enzyme-ligand chromatography (Section 1.1.3.3).

i. Boronate / metal-affinity interactions

The first protein imprint was reported by Glad et al. 1985, who used different functional silane monomers (including boronate silane) for molecular imprinting of a glycoprotein, transferrin, on porous silica microbeads. The boronate silane was proposed to provide specific covalent sites for the carbohydrate moiety, within a polysiloxane matrix. Using a more controlled method, epoxy-activated silica beads were prepared for the specific and selective imprinting of *glycosylated* RNase A (AKA RNase B) (Liu and Mosbach 1998, Fig. 1.9). Boronate esters were used to covalently couple the polysaccharide moieties to the silica surface, without further polymerisation around the template. The 1:1 stoichiometry between template and surface was used as the basis of recognition to form a single surface layer and allow unhindered template removal (Liu and Mosbach 1998).

The potential use of metal-affinity recognition for protein imprinting was described by Frances Arnolds' group ((Mallik et al. 1994a; Mallik et al. 1994b). The first example of fixing a protein on a surface for use in molecular imprinting was demonstrated by the group of Mosbach (Kempe et al. 1995) (Fig. 1.10). Surface imprinting was carried out on methacrylate-derivatised

silica particles using metal-ligand complexes. During polymerisation the chelating monomer N- (4-vinylbenzyl)iminodiacetic acid was co-ordinated to histidines on RNase by Cu^{2+} ions. The polymerisation mediated protein attachment to the silica. The imprint selectively adsorbed RNase A against reference BSA (Kempe et al. 1995). Later, selective separation of a number of proteins (BSA, RNase A, Lyz, chymotrypsin and horseradish peroxidise) was achieved using APBA- and IDA-immobilised silica beads (Liu and Mosbach 1998).

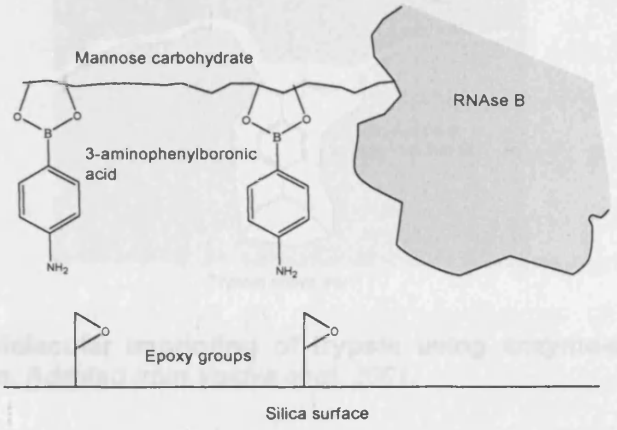


Fig. 1.9 Boronate-affinity molecular imprinting of RNAse B. Covalent links are formed between the glycoprotein and functional monomer, followed by surface attachment. *Adapted from Liu and Mosbach 1998.*

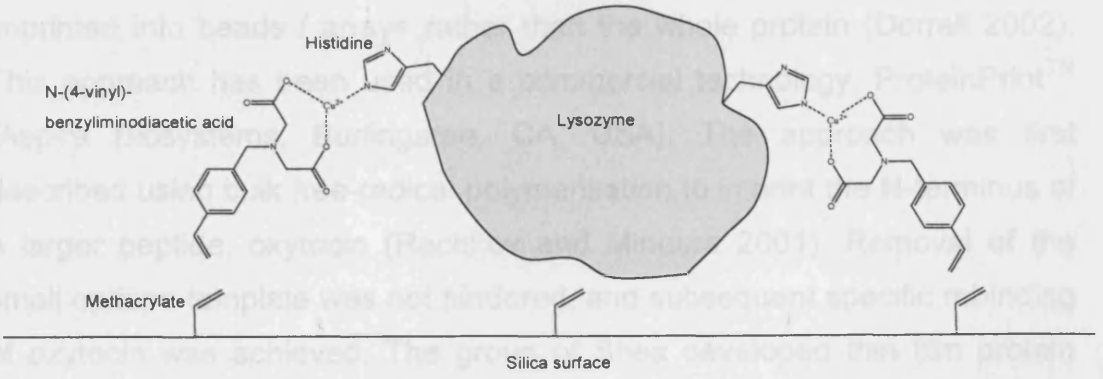


Fig. 1.10 Metal-affinity molecular recognition for lysozyme imprinting. Copper ions coordinate with HIS side-chains and a functional monomer. Polymerisation fixes the protein-monomer complex to the bead surface. *Adapted from Kempe et al. 1995.*

ii. Enzyme-inhibitor / ligand analogue interactions

An enzyme-inhibitor complex (trypsin-N-acryloyl para-aminobenzamidine (PABA)) was imprinted in polyacrylamide gels (Vaidya et al. 2001, Fig. 1.12). Trypsin was cleaved after bulk polymerisation leaving PABA functionality in the polymer cavities. Selective rebinding for trypsin over the closely related

enzyme, chymotrypsin was demonstrated for these MIPs illustrating the importance of shape complementarity (Vaidya et al. 2001). A non-imprinted polymer (NIP) prepared with PABA showed only a small amount of template rebinding. Template rebinding was not observed for polymers imprinted with trypsin only, nor with a hydrochloric acid (HCl)-blocked PABA, showing the importance of the strong enzyme-inhibitor bond.

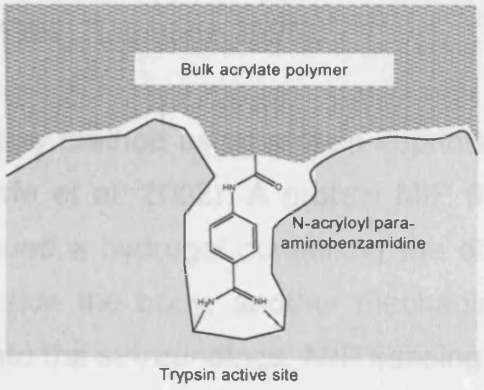


Fig. 1.11 Molecular imprinting of trypsin using enzyme-affinity interactions. *Adapted from Vaidya et al. 2001.*

e. Epitope imprinting approach

A novel approach to protein imprinting is called the 'epitope approach'. A portion of the target protein (often the specific c-terminal sequence) is imprinted into beads / arrays rather than the whole protein (Dorrell 2002). This approach has been used in a commercial technology, ProteinPrint™ (Aspira Biosystems, Burlingame, CA, USA). The approach was first described using bulk free-radical polymerisation to imprint the N-terminus of a larger peptide, oxytocin (Rachkov and Minoura 2001). Removal of the small epitope template was not hindered, and subsequent specific rebinding of oxytocin was achieved. The group of Shea developed thin film protein imprints using the epitope approach (Nishino et al. 2007). C-terminus epitopes of Cyt. C, alcohol dehydrogenase and BSA were covalently linked to flat silica surfaces using EDC / NHS chemistry, followed by polymerisation of surrounding monomer solution. The surface and template were peeled from the polymer after soaking overnight in a buffer solution to leave non-covalently imprinted cavities.

1.4.3.3 Potential applications

Effective synthetic protein recognition systems are particularly sought after and such technology would find applications in biosensing, bioseparation, biotechnology and analytical biochemistry. MIPs are potentially useful in protein separations, drug delivery, as antibody replacements in enzyme-linked immunosorbent assays (ELISA) and radioimmunoassays, or as enzyme replacements in biosensors, biomaterials and biocatalysts (Hjerten et al. 1997; Shi et al 1999; Rathbone 1995).

A potential drug delivery method using protein imprints has been described using hydrogels (Byrne et al. 2002). A protein MIP film specific for a cell receptor would surround a hydrogel containing the drug of interest. Once bound to a tissue inside the body, another mechanism could induce the release of the drug into the surroundings. MIP sensing technology may one day be used as an alternative to chromatography in the detection of biological warfare agents (Huang et al. 2004).

1.4.3.4 Future outlook for protein imprinting

Despite the wide range of protocols, a number of problems are still associated with imprinting proteins including site heterogeneity, non-specific binding and protein aggregation on the polymer backbone, complementary interactions between amino acid side-chains of non-template proteins and the polymer and sensitivity of proteins to environmental conditions e.g. denaturation at surfaces, harsh washing conditions. The use of specific ligand interactions, although exciting, would require the identification of a specific protein-ligand pair for each proposed application. Despite the fairly large number of reported protein imprints, none has approached the high affinity and specificity demonstrated by antibodies.

1.5 A novel protein imprinting concept

A number of different approaches have been used to prepare molecular imprints of proteins. However, due to a range of issues associated with molecular size, solubility and conformational flexibility, a generic and effective technique has not emerged. This project is based on a novel protein imprinting concept and proposes the use of a specific, high affinity, ligand interaction to control protein organisation such that a resulting imprinting step gives rise to an ordered array of homogeneous surface-imprinted sites. A schematic of the concept is given in Fig. 1.12.

Key to the concept is the ability to modify an appropriate flat surface with functional groups such that their distribution is controlled at the nanometer scale. Ligand attachment and subsequent specific protein immobilisation would give rise to a dispersed protein layer. Surface-initiated, controlled polymerisation (Ruckert, Hall and Sellergren, 2002) would be used to part-cover the protein. Template removal would reveal specific protein-shaped 'cups' within the polymer. Importantly, the controlled and specific immobilisation strategy would ensure that template protein was uniformly orientated on the surface. This would result in a 'cup' population that was both dispersed and homogenous.

The most likely application for this protocol would be in the field of biosensors, where surface capacity is not important and flat, functionalised surfaces can be incorporated into e.g. QCMs and SPR.

1.6 Aims and objectives

1.6.1 Aim

The focus of this project was consideration of fundamental aspects of surface nanometer-scale patterning and protein-surface interactions with the aim of preparing an ordered array of surface protein. This is represented in 1-3 of Fig. 1.12.

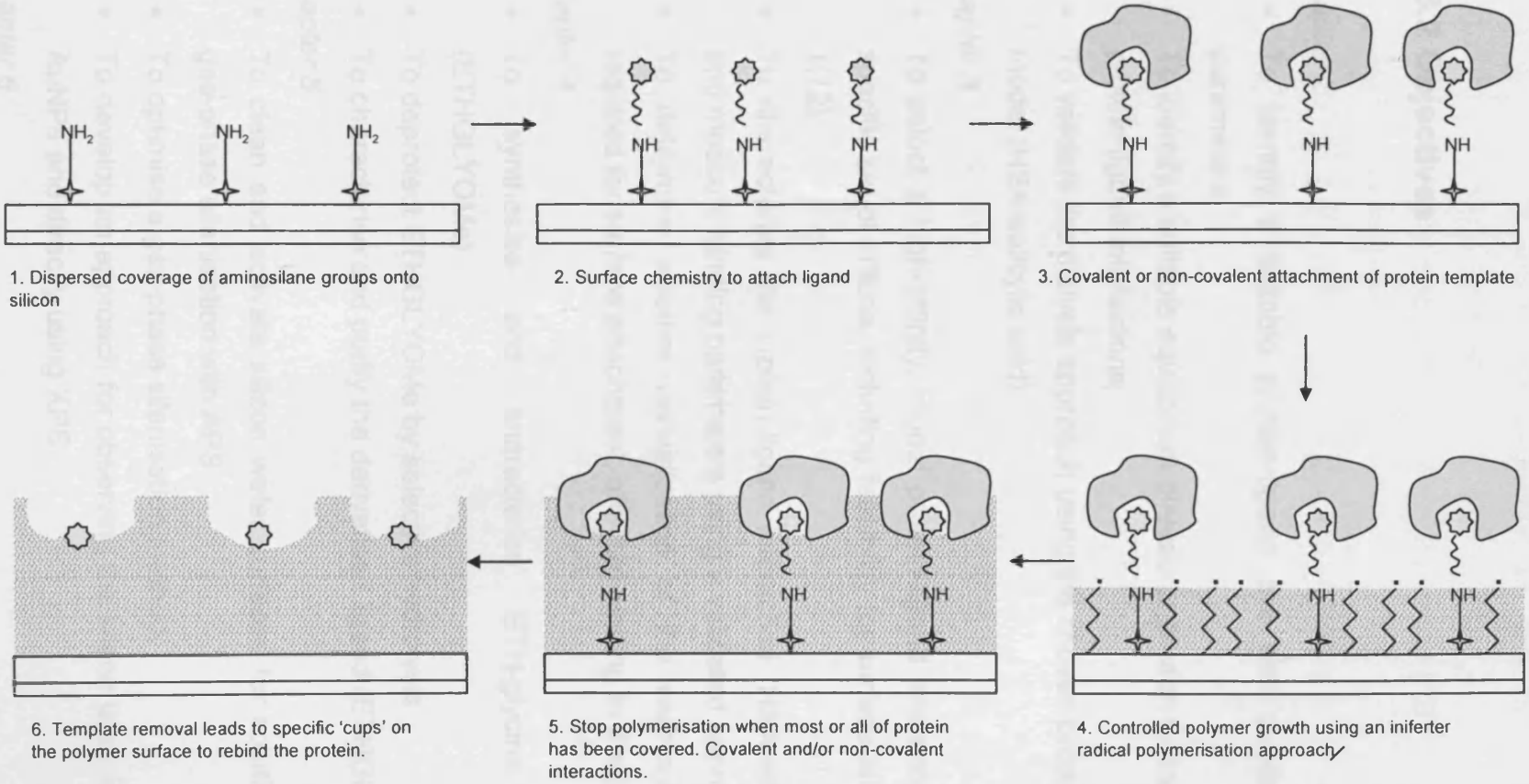


Fig. 1.12 Scheme for creating a specific protein imprint on a flat surface. A flat surface (e.g. silicon wafer) would be derivatised with a controlled distribution of functional molecules (e.g. aminosilane groups) (1). This surface would then be coupled (via e.g. covalent amide bonds) to high affinity ligands (2) for a model protein (3). Controlled layer-by-layer polymerisation (4) around surface-immobilised protein would prevent complete protein entrapment (5) and hindered mass transfer. Protein removal would leave specific cavities in the polymer with a uniform orientation (6).

1.6.2 Objectives

Chapter 2

- To identify a suitable protein-ligand pair with published binding parameters
- To identify a suitable equilibrium dialysis approach for measuring protein-ligand interactions
- To validate the dialysis approach using the chosen protein-ligand model (HSA-salicylic acid)

Chapter 3

- To select a high-affinity, model protein-ligand interaction that met a specific set of criteria, including feasibility for surface attachment (Fig. 1.12).
- To characterise the protein-ligand interaction (HSA-ethacrynic acid) and measure binding parameters using a validated approach.
- To determine whether derivatisation of the carboxylate of ETH, required for surface attachment, affected binding to the protein.

Chapter 4

- To synthesise and characterise ETH-glycine methylester (ETHGLYOMe)
- To deprotect ETHGLYOMe by selective hydrolysis
- To characterise and purify the derivatised ligand (ETHGLY)

Chapter 5

- To clean and activate silicon wafer surfaces for solution-phase and gas-phase silanisation with APS
- To optimise a gas-phase silanisation method.
- To develop an approach for observing the silane layer indirectly using AuNPs and directly using XPS.

Chapter 6

- To prepare a flat surface with a controlled dispersion of functional silane molecules.

- To indirectly monitor the dispersion of APS by measuring AuNP surface binding densities
- To investigate the factors that influence AuNP binding to APS derivatised surfaces.
- To keep the surrounding surface underivatised for a later bottom-up surface polymerisation (Fig. 1.12).

Chapter 7

- To covalently link a high-affinity ligand (or its derivative) to dispersed APS groups on a silicon surface using an amide coupling reagent.
- To characterise ligand immobilisation using AFM and / or XPS

Chapter 8

- To characterise the non-specific adsorption and desorption of the model protein on piranha (PNA) and aminopropyltriethoxysilane (APS)-treated silicon surfaces.
- To selectively immobilise and orientate the model protein onto silicon surfaces derivatised with the dispersed high-affinity ligand.

References

Abad, J. M. et al. 2006. Immobilisation of proteins on gold surfaces. In: Guisan, J.M. ed. *Immobilisation of enzymes and cells.* Humana Press, pp. 229-238.

Ahluwalia, A. et al. 1992. A comparative study of protein immobilization techniques for optical immunosensors. *Biosensors and Bioelectronics* 7(3), pp. 207-214.

Ahmed, S. R. et al. 2006. Controlling the orientation of immobilized proteins on an affinity membrane through chelation of a histidine tag to a chitosan-Ni++ surface. *Journal of Membrane Science* 280(1-2), pp. 553-559.

Allender, C. J. et al. 1999. Molecularly imprinted polymers- preparation, biomedical applications and technical challenges. *Progress in medicinal chemistry* 36, pp. 235-291.

Arshady, R. and Mosbach, K. 1981. Synthesis of substrate-selective polymers by host-guest polymerization. *Makromol. Chem* 182, pp. 687-692.

Banner, D. W. 2003. Principles of enzyme-inhibitor design. In: Bohm, H.J. and Schneider, G. eds. *Protein-ligand interactions.* Wiley-VCH, p. 163.

Bohm, H. J. 2003. Prediction of non-bonded interactions in drug design. In: Bohm, H.J. and Schneider, G. eds. *Protein-ligand interactions.* Wiley-VCH, pp. 4, 5.

Bonini, F. et al. 2007. Surface imprinted beads for the recognition of human serum albumin. *Biosensors and Bioelectronics* 22(9-10), pp. 2322-2328.

Borini, S. et al. 2007. Advanced nanotechnological approaches for designing protein-based "lab-on-chips" sensors on porous silicon wafer. *Recent patents on DNA & gene sequences* 1, pp. 1-7.

Bossi, A. et al. 2001. Surface-grafted molecularly imprinted polymers for protein recognition. *Anal. Chem.* 73, pp. 5281-5286.

Bossi, A. et al. 2007. Molecularly imprinted polymers for the recognition of proteins: The state of the art. *Biosensors and Bioelectronics* 22(6), pp. 1131-1137.

Braco, L. et al. 1990. Production of abiotic receptors by molecular imprinting of proteins. *Proc. Natl Acad. Sci. USA* 87, pp. 274-277.

Brena, B. M. and Batista-Viera, F. 2006. Immobilisation of enzymes. A literature survey. In: Guisan, J.M. ed. *Immobilisation of enzymes and cells.* Humana Press, pp. 15, 17, 23-25.

Berglund, J. et al. 1998. Selection of phage display combinatorial library peptides with affinity for a yohimbine imprinted methacrylate polymer. *Analytical communications* 35, pp. 3-7.

Byrne, M. E. et al. 2002. Molecular imprinting within hydrogels. *Advanced Drug Delivery Reviews* 54(1), pp. 149-161.

Carbajal, M. L. et al. 2003. Oriented immobilization of proteins on grafted porous polymers. *Nuclear Instruments and Methods in Physics Research Section B: Beam Interactions with Materials and Atoms* 208, pp. 416-423.

Cretich, M. et al. 2006. Protein and peptide arrays: Recent trends and new directions. *Biomolecular Engineering* 23(2-3), pp. 77-88.

Dauwe, C. and Sellergren, B. 1996. Influence of template basicity and hydrophobicity on the molecular recognition properties of molecularly imprinted polymers. *Journal of Chromatography A* 753(2), pp. 191-200.

Dorrell, S. 2002. Novel templates for rapid protein separation. *Drug discovery today* 7(10), pp. 539-540.

Dugas, V. and Chevalier, Y. 2003. Surface hydroxylation and silane grafting on fumed and thermal silica. *Journal of Colloid and Interface Science* 264(2), pp. 354-361.

Glad, M. et al. 1985. Use of silane monomers for molecular imprinting and enzyme entrapment in polysiloxane-coated porous silica. *Journal of Chromatography A* 347, pp. 11-23.

Guo, T.-Y. et al. 2005. Chitosan beads as molecularly imprinted polymer matrix for selective separation of proteins. *Biomaterials* 26(28), pp. 5737-5745.

Guo, A. and Zhu, X. Y. 2007. Chapter 4: The critical role of surface chemistry in protein microarrays. In: predki, P. ed. *Functional protein microarrays in drug discovery.* CRC Press, pp. 53-71.

Hansen, D. E. 2007. Recent developments in the molecular imprinting of proteins. *Biomaterials* 28(29), pp. 4178-4191.

Hayden, O. et al. 2003. Mass-sensitive detection of cells, viruses and enzymes with artificial receptors. *Sensors And Actuators B-Chemical* 91(1-3),pp.316-319.

Hermanson, G. T. et al. 1992. *Immobilised affinity ligand techniques.* Academic Press, Inc., pp. 2, 57, 98, 107, 210, 215, 218, 220, 317, 359, 410, 411.

Hjert,n, S. et al. 1997. Gels mimicking antibodies in their selective recognition of proteins. *Chromatographia* 44, pp. 227-234.

Huang, J.-T. et al. 2004. Template imprinting amphoteric polymer for the recognition of proteins. *Journal of Applied Polymer Science* 95, pp. 358-361.

Jeans, C. W.. Molecularly imprinted polyacrylamide gels for protein recognition. PhD 'Thesis' Cardiff University 2004.

Johnson, R. D. and Arnold, F. H. 1995. The Temkin isotherm describes heterogeneous protein adsorption. *Biochimica et Biophysica Acta (BBA) - Protein Structure and Molecular Enzymology* 1247(2), pp. 293-297.

Kempe, M. et al. 1995. An approach towards surface imprinting using the enzyme ribonuclease A. *Journal of Molecular Recognition* 8, pp. 35-39.

Kempe, M. and Mosbach, K. 1995. Separation of amino-acids, peptides and proteins on molecularly imprinted stationary phases. *Journal of Chromatography A* 691(1-2), pp. 317-323.

Komiyama, M. et al. 2003. Chapter 3 Experimental methods (1) Procedures of molecular imprinting.*Molecular imprinting. From fundamentals to applications.* Wiley VCH Verlag GmBH & Co. KGaA, p. 40.

Komiyama, M. et al. 2003. Chapter 2. Fundamentals of molecular imprinting.*Molecular imprinting. From fundamentals to applications.* Wiley VCH Verlag GmBH & Co. KGaA, p. 17.

Kudelski, A. 2003. Influence of electrostatically bound proteins on the structure of linkage monolayers: adsorption of bovine serum albumin on silver and gold substrates coated with monolayers of 2-mercaptoethanesulphonate. *Vibrational Spectroscopy* 33, pp. 197-204.

Lakhiari, H. and Muller, D. 2004. Insulin adsorption on coated silica based supports grafted with N-acetylglucosamine by liquid affinity chromatography. *Journal of Chromatography B* 808(1), pp. 35-41.

Lee, M. et al. 2006. Protein nanoarray on Prolinker surface constructed by atomic force microscopy dip-pen nanolithography for analysis of protein interaction. *Proteomics* 6, pp. 1094-1103.

Lee, Y. W. et al. 1993. Electrophilic siloxane-based self-assembled monolayers for thiol-mediated anchoring of peptides and proteins.*Langmuir* 9,pp.3009-3014.

Liao, J. L. et al. 1996. Novel support with artificially created recognition for the selective removal of proteins and for affinity chromatography. *Chromatographia* 42(5-6), pp. 259-262.

Liao, W. et al. 2004. Characterization of protein immobilization on alkyl monolayer modified silicon(1 1 1) surface. *Sensors and Actuators B: Chemical* 101(3), pp. 361-367.

Li, Y. et al. 2006. Protein recognition via surface molecularly imprinted polymer nanowires. *Analytical chemistry* 78, pp. 317-320.

Lin, T. Y. et al. 2004. Determination of albumin concentration by MIP-QCM sensor. *Biosensors & Bioelectronics* 20(1), pp. 75-81.

Litvak, L. 2003. *Surface Plasmon Resonance* [WWW]. Available at: http://www.inano.dk/sw2565.asp [Accessed: 21st march 2005].

Liu, X. et al. 2004. Synthesis of amino-silane modified superparamagnetic silica supports and their use for protein immobilization. *Colloids and Surfaces A: Physicochemical and Engineering Aspects* 238(1-3), pp. 127-131.

Liu, X. et al. 2006. Characterization of protein immobilisation at silver surfaces by near edge X-ray absorption fine structure spectroscopy. *Langmuir* 22, pp. 7719-7725.

Liu, Y. et al. 2003. Quartz crystal biosensor for real-time monitoring of molecular recognition between protein and small molecular medicinal agents. *Biosensors and Bioelectronics* 19(1), pp. 9-19.

Liu, X.-C. and Mosbach, K. 1998. A novel separation material for boronate affinity chromatography and immobilized metal affinity chromatography. *Analytica Chimica Acta* 435, pp. 3-8.

Lodish, H. et al. 2000. *Molecular cell biology*. 4th Edition ed. Freeman, p. 191.

Lu, H. B. et al. 2001. Protein contact printing for a surface plasmon resonance biosensor with on-chip referencing. *Sensors and Actuators B: Chemical* 74(1-3), pp. 91-99.

Mallik, S. et al. 1994. Synthetic bis-metal ion receptors for bis-imidazole protein analogs. *Journal Of The American Chemical Society* 116(20), pp. 8902-8911.

Mallik, S. et al. 1994. Towards materials for the specific recognition and separation of proteins. *New Journal Of Chemistry* 18, pp. 299-304.

Mateo, C. et al. 2006. Immobilisation-stabilisation of enzymes by multi-point covalent attachment on supports activated with epoxy groups. In: Guisan, J.M. ed. *Immobilisation of enzymes and cells.* Humana Press, p. 47.

McMurray, J. 2000. *Organic Chemistry.* 5th ed. Brooks/Cole, p.191

Metz, G. et al. 2003. Small molecule screening on chemical microarrays. In: Bohm, H.-J. and Schneider, G. eds. *Protein-ligand interactions.* Vol. 19. WILEY-VCH, pp. 222, 231.

Meyer, G. D. et al. 2006. Non-specific binding removal from protein microarrays using thickness shear mode resonators. *IEEE Sensors Journal* 6(2). pp.254-261

Mooney, J. F. et al. 1996. Patterning of functional antibodies and other proteins by photolithography of silane monolayers. *Proceedings of the National Acaemy of Science USA* 93, pp. 12287-12291.

Mrksich, M. and Whitesides, G. M. 1996. Using self-assembled monolayers to understand the interactions of man-made surfaces with proteins and cells. *Annual review of biophysics and biomolecular structure* 25, pp. 55-78.

Nakanishi, K. et al. 2001. On the adsorption of proteins on solid surfaces, a common but very complicated phenomenon. *Journal of Bioscience and Bioengineering* 91(3), pp. 233-244.

Naujoks, N. and Stemmer, A. 2004. Using local surface charges for the fabrication of protein patterns. *Colloids and Surfaces A: Physicochemical and Engineering Aspects* 249(1-3), pp. 69-72.

Neves-Petersen, M. T. et al. eds. 2005. *Chapter 8: Biomicro sensors. New UV light induced molecular switch allows sterically oriented immobilisation of biomolecules and the creation of protein nanoarrays. Technical proceedings of the 2005 NSTI nanotechnology conference and Trade show.* Nanotechnology.

Nicholas, J. et al. 2006. Fluorescenctly tagged polymer bioconjugates from protein derived macroinitiators. *Chemical communications* [WWW]. Available at: http://www.rsc.org/ej/CC/2006/b609935a.pdf [Accessed: 26th October 2006].

Nicholls, I. A. and Rosengren, J. P. 2002. Molecular imprinting of surfaces. *Bioseparation* 10, pp. 301-305.

Nishino, H. et al. 2006. Selective protein capture by epitope imprinting. *Angewandte Chemie International edition. Ed.* 45, pp. 2392-2396.

Ombelli, M. et al. 2002. Biomimetic dextran coatings on silicon wafers: thin film properties and wetting. *Materials research symposium proceedings* [WWW] 374. Available at: http://www.mrs.org/members/proceedings/fall2002/b/B10_7.pdf.

Ong, S. et al. 1994. Phospholipid immobilization on solid surfaces. *Analytical Chemistry* 66, pp. 782-792.

Pang, X. et al. 2006. Soft-wet polyacrylamide gel beads with the imprinting of bovine serum albumin. *Reactive and Functional Polymers* 66(10), pp. 1182-1188.

Pavey, K. D. et al. 2001. A quartz crystal resonant sensor (QCRS) study of HSA-drug interactions. *Analyst* 126, pp. 426-428.

Peters, T. 1996. *All about albumin: Biochemistry, genetics and medical applications.* Academic Press, Inc., p. 51-54, 107.

Pichon, V. and Haupt, K. 2006. Affinity separations on molecularly imprinted polymers with special emphasis on solid phase extraction. *Journal of liquid chromatography & related technologies* 29, pp. 989-1023.

Rachkov, A. and Minoura, N. 2001. Recognition of oxytocin and oxytocin-related peptides in aqueous media using a molecularly imprinted polymer synthesized by the epitope approach. *Journal Of Chromatography A* 889(1-2), pp. 111-118.

Raffa, R. B. 2003. Experimental applications to determine the thermodynamics of protein-ligand interactions. In: Bohm, H.-J. and Schneider, G. eds. *Protein-ligand interactions.* Vol. 19. WILEY-VCH, p. 57.

Ramstrom, O. and Ansell, R. 1998. Molecular imprinting technology. *Chirality* 10, pp. 195-209.

Rathbone, D. L. 2005. Molecularly imprinted polymers in the drug discovery process. *Advanced Drug Delivery Reviews* 57(12), pp. 1854-1874.

Ratner, B. D. and Shi, H. Q. 1999. Recognition templates for biomaterials with engineered bioreactivity. *Current Opinion In Solid State & Materials Science* 4(4), pp. 395-402.

Rick, J. and Chou, T.-C. 2005. Enthalpy changes associated with protein binding to thin films. *Biosensors and Bioelectronics* 20(9), pp. 1878-1883.

Rick, J. and Chou, T.-C. 2005. Imprinting unique motifs formed from protein-protein associations. *Analytica Chimica Acta* 542(1), pp. 26-31.
Roy, I. and Gupta, M. N. 2006. Bioaffinity immobilisation. In: Guisan, J.M. ed. *Immobilisation of enzymes and cells.* Humana Press, p. 108.

Ruckert, B. et al. 2002. Molecularly imprinted composite materials via iniferter- modified supports. *Journal Of Materials Chemistry* 12(8), pp. 2275-2280.

Ruiz, S. A. and Chen, C. S. 2006. Microcontact printing: a tool to pattern. *Soft Matter* 3, pp. 168-177.

Sergi, M. et al. 2004. Proteins, recognition networks and developing interfaces for macromolecular biosensing. *Journal of Molecular Recognition* 17, pp.198-208.

Sharma, S. and Agarwal, G. P. 2001. Interactions of Proteins with Immobilized Metal Ions: A Comparative Analysis Using Various Isotherm Models. *Analytical Biochemistry* 288(2), pp. 126-140.

Sharma, S. et al. 2002. Controlling non-specific protein interactions in Silicon biomicrosystems with nsnostructured poly(ethyleneglycol) films. *Langmuir* 18, pp. 8728-8731.

Shi, H. Q. et al. 1999. Template-imprinted nanostructured surfaces for protein recognition. *Nature* 398(6728), pp. 593-597.

Shi, H. and Ratner, B. D. 2000. Template recognition of protein-imprinted polymer surfaces. *Journal of biomedical materials research* 49(1), pp. 1-11.

Shiomi, T. et al. 2005. A method for the molecular imprinting of hemoglobin on silica surfaces using silanes. *Biomaterials* 26(27), pp. 5564-5571.

Shim, H. Y. et al. 2004. Micropatterning of diacetylenic liposomes on glass surfaces. *Materials Science and Engineering: C* 24(1-2), pp. 157-161.

Smith, J. C. et al. 2003. Nanopatterning the chemospecific immbobilization of cowpea mosaic virus capsid. *Nano Letters* 3(7), pp. 883-886.

Sorribas, H. et al. 2002. Photolithographic generation of protein micropatterns for neuron culture applications. *Biomaterials* 23(3), pp. 893-900.

Soultani-Vigneron, S. et al. 2005. Immobilisation of oligo-peptidic probes for microarray implementation: Characterisation by FTIR, Atomic Force Microscopy and 2D fluorescence. *Journal of Chromatography B* 822(1-2), pp. 304-310.

Stryer, L. 1999. *Biochemistry*. 4th ed. Freeman, pp. 17-19, 33, 60, 61, 107, 191, 225, 367.

Takeuchi, T. and Klotz, I. 1972. Macromolecule-small molecule interactions; Introduction of additional binding sites in polyethyleneimine by disulfide cross-linkages. *Biopolymers* 11, pp. 483-491.

Taussig, M. 2003. *Protein arrays resource page* Genomic solution (A Harvard Bioscience group). Available at: <URL: http://www.functionalgenomics.org.uk/ sections/resources/protein_arrays.htm#int> [Accessed: May 2007]

Tong, D. et al. 2001. Some studies of the chromatographic properties of gels ('artificial antibodies/receptors') for selective adsorption of proteins. *Chromatographia* 54(1-2), pp. 7-14.

Turner, N. W. et al. 2006. From 3D to 2D: A review of the molecular imprinting of proteins. *Biotechnology progress* 22, pp. 1474-1489.

Tyagi, T. et al. 1998. Carbodiimide coupling of enzymes to the reversibly soluble insoluble polymer Eudragit S-100. *Biotechnology Appl. Biochemistry* 28, pp. 201-206.

Unsworth, L. D. et al. 2005. Protein resistance of surfaces prepared by sorption of end-thiolated poly(ethylene glycol) to gold: Effect of surface chain density. *Langmuir* 21, pp. 1036-1041.

Vaidya, A. A. et al. 2001. Creating a macromolecular receptor by affinity imprinting. *Journal Of Applied Polymer Science* 81(5), pp. 1075-1083.

Veiseh, M. et al. 2004. Guided cell patterning on gold-silicon dioxide substrates by surface molecular engineering. *Biomaterials* 25(16), pp. 3315-3324.

Vulfson, E. et al. 1997. Assembling the molecular cast. *Chemistry in Britain* 33(1), pp. 23-26.

Wade, J. D. et al. 2006. An automated peptide and protein thiazolidine coupling chemistry for biosensor immobilization giving a unique N-terminal orientation. *Analytical Biochemistry* 348(2), pp. 315-317.

Whitcombe, M. J. et al. 1995. A new method for the introduction of recognition site functionality into polymers prepared by molecular imprinting: synthesis and characterization of polymeric receptors for cholesterol. *Journal of the American Chemical Society* 117, pp. 7105-7111.

Williams, M. A. and Ladbury, J. E. 2003. Hydrogen bonds in protein-ligand complexes. In: Bohm, H.-J. and Schneider, G. eds. *Protein-ligand interactions*. Vol. 19. WILEY-VCH, pp. 137, 140, 149, 151.

Wulff, G. and Sarhan, A. 1972. The use of polymers with enzyme-analogous structures for the resolution of racemates. *Angewandte Chemie International Edition.* 11(4) , p.341.

Yu, Y. H. et al. 2002. Formation of a class of enzyme inhibitors (drugs), including a chiral compound, by using imprinted polymers or biomolecules as molecular-scale reaction vessels. *Angewandte Chemie-International Edition* 41(23), pp. 4459-4463.

Yilmaz, E. et al. 1999. Influence of functional and cross-linking monomers and the amount of template on the performance of molecularly imprinted polymers in binding assays. *Analytical communications* 36, pp. 167-170.

Zhang, Z. et al. 2006. Molecularly imprinted thin film self-assembled on piezoelectric quartz crystal surface by the sol-gel process for protein recognition. *Biosensors and Bioelectronics* 21(7), pp. 1244-1251.

Zhou, Y. et al. 2007. Chitosan-N-poly(ethylene oxide) brush polymers for reduced nonspecific protein adsorption. *Journal of Colloid and Interface Science* 305(1), pp. 62-71.

Chapter 2

Validation of an approach for determining ligand binding parameters using an HSA / SAL model

2.1 Introduction

An important first step in this project was to identify an appropriate ligand-protein pairing on which to base future work. In order to come to a rational decision, it was necessary to develop an approach for determining ligand-protein binding parameters. This chapter focuses on the validation of such a methodology.

2.1.1 Protein-ligand binding analysis

A number of methods have been reported for characterising the interaction of ligand / protein pairs: fluorescence spectroscopy (Epps et al. 1999; Muresan et al. 2001; Smyk 2003), circular dichroism (CD) spectroscopy (Otigari and Perrin 1976), nuclear magnetic resonance spectroscopy (NMR), (Utsumi et al. 2003, Clarkson and Campbell 2003) and mass spectrometry (Oldham et al. 200, Last 1999). Some more sophisticated methods have been used for characterising protein-ligand binding. These include femtosecond studies and dynamics of binding (Zhong et al. 2000), surface plasmon resonance (SPR) (Morrill et al. 2003) and quartz crystal microbalance (QCM) biosensors, which have been used to monitor molecular recognition between proteins and small medicinal agents (Liu et al. 2003). The latter two are surface-based techniques and require prior immobilisation of the ligand or protein, which may affect the binding interaction.

Theoretical techniques have also been used. Molecular modelling has been used to pre-screen ligands and identify suitable protein-binding candidates (Hetenyi et al. 2003; Keir et al. 1998). Molecular Operating Environment (MOE, Chemical computing group, Quebec, Canada) is one modelling program that can simultaneously align many putative ligands (small molecules) in protein clefts. The structures are downloaded from the Protein Data Bank (PDB, Berman et al. 2000) for example, and each ligand alignment is scored for 'internal strain and overlap of features' (Labute 1997-2004). A modelling method was also used to find active sites and structurally similar sites that may bind a given ligand (Campbell et al. 2003).

In this paper, a docking method was used to validate the sites and predict which ligands will bind. Hetenyi et al. (2003) carried out a docking study of binding aromatic compounds to proteins using Autodock 3.0 (Molecular Graphics Laboratory, La Jolla, USA). Molecular interaction and molecular affinity fingerprints of complexes of 31 proteins and 39 ligands were rapidly calculated. The protein x-ray crystal structures were selected from the PDB (Berman et al. 2000).

The aim of this section of work was to investigate the strength and the extent of ligand-protein binding in solution, and not to determine detailed structural information about the interaction. A number of requirements were identified: 1) the method should use small volumes, 2) the protein ligand pair should be inexpensive and readily available and 3) the method of analysis should be rapid, simple and reliable. On the basis of these requirements equilibrium dialysis was identified as an appropriate method to use.

2.1.2 Equilibrium dialysis

2.1.2.1 Background

Equilibrium dialysis is a simple technique for determining solution-phase ligand-protein binding parameters (Harding and Chowdhry 2001). A semi-permeable membrane separates two compartments. One compartment contains protein; the other contains ligand. The ligand can freely diffuse across the membrane but the protein cannot. As ligand binds to the protein, the amount of free ligand in solution decreases until equilibrium is reached (i.e. the free ligand concentration either side of the membrane is the same). Ligand concentrations in the protein-free compartments may then be determined. Ultrafiltration has been used as an alternative to dialysis, where 'free ligand is separated from free and bound macromolecule by filtration under pressure through a permselective membrane' (Berger and Girault 2003). Times are reduced and small amounts of protein are needed. However, there is a significant disadvantage to ultrafiltration since the protein solution will become concentrated as solvent is removed, increasing the likelihood of protein-protein interactions.

A number of control procedures are commonly associated with protein / ligand dialysis studies and the protein must be purified of all associated small molecules and ligands (Harding and Chowdry 2001). Methods for a) determining the equilibration time for the system b) reducing non-specific binding to membrane, glass, plastic or grease and c) ensuring that no protein leaks through the membrane are described in Section 2.2.4. If the time taken to reach equilibrium is overly long, protein can denature and the number of ligand binding sites decrease (Cheng and Carlson 1983). Another factor to consider is the Donnan Effect (at pH7.4, most proteins will have a net charge and therefore a charged ligand would be unequally distributed across the membrane to balance it (Harding and Chowdry 2001)). The effect can be reduced by decreasing the protein concentration (<30μM), increasing the buffer concentration or by decreasing the pH (Harding and Chowdry 2001). A mass balance experiment measures how much ligand is lost through non-specific binding during the experiment. Bacterial growth is usually not a problem if the experiments have a low temperature and duration (Harding and Chowdry 2001).

A number of disadvantages of equilibrium dialysis have been identified (Berger and Girault 2003). For instance, if the protein-ligand complex is based on weak interactions, there may be limited precision in the calculations. Also, water may diffuse into the protein compartment via osmosis and change the equilibrium concentration of ligand. This effect can be minimised by using low protein concentrations (Harding and Chowdry, 2001).

2.1.2.2 Previously described approaches

A number of different equilibrium dialysis methods for measuring protein-ligand binding interactions have been described ((Muresan et al. 2001; Rubino et al. 1996; Ozer and Tacal 2001). In bulk dialysis a protein / buffer solution is enclosed in a visking tubing bag (semi-permeable) which is lowered into a bath of ligand / buffer and left to equilibrate (Muresan et al. 2001). The concentration of free ligand in the bath is determined. This method is cost effective and simple to perform, however the large volumes

of the dialysis compartments requires a large mass of protein and ligand to allow detection of free ligand at equilibrium (Reinard and Jacobsen 1988) . Specialised equilibrium dialysers are available, which can include membranes with molecular weight cut-offs (MWCOs) of between 100-30,000Da. For instance a Spectra / Por dialyser (Spectrum Laboratories Inc., California, Massachussets) with 5 micron-Teflon cells and a cellulose acetate asymmetric membrane (MWCO 5000) was used to characterise interactions between the canola protein and phenolic ligands (Rubino et al. 1996). Although this method provides good reproducibility, the equipment is expensive. Equilibrium dialysis plates have recently become available, for high-throughput fluorescence analysis of protein-ligand binding interactions which have very low compartment volumes and should speed up the analysis time (96-well equilibrium dialyser, Harvard Apparatus, Massachussets, USA; Rapid equilibrium dialysis, Peirce, Rockford, Illinois).

The relatively high-affinity protein-ligand interaction between salicylic acid (SAL, Fig. 2.1) and human serum albumin (HSA) has been well researched (Table 2.1, APPENDIX II). Methods were validated by comparing SAL-HSA binding data with binding parameters reported in the literature (dissociation constant (Kd) = 25 ± 2.4μM, maximum number of ligand binding sites (BMax) = 3.2 ± 0.10, Ozer and Tacal 2001).

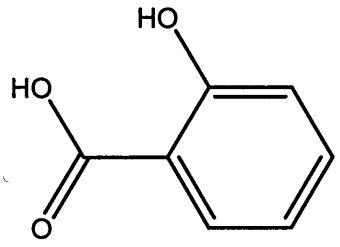


Fig. 2.1 Structure of SAL

For this study two different equilibrium dialysis methods were chosen. The first method used two Franz type diffusion cell receptor compartments placed side by side. HSA (molecular weight (M_W) 67,000 kDa) was to be investigated and therefore visking membranes with MWCO of ~12,000 were used. In a second approach 2ml Eppendorf tubes were modified to act as a

simple two-cell micro-dialysis system (Reinard and Jacobsen 1988; Ozer and Tacal 2001).

2.1.3 Chapter objectives

- To identify a suitable protein-ligand pair with published binding parameters
- To identify a suitable equilibrium dialysis approach for measuring protein-ligand interactions
- To validate the dialysis approach using the chosen protein-ligand model (HSA-SAL)

2.2 Methods

Equilibrium dialysis experiments (Sections 2.2.3 and 2.2.4) were carried out at room temperature in sodium phosphate buffer (NaPB) based on the method of Ozer and Tacal (2001). The HSA concentration ([HSA]) was kept constant and dialysed against different SAL concentrations ([SAL]s). GraphPad Prism (GraphPad Software, California, USA) was used to create non-linear binding curves and Scatchard plots for the calculation of HSA-SAL binding parameters (GraphPad 2003, Appendix I).

A method to detect and measure the free [SAL] after equilibrium dialysis was required. HSA and SAL are both aromatic. HSA contains three aromatic amino acids: tryptophan, tyrosine and phenylalanine (Peters 1992) and so the HSA-SAL interaction was analysed by UV-visible and fluorescence spectroscopy. Other techniques such as HPLC and radio-ligand binding allow very low levels of ligand to be detected, but they can be expensive and time-consuming.

2.2.1 Equipment and materials

Equipment: Perkin-Elmer λ5 UV-Visible Spectrophotometer (Perkin Elmer, Waltham, MA, USA), quartz cuvettes (1.5ml UV, 400µl far-UV, fluorescence), 10mm light path (Hellma, Mullheim, Germany), Series 2 luminescence spectrophotometer (Sim-Aminco Bowmann (AB), Illinois, USA), Fluostar Optima plate-reader (BMG Labtech, Offenburg, Germany), black Greiner microwell plates (Sigma-Aldrich, St Louis, MO, USA), twelve receptor sections of diffusion cells (~3.5ml) (JB and DW Jones, Loughborough, UK), Hamilton Microlitre syringe with Rheodyne valve (500µl) and thin polypropylene tubing (both from Fisher, Waltham, MA, USA).

Materials: SAL (crystalline, minimum 99.5%) and HSA (essentially fatty acid and globulin free) were purchased from Sigma-Aldrich. A 1mM stock solution of SAL in NaPB was prepared (Appendix I) for each experiment

and diluted as required. De-ionised water (dH_2O) was prepared in-house and used for making NaPB (pH7.4, 67mM (unless otherwise stated), Appendix I). BD Plastipak syringes (50ml), dialysis tubing (19mm Dia., Inf. Dia. 24/32", 30 metres, molecular weight cut-off (MWCO) 12-14000Da, Medicell, London, UK), high vacuum grease (Dow Corning, Midland, MI, USA) and Eppendorf tubes (2ml) were purchased from Fisher.

2.2.2 HSA and SAL analysis using UV spectroscopy

UV-visible spectroscopy was used to determine the concentration of ligand and protein. All measurements were carried out using a UV-visible spectrophotometer (UVS).

2.2.2.1 SAL and HSA UV absorbance spectra

SAL and HSA UV absorbance spectra were obtained (scanned wavelength (λ) range: 220nm-500nm). The absorbance maxima (λ_{max}) were 295nm and 279nm respectively (Fig. 2.4). SAL (75µM), HSA (30µM) and blank (NaPB) solutions were analysed in 1cm path-length quartz cuvettes (1.5ml).

2.2.2.2 SAL and HSA UV calibration graphs

The molar absorptivity (ε, μM^{-1}) is a measurement of the ability of a molecule to absorb light at a given wavelength (Burns 1993). Linear regression analysis was used to find the ε for SAL at 295nm (ε_{295}) and HSA at 279nm (ε_{279}). Calibration graphs of concentration (µM) vs. absorbance were plotted.

a. SAL

Dilution series of [SAL] (10µM-1000µM) were measured to get a series of UV calibration graphs (A_{295}). These were added together to obtain the ε_{295}.

b. HSA

HSA was identical to that used in Ozer and Tacal (2001). An HSA calibration graph (A_{279}, 10-50µM) was plotted to obtain the ε_{279}.

2.2.2.3 Detection limits for SAL in the UVS

Sample absorbance measurements can be affected by stray light (reflection and scattering) and absorbance from the buffer (Burn 1993). The upper detection limit for [SAL] was defined as being the upper limit of linearity for the calibration curve. Lower detection limits were determined by measuring blank solutions at λ295nm. UV, quartz cuvettes of different volumes were used in the experiments. The lower detection limit was defined as three times the background variation.

2.2.3 SAL analysis using fluorescence spectroscopy

Fluorescence spectroscopy is commonly more sensitive than UV spectroscopy. SAL was previously shown to be fluorescent (Ozer and Tacal 2001).

2.2.3.1 SAL fluorescence spectra

SAL fluorescence spectra were measured in a Series 2 luminescence spectrophotometer (Sim-Aminco Bowmann (AB). An emission spectrum (300-600nm) was obtained using a fixed excitation wavelength of 295nm (measured from the UV spectrum) and the gain was adjusted to give optimum sensitivity. An excitation spectrum (200-400nm) was then obtained, using the emission wavelength maximum λ_{em}. The emission spectrum and λ_{em} was re-read using the excitation wavelength maximum (λ_{ex}) obtained from the fluorescence spectrum. The λ_{ex} and λ_{em} were used to select the closest excitation and emission wavelength filters available in the Fluostar Optima plate-reader, for subsequent fluorescence measurements of SAL.

2.2.3.3 SAL fluorescence calibration graphs

Calibration graphs were used to determine the detection limit of a fluorescence 96-well plate-reader (Section 2.2.3.4) and were also prepared for each new dialysis experiment (Sections 2.2.4.4 and 2.2.4.5, 2.2.5.4a and 2.2.5.5a). The fluorescence of SAL was measured at fixed λ_{ex} (330nm) and λ_{em} (405nm). Black, 96-well Greiner microplates were used to minimise light scattering and reflection. Sample volumes of 200µl were used for all

readings. Blanks (NaPB) and a set of standards ([SAL] e.g. 20-100μM) were measured for each calibration graph. The fluorescence plate-reader software automatically plotted a calibration graph (after subtracting the average blank value from the standards) using linear regression analysis, which automatically gave the r^2 value.

2.2.3.4 SAL detection limits by fluorescence

a. Lower concentration limit

The lower [SAL] detection limit of the plate-reader was defined as three times the average blank value.

b. Lower volume limit

Four different volumes (150, 100, 75 and 50μl) of a set of SAL standards (20, 40, 60, and 80μM) were measured to give separate calibration graphs (a sample volume of 200μl was routinely used). In each case, the gain was adjusted for the 80μM standard to give 90% of the maximum fluorescence reading.

2.2.4 Dialysis of HSA with SAL using diffusion cells

2.2.4.1 Diffusion cell equilibrium dialysis set-up

For each equilibrium dialysis experiment, up to six dialysis cells were used (Fig 2.2). Membrane dialysis tubing was soaked in dH_2O then NaPB for 1 hr each, and cut into ~$2cm^2$ pieces. Excess buffer was removed by dabbing with a tissue. The membrane was fixed between the two diffusion cell compartments with a small amount of high-vacuum grease, avoiding air bubbles. The compartments were placed side-by-side and held together by a metal clamp. To prevent air bubbles from collecting in the compartments whilst filling, the cell was tipped to one side and solutions were injected, from a Plastipak syringe, into the bulk part of the compartments using a thin polypropylene tube. One side of the cell was the ligand (L) compartment and the other was the protein (P) compartment. Each compartment was continuously stirred with a magnetic bar. The cells were placed between two

spots on a magnetic stirrer to attract the bars outwards and prevent them from sticking together at the membrane surface.

The average volume of the diffusion cell compartments was ~3.4ml. A Hamilton syringe was used for sampling via compartment arms. Before sampling, air bubbles were removed from the syringe and the solution in the compartment arm was thoroughly mixed with that from the bulk of the compartment. Between sampling the syringe was thoroughly washed in NaPB. Samples (up to 200µl) were diluted with NaPB for UV measurement. Samples were measured undiluted by fluorescence. The absorbance / fluorescence of SAL / HSA was measured before and after dialysis experiments and converted to [SAL] / [HSA] using linear regression analysis.

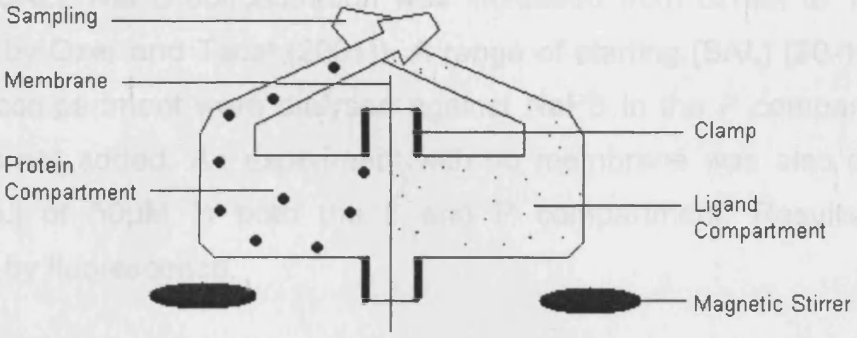


Fig. 2.2 Diffusion cell equilibrium dialysis set–up. A semi-permeable membrane separated two receptor-phase sections of diffusion cells; the protein (P) compartment and the ligand (L) compartment. SAL was small enough to freely diffuse through the pores and equilibrate either side of the membrane, but HSA was not. HSA-SAL equilibrium binding parameters were calculated by measuring changes in [SAL] in the L compartment.

2.2.4.2 Equilibration time and mass balance controls

The time taken for equilibrium of SAL to be reached between the two compartments was determined. SAL (250µM, in the L compartment) was dialysed against NaPB (in the P compartment). HSA was not added in this experiment. At 2, 4, 6, 8, 14 and 24 hours, 200µl was removed from the L and P compartments, diluted 1/3 with NaPB and the A_{295} were measured. NaPB (200µl) was added into each L and P compartment after sample removal to maintain compartmental volume. This was taken account of in subsequent calculations (Appendix I). The final corrected [SAL] for the L

and P compartments were averaged and plotted. The difference in [SAL] before and after equilibration was calculated and converted into mass (µg), giving a mass balance for the experiment.

2.2.4.3 Protein control experiments

It was important to ensure that HSA could not move across the semi-permeable membrane from the P compartment into the L compartment. HSA (4.5µM) in the P compartment was dialysed against NaPB in the L compartment. SAL was not added in this experiment. A 400µl sample was removed from each compartment after 24 hours. The samples were diluted 2/3 in NaPB and the A_{279} were measured.

2.2.4.4 Ligand control experiments

A mass balance for equilibrium dialysis was determined for each different starting [SAL]. NaPB concentration was increased from 67mM to 100mM (as used by Ozer and Tacal (2001)). A range of starting [SAL] (20-100µM) in the L compartment were dialysed against NaPB in the P compartment. HSA was not added. An experiment with no membrane was also set up, with [SAL] of 50µM in both the L and P compartment. Results were analysed by fluorescence.

2.2.4.5 HSA-SAL equilibrium dialysis binding experiments

A range of starting [SAL] (20-100µM) in the L compartment was dialysed against HSA (30µM) in the P compartment. The free [SAL] (after equilibration) was measured (fluorescence) and adjusted for loss of ligand (Section 2.2.4.4). The binding parameters K_d and B_{max} were determined (Appendix I).

2.2.5 Dialysis of HSA with SAL using Eppendorf tubes

A more efficient method was needed to measure ligand-protein binding. Eppendorf tubes were disposable and allowed small-volume, high-throughput analysis, saving on materials and time. The buffer used was 67mM NaPB.

2.2.5.1 Eppendorf dialysis set-up

This method was first described in Reinard and Jacobsen (1988) and later used by Ozer and Tacal (2001). A diagram of the Eppendorf tube set up is shown in Fig. 2.3.

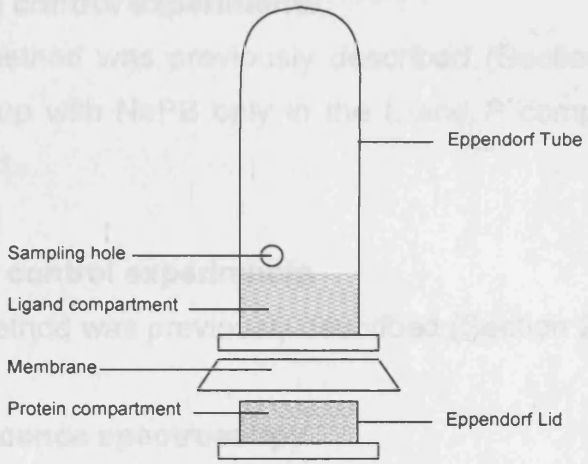


Fig. 2.3 Eppendorf tube set up for equilibrium dialysis. A semi-permeable membrane separated a ligand (L) compartment (Eppendorf tube) and protein (P) compartment (Eppendorf lid). SAL was small enough to freely diffuse through the pores and equilibrate either side of the membrane, but HSA was not. HSA-SAL equilibrium binding parameters were calculated by measuring changes in [SAL] in the L compartment. *Diagram adapted from (Reinard and Jacobsen 1988).*

The lid of the Eppendorf tube was removed along with all excess plastic from the hinge and used as the P compartment (260µl). A hole was pierced on the 1.5ml mark of the tube with a drawing pin to allow for sampling. The membrane was cut to ~1.5cm^2, washed with water (1hr) and NaPB (1hr) and placed over the lid. The tube was pushed onto the lid to fix the membrane in place. A Hamilton syringe was used to inject 520µl samples through the hole into the Eppendorf tube (L compartment). To decrease dialysis time, the tubes were placed in a tube rack on a water bath or mechanical shaker overnight at room temperature. Undiluted samples were measured by UV (400µl unless otherwise stated) or fluorescence (200µl). The starting [SAL] were corrected for a 2/3 dilution due to uneven L and P compartment volumes (Appendix I).

2.2.5.2 Equilibration time and mass balance controls

The equilibration time and mass balance was carried out as in Section 2.2.4.2 except SAL samples (starting [SAL], 85µM) from five different

Eppendorf tubes were taken at each time point; 0, 2, 4, 6, 8, 14, 16 and 24 hours. The P compartment volumes were too low and had to be combined to read >400µl. The NaPB background absorbance was subtracted from the 24 hr time-points only.

2.2.5.3 Protein control experiments

The general method was previously described (Section 2.2.4.3). Controls were also set up with NaPB only in the L and P compartments. Samples were not diluted.

2.2.5.4 Ligand control experiments

The general method was previously described (Section 2.2.4.4).

a. Fluorescence spectroscopy

Three control experiments with different starting [SAL] were carried out to obtain a precise value for mass balance.

b. UV spectroscopy

Ligand control experiments were carried out along-side each ligand-protein binding experiment (having the same starting [SAL]), to obtain a precise value for mass balance.

2.2.5.5 HSA-SAL equilibrium dialysis binding experiments

Aliquots of SAL (300µl) were removed from the L compartment and measured by UV. Each final free [SAL] measured in a binding experiment was adjusted for non-specific binding calculated in the ligand control experiment (Section 2.2.5.4). The binding parameters K_d and B_{max} were determined, following the general procedure of Section 2.2.4.5.

a. Fluorescence spectroscopy

Starting [SAL] of 5-120µM were dialysed with 30µM HSA. The final free [SAL] measured was adjusted for loss of ligand (Section 2.3.4.3a). A separate control was not carried out for each of the experiments.

b. UV spectroscopy

Starting [SAL] of 5-1000μM were dialysed with 30 or 40μM HSA. The [HSA] were measured by UV before each experiment. L compartment samples were obtained either by insertion of a Hamilton syringe through the Eppendorf tube hole (Fig 2.3), or by disassembly of the Eppendorf tubes and subsequent collection using a Gilson pipette.

2.3 Results and discussion

2.3.1 HSA and SAL analysis using UV spectroscopy

2.3.1.1 SAL and HSA UV absorbance spectra

a. SAL

The λ_{max} of SAL was measured as 295nm (A_{295}) (Fig. 2.3.1). The λ_{max} was measured >240nm, to distinguish the specific absorption of the conjugated system from non-specific individual chromophores (Threllfall 1993).

b. HSA

The λ_{max} for HSA was measured as 279nm (A_{279}) (Fig. 2.4), as reported in the literature (Peters 1992).

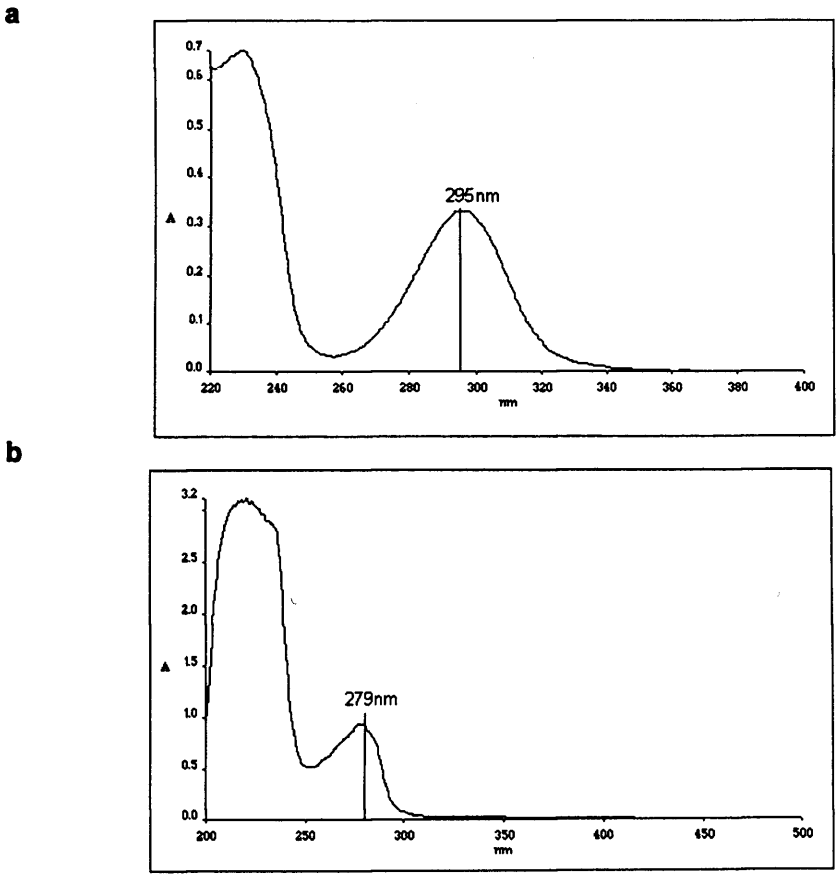


Fig. 2.4 UV absorbance spectra of SAL and HSA. Solutions of **a**) SAL (75µM) and **b**) HSA (30µM) were scanned to find the λ_{max} (vertical contours).

2.3.1.2 SAL and HSA UV calibration graphs

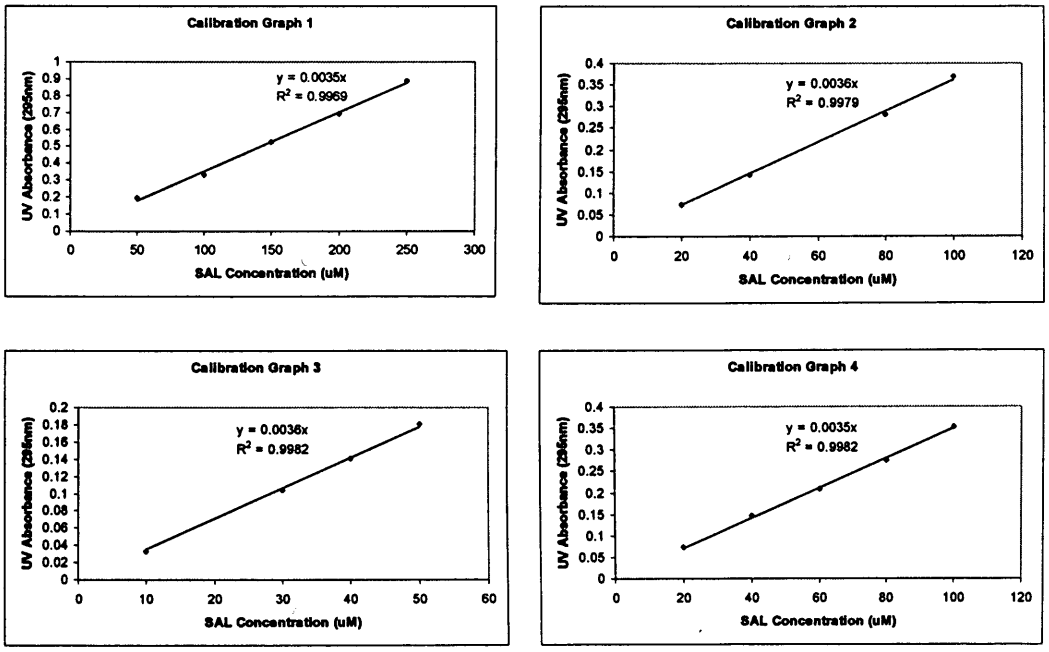
a. SAL

Four sets of data (Fig. 2.5a) were combined to create an overall calibration graph for SAL (Fig. 2.5b). Linear regression analysis gave an ε_{295} of $0.0035\mu M^{-1}$ and an r^2 of 0.9985, showing precision in the line of best fit. This was higher than reported in Ozer and Tacal (2001, $0.0028\mu M^{-1}$), possibly due to different experimental conditions. Only one [SAL] was below the (lower) detection limit (Section 2.3.1.4a) (calibration graph 3, A_{295} =0.033, Fig. 2.5a). SAL calibration curves in all subsequent experiments gave ε = $0.0035 \pm 0.0001\ \mu M^{-1}$.

b. HSA

Linear regression analysis calculated ε_{279} as $0.0313\mu M^{-1}$ for HSA in NaPB (Fig. 2.6). This is comparable to published data ($0.0322\mu M^{-1}$, Elwell and Shellman 1977). The r^2 value was 0.9987. The upper limit for UV analysis of HSA was ~50μM. The HSA concentration was kept constant at 30μM for all subsequent experiments (unless otherwise stated) as recommended in Harding and Chowdry (2001).

a



b

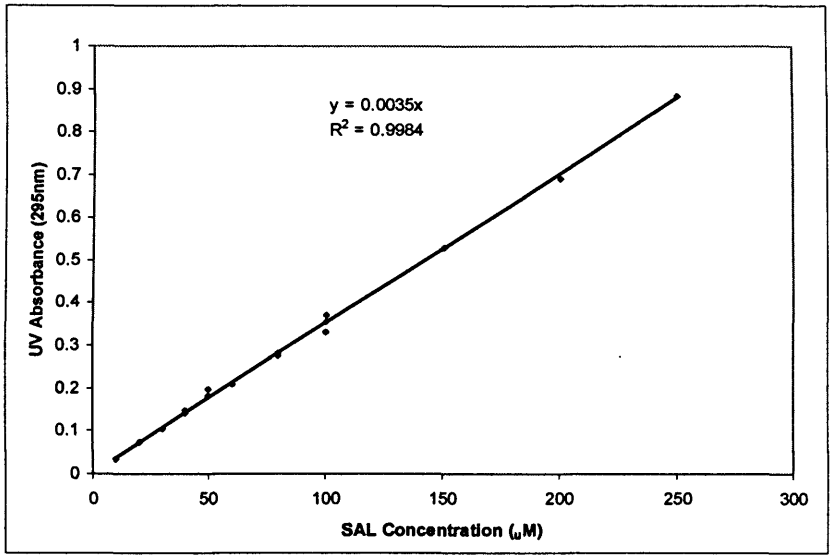


Fig. 2.5 UV calibration graphs for SAL. Calibration graphs of **a**) four different SAL solutions (1-4) were combined to give **b**) an overall calibration graph. Linear regression analysis was used to calculate ε_{295} (n=1).

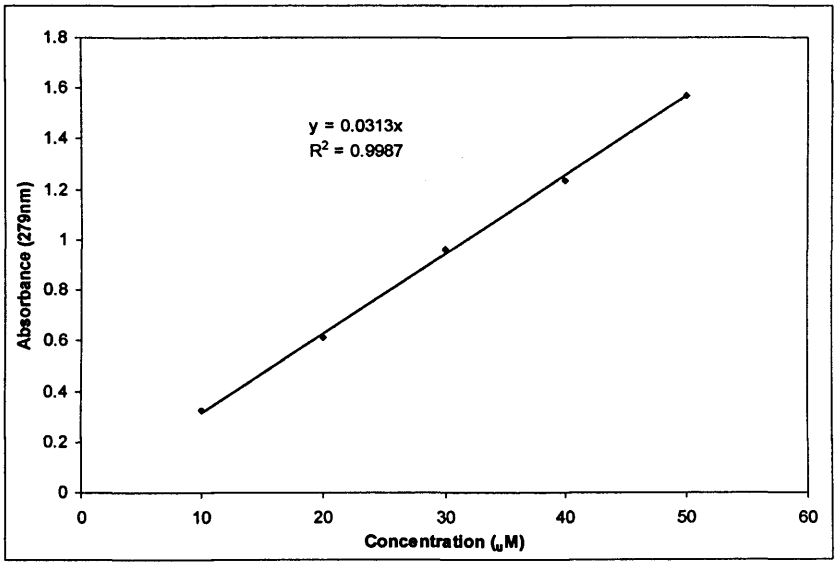


Fig. 2.6 UV calibration graph for HSA. Linear regression analysis was used to calculate ε_{279} (n=1).

2.3.1.3 Detection limits for SAL by UVS

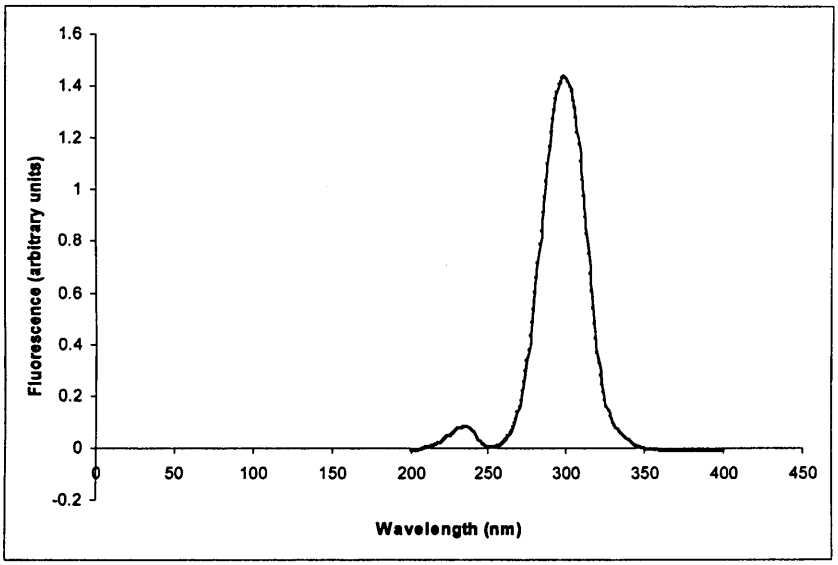
The upper limit of [SAL] that could be measured by UV was 250μM, before stray light caused the calibration graphs to become non-linear (Burns 1993). A lower [SAL] detection limit of 10.33μM was calculated for experiments using 1.5ml cuvettes Section 2.3.1.4a (ii) and 5.66μM for experiments using 0.4ml cuvettes Section 2.3.1.4b (ii).

2.3.2 SAL analysis using fluorescence spectroscopy

2.3.2.1 SAL fluorescence spectra

The fluorescence λ_{ex} and λ_{em} of SAL, measured in the luminescence spectrophotometer were 298nm and 405nm respectively (Fig 2.7). The λ_{ex} was close to the λ_{max} value observed by UV absorbance spectroscopy (295nm, Section 2.3.1.2a), but different to that previously reported (320nm, Ozer and Tacal, 2001). The λ_{ex} and λ_{em} filters used for subsequent SAL fluorescence measurements in the plate-reader (330nm and 405nm respectively) were the closest available.

a



b

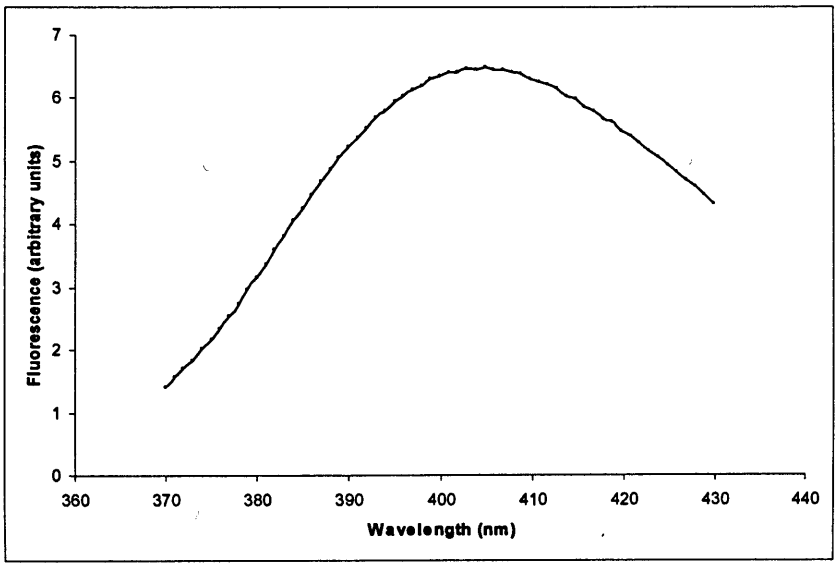


Fig. 2.7 Fluorescence spectra of SAL. The SAL **a**) excitation spectrum (λ_{max} = 298nm) and **b**) emission spectrum (λ_{max} = 405nm) are shown.

2.3.2.2 SAL detection limits by fluorescence

a. Lower concentration limit

The detection limit was between 2-4μM. Starting [SAL] were kept above 5μM for subsequent HSA-SAL binding experiments (Section 2.3.4.5a and 2.3.4.6 a).

b. Lower volume limit

The r^2 value was largely consistent over the range 150–75μM (r^2 >0.99), whilst sensitivity logically decreased (instrument gain was increased). A 50μl volume did not entirely cover the well. Volumes of 200μl were used for all subsequent experiments.

Volume of Standards	[SAL] (μM) that gain was set to	Gain	Standard Curve	R^2
150	80	2185	y= 628.7x + 798.1	0.99981
100	80	2342	y= 638.4x – 81.7	0.99982
75	80	2442	y= 628.6x – 1096	0.99985
50	80	2613	y= 6193x - 1339	0.99168

Table 2.1 Volume detection limit of the fluorescence plate-reader for SAL. A range of volumes (50-150μl) were tested for the same standard SAL solutions (20-80μM). The gain was set to the same [SAL] each time (80μl).

2.3.3 Equilibrium dialysis of HSA with SAL using diffusion cells

2.3.3.1 Equilibration time and mass balance controls

The final corrected [SAL] in the L and P compartments were averaged and plotted (Fig. 2.8). Equilibrium appears to be reached by 24 hours, and this was used as the equilibration time for subsequent experiments. From mass balance calculations, it was determined that 19.77μg of SAL was lost during dialysis, due to non-specific binding to the membrane, grease, diffusion cells and/ or syringe. Accidental dilution of the samples in the syringe, due

to residual rinsing buffer, may have decreased the measured [SAL] and subsequently increased the apparent SAL lost (Section 2.3).

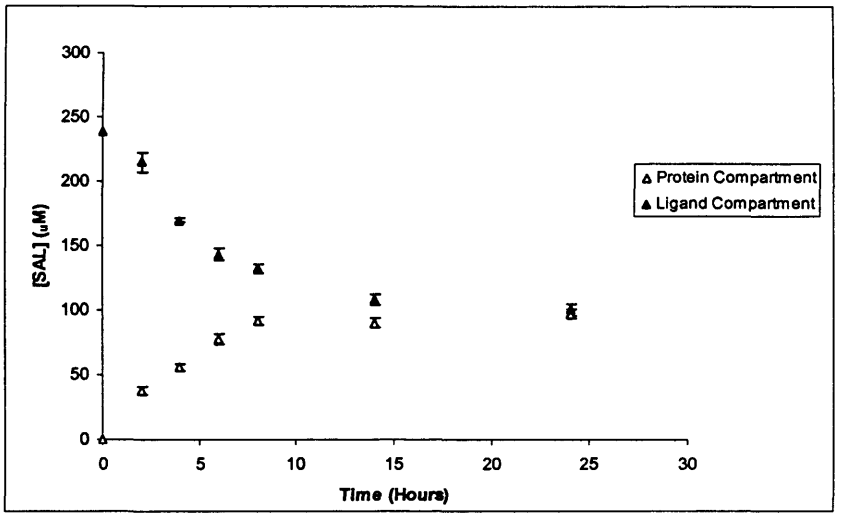


Fig. 2.8 Equilibrium control experiment for diffusion cell dialysis using UV analysis. SAL (L compartment: n = 5 ± SEM) was dialysed with buffer (P compartment: n = 5 ± SEM) for 24 hours. Samples were removed from both compartments at each time-point and analysed by UV spectroscopy. [SAL] are shown after correcting for a 1/3 dilution in the UV cuvettes and a 6.6% dilution during sampling (Appendix I) after replacement of 200μl buffer in each compartment at each time-point. (n = 4-6 ± SEM). The graph was used to calculate equilibration time and mass balance.

2.3.3.2 Protein control experiments

Table 2.7 shows the absorbance of HSA and NaPB in the P and L compartments respectively, before and after dialysis. The starting HSA A_{279} was measured as 0.1163 and the average final HSA A_{279} was measured as 0.1086. The difference was negligible (0.008). In addition, HSA absorbance was not detected in the L compartment before or after dialysis. It was concluded that HSA did not pass through the semi-permeable membrane. The [HSA] lost should be the same for any starting [HSA] due to a limited number of non-specific binding sites. Very low starting [HSA] would be more sensitive to change, as a higher percentage would be lost on the glass/ membrane/ grease.

2.3.3.3 Ligand control experiments

The [SAL] lost using different starting [SAL] is plotted in Fig 2.9. The actual [SAL] lost (Fig 2.9a) increased with starting [SAL] but the percentage [SAL] lost (Fig 2.9b) stayed constant at ~14% (except at low starting [SAL]. The experiment without a membrane also showed a 14% loss of ligand. At

higher starting [SAL], the % lost is relatively constant suggesting that saturation of non-specific binding sites does not occur. There was little difference with or without membrane, suggesting that HSA-membrane binding was negligible. However, SAL may have been able to diffuse into the gaps at the interface of the two diffusion compartments more easily when the membrane was not present. Alternatively, binding to the diffusion cells and syringe is also possible. A consistent percentage loss suggests a dilution factor during analysis, either from excess buffer on the membrane during the diffusion cell set-up or dilution in the syringe during sampling. It is not possible to identify a specific cause based on this data.

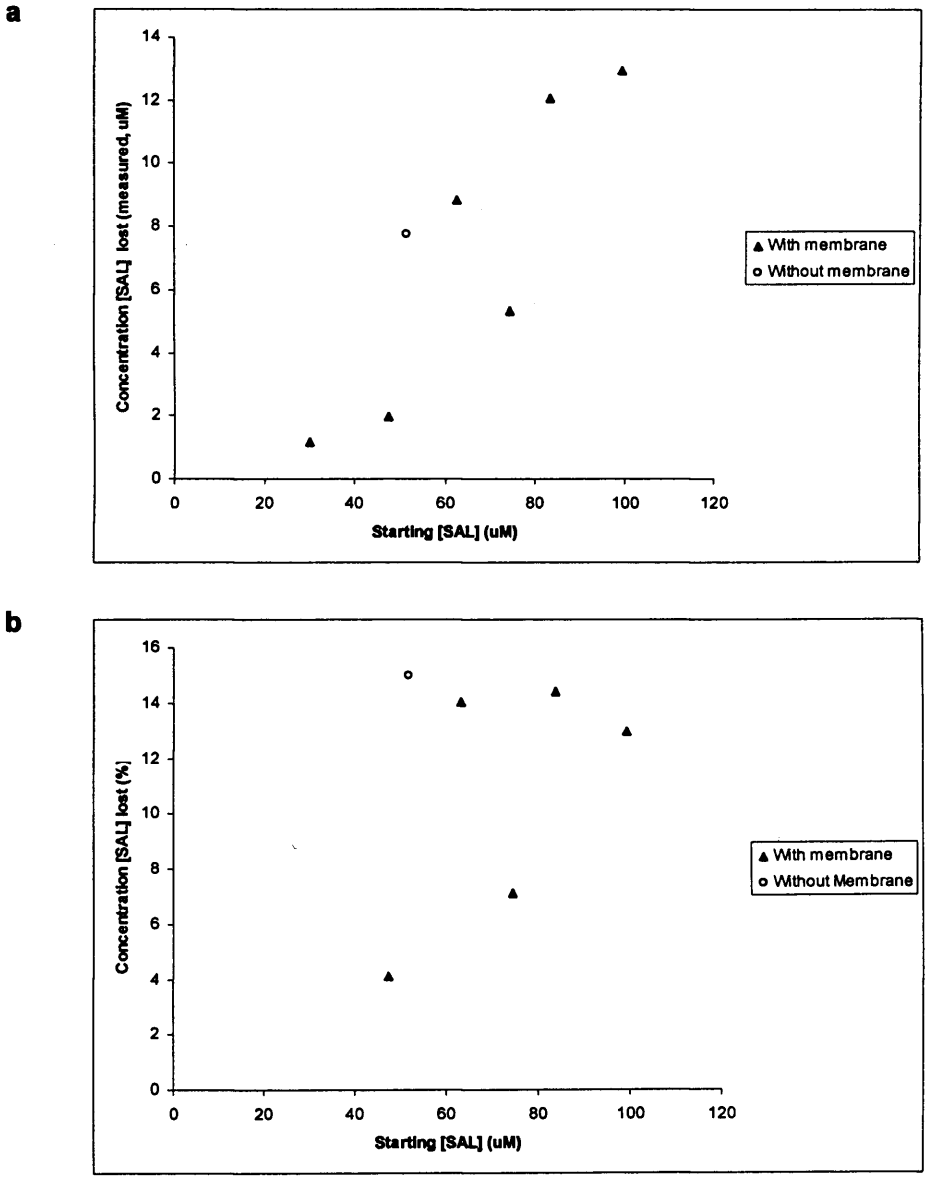


Fig. 2.9 Ligand control experiment for diffusion cell dialysis using fluorescence analysis. The apparent loss of [SAL] in 24 hour equilibrium dialysis experiments. The **a**) actual [SAL] lost and **b**) percentage [SAL] lost using different starting [SAL] was measured (n = 6). One control without membrane in the diffusion cell set up is also shown. SEM was <3% of the mean free [SAL].

2.3.3.4 HSA-SAL equilibrium dialysis binding experiments

For starting [SAL] >50μM, a 14% adjustment for loss of ligand was calculated. For starting [SAL] <50μM, 4% was used (Section 2.3.3.5a). GraphPad Prism (GraphPad Software, California, USA) was used to create non-linear binding curves and Scatchard plots for the calculation of HSA-SAL binding parameters (Appendix I). Without adjusting the final [SAL] for loss of ligand, the dissociation constant (K_d) was calculated as 37.54 ± 7.45μM and the maximum number of binding sites (B_{max}) was 3.10 ± 0.29 (Fig 2.10a) for a one-site binding model (Scatchard plot not shown). Non-specific binding values from Fig 2.9a are also shown on this curve. The binding parameters were fairly close to those given by Ozer and Tacal (2001) (K_d 25 ± 2.4 μM and B_{max} 3.20 ± 0.1, r^2 0.9489). However, the control experiments clearly showed significant loss of ligand as [SAL] increased.

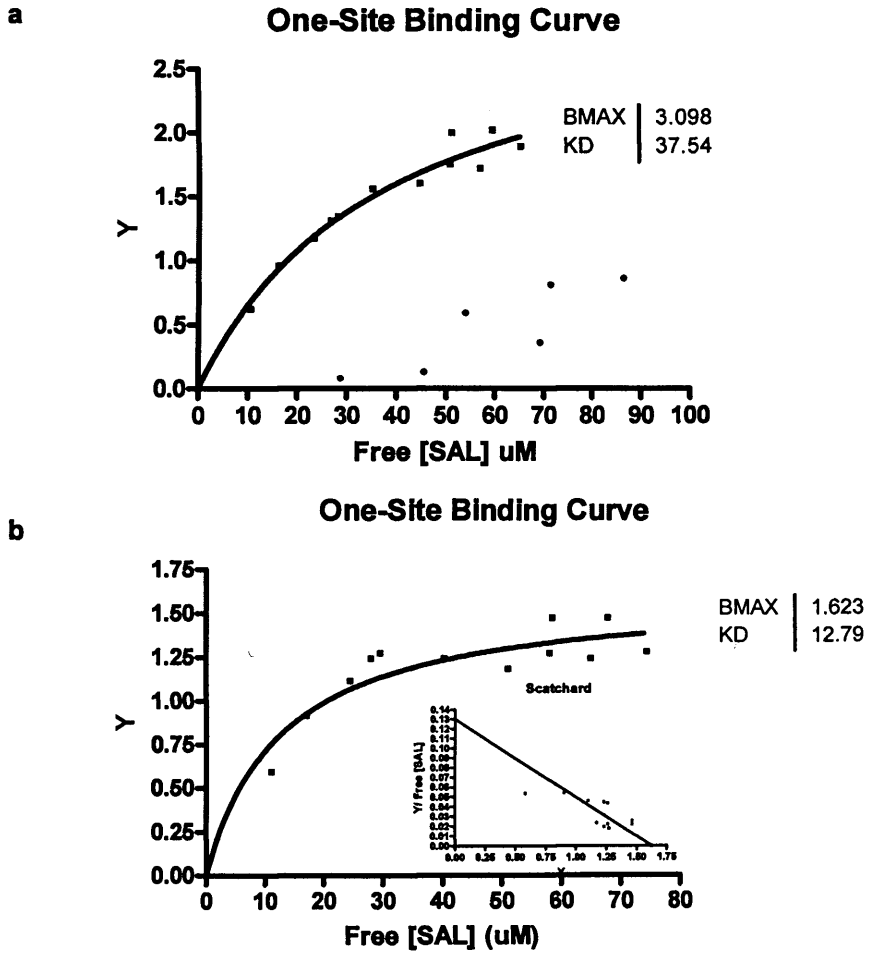


Fig. 2.10 HSA-SAL binding curve measured from diffusion cell dialysis. A non-linear binding curve was created for the HSA-SAL interaction **a**) without removing and **b**) removing non-specific binding from the curve. Non-specific binding is also shown on curve a (circles). Scatchard analysis (inset) was used to find binding parameters Y = bound [SAL] / total [HSA]. (n = 4-6). SEM was <3% of the mean free [SAL].

Adjusting for loss of ligand, the K_d value was 12.79 ± 3.75 and B_{max} was 1.62 ± 0.12 (Fig 2.10b) for a one-site binding model (Scatchard plot not shown). Precision seemed poor (r^2 0.7835). The controls had to be carried out separately from the experiments (insufficient diffusion cell compartments) making it harder to adjust accurately for loss of ligand. These K_d and B_{max} values are far from those reported for a one-site Scatchard binding model (Ozer and Tacal, 2001).

It is possible that the binding curve would fit to a two-site Scatchard binding model, however this would have to be determined by dialysing higher starting [SAL] with HSA. The method was very low-throughput and a more efficient Eppendorf dialysis method was used for future experiments (Section 2.3.4).

2.3.4 Equilibrium dialysis of HSA with SAL using Eppendorf tubes

2.3.4.1 Equilibration time and mass balance controls

The [SAL] reached equilibrium between 12 and 24 hours (Fig. 2.11). The amount of ligand lost (mass balance) during the experiments was calculated as 0.2µg (equivalent to 41.10µM). This is lower than observed for the diffusion cell method (19.77µg, Section 2.3.3.3). This could be explained due to the differences in compartment surface areas and compartment materials. Equilibrium appears to be reached after 12 hours which is a lot quicker than was observed for the diffusion cell method. Subsequent experiments were dialysed for at least 16 hours (overnight).

2.3.4.2 Protein control experiments

There was no significant difference between the absorbance of HSA before (0.961) and after (0.926) dialysis. An average absorbance of 0.015 ± 0.001 was observed in the L compartments after dialysis with HSA and 0.019 ± 0.001 without (compared to 0.000 at the start). It was concluded that HSA did not pass across the semi-permeable membrane.

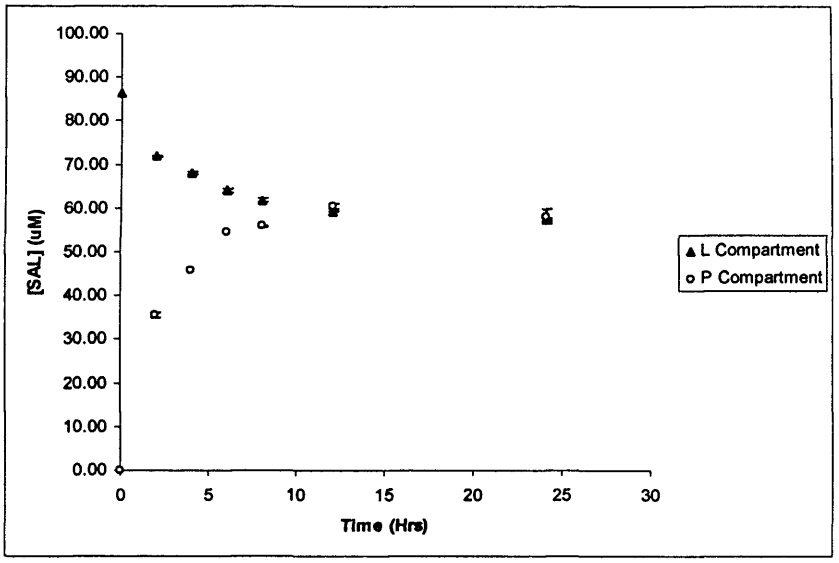


Fig. 2.11 Equilibrium control experiment for Eppendorf tube dialysis. SAL (L compartment: n = 5 ± SEM) was dialysed with buffer (P compartment: n = 1-2 ± SEM) for 24 hours. Samples were removed from both compartments at each time-point and analysed by UV spectroscopy. [SAL] are shown after compartment volume correction. The graph was used to calculate equilibration time and mass balance.

2.3.4.3 Ligand control experiments

a. Fluorescence spectroscopy

SAL lost after 18 hours was measured as 2.00 ± 0.42μM. The values were considerably more precise than was observed using the diffusion cell method (Section 2.3.3.3).

b. UV spectroscopy

Non-specific ligand binding graphs were plotted for samples obtained using a Hamilton syringe (Fig. 2.12a) and using a Gilson pipette (Fig. 2.12b) (Section 2.2.5.5b). When using the Hamilton syringe to sample the L compartments, the loss [SAL] increased with starting [SAL], (as seen in the diffusion cell experiments). Since the loss of SAL did not appear to be saturable, it was proposed that some dilution of the sample was occurring during the sampling process. This process involved washing the syringe in clean buffer between samples. In order to fully remove buffer from the needle, the syringe was rapidly pumped. This meant that the syringe and needle were full of air when inserted into the sample. In order to fully fill the needle and syringe with sample, it was found necessary to rapidly pump the syringe once introduced into the sample. However, this approach resulted in

the formation of air bubbles, which interfered with the UV measurements. For rapid analysis of hundreds of samples it was not feasible to remove these bubbles for each sample. Therefore, the washing buffer was not removed from the syringe needle prior to sampling and it was anticipated this would make a very small difference to the sample concentration. However, this was not the case and the data suggested that a significant dilution had occurred. In fact, a measurement carried out at a much later date showed that ~30µl of washing buffer remained in the syringe, leading to a sample (300-400µl) dilution of 7-10%. This would have lead to a decrease in sample concentration and would fully explain the observed results (Fig. 2.12a).

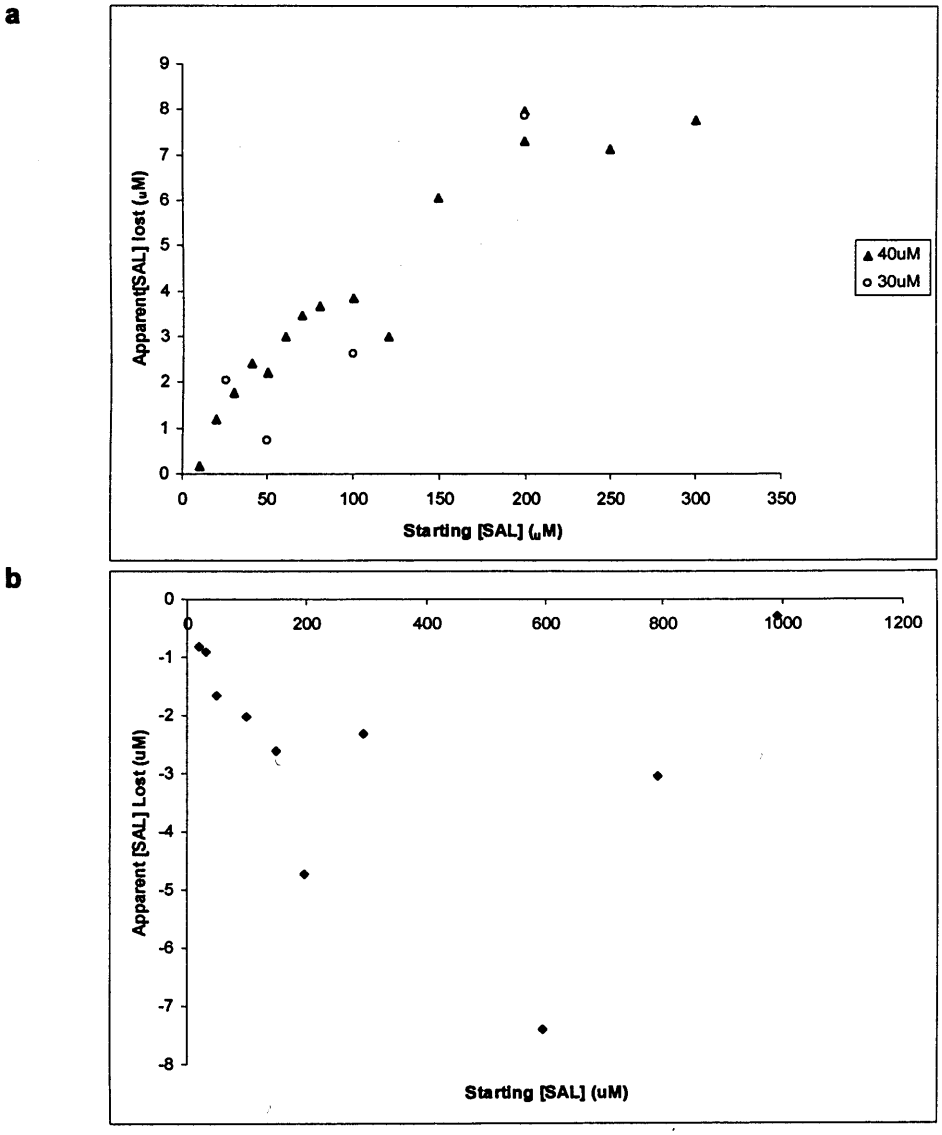


Fig. 2.12 Ligand control experiment for diffusion cell dialysis using UV analysis. The apparent loss of [SAL] in 24 hour equilibrium dialysis experiments, analysed using **a**) Hamilton syringe sampling and **b**) Gilson pipette sampling. The apparent [SAL] lost for all the equilibrium dialysis experiments are plotted (n = 4-6). SEM was <3% of the mean free [SAL] and <6% when below the detection limit.

When sampling from disassembled L compartments using a Gilson pipette, dilution of the samples would not have occurred. Care was taken with the disassembly of the Eppendorf tubes to prevent contaminating L compartments with HSA. For this sampling method, the apparent [SAL] loss was negative (indicating an actual gain) as the starting [SAL] increased. On close examination of the Eppendorf tubes, condensation droplets were observed on the L compartment surfaces after 24 hrs dialysis. It would be predicted that this loss due to evaporation could have given rise to the near-linear *decrease in [SAL] loss* that was observed (Fig. 2.12b).

2.3.4.4 HSA-SAL equilibrium dialysis binding experiments

a. Fluorescence spectroscopy

Adjusting for loss of ligand, the K_d value was 19.18 ± 4.65μM and B_{max} was 2.532 ± 0.27 (Fig. 2.3.13) for a one-site binding model. The controls were carried out separately from the experiments making it harder to adjust accurately for loss of ligand. However, the values for K_d and B_{max} were within those given by Ozer and Tacal (2001) (25 ± 2.4μM and 3.20 ± 0.1). The r^2 value was 0.9002. Each experiment used a fresh 30μM HSA solution, to account for any error in the preparation of the HSA solution.

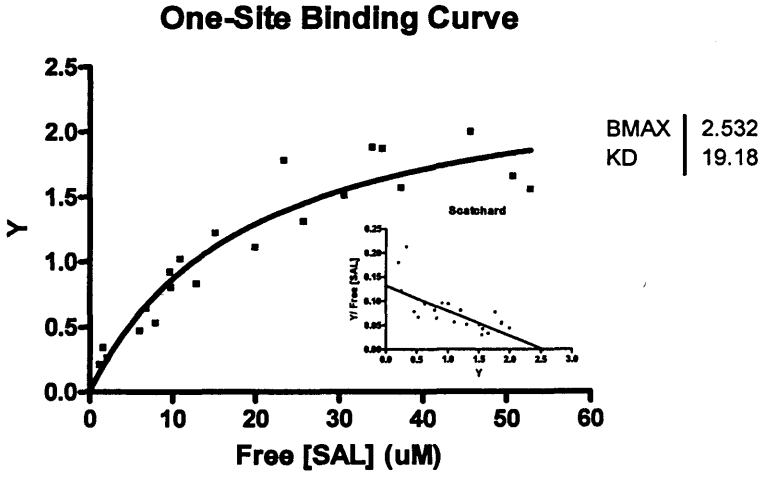


Fig. 2.13 HSA-SAL binding curve using Eppendorf tube dialysis and fluorescence analysis. A non-linear binding curve was created and Scatchard analysis (inset) was used to find binding parameters for the HSA-SAL interaction. (n = 4-6). Y = $[SAL]_{bound}$ / $[HSA]_{total}$. SEM was <3% of the mean free [SAL] and <6% when below the detection limit.

b. UV spectroscopy

Previously reported HSA-SAL binding experiments and parameters are given in Appendix II. In this research, the data for 30 and 40μM HSA solutions and the Hamilton and Gilson sampling methods were combined and plotted in Fig. 2.14 (n=4-6). Ozer and Tacal (2001) used 38μM HSA, but a 30μM [HSA] has been widely used in other dialysis protocols (Appendix I) and was used in these experiments. Little difference between the binding data was observed for the different sampling methods and [HSA]s. For a one-site Scatchard binding model, the K_d value was 32.28 ± 4.10μM and B_{max} was 3.21 ± 0.12 (Fig. 2.14 a). This was comparable to the values reported in Ozer and Tacal (2001) (K_d 25 ± 2.4 and B_{max} 3.2 ± 1.6), using the same dialysis method, temperature and preparation of protein. Sjoholm et al. (1976) reported a higher K_d (55.6) at higher temperature 37°C but B_{max} was similar (2.7). This could be explained by results from another study (Zaroslinski et al. 1974), showing that a decrease in temperature leads to a decrease in K_d for the SAL-HSA interaction. In this study, the data was shown to better fit a two-site binding model (r^2 0.9719) rather than a one-site model (r^2 0.9195). The one-site model suggests that there are ~3 identical ligand binding sites for SAL (Ozer and Tacal (2001)). This contradicts much of the literature, where, commonly, a two-site model has been predicted (Appendix II).

In the two-site binding model (Fig. 2.14b), the first K_d values was calculated as 14.97 ± 2.30μM. The second K_d value was not well defined (2.32×10^{15} ± 4.23×10^{27} μM). B_{max} values were (1) 2.30 ± 0.10 and (2) 5.24×10^{12} ± 5.24×10^{24} respectively (Fig. 2.14b). More data points would have to be measured to better define the second site. B_{max} (1) suggested two identical high-affinity sites. Many of the groups who reported two-site binding models used non-defatted albumin preparations or different methods of analysis, and so comparison between binding parameters was complicated (Appendix II). However, similar values have been reported for K_d1 using CD spectroscopy (8.3μM, Otagiri and Perrin 1976) and gel filtration frontal analysis (18.55uM, Zaroslinski et al. 1974). The one-site and two-site binding data suggests that the Eppendorf tube dialysis approach was a valid method for measuring unknown protein-ligand binding parameters.

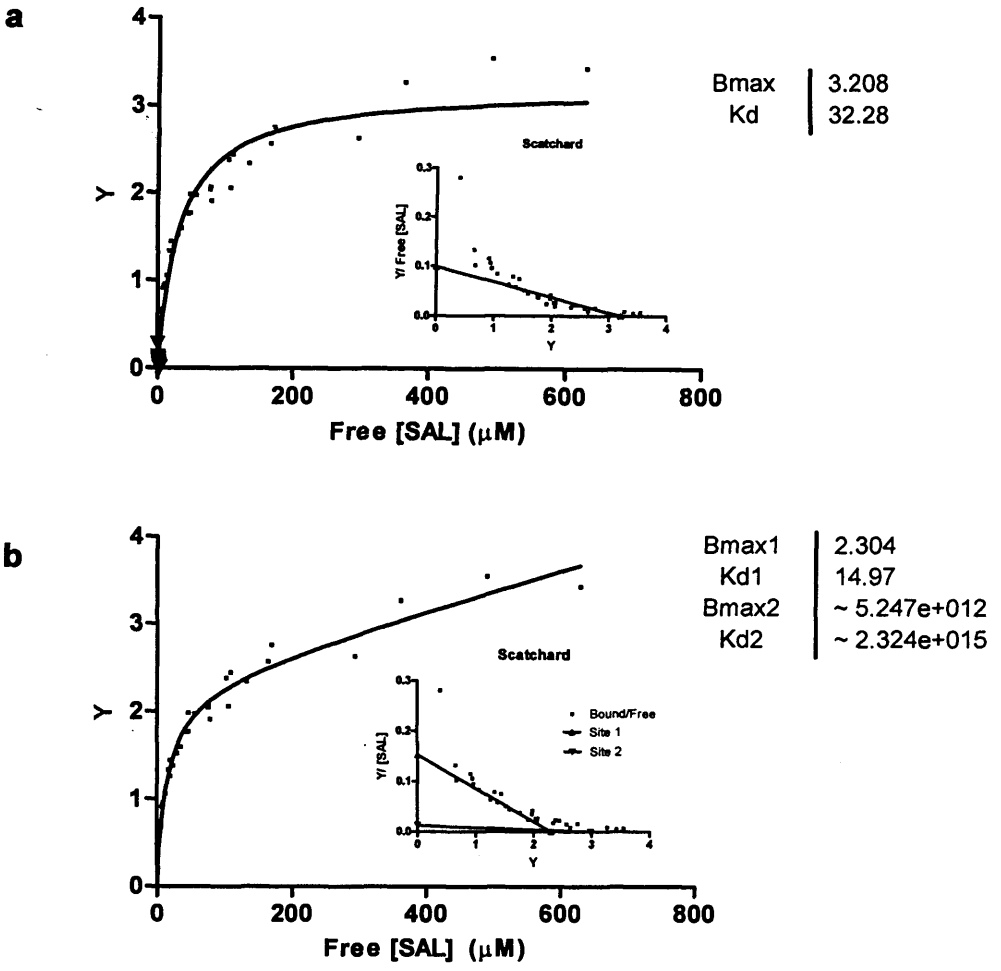


Fig. 2.14 HSA-SAL binding curve measured after Eppendorf tube dialysis and UV analysis. A non-linear binding curve was created and Scatchard analysis (inset) was used to find binding parameters (table) for the HSA-SAL interaction. **a**) One-site binding analysis. **b**) Two-site binding analysis. (n = 4-6). Y = bound [SAL] / total [HSA]. SEM was <3% of the mean free [SAL] and <6% when below the detection limit.

2.3.5 Conclusions

An equilibrium dialysis method using receptor compartments of diffusion cells was not successfully validated. HSA-SAL binding parameters (K_d 12.79 ± 3.75μM and B_{max} 1.62 ± 0.12) (Fig 2.10b) did not match those previously reported for a one-site binding model (Kd 25 ± 2.4μM and BMax 3.20 ± 0.1) (Ozer and Tacal 2001). Inconsistent, non-specific binding of SAL to the apparatus did not allow precise determination of binding parameters. This technique only allowed for very slow through-put analysis. Validation of an equilibrium dialysis method using Eppendorf tubes was successful. Equilibrium was reached must faster than for diffusion cells and non-specific binding of SAL to the apparatus was lower. Two sampling methods using a

Hamilton syringe and a Gilson pipette appeared to give similar HSA-SAL binding curve data, although the corresponding ligand control experiments were non-identical. The binding curve was shown to fit a one-site binding model and parameters were comparable to those previously reported (Ozer and Tacal 2001) using both UV (K_d 32.28 ± 4.10μM and B_{max} 3.21 ± 0.12) and fluorescence (Kd 19.18 ± 4.65μM and B_{max} 2.532 ± 0.27) spectroscopic analysis. UV spectroscopic data was more precise although the fluorescence technique allowed higher through-put analysis. The curve was also shown to fit a two-site binding model with a K_d1 (14.97 ± 2.30μM) comparable to published values (Otagiri and Perrin 1976, Zaroslinski et al. 1974).

References

2003. GraphPad Prism Version 4.0.San Diego CA: GraphPad Software, Inc.

PDB, H.M. Berman et al. 2000, J. Westbrook, Z. Feng, G. Gilliland, T.N. Bhat, H. Weissig, I. N. Shindyalov, P. E. Bourne: The protein data bank. *Nucleic acids research*, 28 pp. 235-242.

Aarons, L. et al. 1980. Aspirin binding and the effect of albumin on spontaneous and enzyme-catalysed hydrolysis. *Journal of Pharmacy and Pharmacology* 32, pp. 537-543.

Berger, G. and Girault, G. 2003. Macromolecule-ligand binding studied by the Hummel and Dreyer method: current state of the methodology. *Journal of Chromatography B* 797(1-2 SU -), pp. 51-61.

Beynon, R. 1996. *Buffers for pH control* Available at: <URL: http://www.liv.ac.uk/buffers/buffercalc.html > [Accessed: 22 april 2004]

Brown, K. F. and Crooks, M. J. 1976. Displacement of tolbutamide, glibenclamide and chlorpropamide from serum albumin by anionic drugs. *Biochemical pharmacology* 25, pp. 1175-1178.

Burns, D. T. 1993. Principles of photometric measurements with particular reference to the UV-visible region. In: Clark, B.J. et al. eds. *UV spectroscopy: Techniques, instrumentation, data handling*. Chapman & Hall, p. 12.

Campbell, S. J. et al. 2003. Ligand binding: functional site location, similarity and docking. *Current Opinion in Structural Biology* 13(3), pp. 389-395.

Cheng, A. and Carlson, G. M. 1983. Utilization of conical equilibrium dialysis cells to shorten equlibriation time. *Analytical Biochemistry* 134, pp. 505-511.

Clarkson, J. and Campbell, I. D. 2003. Studies of protein-ligand interactions by NMR. *Biochemical society transactions* 31, pp. 1006-1009.

Ellwell, M. L. and Schellman, J. A. 1977. Stability of phage T4 lysozymes. *Biochimica et Biophysica Acta* 494, pp. 367-383.

Epps, D. E. et al. 1999. Determination of the affinity of drugs toward serum albumin by measurement of the quenching of the intrinsic tryptophan fluorescence of the protein. *Journal of Pharmacy and Pharmacology* 51(1), pp. 41-48.

Hetenyi, C. et al. 2003. A comprehensive docking study on the selectivity of binding of aromatic compounds to proteins. *Journal of Chemical Information and Computer Sciences* 43(5), pp. 1576-1583.

Honore, B. and Brodersen, R. 1983. Albumin binding of anti-inflammatory drugs. *Molecular pharmacology* 25, pp. 137-150.

Honore, B. 2001. Equilibrium dialysis and rate dialysis. In: Harding, S.E. and Chowdhry, B.Z. eds. *Protein-ligand interactions: hydrodynamics and calorimetry*. Oxford University Press, pp. 19-46.

Kier, L. B. 2002. QSAR modeling of drug binding to protein: beta-lactam serum binding and albumin binding affinity.MDL Discovery Predictive Science. pp. 1-18

Labute, P. 1997-2004. *Flexible alignment of small molecules* [WWW]. Available at: <URL: www.chemcomp.com/journal/malign.htm> [Accessed: 26th August 2004]

Last, A. M. and Robinson, C. V. 1999. Protein folding and interactions revealed by mass spectrometry. *Current Opinion in Chemical Biology* 3(5), pp. 564-570.

Liu, Y. et al. 2003. Quartz crystal biosensor for real-time monitoring of molecular recognition between protein and small molecular medicinal agents. *Biosensors and Bioelectronics* 19(1), pp. 9-19.

Morrill, P. R. et al. 2003. Imaging surface plasmon resonance system for screening affinity ligands. *Journal of chromatography B* 793, pp. 229-251.

Muresan, S. et al. 2001. Interaction of beta-lactoglobulin with small hydrophobic ligands as monitored by fluorometry and equilibrium dialysis: Nonlinear quenching effects related to protein-protein association. *Journal of Agricultural and Food Chemistry* 49(5), pp. 2609-2618.

Oldham, N. J. et al. 2003. Non-denaturing electrospray ionisation-mass spectrometry reveals ligand selectivity in histamine-binding protein RaHBP2. *Organic & Biomolecular Chemistry* 1(21), pp. 3645-3646.

Otagiri, M. and Perrin, J. H. 1976. Circular dichroic investigations of the binding of salicylate and related compounds to human serum albumin. *Biochemical Pharmacology* 26, pp. 283-288.

Ozer, I. and Tacal, O. 2001. Method dependence of apparent stoichiometry in the binding of salicylate ion to human serum albumin: A comparison between equilibrium dialysis and flourescence titration. *Analytical biochemistry* 294, pp. 1-6.

Peters, T. 1996. *All about albumin: Biochemistry, genetics and medical applications.* Academic Press, Inc., p. 39.

Reinard, T. and Jacobsen, H.-J. 1988. A simple and inexpensive system for protein-ligand binding assays. pp. 157-160.

Rubino, M. I. et al. 1996. Phenolic protein interactions in relation to the gelation properties of canola protein. *Food Research International* 29(7 SU -), pp. 653-659.

Sjoholm, I. et al. 1975. Protein binding of drugs in uremic and normal serum: The role of endogenous binding inhibitors. *Biochemical pharmacology* 25, pp. 1205-1213.

Smyk, B. 2003. Fluorescence study of sinapic acid interaction with bovine serum albumin and egg albumin. *Journal of Fluorescence* 13(4), pp. 349-356.

Threllfall, T. L. 1993. Spectra-structure correllation. In: Clark, B.J. et al. eds. *UV spectroscopy: Techniques, instrumentation, data handling.* Chapman & Hall, pp. 68-87.

Utsumi, H. et al. 2003. Segment identification of a ligand binding with a protein receptor using multidimensional T_{1P}-, diffusion-filtered and diffusion-ordered NOESY experiments. *Analytical Sciences* 19, pp. 1441-1443.

Zaroslinski, J. F. et al. 1973. Effect of temperature on the binding of salicylate by human serum albumin. *Biochemical pharmacology* 23, pp. 1767-1776.

Zhong, D. et al. 2000. Femtosecond studies of protein-ligand hydrophobic binding and dynamics: Human serum albumin. *PNAS* 97(26), pp. 14056-14061.

Chapter 3

Selection and characterisation of a high-affinity protein-ligand interaction

3.1 Introduction

A novel protein imprinting approach was proposed (Section 1.5) using high-affinity ligands to provide strong protein recognition sites on a flat surface. Covalent and non-covalent ligand-protein interactions were investigated. The covalent binding interaction of human serum albumin (HSA)-ethacrynic acid (ETH) was selected and characterised.

3.1.1 Selection of a high-affinity protein-ligand interaction

3.1.1.1 Criteria for choosing a high-affinity ligand and model protein

The criteria for finding a suitable ligand-protein interaction were quite limiting. The protein and ligand were required to be inexpensive, stable and commercially available. Ligands would preferably be UV / fluorescence detectable (after dialysis), soluble in aqueous solutions at physiological pH (protein conformations are usually retained in narrow pH range), have high affinity and specificity and lastly, the ligand should have a solvent-accessible group available for derivatisation and surface attachment (Fig. 3.1).

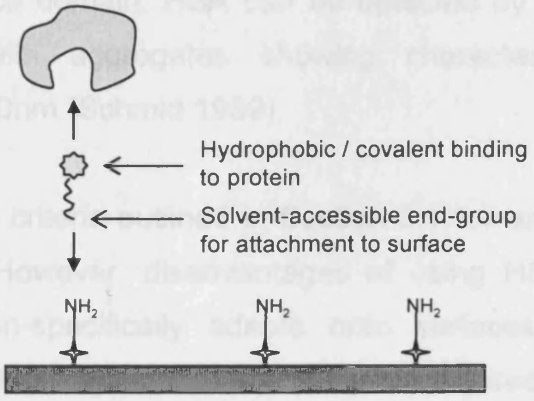


Fig. 3.1 The requirements of a high-affinity ligand for specific protein surface orientation. A high-affinity ligand binds HSA through hydrophobic / covalent bonding at one end, and can be surface-immobilised by modification and chemical attachment at the other.

A 1:1 protein-ligand interaction was desirable for uniform protein orientation and molecularly imprinted polymer (MIP) binding site homogeneity. This has been a challenge in itself for biotechnological applications such as biosensors and arrays (Meyer et al. 2006). The combination of a high

affinity interaction (non-covalent, K_d ~10^{-6}M) and multipoint weak interactions (e.g. H-bonds) in the imprinted site, could potentially create affinity sites comparable to that of antibodies (K_d >10^{-8}M) and small-molecule MIPs (K_d ~10^{-7}M) (Andersson et al. 1995). An aromatic group (required for UV / fluorescence detection) could facilitate hydrophobic binding inside a specific protein pocket, but a hydrophilic moiety would be required to maintain aqueous solubility. Alternatively, a reversible covalent protein-ligand interaction could be used. However, in this case, template-protein removal would require bond cleavage.

3.1.1.2 Selection of a model protein

Ovalbumin was initially investigated, as a cheap and stable template protein. Ovalbumin has a very tight conformation in solution, and no known physiological function (Grinberg et al. 2002). Very little information about ligand binding was available. On the other hand, HSA has been thoroughly characterised (Peters 1996; Fasano et al. 2005). The structure of HSA is well known, as characterised by sequencing analysis (Minghetti et al. 1986 in Peters 1996) and X-ray crystallography (Sugio et al. 1999). It has three homologous domains (I, II, III) all comprising the same amino acid chain linked by 17 disulfide bonds (Peters 1996). Nine loops form the subdomains A and B for each domain. HSA can be detected by UV and fluorescence spectroscopy with aggregates showing characteristic UV absorption between 310-400nm (Schmid 1989).

HSA fulfilled the criteria outlined in Section 3.1.1.1 and was chosen as the model protein. However, disadvantages of using HSA were its size and tendency to non-specifically adsorb onto surfaces (Chapter 8). Other proteins (and their ligands) were also considered, but either binding interactions were too weak, the protein was too expensive or the protein was not commercially available (e.g. β-lactoglobulin, immunoglobulins, RNase A, transferrin, carbonic anhydrase, cytochrome C and acetylcholinesterase).

3.1.1.3 Selection of a ligand

Initially, equilibrium dialysis was to be used to screen a number of candidate ligands for binding to HSA. It was anticipated however that for unknown ligand-protein interactions, this would take too long, especially if all of the criteria outlined in Section 3.1.1.1 were to be fulfilled.

A large literature search of ligands and their interaction with HSA was carried out to identify a ligand 'shortlist'. Suitable ligand-protein pairs would then be characterised by equilibrium dialysis (Chapter 2). As a component of blood serum, HSA is involved in the transport of many endogenous substances such as bilirubin and fatty acids, and also exogenous molecules including many drugs, which would otherwise be insoluble (Peters 1996). Most ligands bind non-covalently in specified binding pockets (these include sites I (Sudlow, domain IIA) and II (Benzodiazepine, domain IIIA), Peters 1996). The binding sites are likely to be flexible with varying (rather than pre-defined) binding interactions for different ligands (Russeva et al. 1998). Many small ligands that bind strongly to HSA are hydrophobic, insoluble in water and therefore difficult to analyse by equilibrium dialysis.

A shortlist of non-covalent, aromatic ligands was drawn up (structures in Appendix III). These were salicylic acid (SAL, Ozer and Tacal 2001), 5-aminosalicylic acid (ASA, Ilichev et al. 2002), vanillic acid (VAC), vanillin (VAN), ibuprofen (IBU, Cheruvellath et al. 1997), naproxen (NAP, Cheruvellath et al. 1997), diclofenac (DIF Boeckel et al. 1992), and L-Tryptophan (Trp, McMenamy and Oncley 1958 in Peters 1996). All were either fluorescent (e.g. NAP) or UV detectable (e.g. VAN). For some of the ligands, HSA binding parameters had been previously reported (e.g. NAP), whilst for others this information was not available (e.g. VAC and VAN). All were inexpensive and commercially available and possessed potentially derivatisable solvent-free groups.

A number of ligands have been shown to modify HSA covalently at specific amino acids including aspirin at Lys-199 (Gerig et al. 1981 in Peters 1996), pyridoxal 5'-phosphate at Lys-190 (P5P, Bohney et al. 1992) and glutathione and ethacrynic acid (ETH) at Cys-34 (Peters 1996).

3.1.2 Chapter objectives

- To select a high-affinity, model protein-ligand interaction that met a specific set of criteria, including feasibility for surface attachment (Fig. 1.12).
- To characterise the protein-ligand interaction (HSA-ETH) and measure binding parameters using a validated approach.
- To determine whether derivatisation of the carboxylate of ETH, required for surface attachment, affected binding to the protein.

3.2 Methods

3.2.1 Equipment and materials

As for Chapter 2. Additional equipment and materials also used:

Equipment: MicroModulyo Lyophiliser (Thermo-Savant, Fisher, Waltham, MA, USA) with XDS 5 pump (Edwards, Livermore, CA, USA).

Materials: Bradford Reagent was purchased from Sigma-Aldrich (St Louis, MO, USA). PD10 columns (with a matrix of Sephadex G-25 medium, stored in distilled water containing 0.15% Kathon CG / ICP biocide were from Amersham Biosciences (Buckinghamshire, UK).

Buffers: Phosphate buffered saline (PBS) (x1, pH7.4, [WWW] The lab rat 2005) was made from sodium chloride (NaCl, 8g, Fisher), potassium chloride (KCl, 0.2g, Fisher), potassium phosphate (KH_2PO_4, 0.24g, Bdh chemicals, Merck, Poole, Dorset) and sodium phosphate (Na_2HPO_4, Sorensens salt, 2.3g, Fisher) diluted to 1L with de-ionised water (dH_2O). Acetate buffer (acetic acid, 10mM, pH5.5, Fisher), NaPB (10mM, pH7.4), NaPB (67mM pH6.5) and NaPB (67mM, pH7.9) were made as directed in [WWW] Beynon (1996) ; chemicals in Section 2.2.1).

3.2.2 Identifying a high-affinity ligand

3.2.2.1 UV spectroscopic measurements of aromatic ligands

UV spectra of a number of potential HSA ligands (Section 3.1.1.3: Trp, VAC, NAP, ASA, HPA, IBU, VAN, DIF, P5P and ETH) were scanned to determine λ_{max}, as in Section 2.2.2.1, except 400µl cuvettes were used. Ligand concentrations [L] of between 50 and 100µM were scanned.

3.2.2.2 Fluorescence spectroscopic measurements of aromatic ligands

Fluorescence spectra were measured in a Series 2 luminescence spectrophotometer (Section 2.2.3.1). The UV λ_{max} of each ligand (Section

3.2.2.1) was used as the initial excitation wavelength (λ_{ex}) for fluorescence measurements. [L] of between 50 and 100μM were scanned to find the λ_{ex} and λ_{em}. The appropriate fluorescence excitation and emission filters of the Fluostar plate-reader were used to produce a calibration graph for each ligand.

3.2.3 Evaluation of HSA-ETH binding

3.2.3.1 UV spectroscopic analysis of ETH

- **ETH UV calibration graph**

The method was as used for SAL-HSA binding analysis (Section 2.2.2.2). A number of dilution series (between 1000 and 10μM ETH) were made from different stock solutions of ETH (1000μM).

3.2.3.2 Equilibrium dialysis of HSA with ETH without pre-saturation of the covalent site (Cys-34)

a. Equilibrium control experiment and mass balance

The general method is described in Section 2.2.5.2. The concentration of ETH in ligand (L) and protein (P) compartments, at 0, 2, 4, 6, 8, 14 and 24 hours, were determined from A_{280} measurements. The starting concentrations of ETH were corrected for a 2/3 dilution in the Eppendorf tubes (Appendix I). The 24 hour time-points were adjusted for NaPB background absorbance at 280nm.

b. Ligand control experiments

The general method of Section 2.2.5.4 was followed.

c. HSA-ETH binding graph

The general method of Section 2.2.5.5 was followed. HSA was dialysed with ETH for 72 hours. Calculation of equilibrium dialysis binding parameters is described in Appendix I.

3.2.3.3 Pre-saturation of the covalent HSA sites (CYS34) with ETH

a. Saturation

A published method (Bertucci et al. 1998) was modified to saturate the HSA covalent sites with ETH. A 5:1 molar ratio of ETH (1.24mM): HSA (0.25mM) in 10 ml NaPB (67mM, pH7.4) was slowly stirred overnight at room temperature. In subsequent experiments the resulting complex is referred to as HSA-ETH.

b. Freeze-drying

After saturation the HSA-ETH solution was transferred to a freeze-drying vial, covered in parafilm (punctured with small holes) and frozen in liquid nitrogen. The vials were placed in a freeze-drier for 20 hours or until samples were dry.

c. Removal of vast excess ETH by bulk dialysis

Free ETH was slowly removed from HSA-ETH by large-scale dialysis. HSA-ETH solution (~20ml) was poured into semi-permeable dialysis tubing (tied with a knot at the bottom and clamped at the top). The tubing was placed in 2 litres of solvent in a large conical flask on a magnetic stirrer (Fig. 3.2). Ligand was freely diffusible through the membrane and protein remained in the P compartment. The buffer was replaced in order to maximise ligand removal. The tubing was removed and the protein freeze-dried for analysis.

i. First method (M1)

After freeze-drying, the HSA-ETH solution was dissolved in 20ml dH_2O and dialysed against NaPB (pH7.4, 67mM, 2 litres) for 24 hours and then dH_2O (2 litres) for 24 hours (room temperature). ETH reduction was monitored by UV.

ii. Second method (M2)

The HSA-ETH containing solid was dissolved in NaPB (pH 7.4, 10mM) and transferred to the dialysis tubing without prior freeze-drying. Bulk dialysis

was carried out at 25 ± 5°C for a total of $4^1/_4$ days. The dialysis fluid in the L compartment was replaced every 6-12 hours with fresh 10mM NaPB (pH7.4, (0-78 hours), 67mM NaPB (78-102 hours) and dH_2O (102-114 hours).

At each time point a 520µl aliquot was removed directly from the bulk dialysis tubing. The UV absorbance of 260µl of the sample was determined. The remaining 260µl was diluted 1/3 in NaPB (to an absorbance (279nm) of ~0.65) and analysed by equilibrium dialysis (Section 2.2.5). The sample was placed in the P compartments of Eppendorf tubes and dialysed against NaPB for 24 hours. The UV absorbance (280nm) of the L compartments were measured to monitor the removal of free ETH

After $4^1/_4$ days of bulk dialysis, the sample was transferred to glass vials and a aliquot was diluted 1/2 in NaPB to give an absorbance (279nm) of ~1.20, then analysed by equilibrium dialysis. This sample, pure HSA (30µM) and NaPB were added to P compartments of Eppendorf tubes (Section 2.2.5) and dialysed against NaPB (control) for 72 hours (as for Section 3.2.3.2c). The remaining HSA-ETH solution was freeze-dried and stored.

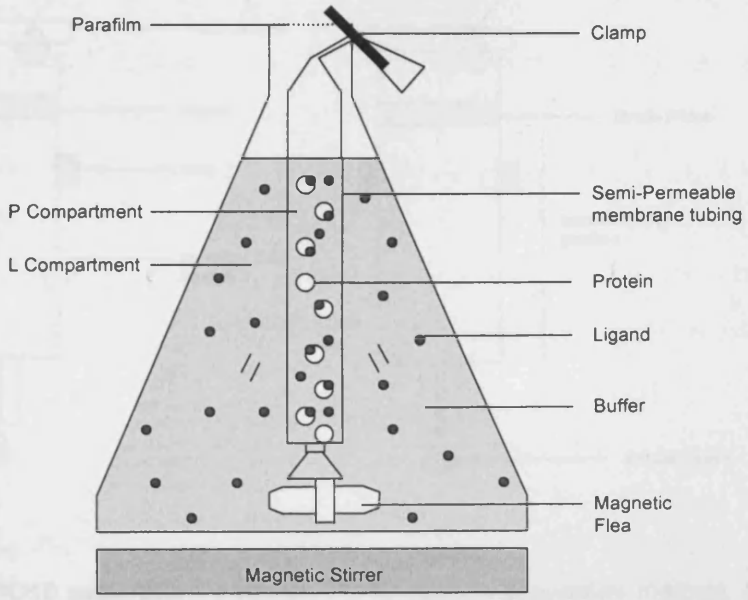


Fig. 3.2 Bulk dialysis removal of excess ligand HSA saturated with ETH was placed in the P compartment. ETH was freely diffusible through the membrane, reaching equilibrium with the L Compartment. HSA remained in the P Compartment, and excess ETH was gradually removed from HSA.

d. Removal of excess ETH using size exclusion chromatography (PD10 columns)

UV spectroscopy (A_{280}) was used to detect elution of HSA-ETH and free ETH. The chromatographic method is described in Fig 3.3. The maximum capacity of the columns was 10mg ml^{-1} protein. The column was pre-equilibrated with 20ml mobile phase (e.g. PBS). 1ml of the sample (~10mg ml^{-1} protein) was added gently to the column. Mobile phase was added in 0.5ml aliquots and the eluent collected in Eppendorf tubes. Up to a total of 48 fractions were collected. Bradford reagent was used to qualitatively monitor elution of protein. Small drops of Bradford reagent were pipetted onto grease-proof paper and 6µl volumes of each fraction added. Sample containing protein (HSA-ETH) changed from pale brown / blue to deep blue. The UV absorbance of each fraction was measured and plotted as an elution profile. Fractions containing HSA-ETH were grouped together and freeze-dried. Five different columns were used to optimise the separation of ETH from HSA-ETH. Each PD10 column was used for a maximum of 10 runs.

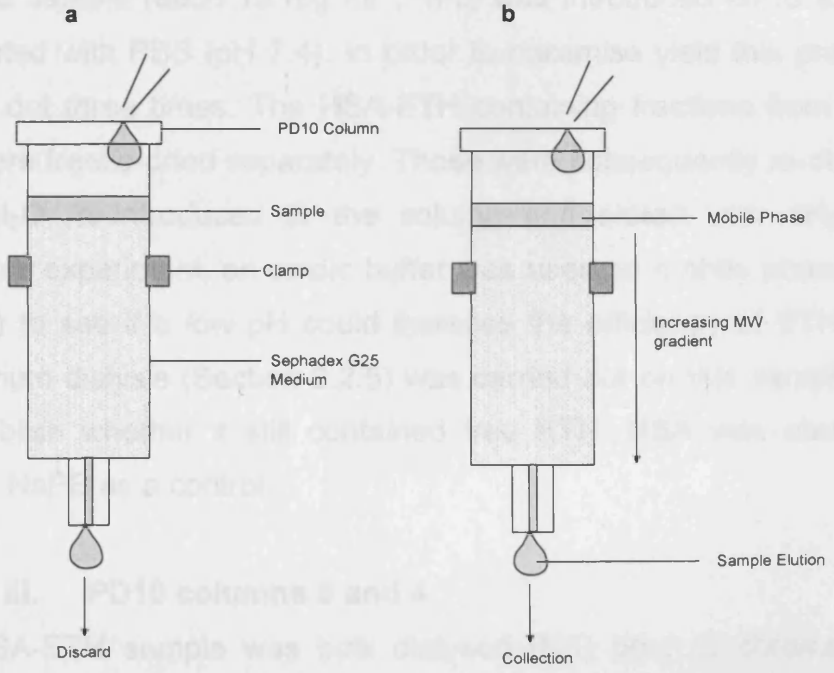


Fig. 3.3 PD10 separation column. PD10 column separation method. **a**) After equilibration of the column with mobile phase (20ml), sample (1ml HSA-ETH solution, 10mg ml^{-1}) was pipetted onto the column. Eluent was discarded. **b**) Mobile phase was added in 0.5ml aliquots and the displaced eluent (0.5ml) was collected into Eppendorf tubes.

i. PD10 column 1

The HSA-ETH sample was not bulk-dialysed prior to chromatography. Initially the samples were eluted with PBS and the fractions containing protein grouped and freeze dried. The solid was then re-dissolved in dH_2O to give a protein concentration of ~10mg ml^{-1}. This was then re-introduced on to the column and eluted with dH_2O. The protein containing fractions were again grouped and freeze dried. Equilibrium dialysis (Section 2.2.5) was carried out on this sample in order to establish whether it still contained free ETH. Since the free dried sample contained an unknown amount of buffer salts it was not possible to weigh a known amount of HSA-ETH. Instead, a solution was prepared with an absorbance (280nm) roughly equivalent to 30-35μM [HSA] based on a HSA calibration graph (Fig. 2.6). HSA was also dialysed against NaPB as a control.

ii. PD10 column 2

The HSA-ETH sample was bulk dialysed (M1) prior to chromatography. The dialysed sample (each 10 mg ml^{-1}, 1ml) was introduced on to the column and eluted with PBS (pH 7.4). In order to maximise yield this process was carried out three times. The HSA-ETH containing fractions from the three runs were freeze-dried separately. These were subsequently re-dissolved in 1ml dH_2O, re-introduced to the column and eluted with dH_2O. In an additional experiment, an acidic buffer was used as mobile phase (acetate pH 5.5) to see if a low pH could increase the efficiency of ETH removal. Equilibrium dialysis (Section 2.2.5) was carried out on this sample in order to establish whether it still contained free ETH. HSA was also dialysed against NaPB as a control.

iii. PD10 columns 3 and 4

The HSA-ETH sample was bulk dialysed (M1) prior to chromatography. HSA irreversibly denatures outside the pH range 5-8 (Peters 1992), therefore pH 7.5, 6.5 and 7.9 NaPB mobile phases (Section 3.2.1) were used. The column was rendered unusable after elution with the pH 6.5 buffer and subsequent experiments used a new column.

iv. PD10 column 5

The HSA-ETH sample was bulk dialysed (M1 was modified slightly with a buffer replacement after 6 hours) prior to chromatography. The dialysed sample (each 10mg ml^{-1}, 1ml) was introduced on to the column and eluted with NaPB (pH 7.4, 67mM). In order to maximise yield this was carried out three times. The HSA-ETH containing fractions from the three runs were grouped and freeze-dried and subsequently run through PD10 column 5 three times to see if all ETH could be removed. This process was repeated using NaPB and dH_2O as mobile phases. Equilibrium dialysis (Section 2.2.5) was subsequently carried out in order to establish the presence of free ETH. NaPB (1), HSA (2), HSA-ETH after bulk dialysis (M1) (3) and HSA-ETH after elution through PD10 column 5 (4) were dialysed against NaPB.

e. Equilibrium dialysis removal of ETH

A modification of the equilibrium dialysis method outlined in Section 2.2.5 was employed to maximise free ETH removal from the HSA-ETH samples. NaPB (1), HSA (2), freeze-dried HSA-ETH after bulk dialysis (M1) (3) and HSA-ETH after elution through PD10 column 5 (4) were dialysed against NaPB. Protein concentration was quantified by UV absorbance at 280nm. The L compartment solutions were replaced with 390µl buffer every 24 hours, for a total of 168 hours. UV scans of the L compartment solutions were obtained to confirm ETH removal.

3.3 Results and discussion

3.3.1 Identifying a high-affinity ligand

3.3.1.1 UV spectroscopic measurements of aromatic ligands

The UV spectrum of each ligand is given in Appendix III.

3.3.1.2 Fluorescence spectroscopic measurements of aromatic ligands

Only Trp, VAC, NAP, ASA and P5P were fluorescent. Fluorescence spectra are given in Appendix III.

3.3.1.3 Ligand selection

ETH was chosen as a readily available and low-cost aromatic (UV-detectable) ligand that has demonstrable covalent binding to Cys-34 via its unsaturated bond (1:1 stoichiometry) and also non-covalent interactions with high affinity to HSA (Bertucci et al. 1997, 1998 & 1999). ETH possesses a carboxylic acid group at the non-HSA binding end i.e. the covalent site, which could be used to attach the ligand to a surface. A 1:1 HSA-ETH covalent interaction would be useful for specific protein surface orientation (Section 1.2.1). Additionally the complex needs to be resistant to the harsh washing conditions likely to be required for removal of non-specifically bound protein on the surface.

ETH has been used as a diuretic (Koechel and Cafruny 1973) and in glaucoma treatment (Bertucci et al. 1998). Binding to a number of different serum proteins has been demonstrated, and its diuretic properties are as a result of its ability to bind proteins containing sulfhydryl / thiol (SH) groups in renal tissue (Komorn and Cafruny 1965 in Koechel and Cafruny 1973). It also has the ability to bind a number of other nucleophilic compounds such as glutathione, via Michael addition (McMurray 2000) (Fig 4.10).

Covalent and non-covalent binding of ETH to HSA (and BSA) has previously been studied by a number of groups (Ronwin and Zacchei 1966, Koechel et al. 1977, Fehske and Muller 1986, Bertucci et al. 1998 & 1999). Covalent HSA-ETH interactions were first suggested by Ronwin and

Zacchei (1966) who reported four irreversible high-affinity sites and twelve reversible sites. Covalent BSA-ETH binding was demonstrated by Koechel et al. (1977) using DNTB to assay the free Cys-34 site. However, using equilibrium dialysis to characterise non-covalent binding sites of HSA, Fehske and Muller (1986) reported that, unlike for BSA, ETH did not modify the Cys-34 site. Iodoacetate modification and 'inactivation' of Cys-34 did not change binding parameters of ETH for HSA. Scatchard analysis suggested that there were two high-affinity non-covalent sites and four low-affinity sites. Despite this report, Bertucci et al. (1997, 1998 & 1999) proposed that ETH does covalently modify the Cys-34 site of HSA via an acrylate-SH bond (Fig 3.4) and also non-covalently at two separate high affinity sites. The main evidence for covalent modification was from mass spectrometry analysis which showed a peak relating to HSA plus one ETH molecule after extensive bulk dialysis to remove reversibly-bound ETH. After Cys-34 modification, the structure of HSA and its ability to bind various non-covalent drugs at the high-affinity sites I and II (Section 3.3.1.3) remained unchanged as shown by CD spectroscopy. Also, the CD spectrum did not show a significant change in secondary structure. This was attributed to the location of the binding site towards the *N*-terminus of the protein (Bertucci et al. 1998). However, binding to lower affinity sites was reduced by ≈50%.

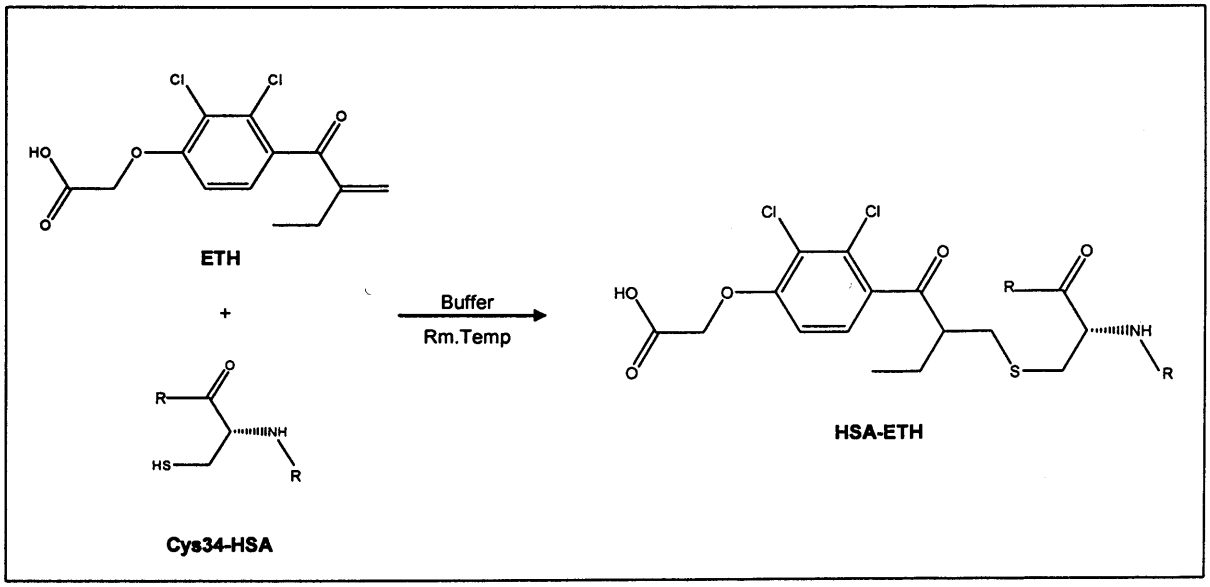


Fig. 3.4 Covalent binding of ETH to HSA. The β-unsaturated ketone group of ETH is modified by nucleophilic attack from Cys-34 (the single free SH on HSA) to form HSA-ETH (*Diagram adapted from Bertucci et al 1998*).

The crystal structure of HSA (2.5Å resolution) has been described (Sugio et al. 1999). The Cys-34-SH group is shown to be enclosed by a number of amino acid side chains: proline (Pro) 35, histidine (His) 39, valine (Val) 77 and tyrosine (Tyr) 84 (Sugio et al. 1999). This may be the cause of the relatively low reactivity of the Cys-34-SH group (pKa ≈7 (Shaked et al. 1980 in Stewart et al. 2005)) compared to free Cys (pKa 8.3, Huber et al. 1967 in Shrift et al. 1996). Reduction in pKa of Cys-12 of arsenic reductase was attributed to ion pairing with a proximal His group (Gladysheva et al. 1996). Cys-34 is obstructed by the Tyr-84 sidechain (Stewart et al. 2004). In solution, ligand binding to Cys-34 is thought to occur because Tyr-84 flips outwards, removing the obstruction (Sugio et al. 1999). Protein dimers formed from disulfide bonding of the free Cys-SH are unlikely because of steric hindrance (Carballal et al. 2003).

Equilibrium dialysis was chosen to characterise covalent and non-covalent binding of ETH to HSA (Section 3.2.3) using a validated method (Chapter 2). Reversible non-covalent binding of ETH to HSA was previously characterised using CD spectroscopy (Bertucci et al. 1999). HSA-Cys-34 was blocked either with Cys, glutathione or captopril. Competition experiments between ETH and different site markers (phenylbutazone / salicylate (site I), diazepam (site II), bilirubin (site III) and fatty acid (FA) binding sites) were carried out to determine the location of non-covalent sites. Competitive binding was seen at two high-affinity sites (site II, K_d 0.56μM and a FA binding site, 7.14μM). The orientation of binding to the non-covalent sites was not determined.

It was possible to model the active form of the Cys-34 binding site (Appendix III). The lowest energy conformation for the covalent HSA-ETH interaction was calculated. The results suggested that the carboxylic acid group will stick out in solution and be free for derivatisation. Molecular modelling was carried out in conjunction with laboratory methods.

Chemical analysis was considered as a means of determining covalent coupling of ETH to HSA. ETH has two chlorine (Cl) groups which would distinguish the ETH-HSA complex from HSA. However, the % of Cl in the

HSA-ETH complex would be much lower (0.001137% of the Mr of ETH-HSA compared to the limit of detection of 0.01%).

3.3.2 Evaluation of HSA-ETH binding

3.3.2.1 UV spectroscopic analysis of ETH

- **UV scan of ETH to find λ_{max}**

The λ_{max} of ETH was measured as 280nm (A_{280}) (Fig. 3.5). Although the spectra of HSA (A_{279}, Fig. 2.4b) and ETH were quite different the λ_{max} was almost identical.

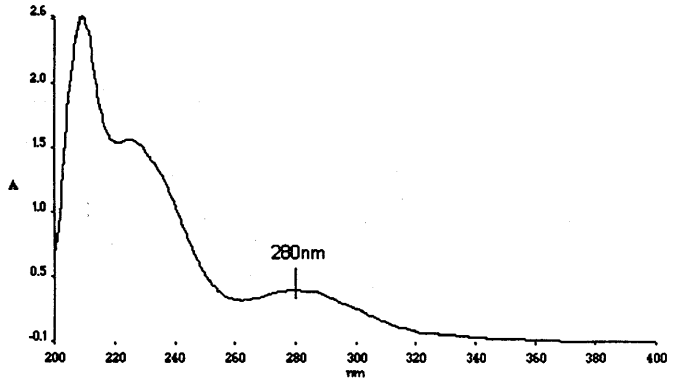


Fig. 3.5 UV scan of ETH ETH spectrum scanned in NaPB at room temperature. λmax = 280nm.

- **ETH UV calibration graph**

The calibration graph for ETH gave an ε_{280} of 0.0039μM^{-1} (r^2 = 0.9985). All subsequent ETH solutions used in equilibrium dialysis experiments were within ± 0.0001μM^{-1} of this value.

3.3.2.2 Equilibrium dialysis of HSA with ETH without pre-saturation of the covalent site (CYS-34)

a. Equilibrium control experiment and mass balance

The final corrected [ETH] in the L and P compartments were averaged and plotted (Fig 3.6). Equilibrium was reached by 15 hours. However, the equilibration time used for subsequent experiments was 24 or 72 hours to account for covalent bond formation. The initial mass of ETH in the system was 11.88μg and the final mass was 12.45μg. This suggests a small gain

(4.8%) probably resulting from solvent evaporation (Section 2.2.5.5b). To ensure accurate non-specific binding measurements for each starting [ETH] a control experiment was carried out alongside each protein binding experiment.

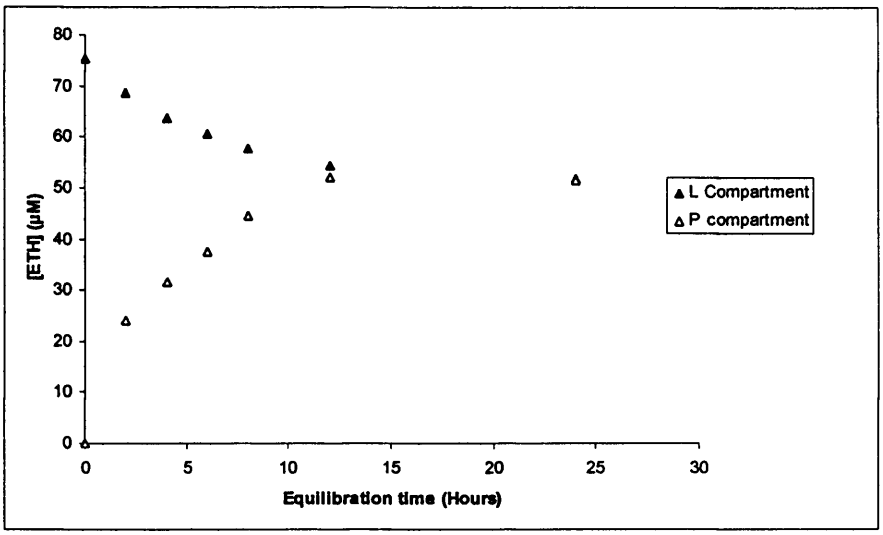


Fig. 3.6 Equilibrium control graph. ETH (L compartment: n = 5 ± SEM) was dialysed with buffer (P compartment: n = 1-2 ± SEM) for 24 hours. Samples were removed from both compartments at each time-point and analysed by UV spectroscopy. [ETH] are shown after compartment volume correction. The graph was used to calculate equilibration time and mass balance.

b. Ligand control experiments

Non-specific ligand binding graphs were plotted for the Hamilton syringe analysis method (Section 2.2.5.5b) (Fig 3.7a). The apparent [ETH] loss increased as the starting [ETH] increased. This was attributed to dilution in the syringe (Section 2.3.4.3b). For the Gilson analysis method (Section 2.2.5.5b), the apparent [ETH] loss decreased as the starting [ETH] increased (Fig 3.7b). This may be due solvent evaporation as described in Section 2.3.4.3b.

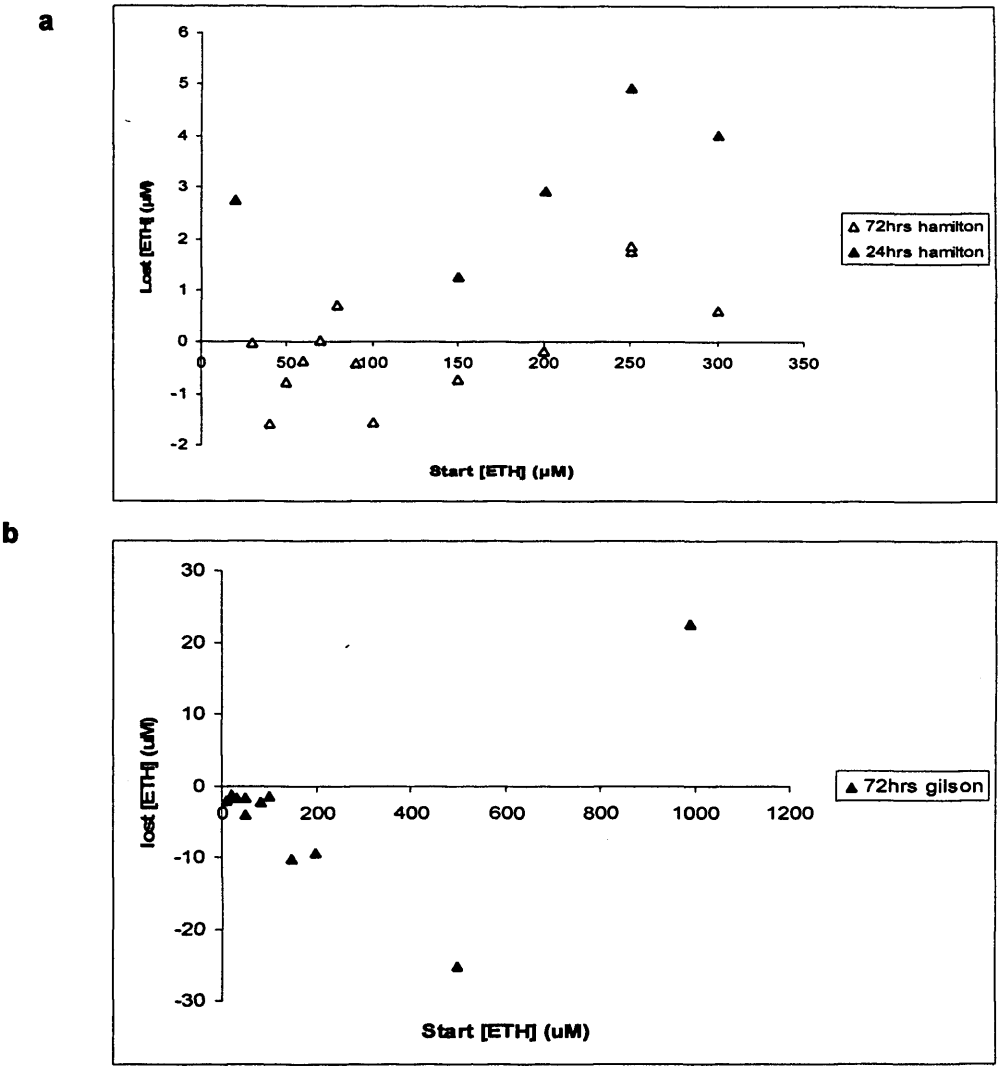


Fig. 3.7 Apparent [ETH] loss with increasing starting [ETH] for equilibrium dialysis binding experiments. a) Hamilton syringe sampling. **b**) Gilson pipette sampling. SEM <3% of the mean free [SAL].

c. HSA-ETH binding curve

Data points from experiments with free [ETH] below the detection limit (Section 2.3.1.3) were removed (i.e. starting [ETH] of <30µM). The binding graphs obtained using both sampling approaches (Hamilton and Gilson) were similar at low starting [ETH]. The effects of dilution and evaporation were less noticeable at these low [ETH] (Section 3.3.2.2b), hence [ETH] <250µM were used. A starting [ETH] of 45µM (L compartment) was used in order to obtain a post-dialysis [ETH]:[HSA] equilibration ratio of ~1:1 (required for covalent derivatisation of the BSA Cys-34 group with ETH, Koechel et al. 1977). Therefore, starting concentrations of 225µM would have been required for a 5:1 mole ratio (as used to covalently derivatise HSA with ETH, Bertucci et al. 1998). It was reported previously that

covalent saturation was not attained at 16 hours dialysis under near-identical conditions (Fehske and Muller 1986). After 72 hours equilibrium dialysis in the current experiments, it might be expected that covalent saturation of HSA was reached. Assuming that HSA possesses one covalent ETH binding site and six non-covalent binding sites (2 high affinity and 4 low affinity) (Bertucci et al 1998 and 1999, Fig. 3.10a) (Fehske and Muller 1986) the maximum binding capacity (Y) of HSA for ETH would be 7.

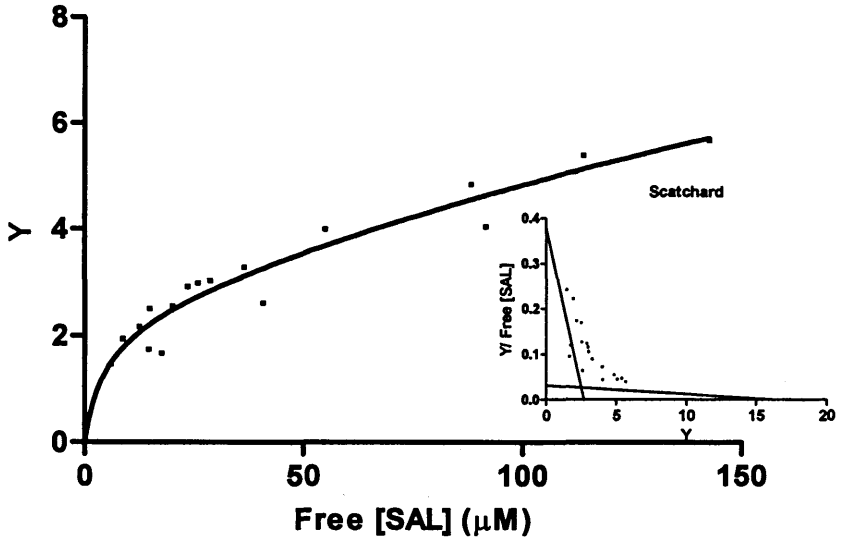


Fig. 3.8 HSA-ETH two-site binding curve measured after Eppendorf tube dialysis and UV analysis. A non-linear binding graph was created and Scatchard analysis (inset) used to find binding parameters for the HSA-SAL interaction (n=4-6). Y = bound [SAL] / total [HSA]. SEM were <3% of the mean free [SAL].

The data was fitted to a two-site binding graph (GraphPad Prism version 5.0 (GraphPad Software, San Diego, CA, USA) (Fig. 3.8). The binding parameters for the high-affinity binding sites were K_d 4.65 ± 6.79μM and B_{max} 2.31± 1.38, and for the low-affinity sites were K_d 517.6 ± 1855μM and B_{max} 16.24 ± 41.58 (r^2 = 0.93). In both cases, the SEM was larger than the Kd values. UV analysis restricted the range of [SAL] that could be dialysed with ETH and therefore binding parameters could not be more precisely determined. A different technique e.g. HPLC / radioligand assay may have been more useful. B_{max} seemed to increase slowly, but constantly and reached a value of ~6 for a starting [ETH] of 250μM. It is possible that at the highest ETH:HSA ratios, increased binding to the covalent sites resulted in an overestimation of K_d and B_{max}. It is also possible that the apparent B_{max} was overestimated due to syringe dilution (Section 2.3.4.3b). Therefore, in

order to more effectively investigate the binding affinity of the non-covalent sites, the covalent site must first be inactivated or 'blocked'.

3.3.2.3 Pre-saturation of the covalent HSA sites (CYS-34) with ETH

ETH was used to derivatise or 'block' the Cys-34 covalent binding site (to give HSA-ETH) prior to the evaluation of non-covalent binding. The aim of this experiment was to compare the ETH binding to HSA-ETH (non-covalently) with published data for ETH binding to HSA that had been covalently blocked with other Cys-34 modifying reagents (Bertucci et al. 1999). In addition the binding parameters for ETH binding to HSA-ETH would be compared with binding parameters obtained for HSA (unblocked) (Fehske and Muller 1986).

a. Removal of free ETH by bulk dialysis

i. First method (M1)

Excess free ETH was removed during the initial NaPB dialysis step. Subsequently the sample was dialysed against dH_2O to remove buffer salts. A UV scan of the HSA-ETH sample in NaPB is shown (Fig. 3.9). The spectrum resembled that of HSA (Fig. 2.4b). The ETH absorbance spectrum (Fig. 3.5) was masked by that of HSA-ETH.

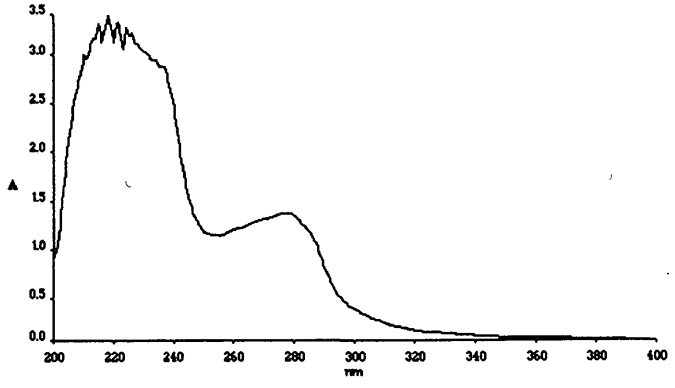


Fig. 3.9 UV spectrum of HSA-ETH after bulk dialysis removal of excess ETH

ii. Second method (M2)

The HSA-ETH UV absorbance (A_{279}) in the bulk dialysis tubing remained fairly constant throughout bulk dialysis (Fig. 3.10). Therefore it is unlikely

that protein was moving across from the P compartment into the L compartment (Fig. 3.4). It was not possible to directly monitor the migration of ETH into the L compartment due to dilution. Therefore in order to monitor the removal of ETH from the HSA-ETH sample, aliquots were removed from the P compartment at each change of L compartment solvent. In order to increase the volume available for analysis the samples were diluted. The resulting solutions had a UV absorbance (280nm) of ~0.65. This correlated to a protein concentration of ~20μM. These samples were analysed using equilibrium dialysis (Fig. 2.3). The presence of ETH in the L compartments (Eppendorf tubes) was indicative of free ETH in the ETH-HSA sample. The UV absorbances (A_{280}) of L compartment samples, following equilibrium dialysis, were plotted in Fig. 3.10. [ETH] gradually decreased between 0 and 30 hours of bulk dialysis indicating that excess ETH was being removed. After 30 hours of bulk dialysis, the absorbance of free ETH in the L compartments was below the detection limit. The HSA-ETH sample was bulk dialysed for a further 60 hours to ensure maximum removal of ETH.

After $4^1/_4$ days of bulk dialysis, diluted HSA-ETH samples (~37μM) were dialysed against NaPB. After consideration of the HSA and NaPB controls, the L compartment [ETH] was ~5μM. This suggests that not all excess ETH had been removed using the bulk dialysis process. During bulk dialysis, some ETH may have precipitated inside the tubing (ETH was sparingly soluble in NaPB). This may explain why free ETH was not observed in the equilibrium dialysis experiments of HSA-ETH sampled directly from the dialysis tubing (Fig. 3.10). Ideally bulk dialysis would have been carried out at lower temperatures to encourage protein stability, however this would have decreased ETH solubility further.

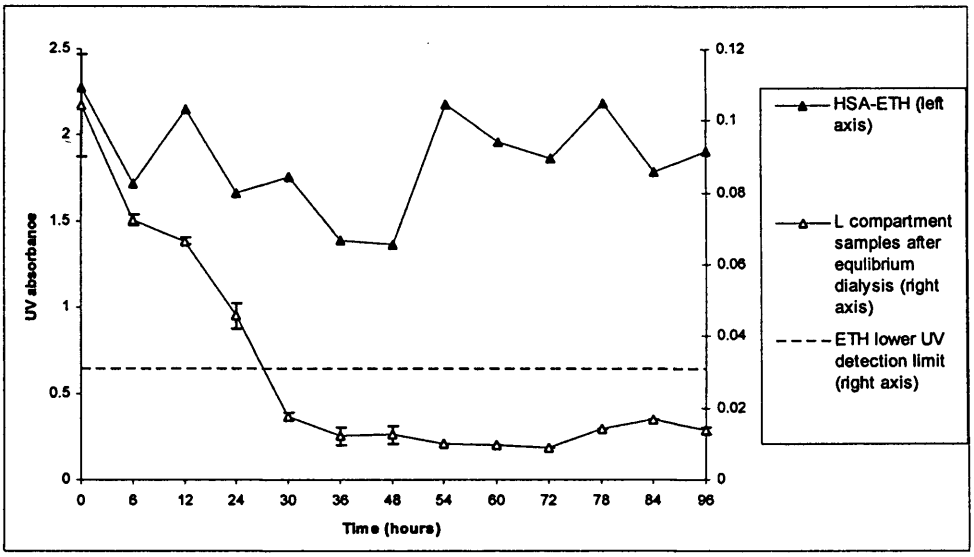


Fig. 3.10 Gradual removal of free ETH from HSA-ETH after bulk dialysis (M2), measured by equilibrium dialysis experiments. HSA-ETH samples were taken directly from the bulk dialysis tubing, diluted 1/2 with NaPB and measured by UV spectroscopy (A_{279}, λ_{max} of HSA). HSA-ETH (~20μM) was added to protein compartments of Eppendorf tubes (equilibrium dialysis experiments, Section 2.2.5) and dialysed against NaPB for 72 hours. The UV absorbance (A_{280}, λ_{max} of ETH) of the L compartments after equilibrium dialysis (corrected for a 1/3 dilution with NaPB) are plotted.

b. Removal of ETH using size exclusion chromatography (PD10 columns)

A PD10 column is suitable for the separation of large molecules (Mr >5000) from small molecules (Mr <1000) (Amersham Biosciences (Uppsala, Sweden) 2003). Therefore PD10s were used to separate ETH from HSA. Bradford reagent was used to qualitatively assay HSA elution from the PD10 columns. The weight of protein (~10mg ml^{-1}) added to the PD10s columns may have been underestimated due to contribution from free ETH, excess moisture and buffer salts. The manufacturers quote the column capacity as 10mg ml^{-1} (Amersham Biosciences (Uppsala, Sweden) 2003).

i. PD10 columns 1 and 2

For PD10 column 1 there was a very large excess of ETH because a bulk dialysis step (Section 3.2.3.3a) was not carried out. Consequently, ETH may have precipitated in the column due to its low solubility in NaPB. The PBS elution profile was similar to that observed with PD10 column 2 (Fig. 3.11a). Bradford reagent confirmed the presence of HSA in PBS fractions 4-9 (2-4.5ml) for columns 1 and 2. This coincided with peak 1 of the UV absorbance elution profile (which was consistently observed at fractions 4-

11 (2-5.5ml) (Fig. 3.11a). Free ETH eluted in fractions 10-40 (5-20ml). The HSA-ETH samples were re-applied to the column and eluted with dH_2O. ETH was still observed, however using dH_2O as a mobile phase resulted in peak 2 appearing much sharper (Fig. 3.11b). It was observed that elution volume of the ETH peak decreased with successive samples (Fig. 3.11b).

Equilibrium dialysis experiments were carried out on HSA-ETH samples after chromatographic clean-up. After consideration of the HSA and NaPB controls, the L compartment [ETH] was ~11μM. This showed that even after chromatography, free ETH was present in the HSA-ETH sample.

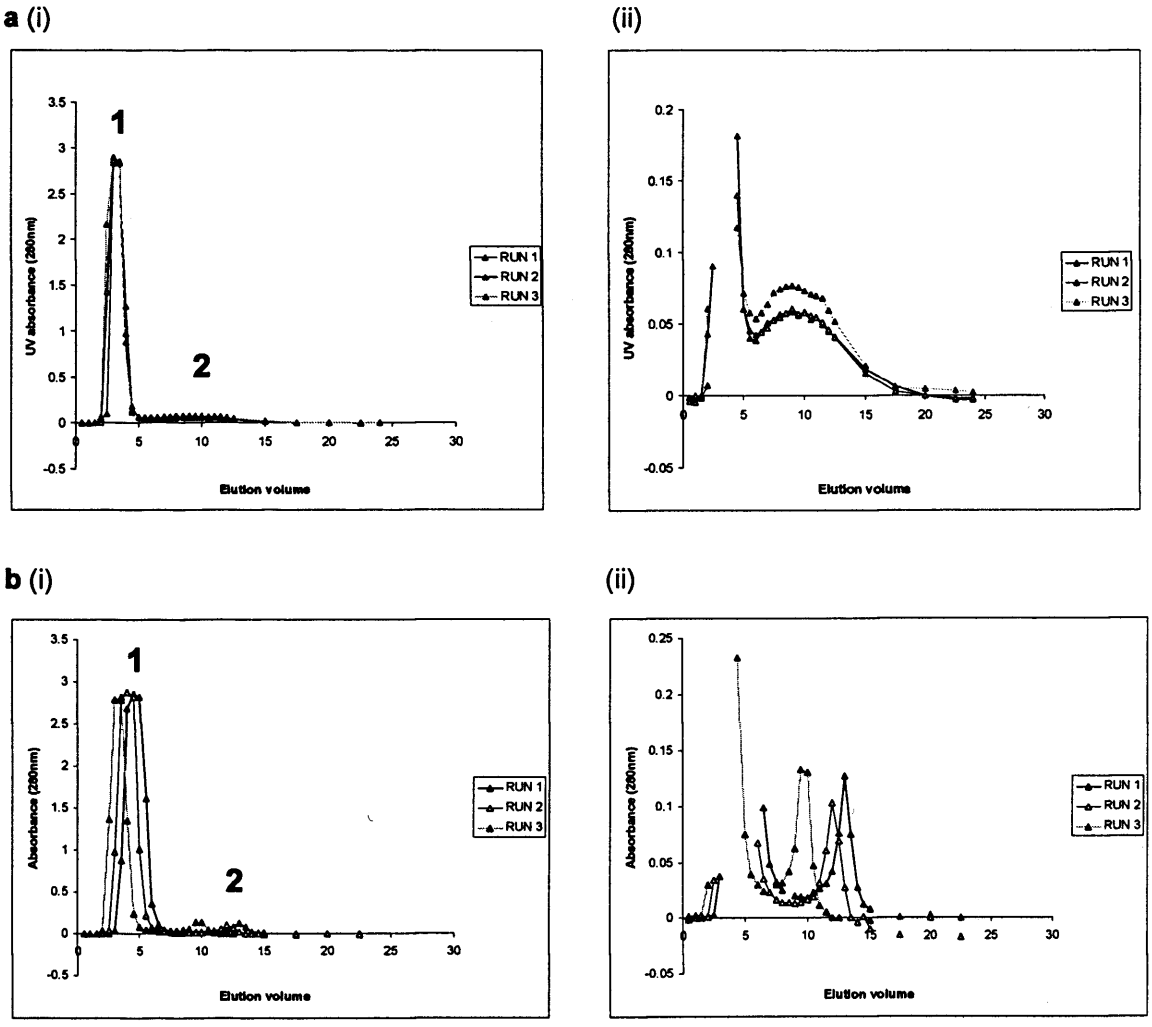


Fig. 3.11 Consistency of HSA-ETH and ETH Elution in PBS and dH_2O The elution of HSA-ETH (peak 1) and free ETH (peak 2) from PD-10 column 2. HSA elution at 2-4.5ml was previously confirmed by Bradford reagent. **a**) Mobile phase: 1 x PBS (10mM) pH 7.4. Three runs of same batch of HSA-ETH. HSA elutes at 2-5ml, ETH elutes at 6-20ml. (i) Showing full HSA A_{280}, (ii) Focused on ETH A_{280}. **b**) Mobile phase: dH_2O. Three runs after PBS runs (**a**). HSA elutes at 3-6ml, ETH elutes at 7-15ml. (i) Showing full HSA A_{280}, (ii) Focused on ETH A_{280}.

ii. PD10 columns 3 and 4

Using PBS and NaPB produced virtually the same elution profile (Fig 3.12) for the HSA-ETH sample used for PD10 column 2. Very little difference in ETH elution was observed for different mobile phase pH (6.5, 7.5 and 7.9) (Fig. 3.13). Subsequent PD10 experiments were carried out in PBS (pH 7.4).

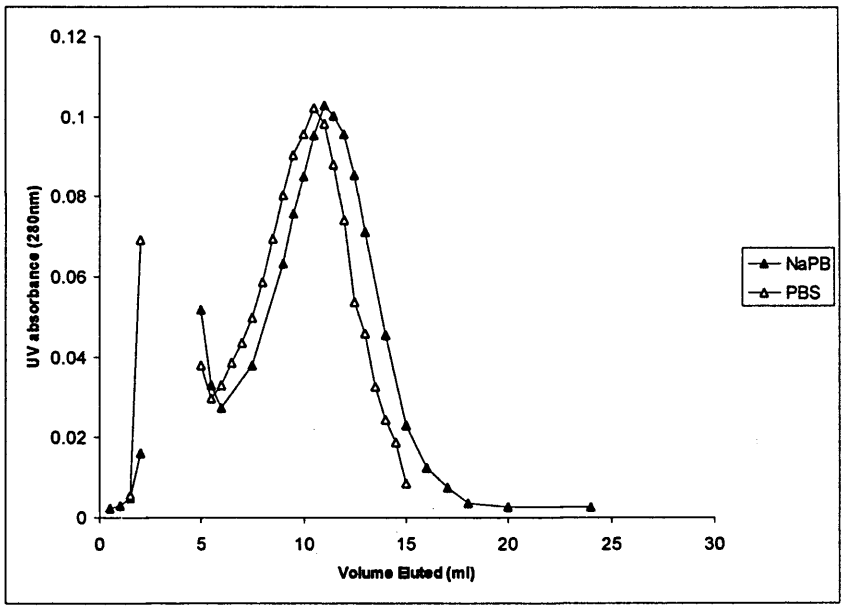


Fig. 3.12 Comparison of PBS and NaPB (pH 7.4) as PD10 mobile phases. The HSA A_{280} between 2.5 and 5ml is removed to view the ETH elution.

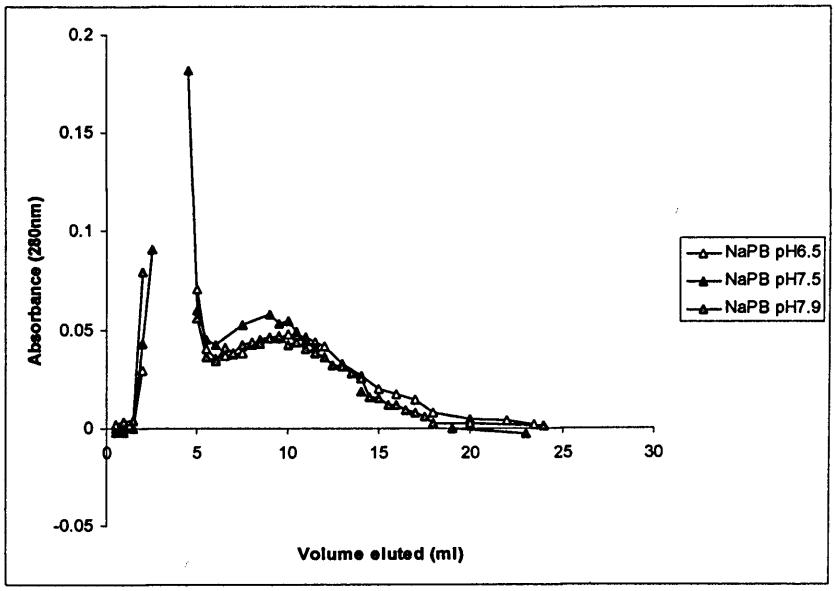


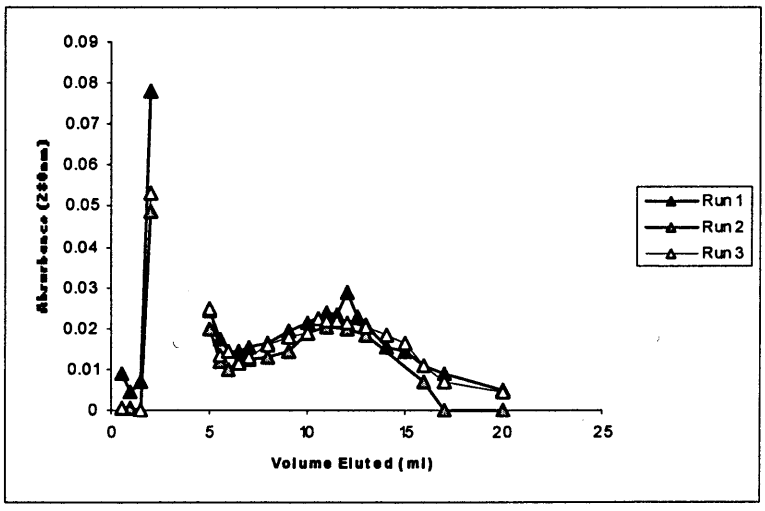
Fig. 3.13 Effect of varying pH of the mobile phase on UV absorbance elution profiles of ETH from PD10 column 4. Mobile phase: NaPB pH6.5, 7.5 and 7.9. The HSA A_{280} between 2.5 and 5ml is removed to view the ETH elution.

iii. PD10 column 5

The amount of ETH eluting gradually decreased with each chromatographic run (Fig. 3.14). This suggests a progressive decrease in the free [ETH] associated with the HSA-ETH sample. After chromatographic clean-up, equilibrium dialysis was again carried out on HSA-ETH samples. The L compartment [ETH] was reduced to ~1.5μM.

Fig. 3.15 shows the UV spectra for protein preparations (2), (3) and (4). Although the spectra are similar, there appears to be a difference in the slope between 290-340nm for the HSA-ETH samples compared to HSA. The spectrum of ETH shows a similar progressive slope, suggesting a contribution from ETH in the HSA-ETH spectra. However, because the removal of free ETH was shown to be incomplete, it was not possible to confidently assign this to a HSA-ETH spectral feature. An alternative explanation, as proposed by Schmidt (1997), is that absorbance between 310 and 400nm was due to the presence of HSA aggregates formed during repeated dialysis and freeze-drying steps.

a



(P.T.O.)

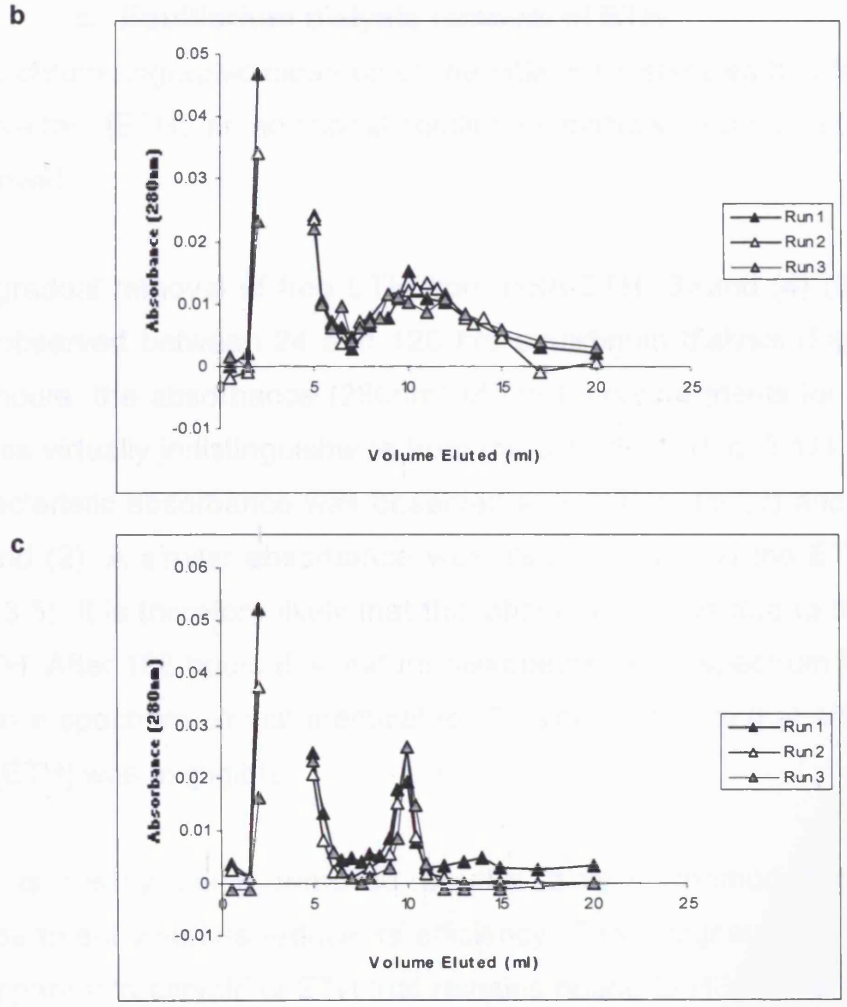


Fig. 3.14 Separation of free ETH from HSA-ETH using three PD10 runs Removal of ETH from HSA-ETH in PD10 column. **a**) Mobile phase: NaPB (67mM) pH 7.4. Three runs of same batch of HSA-ETH. **b**) Mobile phase: NaPB (67mM) pH 7.4. Three runs of HSA-ETH after **a**) and freeze-drying. **c**) Mobile phase: dH_2O. Three runs of HSA-ETH after after **b**) and freeze-drying.

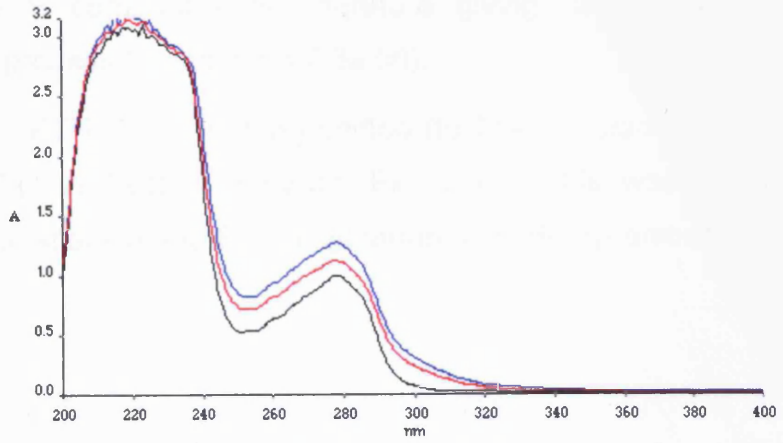


Fig. 3.15 A comparison of HSA and HSA-ETH UV scans. The UV spectra (200-400nm) of HSA (black), HSA-ETH after bulk dialysis purification (blue) and HSA-ETH after bulk dialysis and PD10 purification (red) are shown.

PRIFYSGOL CAERDYDD CARDIFF UNIVERSITY

c. Equilibrium dialysis removal of ETH

Since chromatographic clean-up of the HSA-ETH samples had failed to fully remove free [ETH], an additional equilibrium dialysis 'clean-up' step was also employed.

The gradual removal of free ETH from HSA-ETH (3) and (4) (3.3.2.3b (iii)) was observed between 24 and 120 hrs equilibrium dialysis (Fig 3.16).After 120 hours, the absorbance (280nm) of the L compartments for (2), (3) and (4) was virtually indistinguishable from the control (1) (Fig. 3.17). However, a characteristic absorbance was observed at ~ 230nm for (3) and (4), but not (1) and (2). A similar absorbance was also observed in the ETH spectrum (Fig. 3.5). It is therefore likely that this absorbance was due to the presence of ETH. After 168 hours this feature disappears in the spectrum for (4) giving rise to a spectrum almost identical to (2). This suggests that after this time, free [ETH] was negligible.

ETH is clearly being removed by this dialysis method but the small compartment volumes reduce its efficiency. This suggests that there is not an apparent 'reservoir' of ETH that remains bound to HSA. The bulk dialysis method did not have the same agitation as the Eppendorfs, which may explain why ETH removal was less efficient over the same time scale. In addition, the temperature inside the Eppendorf tubes may have risen due to constant agitation. This may then have prevented precipitation of ETH within the P compartments, therefore giving rise to a more efficient extraction process (Section 3.3.2.3a (ii)).

The λ_{max} of ETH (280nm, blue) shifted (to 264nm, black) after preparation of HSA-ETH in Section 3.3.2.3c (Fig. 3.18). This was possibly due to nucleophilic attack of the ETH vinyl group by hydroxyl anions (Chapter 4).

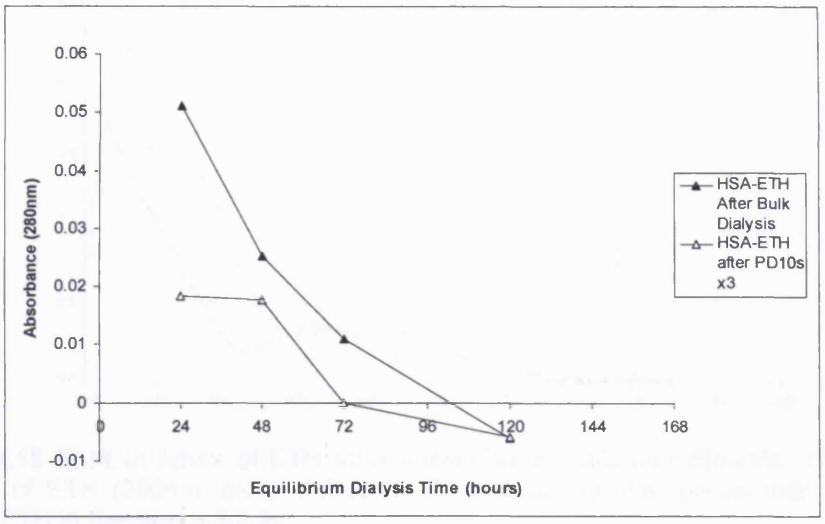


Fig. 3.16 Gradual removal of free ETH from HSA-ETH by equilibrium dialysis. The average Abs_{280} of the ligand compartments after dialysis of HSA-ETH fractions (before and after PD10 separation) with NaPB.

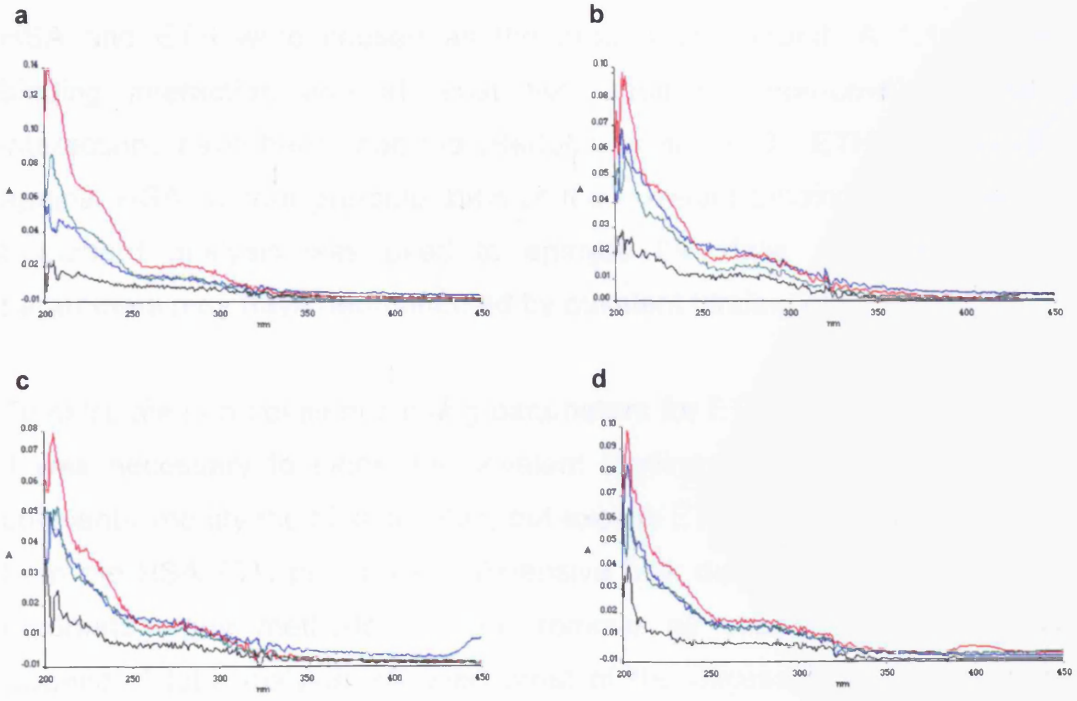


Fig. 3.17 UV scans of free ETH removal by equilibrium dialysis. The UV spectra ($Abs_{200-400}$) of L compartments after equilibrium dialysis of NaPB (black), pure HSA (blue), HSA-ETH PD10s x3 (green) and HSA-ETH after bulk dialysis (red) with NaPB. for **a**) 72, **b**) 120, **c**) 144 and **d**) 168 hours. L compartment solutions (390µl) were replaced with fresh NaPB at each time-point.

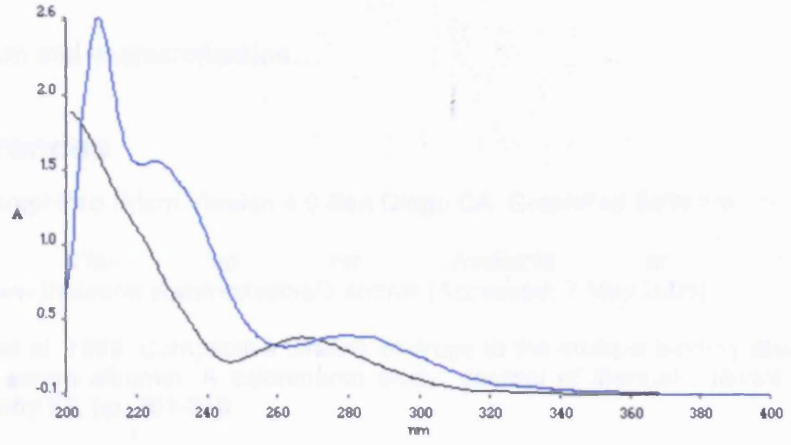


Fig. 3.18 Shift in λmax of ETH after extensive equilibrium dialysis. The λmax of ETH (280nm, blue) shifted (to 264nm, black) after preparation of HSA-ETH in **Section 3.3.2.3c**.

3.3.3 Conclusions

HSA and ETH were chosen as the protein and ligand. A 1:1 covalent binding interaction and at least two additional non-covalent binding interactions have been reported (Bertucci et al. 1999). ETH was dialysed against HSA without pre-saturation of the covalent binding sites. Two-site Scatchard analysis was used to analyse the data. However, binding parameters may have been affected by covalent binding of ETH to HSA.

To calculate non-covalent binding parameters for ETH interaction with HSA, it was necessary to block the covalent binding sites. ETH was used to covalently modify the binding sites, but excess ETH was not easily removed from the HSA-ETH preparation. Extensive bulk dialysis and size-exclusion chromatography methods did not remove all excess ETH. Extensive Eppendorf tube dialysis removed most of the excess ETH; however this method was very inefficient and time-consuming.

References

2003. GraphPad Prism Version 4.0.San Diego CA: GraphPad Software, Inc.

2005. *The lab rat* Available at: <URL: http://www.thelabrat.com/protocols/3.shtml> [Accessed: 7 May 2005]

Aki, H. et al. 1999. Competitive binding of drugs to the multiple binding sites on human serum albumin. A calorimetric study. *Journal of thermal analysis and calorimetry* 57, pp. 361-370.

Andersson, L. I. 1995. Mimics of the binding sites of opoid receptors obtained by molecular imprinting of enkephalin and morphine. *PNAS. USA* 93(11), pp. 4788-4792.

Beynon, R. 1996. *Buffers for pH control* Available at: <URL: http://www.bi.umist.ac.uk/users/mifrbn/buffers/makebuf.asp> [Accessed: 22 april 2004]

Bertucci, C. and Wainer, I. W. 1997. Improved chromatographic performance of a modified human albumin based stationary phase. *Chirality* 9, pp. 335-340.

Bertucci, C. et al. 1998. Chemical modification of human albumin at cys34 by ethacrynic acid: structural characterisation and binding properties. *Journal of Pharmaceutical and Biomedical Analysis* 18(1-2), pp. 127-136.

Bertucci, C. et al. 1999. Reversible binding of ethacrynic acid to human serum albumin: Difference circular dichroism study. *Chirality* 11, pp. 33-38.

Boeckel, M. A. M. v. et al. 1992. Glycation of human serum albumin: inhibition by diclofenac. *Biochimica et biophysica acta* 1120, pp. 201-204.

Bohney, J. P. et al. 1992. Identification of Lys190 as the primary binding site for pyridoxal 5'-phosphate in human serum albumin. *FEBS Letters* 298(2-3), pp. 266-268.

Carballal, S. et al. 2005. Sulfenic acid formation in human serum albumin by hydrogen peroxide and peroxynitrite. *Biochemistry* 42, pp. 9906-9914.

Cheruvallath, V. K. et al. 1997. A quantitative circular dichroic investigation of the binding of the enantiomers of ibuprofen and naproxen to human serum albumin. *Journal of Pharmaceutical and biomedical analysis* 15, pp. 1719-1724.

Fasano, M. et al. 2005. The extraordinary ligand binding properties of human serum albumin. *IUMBU Life* 57(12), pp. 787-796.

Fehske, K. J. and Muller, W. E. 1986. High-affinity binding of ethacrynic acid is mediated by the two most important drug binding sites of human serum albumin. *Pharmacology* 32, pp. 208-213.

Gladysheva, T. et al. 1996. His-8 lowers the pKa of the essential CYS-12 residue of the ArsC arsenate reductase of plasmid R773. *Journal of Biological Chemistry* 271(52), pp. 33256-33260.

Huber, R. E. and Criddle, R. S. 1967. The isolation and purification properties of beta-galactosidase from Escherichia coli grown on sodium selenate. In: Shrift et al. 1996 Plant Physiology.

Koechel, D. A. and Cafruny, E. J. 1973. Synthesis ans structure-activity relationship of some thiol adducts of ethacrynic acid. *Journal of medicinal chemistry* 16(10), pp. 1147-1152.

Koechel, D. A. et al. 1977. An extracorporeal complexing hemodialysis system for the treatment of methylmercury poisoning. II. In vivo applications in the dog. *The journal of pharmacology and experimental therapeutics* 203(2), pp. 272-283.

Il'ichev, Y. V. et al. 2002. Interaction of ochratoxin A with human serum albumin. Binding sites localized by competitive interactions with the native protein and its recombinant fragments. *Chemico-Biological Interactions* 141(3), pp. 275-293.

Gerig, J. T. et al. 1981 Examination of the aspirin acetylation site of human serum albumin by 13C NMR spectroscopy. In: Peters, T. 1996. *All about albumin: Biochemistry, genetics and medical applications.* Academic Press, Inc., p. 15, 17, 76-132.

Grinberg, V. Y. et al. 2002. Calorimetric study of interaction of ovalbumin with vanillin. *Food Hydrocolloids* 16(4), pp. 333-343.

McMurray, J. 2000. *Organic Chemistry.* 5th ed. Brooks/Cole, p. 956.

McMenamy, R. H. and Oncley, J. L. 1958 The specific binding of L-tryptophan to serum albumin. In: Peters, T. 1996. *All about albumin: Biochemistry, genetics and medical applications.* Academic Press, Inc., p. 15, 17, 76-132.

Meyer, G. D. et al. 2006. Non-specific binding removal from protein microarrays using thickness shear mode resonators. *IEEE Sensors Journal* 6(2), pp. 254-261.

Ozer, I. and Tacal, O. 2001. Method dependence of apparent stoichiometry in the binding of salicylate ion to human serum albumin: A comparison between equilibrium dialysis and flourescence titration. *Analytical biochemistry* 294, pp. 1-6.

Peters, T. 1996. *All about albumin: Biochemistry, genetics and medical applications.* Academic Press, Inc., p. 15, 17, 76-132.

Raffa, R. B. 2003. Experimental applications to determine the thermodynamics of protein-ligand interactions. In: Bohm, H.-J. and Schneider, G. eds. *Protein-ligand interactions.* Vol. 19. WILEY-VCH, p. 57.

Ronwin, E. and Zacchei, A. G. 1966. The binding of ethacrynic acid to bovine serum albumin. *Canadian Journal of Biochemistry* 45, pp. 1433-1443.

Russeva, V. N. and Zhivkova, Z. D. 1999. Protein binding of some non-steroidal anit-inflammatory drugs studied by high-performance liquid affinity chromatography. *International Journal of Pharmaceutics* 180, pp. 69-74.

Schmid, F. X. 1989. Spectral methods of characterising protein conformation and conformational changes. In: Creighton, T.E. ed. *Protein structure: A practical approach.* Oxford University Press, p. 254.

Stewart, A. J. et al. 2005. Role of Tyr84 in controlling the reactivity of Cys34 of human albumin. *FEBs journal* 272, pp. 353-362.

Sugio, S. et al. 1999. Crystal structure of human serum albumin at 2.5 Å resolution. *Protein Enineering.* 12(6), pp. 439-446.

Williams, M. A. and Ladbury, J. E. 2003. Hydrogen bonds in protein-ligand complexes. In: Bohm, H.-J. and Schneider, G. eds. *Protein-ligand interactions.* Vol. 19. WILEY-VCH, pp. 137-161.

Wolfson. 2003. *PD10 desalting column* [WWW]. Amersham Biosciences. Available at: <URL: http://wolfson.huji.ac.il/purification/PDF/dialysis/AmershemPD10Desalting.pdf> [Accessed: 8 August 2006]

Chapter 4

Synthesis and purification of N-{[2,3-dichloro-4-(2-methylenebutyryl)phenoxy]-acetyl}glycine (ETHGly)

4.1 Introduction

4.1.1 Coupling of ETH to a spacer molecule to minimise HSA surface denaturation

Ethacrynic acid (ETH, Fig. 4.1) is ~10 bonds in length (10-20Å) and binds to the CYS-34 containing cleft of HSA (Stewart et al. 2005). Molecular modelling suggested that ETH protrudes into the surrounding media beyond this cleft by ~10Å (Appendix III). Modelling also suggested that in places the surfaces of the protein extended beyond bound ETH. Therefore if ETH was attached directly to the surface of a substrate, utilising its free carboxylic acid group, then for HSA subsequently to interact with ETH it would have to get close to the surface and in doing so risk non-specific adsorption and possible denaturation.

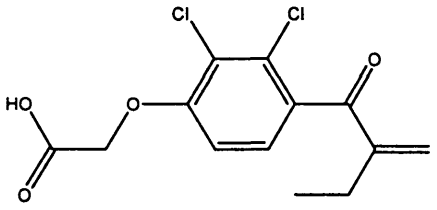


Fig. 4.1 Structure of ETH

Spacer molecules have often been used for protein-surface immobilisations in order that a successful interaction between the protein and ligand occurs and to minimise protein-surface contact (Cuartecasas et al. 1970 in Hermansen et al. 1992). The length of the linker has been shown to be important. If the linker is too short the protein will adsorb to the surface, and if too long the linker could fold over (Hermansen et al. 1992, Fig 4.2). For large proteins a linker may not have much effect (Hermansen et al. 1992; Battistel and Rialdi 2006).

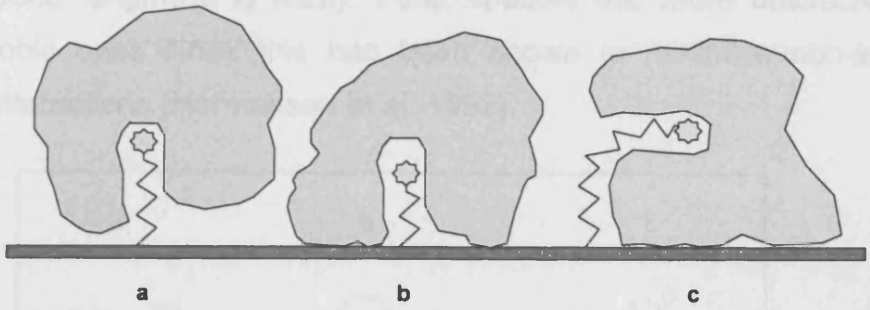


Fig. 4.2 Spacer Length Affects Protein Binding. a) Ideal length linker, protein binds ligand and retains conformation. **b**) Too short linker, protein adsorbs to surface before ligand. **c**) Too long linker, protein binds to ligand and folds over to adsorb at surface. *Diagram adapted from Hermanson et al. 1992.*

4.1.2 Amide coupling of ETH to a spacer molecule

Molecular modelling suggested that the carboxylic acid group, of HSA-bound ETH, was solvent accessible (Appendix III) and therefore could be used to couple ETH to a bifunctional spacer molecule for subsequent surface immobilisation. Carboxylic acids undergo simple chemical reactions with alcohols (ester formation) and amines (amide formation). Since amides tend to be more stable to hydrolysis than esters, an amide link was used to attach a spacer group to ETH.

4.1.3 Glycine as the spacer molecule

Common spacers include diamines such as ethylene diamine (EDA, three bond lengths, Fig 4.3a) and diaminodipropylamine (DADPA, eight bond lengths) (Hermansen et al. 1992). These molecules are symmetrical (can couple with ETH at either end) and will not polymerise. However the surface functional groups were also amines (aminopropyltriethoxysilane (APS), Chapter 5) and would not be able to link directly to the diamine spacers. Alternatively N-hydroxysuccinimide (NHS) esters could be used, including homobifunctional cross-linkers such as bis(sulfosuccinimidyl) suberate (which binds amines at either end (Locascio-brown et al. 1990) or heterobifunctional linkers such as n-γ-maleimidobutyrlyloxy succinimide (GMBS) ester (which binds a sulfhydryl (SH) at one end and an amine (NH_2) at the other (Singh et al. 1999)). Should a longer linker be necessary, unnatural amino acids are also available e.g. 6-aminocaproic acid (ACA)

with 6 bond lengths (Fig 4.2b). Polar spacers are more desirable than hydrophobic ones since this has been shown to minimise non-specific protein interactions (Hermansen et al. 1992).

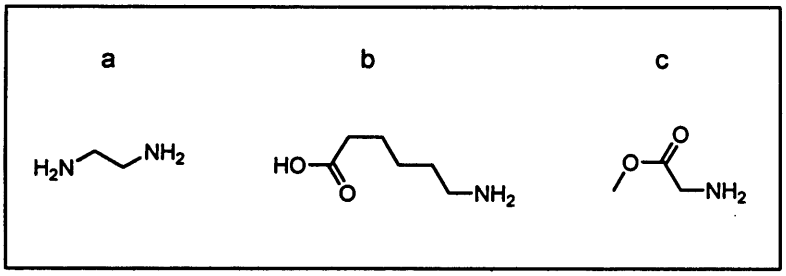


Fig 4.3 Structures of amine spacer molecules. a) EDA, **b)** ACA and **c)** GlyOMe.HCl.

Amide coupling (between an amine and a carboxylic acid) is used to couple amino acids in solid-phase peptide synthesis and a wide range of strategies have resulted (Jones 1994). In this application it is particularly important that polymerisation of the free amino acids is prevented and so a wide range of protecting strategies have emerged (Jones 1994). N-protecting groups are most common (e.g. butoxycarbonyl (Boc), H-fluorenylmethoxycarbonyl (FMoc)), as solid phase peptide synthesis commonly builds on the free NH_2 group of immobilised amino acids. Carboxyl-protected amino acids are also available and in this instance glycine methylester hydrochloride (GlyOMe.HCl) was chosen to derivatise the carboxylic acid of ETH. The OMe moiety can be selectively cleaved after amide formation. Glycine (Gly) would add three bond lengths to ETH. It was anticipated that this modification would not unduly reduce the aqueous solubility of the ligand. However, in order to generate the free carboxylic acid group for surface attachment, deprotection of the ETHGlyOMe product was necessary. To achieve this it was necessary to selectively hydrolyse an ester in the presence of an amide (Fig. 4.4).

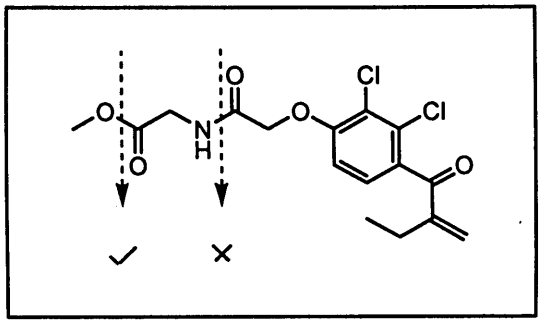


Fig. 4.4 Selective ester hydrolysis of ETHGlyOMe.

A standard procedure for ester hydrolysis is aqueous acid (HCl) or base (NaOH) reflux. Acid hydrolysis is reversible (under thermodynamic control), and more amide would be cleaved than ester (Alexander Delf et al. 2005). Also, vinyl-ketones can polymerise (or dimerise) in strong acid conditions (Firouzibadi et al. 2005). In basic conditions the reaction is irreversible (under kinetic control) and ester hydrolysis tends to be faster than amide hydrolysis (Alexander Delf et al. 2005). Hydroxide ions (OH^-) attack the electrophilic centre of the ester carbon, forming a tetrahedral intermediate (Fig. 4.5). A carboxylic acid is formed after the alkoxide group (OR) leaves, extracting a proton from the carboxylic acid, resulting in the formation of the product as a carboxylate ion. ETH was reported to be stable in NaOH (1M) for at least 1hr (Dehsler and Zuman. 1974), but also unstable in mildly basic conditions (NaPB, pH8.2) after several days incubation at 60°C (Yarwood et al. 1987). Some vinyl ketones (such as ETH) are susceptible to nucleophilic attack from hydroxyl (^-OH) ions (Dehsler and Zuman 1974).

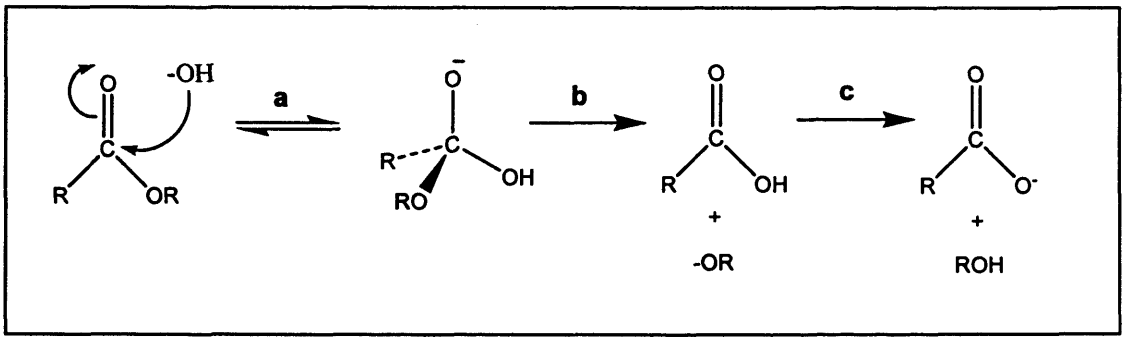


Fig. 4.5 Base hydrolysis. a) nucleophilic attack of an ester by a hydroxide ion to form a tetrahedral intermediate **b)** Carboxylic generated by elimination of alkoxide ion. **c:** Alkoxide ion extracts proton to form an alcohol leaving a carboxylate ion. The latter can be reprotonated in aqueous acid to yield a carboxylic acid. *Adapted from McMurray2000*

Published base hydrolysis methods were attempted for methyl ester cleavage of ETHGlyOMe to the carboxylic acid, ETHGly (Dayal et al. 1990; Kaestle et al. 1991). Other mild ester hydrolysis methods have been reviewed in Saloman et al. 1993.

4.1.4 Amide coupling reactions

A quick and inexpensive procedure using the zero-length coupling reagent carbonyldiimidazole (CDI) was described by Paul and Anderson (1958 & 1960). In this study the reaction was carried out either in dry tetrahydrofuran

(THF) or dimethylformamide (DMF) at 25°C. An acylimidazole intermediate was formed from the reaction of carboxylic acid with CDI. Amide bond formation proceeded as the imidazole group was substituted by the amine. The by-products, imidazole (Iz) and CDI were water soluble and easily removed from the insoluble product.

ETHGly (carboxylic acid) has been synthesised previously (Chemical name: N-{[2,3-Dichloro-4-(2-methylenebutyryl)phenoxy]-acetyl}glycine, Cragoe 1983; Abraham et al. 1989) using thionyl chloride to activate the carboxylic acid of ETH to a reactive acyl chloride (dry benzene reflux). The subsequent addition of Gly resulted in the formation of the ETHGly amide. ETHGly was shown to have antidiuretic activity (dependent on coupling with thiols), although reduced by half compared to ETH (Cragoe 1983).

1-Ethyl-3-(3-dimethylaminopropyl) carbodiimide (EDC) comes from a family of amide coupling reagents, called carbodiimides. EDC is water-soluble and has been commonly used to activate carboxylic acids for coupling with amines via O-acylurea intermediates. One of the problems with this approach is that the latter can rapidly rearrange to form N-acylurea by-products (Fig. 4.6) [www] Pokorski 2004). In aqueous solvents, O-acylurea intermediate formation is favoured at pH 3-5 (Nakajima and Ikada 1995) whilst amide coupling then proceeds via nucleophilic attached of the amine on the O-acylurea intermediate. However for this to occur efficiently the amine must be in its nucleophilic (unprotonated) form and for most amines this requires a pH of between 8 and 12 (Nakajima and Ikada 1995). Buffers such as 4-(2-hydroxyethyl)-1-piperazineethanesulfonic acid (HEPES) pH 7-8 and 2-(N-morpholino) ethanesulfonic acid (MES pH 4-6) have been shown to be effective as a compromise environment (Danishefsky and Siskovic 1970). EDC and other carbodiimides are often used in conjunction with N-hydroxy succinimide (NHS) or sulfo-NHS in aqueous systems to stabilise the O-acylurea intermediates (Seghal and Vijay 1994) (Grabarek and Gergeley 1990 in [www] Pierce 2006 (Pierce, Rockford, Illinois, USA).

EDC coupling has also been described in aprotic (non H-bond donating) organic solvents such as chloroform ($CHCl_3$), DCM and DMF (Desai and

Stramiello 1993; Ho et al. 1995; Yang et al. 2000). Apolar (low dielectric constant) solvents (e.g. $CHCl_3$ and DCM) minimise intermolecular arrangements of the O-acylurea intermediate, whilst polar organic solvents such as MeOH and DMF can solubilise polar and apolar compounds, but lead to the rapid formation of N-acylurea by-products ([www] Ed. Wipf 2005; Jones 1994) (Fig. 4.6).

Amide-coupling reagents such as phosphonium and uronium salts have been shown to be more effective than EDC but such reagents can be very expensive ([www] Marder and Albercio 2003; [www] Merck 2006).

4.1.5 Chapter objectives

- To synthesise and characterise ETHGlyOMe
- To deprotect ETHGlyOMe by selective hydrolysis
- To characterise and purify the derivatised ligand (ETHGly)

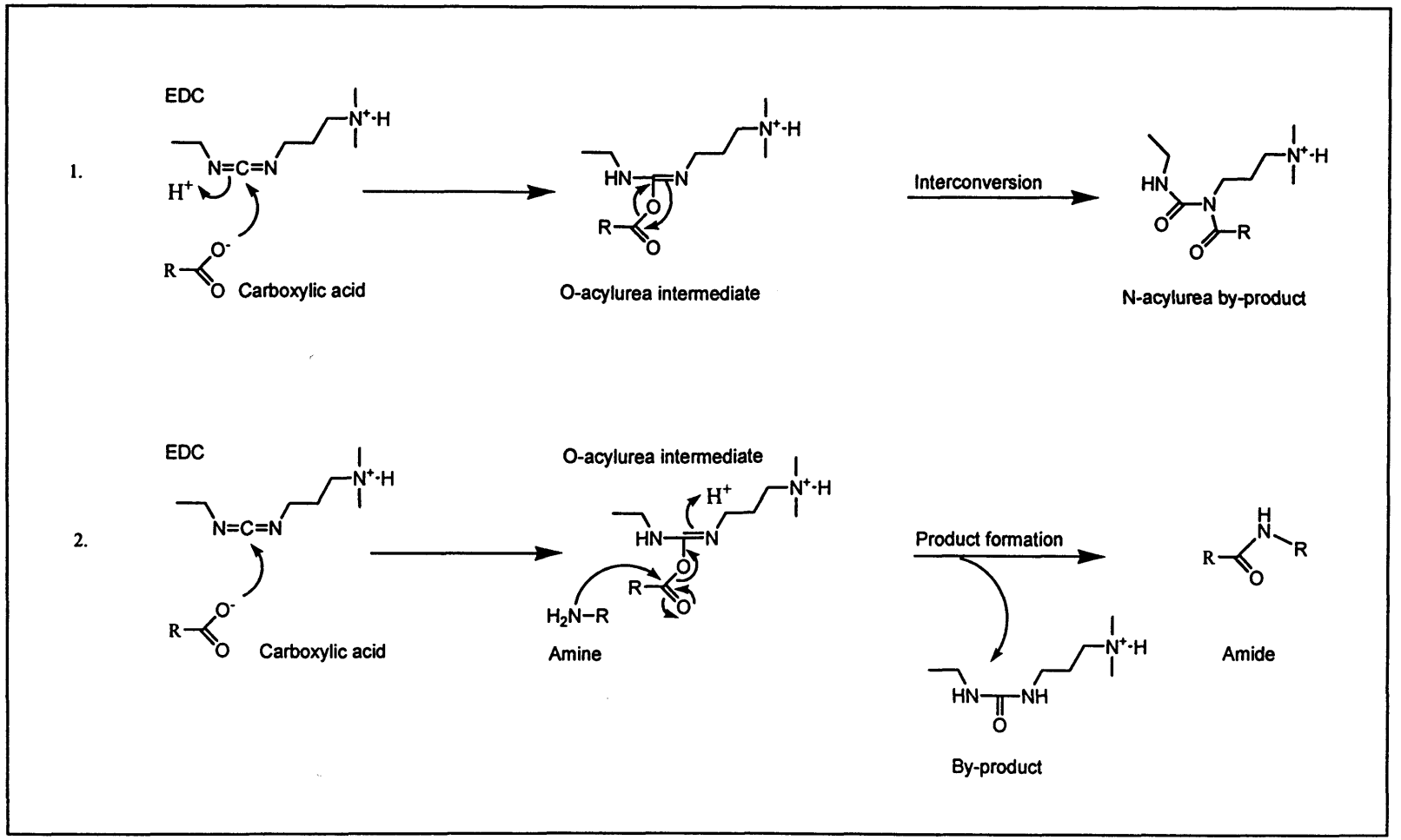


Fig. 4.6 EDC structure and mechanism of amide coupling. *Adapted from Pokorski 2004.*

4.2 Methods

4.2.1 Equipment and Materials

Equipment:: Short-wave (245nm) Minervalight UV lamp, Bruker Avance 500 nuclear magnetic resonance (NMR) instrument (500MHz, Bruker Biospin Ltd, Coventry, UK), Griffin melting point apparatus (Griffin, Loughborough, UK), Thermo Separations Products high performance liquid chromatography (HPLC) instrument (Thermo Scientific/ Fisher (Waltham, MA, USA)), Genesis reverse-phase C18 column (Kinesis, Cambridgeshire, UK) and Phenomenex reverse-phase C18 preparative HPLC column (internal diameter: 250 x 10mm) (Phenomenex, Cheshire, UK).

Materials: DMF and DCM (both extra dry with molecular sieves) and $SOCl_2$ were purchased from Acros Organics (Geel, Belgium). $MgSO_4$ (anhydrous, reagent grade, >97%), HCl (analytical grade, 37% wt in water), ETH, CDI (Fluka), EDC (Fluka), lithium hydroxide (LiOH) (anhydrous, min 99%), NaOH pellets (min 98%), Na_2CO_3 (anhydrous, min 99%), $NaHCO_3$, trifluoroacetic acid (TFA, Fluka, HPLC grade, >99.0%) and SPE adaptors (Supelco) were purchased from Sigma-Aldrich (St Louis, MO, USA). GlyOMe.HCl was purchased from (Novabiochem). Chloroform-d ($CDCl_3$) over molecular sieves and Methanol-d_4 (CD_3OD, D 99.8%) were purchased from GOSS Scientific Instruments Ltd (Great Baddow, Essex, UK). MKC18F Silica gel 60 Å reverse-phase TLC plates were purchased from Merck (Whitehouse station, NJ, USA). MeOH and Ethylacetate (both HPLC grade), Whatman 55mm filter paper and silica gel reverse-phase C18 thin-layer chromatography (TLC) plates were purchased from Fisher (Waltham, MA, USA). Bond Elute reverse phase C18, 3ml solid-phase extraction (SPE) cartridges were purchased from Varian (Harbor City, USA, supplied by Anachem, Luton, Bedfordshire).

4.2.2 TLC analysis

Silica gel TLC plates were used to follow ETHGlyOMe synthesis and ester hydrolysis. Silica gel reverse-phase C18 TLC plates were used to optimise

separation of ester hydrolysis products before HPLC. Aromatic molecules were viewed with a short-wave Minervalight UV lamp (245nm). A ratio of 1:1 (v/v) MeOH:ethylacetate was used as the optimal mobile phase for all EGOMe synthesis TLC experiments.

4.2.3 NMR analysis

Samples were analysed in a Bruker Advance NMR machine (500MHz). The spectra were expanded and analysed using the Topspin software program (Bruker). Solvent peaks are crossed out. Proton (^1H) spectra were autocalibrated to the deuterated solvent.

4.2.4 Amide coupling of ETH and GlyOMe.HCl

4.2.4.1 CDI as coupling reagent

A published amide coupling method was followed (Section 4.1.4; Paul and Anderson, 1958 & 1960). ETH (0.1mmol, 30.3mg) was dissolved in DMF (10ml) and added to CDI (0.1mmol, 19.4mg) in a N_2 atmosphere for 3 hours at room temperature. Effervescence was observed as carbon dioxide (CO_2) was evolved. GlyOMe.HCl (0.1mmol, 12.5mg) was dissolved in DMF (10ml) and added to the reaction, stirring overnight at room temperature. DMF was removed by rotary evaporation (80°C). The product was recrystallised from ethanol-water. A yield was not obtained.

The reaction was scaled up to 1mmole of each reactant. No effervescence was observed. The solution was evaporated, to yield a yellow oil. The product did not form a solid upon cooling, but nevertheless, was washed with a few ml each of 1M HCl, water, 50mM sodium bicarbonate ($NaHCO_3$) and finally water. The resulting product was not recrystallised and a yield was not obtained. The reaction was unsuccessful.

4.2.4.2 $SOCl_2$ as coupling reagent

A published method was followed with one modification (Section 4.1.4; Cragoe 1983). DCM was used rather than benzene. ETH (5.9mmol, 1.79g) was added to an argon filled flask and dissolved in DCM (5ml). $SOCl_2$

(1.2ml) was added (effervescence was observed) and the solution was heated at reflux for 2 hours. An aliquout was removed from the flask, solvent removed by rotary evaporation, and analysed by NMR. The reaction is not described further as product formation was not observed.

4.2.4.3 EDC as a coupling reagent

ETH (5.4mmol, 1.64g) was dissolved in DMF (20ml), added to a solution of EDC (5.72 mmol, 1.10g) and GlyOMe.HCl (15 mmol, 1.88g) in DMF (50ml) and stirred overnight under inert atmosphere (N_2). The majority of the added GlyOMe.HCl was insoluble. EDC was fully dissolved by sonication. After 18 hours, one additional equivalent of EDC (5.72 mmol, 1.10g) was added in DMF (30ml), which dissolved the excess GlyOMe.HCl. The DMF was evaporated under high vacuum leaving bright yellow oily droplets and a few visible white crystals (unreacted GlyOMe.HCl). $CHCl_3$ (50ml) was added and the solution washed with saline (x2), dried over magnesium sulphate ($MgSO_4$) and the solvent removed by rotary evaporation (60°C) to yield a yellow oil, which crystallised upon cooling. 1H-NMR showed ETHGlyOMe at a purity of ~90% (Appendix IV). This crude product was used for ester hydrolysis without further purification, and a yield was not obtained.

4.2.2 Ester hydrolysis of ETHGlyOMe

4.2.4.1 Base-catalysed ester hydrolysis using NaOH or LiOH

A number of attempts at NaOH or LiOH base hydrolysis were carried out by modification of published methods (Kaestle et al. 1991; Dayal et al. 1990, McMurray 2000). These hydrolysis experiments were carried out on the product of the CDI reaction (Section 4.3.1.1). The base (NaOH or LiOH, 0.1-0.4M in dH_2O (5ml)) was added drop-wise to the ester (1mmol, 0.338g in MeOH, THF or a combination (5ml)) in a 25ml glass vial and stirred using a magnetic flea for up to 30 minutes. Molar ratios of 1:1 to 5:1 (base:ester) were used. The reactions were monitored by TLC (1:1 (v/v) MeOH:ethylacetate) and 1H-NMR.

4.2.4.2 Base-catalysed ester hydrolysis using $NaHCO_3$

A number of attempts at $NaHCO_3$ base hydrolysis were carried out by modification of a published method (Kaestle et al. 1991), using the same general method as Section 4.2.4.1. Molar ratios of 2:1 (base:ester) were used. A reflux experiment was also carried out. An aqueous solution of $NaHCO_3$ (0.2M, 5ml) was added to a round bottom flask. The ester (0.59mmol, 0.24g) was dissolved in MeOH (5ml) in a glass vial, added to the flask and heated at reflux for 30 minutes. The reactions were monitored by TLC (1:1 (v/v) MeOH:ethylacetate) and 1H-NMR (CD_3OD).

4.2.4.3 Base-catalysed ester hydrolysis using Na_2CO_3

A method using Na_2CO_3 was modified (Kaestle et al. 1991), using the same general method as Section 4.2.4.1. Initially, these hydrolysis experiments were carried out on the product of the CDI coupling reaction. Later, the same method was optimised and used to hydrolyse the product of the EDC coupling reaction (Section 4.3.1.3). Na_2CO_3 (0.1g in dH_2O (6ml)) was added drop-wise for 15minutes to ETHGlyOMe (0.24g in MeOH (6ml)), stirring for a total of 30 minutes at RT. Progress of the reaction was monitored by TLC on silica (mobile phase: 1:1 ethyl acetate-MeOH). The reaction product was diluted with MeOH (10ml) to slow the reaction until the product could be recovered by rotary evaporation (high vacuum, 50°C). The product (yellow oil) was washed with 2ml HCl (1M) to form the acid. The resulting solid was neutralised with 30ml $NaHCO_3$ (50mM). The product was again recovered by rotary evaporation (high vacuum, 50°C), dissolved in MeOH and the insoluble salts removed by filtration. The MeOH was then removed by rotary evaopartion (50°C), yielding a white powder.

4.2.5 HPLC purification of ETHGly

An isocratic analytical HPLC method was developed to assess product purity (Genesis reverse-phase C18, mobile phase 1:1 (v/v) MeOH:water (0.1% TFA); flow rate 1ml/min, injection volume 20µl, detection UV 210, 264 and 280nm). Subsequently preparative HPLC was used for purification of the product (Phenomenex reverse-phase C18, 250 x 10mm id; mobile phase 1:1 (v/v) MeOH:water (0.1% TFA); flow rate 4ml/min, injection volume 1ml, detection UV 210, 264 and 280nm). Fractions corresponding to each of the major peaks were collected (~20ml, 5 minutes) and further

concentrated using solid-phase extraction (SPE) (Section 4.2.6). Purity of the final product was evaluated by analytical HPLC.

4.2.6 Solid-phase extraction of ETHGly

HPLC fractions identified as products and side-products (Section 4.3.3) were collected and concentrated using SPE (Fig 4.7). Samples were diluted to 50% with water and pushed through an SPE cartridge at ~3ml/min using a syringe. The column was then washed with water (~20ml) until the pH of the eluent changed from acidic to neutral (Litmus test). The product was then eluted with MeOH (2ml). The MeOH was subsequently evaporated under a N_2 stream.

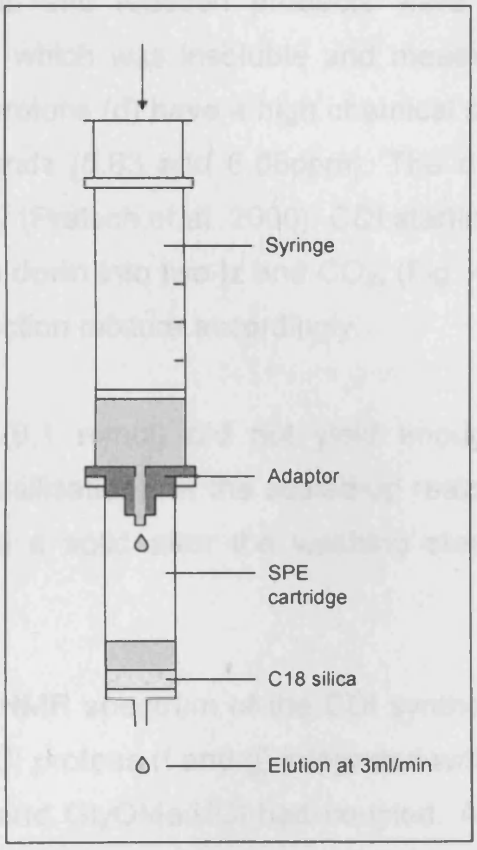


Fig. 4.7 Solid phase extraction of ETHGly. Method: Column loaded with sample in acidic mobile phase; Column washed with water to remove acid; Sample eluted with methanol.

4.3 Results and discussion

4.3.1 Amide coupling of ETH and GlyOMe.HCl

A number of amide-coupling reactions were investigated. ^1H NMR peak shifts (ppm) are included in Appendix IV.

4.3.1.1 CDI as coupling reagent

NMR spectra of the starting materials (ETH, GlyOMe.HCl and CDI) are shown in Fig. 4.8a). All peaks were accounted for as shown by the alphabetical labelling (solvent peaks are crossed out). The NMR spectra for the starting materials and reaction products were measured in $CDCl_3$ (except GlyOMe.HCl which was insoluble and measured in CD_3OD) (Fig. 4.8). The ETH vinyl protons (d) have a high chemical shift, usually observed for aromatic compounds (5.63 and 6.05ppm). The d and e protons were assigned theoretically (Pretsch et al. 2000). CDI starting material was ~80% pure, partially broken down into two Iz and CO_2, (Fig. 4.8a (iii)). Excess CDI was added to the reaction mixture accordingly.

The first synthesis (0.1 mmol) did not yield enough product for NMR analysis (after recrystallisation). In the scaled-up reaction (1mmol), the oily product did not form a solid after the washing steps and could not be recrystallised.

Fig. 4.8b shows the NMR spectrum of the CDI synthesis reaction products in $CDCl_3$. GlyOMe.HCl protons (f and g) integrated with the ETH protons (a-e), suggesting ETH and GlyOMe.HCl had coupled. Amide ($NHCH_2$, f) and ester (OCH_3, g) peaks were visible at 4.09ppm and 3.79ppm respectively. These were shifted compared to GlyOMe.HCl starting material in CD_3OD (3.88 and 3.86ppm respectively), and the amide peak was a doublet rather than a singlet. The singlet to doublet effect was not observed for amidic protons (f) for EDC synthesis in CD_3OD (Appendix IV).

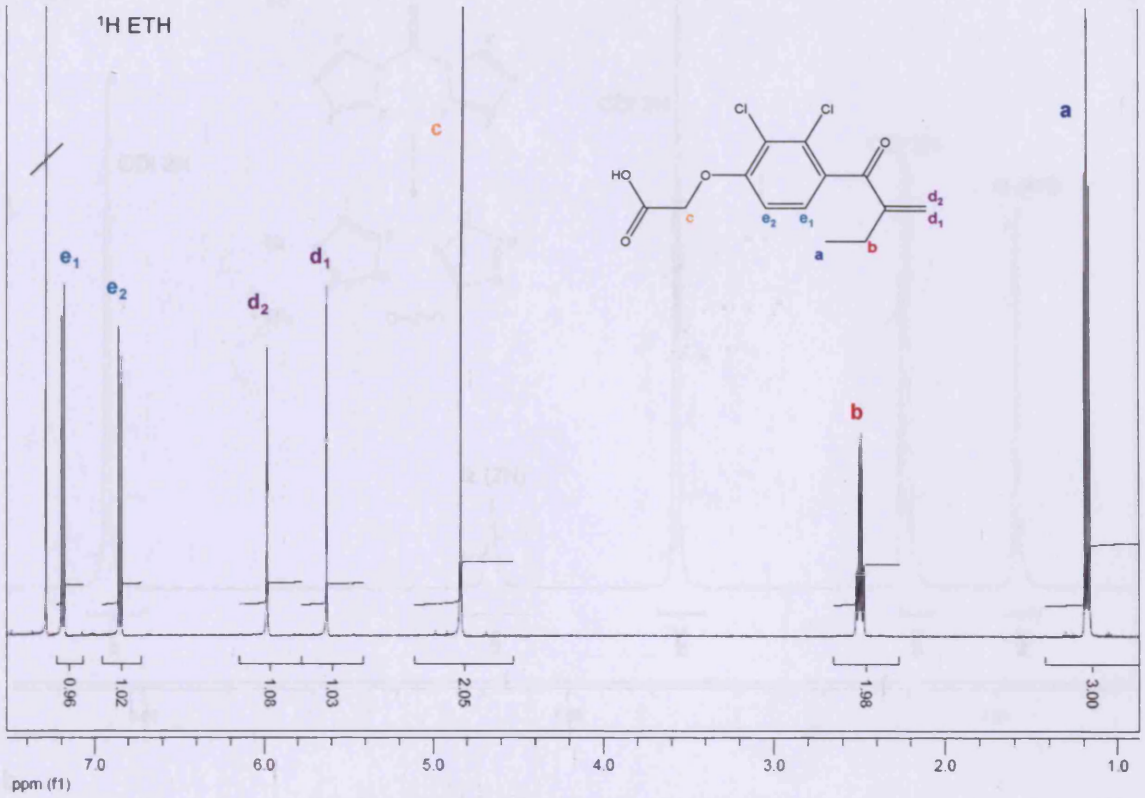
Three peaks were observed in the aromatic region (6.8-7.6ppm, Fig. 4.8b), integrating with the rest of the ETH and GlyOMe.HCl protons. However, the

vinyl peaks of ETH (d) were shifted upfield from the aromatic region (5.63 and 6.05ppm) to the non-aromatic region (4.20ppm).

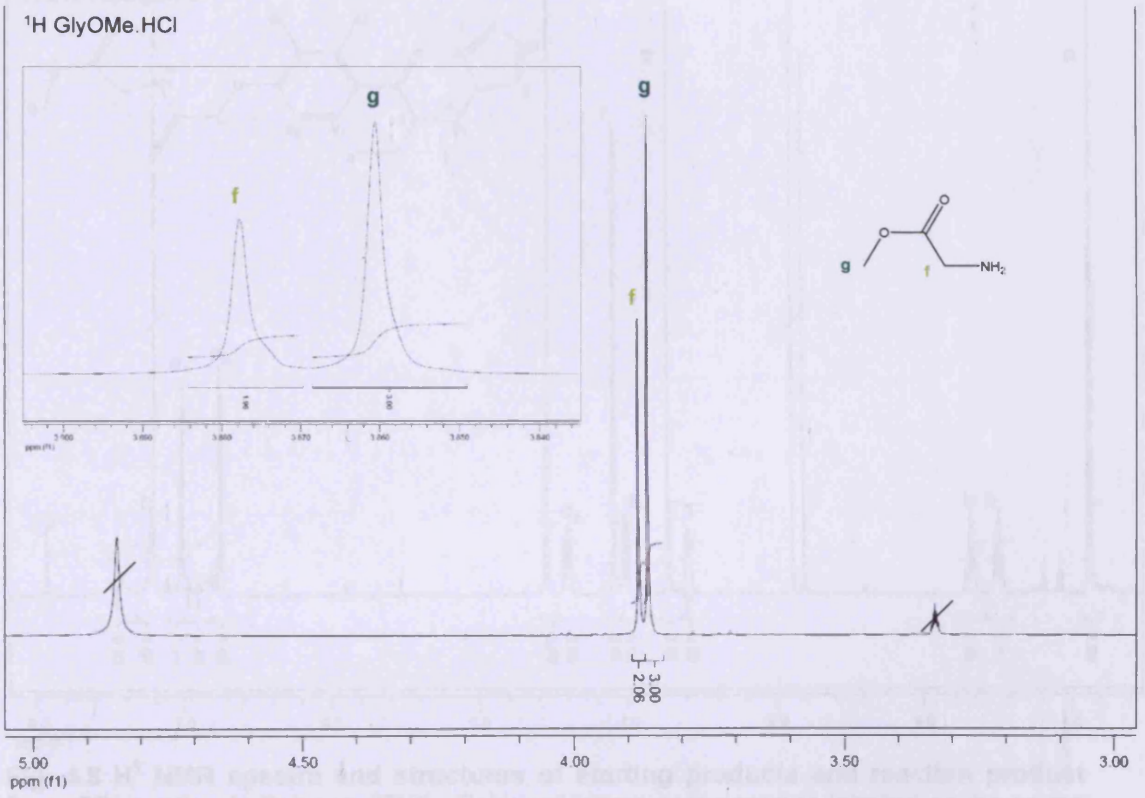
An alternative outcome of the CDI reaction was that Iz (released as a by-product during the reaction) had added to the CH_2=C (α,β-unsaturated ketone) group of ETH, giving the intermediate ETH(Iz)$_2$ (Fig. 4.9). Iz (and histidine, HIS) has a nucleophilic nitrogen which has previously been shown to attack the α, β-unsaturated ketone group of ETH (Gunther and Ahlers 1976; Firouzibadi et al. 2005) via Michael addition in aqueous solutions (McMurray 2000, Fig. 4.10). Subsequently, following GlyOMe.HCl coupling, ETH(Iz)GlyOMe was formed rather than the desired product ETHGlyOMe (Fig. 4.9). Free Iz is very soluble in water and was not observed after extraction of ETH(Iz)GlyOMe into chloroform (Fig. 4.8b). To confirm this, a separate reaction was carried out between Iz (5 equivalents) and ETH (1 equivalent) in DMF overnight, giving the unactivated ETH(Iz) product (Fig. 4.11). Further evidence that Iz had modified the product was apparent in the NMR spectrum. An extra proton was observed at 3.56-3.61ppm, and was assignable to position 1 (Fig. 4.8b). The multiplet at 3.56-3.61ppm was a sextuplet or octuplet (Fig. 4.12b). Additionally, the $\underline{CH_2}CH_3$ protons (b) split into doublets of septuplets (1.49 and 1.68ppm) (Fig. 4.12a). Upon Iz coupling, a chiral centre was formed. This probably affected the coupling and therefore peak splitting of the relevent proton peaks.

a

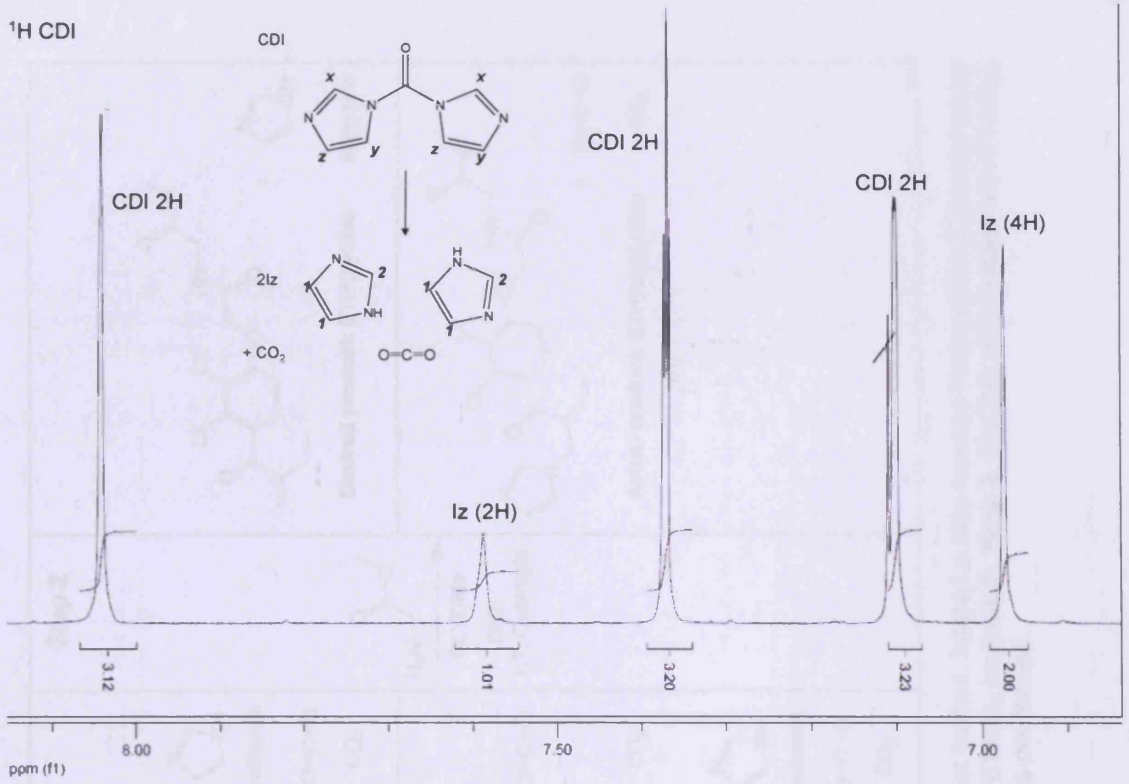
(i)


¹H ETH
e1
e2
d2
d1
c
b
a
0.96
1.02
1.08
1.03
2.05
1.98
3.00
7.0
6.0
5.0
4.0
3.0
2.0
1.0
ppm (f1)
HO
Cl
Cl
O
d2
d1
e2
e1
c
a
b

(ii)


¹H GlyOMe.HCl
g
f
2.06
3.00
5.00
4.50
4.00
3.50
3.00
ppm (f1)
NH2

(iii)



b

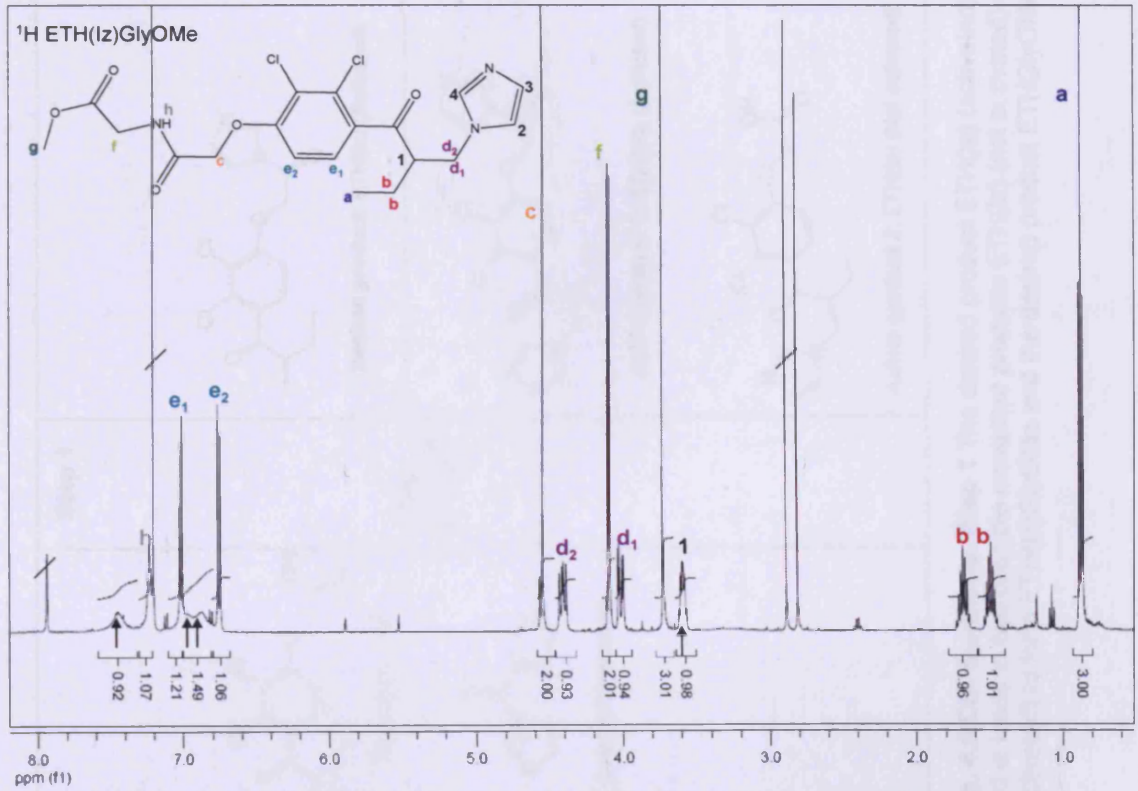


Fig. 4.8 H[1] NMR spectra and structures of starting products and reaction product from CDI synthesis Solvent: $CDCl_3$. Coloured letters correspond to labelled peaks on the spectra. **a**) (i) ETH, (ii) GlyOMe.HCl, (iii) CDI. **b**) ETH(Iz)GlyOMe. Numbered protons are labelled with arrows on the spectra.

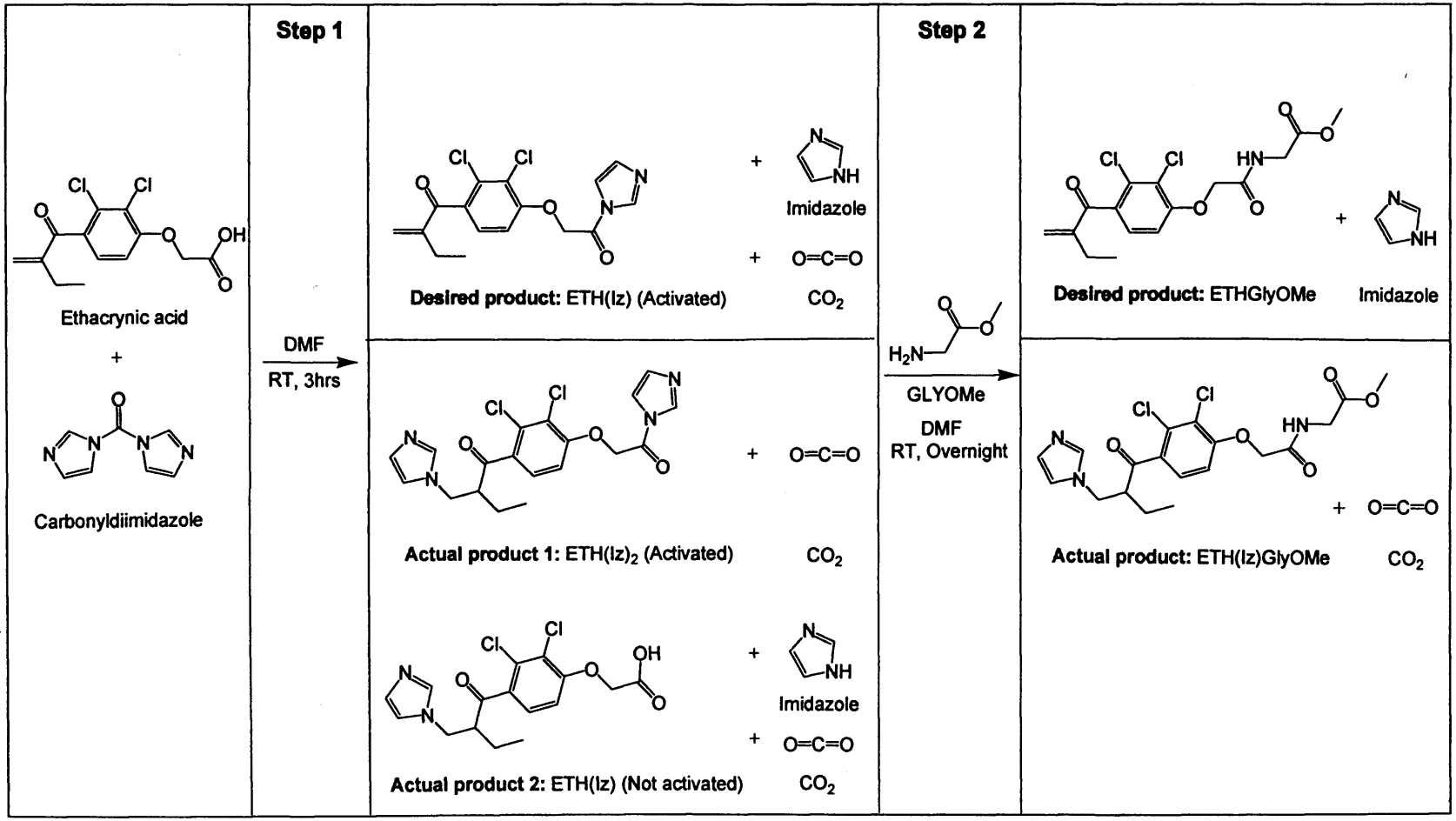


Fig. 4.9 CDI Synthesis. Step 1 The desired product ETH(Iz) (activated) is not formed. Instead a side-reaction between the ETH vinyl group and Iz leads to two possible unwanted products ETH(Iz) (not activated) and ETH-Iz_2 (activated). **Step 2.** GlyOMe.HCl coupled with $ETH(Iz)_2$ (activated) to form ETH(Iz)GlyOMe and the desired product ETHGlyOMe was not formed.

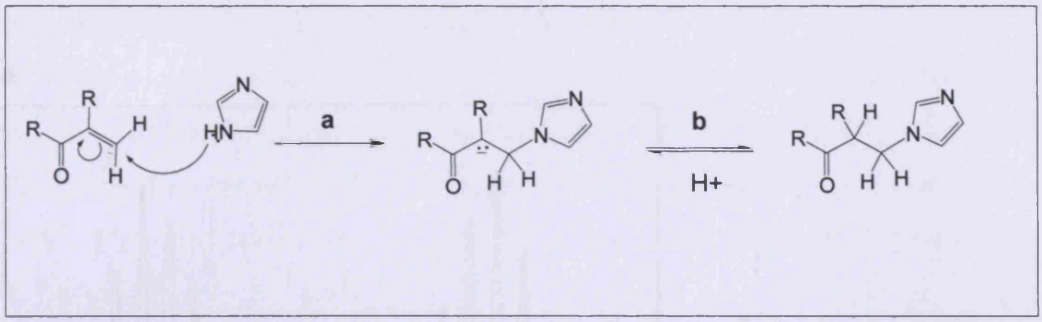


Fig. 4.10 Michael addition of imidazole to an α,β-unsaturated ketone. a: imidazole nucleophile adds to α,β-unsaturated ketone electrophile, **b:** extraction of an acidic proton from the solvent to yield addition product. *Adapted from p.956, McMurray*

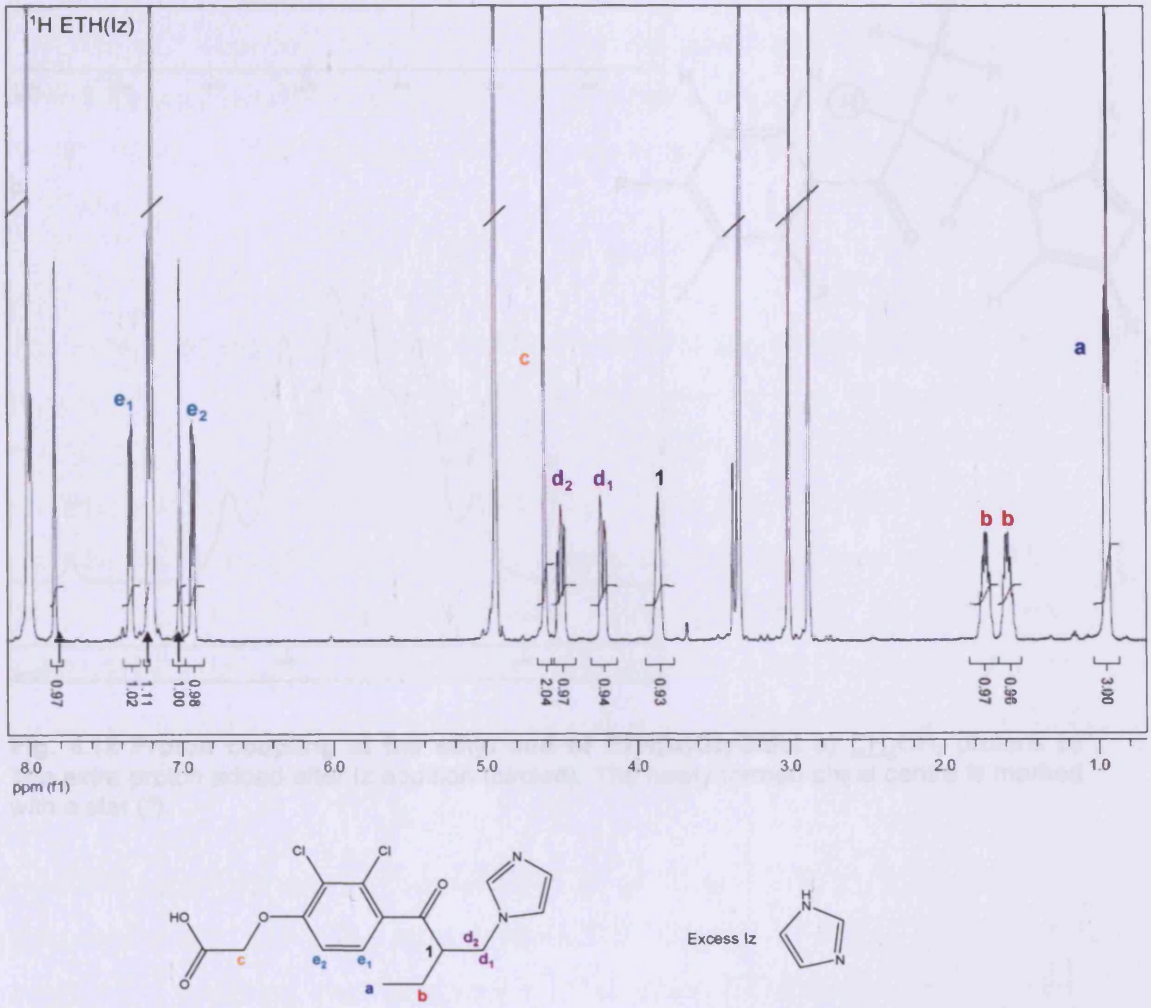


Fig. 4.11 H^1 NMR of ETH(Iz). Solvent: CD_3OD. Coloured letters correspond to labelled peaks on the spectra. Iz protons are labelled with arrows on the spectra.

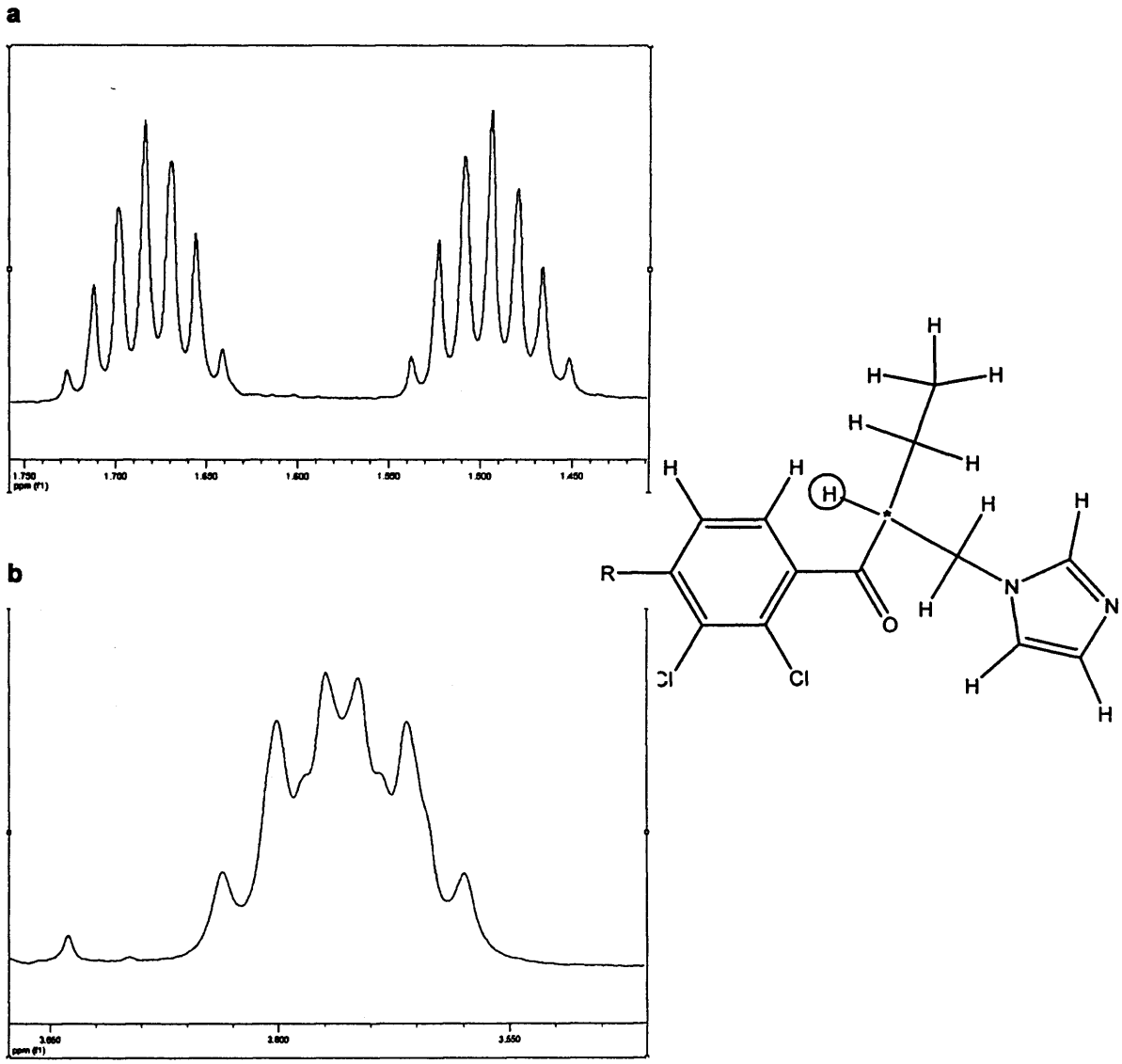


Fig. 4.12 Proton coupling at the ethyl end of ETH(Iz)GlyOMe. a) $\underline{CH_2}CH_3$ protons **b)** The extra proton added after Iz addition (circled). The newly formed chiral centre is marked with a star (*).

4.3.1.2 $SOCl_2$ as coupling reagent

DCM was used as an alternative to benzene because ETH was insoluble in toluene. Protic solvents were inappropriate since they react with $SOCl_2$. Following two hours under reflux, only starting material was observed by NMR. This may have been due to the lower boiling point of DCM compared to benzene.

4.3.1.3 EDC as a coupling reagent

ETH was too insoluble for the reaction to take place in aqueous buffers, and GlyOMe.HCl required a polar solvent to dissolve (only the HCl salt of GLYOMe was available, because the free base polymerises, Myers et al. 1999). DMF (polar, aprotic), was chosen as it solubilised ETH and GlyOMe.HCl.

The structures and NMR spectra of the reactants are shown in Fig. 4.9a (i), (ii) and Fig. 4.13a. In order to reduce side-reactions, a large excess of amine (GlyOMe.HCl) was added to the carboxylic acid (ETH) to allow immediate coupling upon addition of EDC (Fig. 4.14). The GlyOMe.HCl did not fully dissolve in DMF until a second equivalent of EDC was added. EDC, like CDI, is moisture sensitive, and some breakdown products were observed (not all of the NMR peaks integrate, Fig. 4.8a (i). EDC is a zero-length cross-linker (is not included in the final product) and so individual protons were not assigned.

H^1 NMR peaks for amide (f) and ester (g) (4.10 and 3.73ppm respectively) integrated with the ETH peaks (CH_2CH3, CH_2CH_3, OCH_2, CH_2=C, Ar) suggesting coupling was successful. The latter ETH peaks were shifted downfield slightly upon coupling with GlyOMe.HCl (Fig. 4.13b and Appendix IV), suggesting a conformational change. With addition of a second equivalent of EDC, the efficiency of ETHGlyOMe synthesis was increased >90% (Fig. 4.13b). The vinyl protons (d) retained their aromatic character (5.52 and 5.89ppm), and there was no addition of an extra proton (as seen for CDI, Fig. 4.8b).

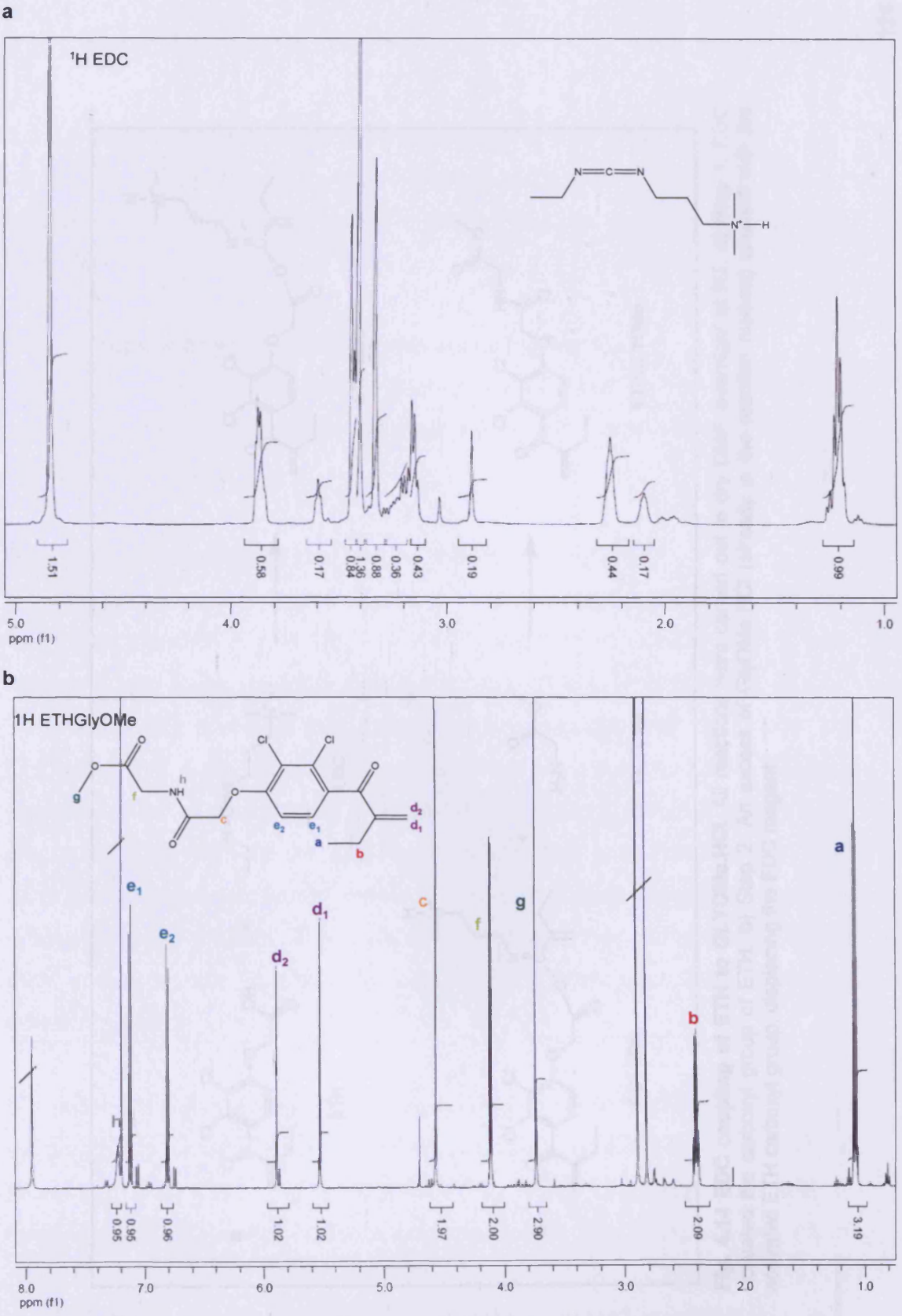


Fig. 4.13 H^1 NMR spectra of EDC coupling reagent and ETHGlyOMe product. a) EDC. Solvent: CD_3OD. **b)** ETHGlyOMe. Solvent: $CHCl_3$. Coloured letters correspond to labelled peaks on the spectra. Some ETH starting product is also visible in the spectrum. Excess EDC was removed by solvent extraction.

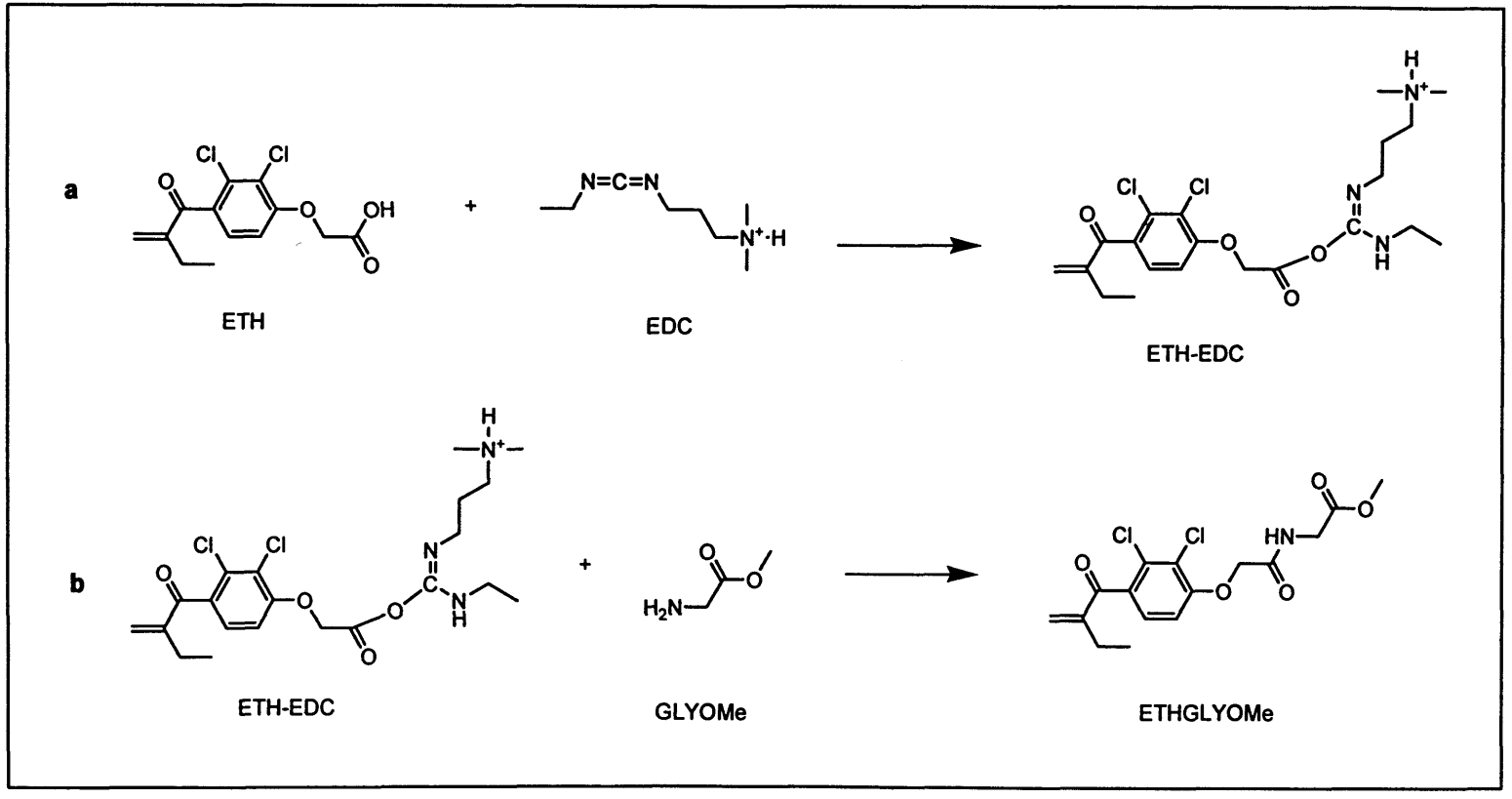


Fig. 4.14 EDC coupling of ETH to GLYOMe.HCl. All reactions were carried out in dry DMF, overnight at RT. **a**) Step 1. EDC activated the carboxyl group of ETH. **b**) Step 2. An excess of GlyOMe.HCl (already in the reaction mixture) coupled with the activated ETH carboxyl group, displacing the EDC reagent.

4.3.2 Ester Hydrolysis

4.3.2.1 Base-catalysed ester hydrolysis using NaOH or LiOH

Under the conditions employed in Section 4.2.4.1 both NaOH and LiOH catalysed the hydrolysis of the amide bond. This was observed by both TLC and NMR.

4.3.2.2 Base-catalysed ester hydrolysis using $NaHCO_3$

Under the conditions employed in Section 4.2.4.2 $NaHCO_3$ did not catalyse hydrolysis of either the amide or ester bond, even after reflux. This was confirmed by NMR.

4.3.2.3 Base-catalysed ester hydrolysis using Na_2CO_3

NMR of the product suggested that the methyl protecting group (3.72ppm) had been cleaved (Fig. 4.15). The NMR was run in CD_3OD and it was observed that all peaks shifted upfield compared to ETHGlyOMe in $CDCl_3$. TLC and NMR revealed that some amide cleavage had also occurred (3.93ppm, Fig. 4.15). In addition, some of the vinyl peaks (5.53-5.89ppm) were observed to shift upfield to the aliphatic region (3.5-3.65ppm) (it was calculated that ~40% of the total vinyl proton peak area had shifted). The extra proton signal (4.59ppm) previously observed upon Iz addition (Section 4.8b), was also present. This was accompanied by an upfield shift in the ethyl group signals to 0.95ppm and 1.57-1.58ppm, also seen upon Iz addition (Section 4.8b).

It is proposed that the vinyl group was subject to nucleophilic attack by OH^-, as previously observed for extended incubation of ETH in basic buffers (Yarwood et al. 1987, Fig 4.15). NMR (Fig. 4.15) suggested that loss of formaldehyde (Fig. 4.16) had not occurred, since total integratable proton number was observed to increase not decrease. Therefore it was concluded that hydroxyl addition products had been formed during this reaction.

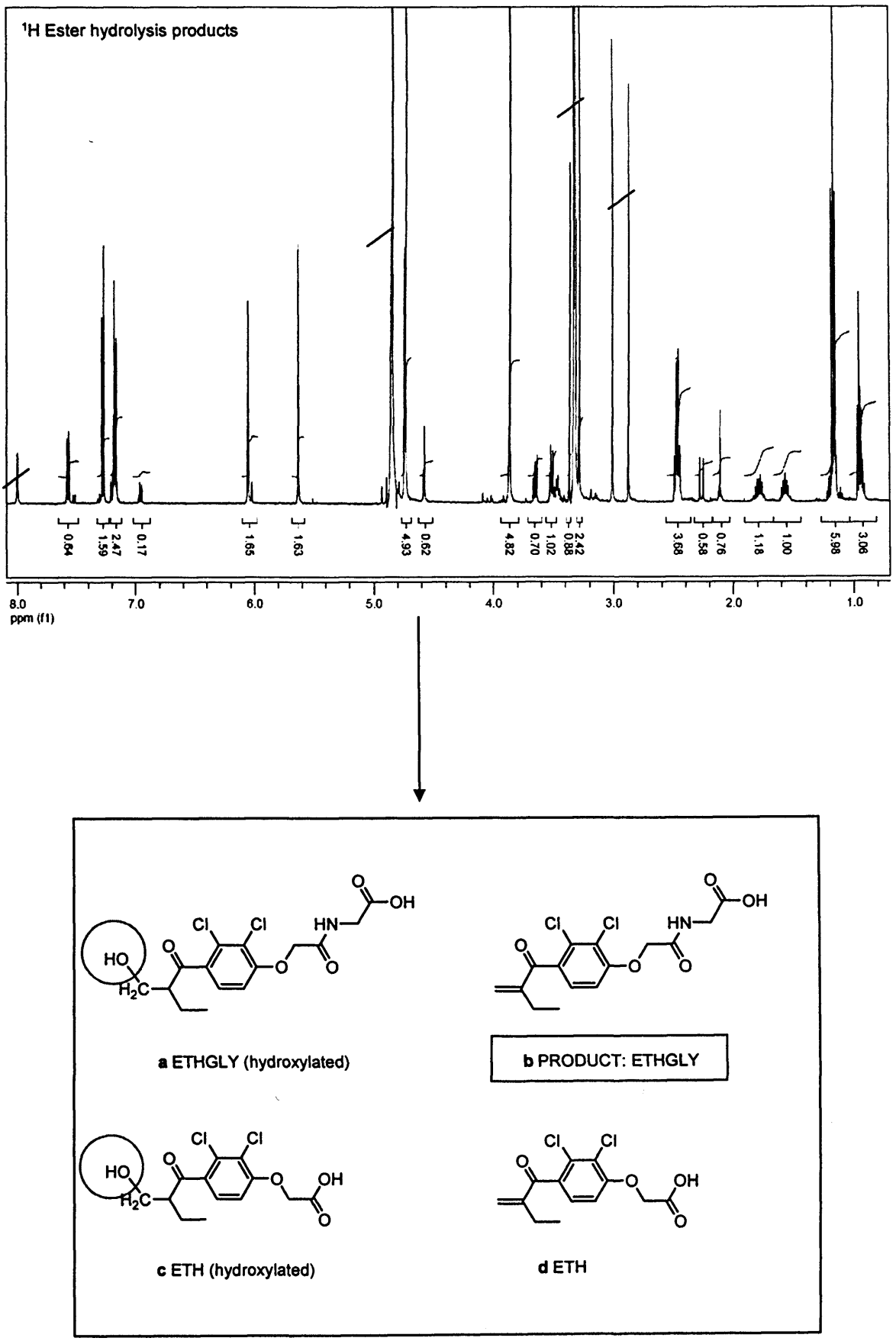


Fig. 4.15 Ester hydrolysis products Four structures were identified from the NMR spectrum after ester hydrolysis of ETHGLYOMe (and subsequent HPLC analysis). Hydroxylation of the vinyl group is circled.

The NMR of the ETHGlyOMe hydrolysis products and consideration of the literature (Yarwood et al. 1987) suggested that four products were likely: ETHGly, ETHGly (hydroxylated), ETH and ETH (hydroxylated) (Fig. 4.15) (These products were confirmed in Section 4.3.4). A small amount of ETH starting material was present in the crude ETHGlyOMe preparation. Additional ETH also resulted from amide hydrolysis. Gly and EDC were removed by solvent extraction.

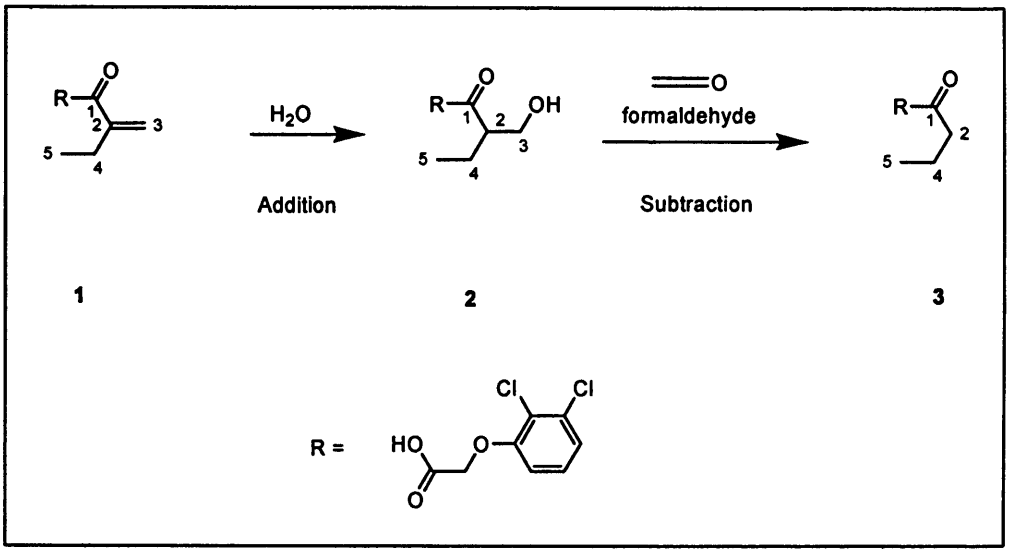


Fig. 4.16 The instability of ETH in mildly basic conditions. ETH (1) can degrade to 2 and 3 in NaPB (pH8, 60°C) according to Yarwood et al. 1987. ETH dimers (not shown) were much slower to form. Carbon atoms are labelled 1-5. *Diagram adapted from Yarwood et al 1987.*

4.3.3 HPLC purification of ETHGLY

HPLC was used to purify the product mixture after selective ester hydrolysis of ETHGlyOMe. The product mixture had a complex UV spectrum with an apparent λ_{max} of 262-266nm (Fig. 4.17). Therefore a wavelength of 264nm was used for HPLC analysis, as well as 280nm (λ_{max} of ETH, Fig. 3.5) and 210nm (for observing non-aromatic impurities). TLC analysis (reverse-phase, optimised mobile phase: MeOH: water (6:4) (0.1% TFA)) was only able to separate the ester hydrolysis products into two distinctive components (retention factors (Rfs) 0.65 and 0.67). ETH alone had a Rf of 0.65. The same mobile phase was used for HPLC and a clear separation of the ester hydrolysis products was observed at 210nm, 264nm and 280nm (Fig 4.18).

The individual compounds corresponding to peaks 1-4 were conclusively identified in Section 4.3.4. HPLC peaks are labelled 1, 2, 3 and 4 corresponding to ETHGly (hydroxylated, retention time (RT) = 21.18), ETHGly (RT = 26.93), ETH (hydroxylated, RT = 31.48) and ETH (RT = 40.28) respectively. Peak 4 was identified by spiking the same product mixture with ETH and observing an increase in peak area. ETHGlyOMe was not present as it eluted (in a separate experiment) at ~50minutes.

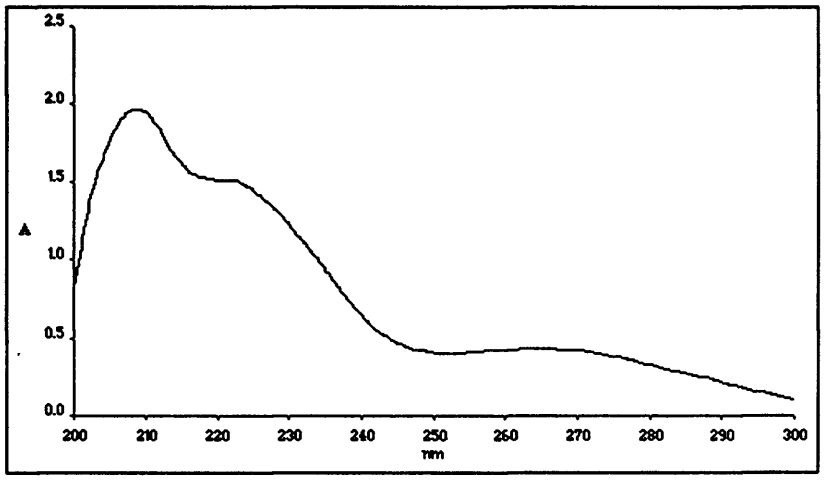


Fig. 4.17 UV spectrum of the product mixture after ester hydrolysis of ETHGlyOMe. A mixture of products gives a flattened spectrum, with an overall λ_{max} of 262-266nm.

Hydroxylated compounds (1 and 3) absorbed more strongly at 264nm than they did at 280nm whilst there was little difference in peak area of ETH at these wavelengths. Upon reduction of the vinyl group, the λ_{max} of the conjugated molecules is likely to shift away from the aromatic region due to loss of 'resonance transfer' contribution from the β-unsaturated ketone. The λ_{max} of ETH appeared to shift from 280 to 264nm after long periods in buffer (Fig. 3.18) suggesting that hydroxylated ETH may have formed (Fig. 4.16, Yarwood et al. 1987).

ETHGly and ETH (1 and 2) eluted first and probably corresponded to the TLC spot: Rf = 0.67. ETHGly had been reported to be more soluble in water than ETH (Cragoe 1983). This was consistent with observations made in this study and with the reverse-phase HPLC elution order.

The fortuitous spacing of the major peaks (1-4) meant that each compound could be collected in a pure form in ~20ml of mobile phase.

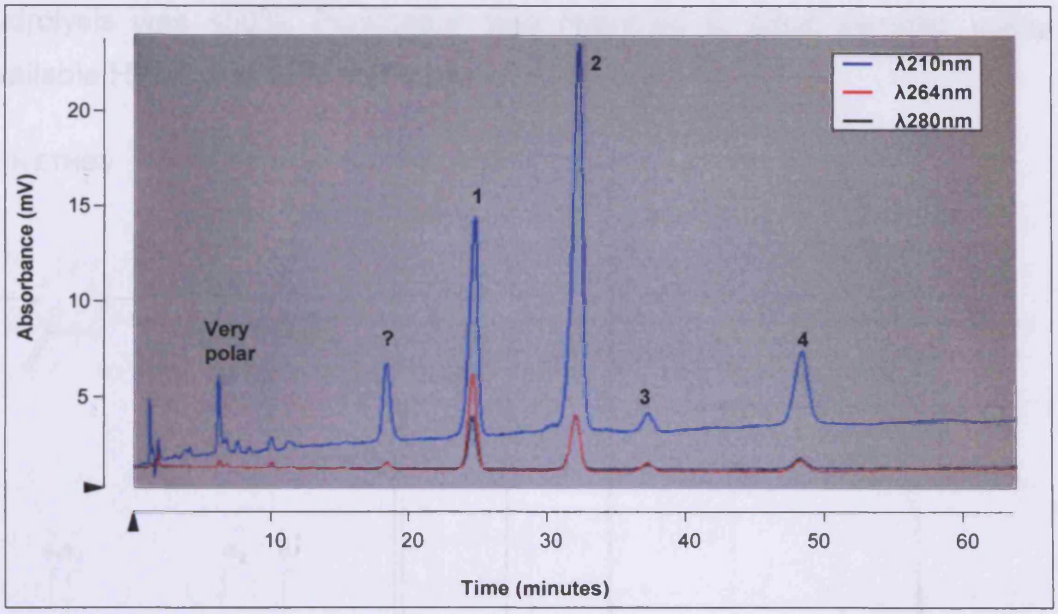


Fig. 4.18 Analytical HPLC spectrum showing separation of four predicted products from ester hydrolysis. An isocratic HPLC method was used on an analytical column. Peaks are numbered **1**: ETHGly (hydroxylated), **2**: ETHGly, **3**: ETH (hydroxylated) and **4**: ETH. An unidentified peak (?) was also observed.

4.3.4 Solid-phase extraction of ETHGLY

SPE was used to successfully concentrate and isolate the four ester hydrolysis products from HPLC fractions 1-4, since simple evaporation of the mobile phase would have concentrated the TFA, risking product degradation. NMR was used to confirm the identity of the individual compounds (Fig. 4.19 and Appendix IV). Analytical HPLC of the purified product (ETHGly, COOH form) at 264nm and 280nm (using fresh mobile phase) gave a single peak (RT 18 minutes, Fig 4.20), with no trace of 1, 3, or 4. Some minor impurities were observed (arrow, Fig. 4.20, RT ~20-30 minutes). However, this was also observed in the blank spectrum and therefore was not associated with the purified product.

Electro-spray mass spectroscopy (negative mode) (MS (ES^-) further confirmed product identity. Calculated mass: 358.0255; measured mass: m/z 358.0257).

A yield was not obtained because a small amount of ETHGly was used for each ester hydrolysis experiment and only a small amount of product was isolated after purification. Synthesis of ETHGlyOMe was relatively straightforward, however the percentage of ETHGly obtained after ester

hydrolysis was <50%. Purification was restricted to small samples using available HPLC and SPE methods.

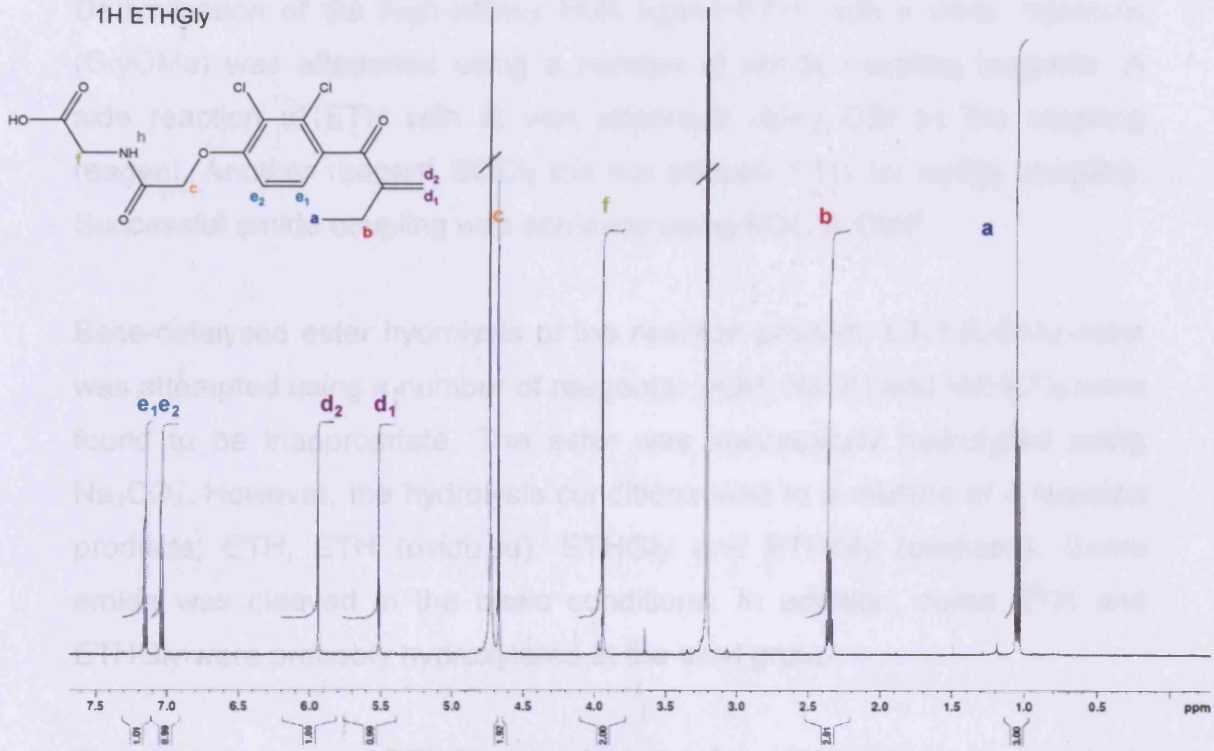


Fig. 4.19 H^1 NMR spectrum of final product: ETHGly. (CD_3OD)

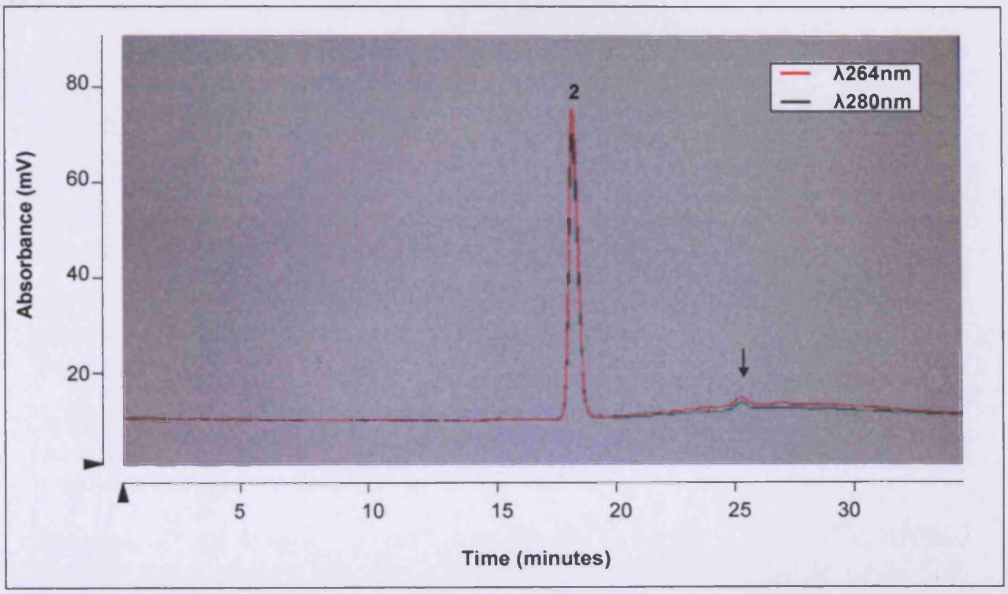


Fig. 4.20 HPLC purity of ETHGly. An isocratic HPLC method was used on an analytical column. Mobile phase: MeOH: water (0.1% TFA) Peak **2**: ETHGly. Arrow shows impurities that were also present in the blank spectrum, probably from a build-up of material after preparative HPLC.

4.3.5 Conclusions

Derivatisation of the high-affinity HSA ligand ETH, with a linker molecule (GlyOMe) was attempted using a number of amide coupling reagents. A side reaction of ETH with Iz was observed using CDI as the coupling reagent. Another reagent $SOCl_2$ did not activate ETH for amide coupling. Successful amide coupling was achieved using EDC in DMF.

Base-catalysed ester hydrolysis of the reaction product, ETHGlyOMe ester was attempted using a number of reagents. LiOH, NaOH and $NaHCO_3$ were found to be inappropriate. The ester was successfully hydrolysed using Na_2CO_3. However, the hydrolysis conditions lead to a mixture of 4 reaction products; ETH, ETH (oxidized), ETHGly and ETHGly (oxidized). Some amide was cleaved in the basic conditions. In addition, some ETH and ETHGly were probably hydroxylated at the vinyl group.

The desired product ETHGly was isolated from the mixture to very high purity using HPLC and SPE, and characterized by NMR, HPLC and MS (ES^-).

References

2006. *Novabiochem Letters. Product focus: reagents for Peptide synthesis* [Online]. Merck. Available at: http://www.merckbiosciences.co.uk/SharedImages/novabiochem/01_06_letterM.pdf [Accessed: 9th march 2006].

Cragoe, Jr. and Edward, J. 1982. 1-(Substituted-aminoalkoxyphenyl)-2-methylene-1-alkanones, compositions and use. In: Patent, U.S. ed. U.S.: Merck and Co., Inc. In: Abraham, D. J. et al. 1989. Design, synthesis and testing of potential antisickling agents. 7. Ethacrynic acid analogues. *Journal of medicinal chemistry* 32, pp. 2460-2467.

Anderson, G. W. and Rolf, P. 1958. N,N'-carbonyldiimidazole, a new reagent for peptide synthesis. *Journal of the American Chemical Society* 80, p. 4423.

Anderson, G. W. and Rolf, P. 1960. N,N'-carbonyldiimidazole, a new peptide-forming reagent. *Journal of the American Chemical Society* 82, pp. 4596-4600.

Battistel, E. and Rialdi, G. 2006. Characterization of immobilised enzymes by microcalorimetry. In: Guisan, J.M. ed. *Immobilisation of enzymes and cells.* Humana Press, p. 297.

Cuatrecasas, P. 1970. In: Hermanson, G. T. et al. 1992. *Immobilised affinity ligand techniques.* Academic Press, Inc., pp. 2, 57, 98, 107, 210, 215, 218, 220, 317, 410, 411.

Danishefsky, I. and Siskovic, E. 1971. Conversion of carboxyl groups of mucopolysaccharides into amides of amino acid esters. *Carbohydrate Research* 16(1), pp. 199-205.

Dayal, B. et al. 1990. Lithium hydroxide/aqueous methanol: mild reagent for the hydrolysis of bile acid methyl esters. *Steroids* 55(5), pp. 233-237.

Desai, M. C. and Stramiello, L. M. S. 1993. Polymer bound EDC (P-EDC): A convenient reagent for formation of an amide bond. *Tetrahedron letters* 34(48), pp. 7685-7688.

Deshler, L. and Zuman, P. 1974. Polarographic reduction of aldehydes and ketones : Part XVIII. Ethacrynic acid. *Analytica Chimica Acta* 73(2), pp. 337-354.

Delf, A. Physical basis of organic reactions. [WWW]. Available at: http://www.chem.ed.ac.uk/bunsen_learner/machan.html [Accessed: 2nd September 2005].

Firouzibadi, H. et al. 2005. Micellar solution of sodium decyl sulfate (SDS) catalyzes facile michael addition of amines and thiols to α,β-unsaturated ketones in water under neutral conditions. *Adv. Synth. Catal.* 347, pp. 655-661.

Grabarek, Z. and Gergely, J. 1990. Zero-length crosslinking procedure with the use of active esters. In: *EDC (1-Ethyl-3-dimethylaminopropyl]carbodiimide Hydrochloride). A water-soluble carbodiimide for rapid preparation of peptide conjugates* [WWW]. Available at: http://www.piercenet.com/browse.cfm?fldID=02030312 [Accessed: 9th march 2006].

Gunther, T. and Ahlers, J. 1976. Specificity of ethacrynic acid as a sulfhydryl reagent. *Arzneim.-Forsch. (Drug Res.)* 26(1), pp. 13-14.

Hermanson, G. T. et al. 1992. *Immobilised affinity ligand techniques.* Academic Press, Inc., pp. 137-141.

Ho, G. J. et al. 1995. Carbodiimide-mediated amide formation in a two-phase system. A high yield and low-racemization procedure for peptide synthesis. *journal of organic chemistry* 60, pp. 3569-3570.

Jones, J. 1994. *The chemical synthesis of peptides.* Clarendon Press, pp. 14, 42, 52.

Kaestle, K. L. et al. 1991. Cleavage of esters using carbonates and bicarbonates of alkali metals: synthesis of thymopentin. *Tetrahedron Letters* 32(3), pp. 327-330.

Locascio-Brown, L. et al. 1990. Radiometric and fluorimetric determination of aminosilanes and protein covalently bound to thermally pretreated glass substrates. *Analytica Chimica Acta* 228, pp. 107-116.

Marder, O. and Albercio, F. 2003. Industrial application of coupling reagents in peptides. *Chimica Oggi chemistry today*, pp. 6-11.

McMurray, J. 2000. *Organic Chemistry.* 5th ed. Brooks/Cole, p. 956.

Meyer, G. D. et al. 2006. Non-specific binding removal from protein microarrays using thickness shear mode resonators. *IEEE Sensors Journal* 6(2). pp. 254-261

Nakajima, N. and Ikada, Y. 1995. Mechanism of amide formation by carbodiimide for bioconjugation in aqueous media. *Bioconjugate chemistry* 6, pp. 123-130.

Pokorski 2004. *Strategies for peptide synthesis: an overview. Carbodiimides: basic structure and mechanism* [Online]. Available at: www.chem.northwestern.edu/~scheidt/PDFs/2004_pdfs/04_Pokorski_AmidePres.pdf [Accessed: 10th May 2005].

Pretsch, E. et al. 2000. *Structure determination of organic compunds.* Springer, pp. 172, 182.

Salomon, C. J. et al. 1993. Recent developments in chemical deprotection of ester functional groups. *Tetrahedron* 49(18), pp. 3691-3734.

Sehgal, D. and Vijay, I. K. 1994. A Method for the High Efficiency of Water-Soluble Carbodiimide-Mediated Amidation. *Analytical Biochemistry* 218(1), pp. 87-91.

Singh, A. K. et al. 1999. Development of sensors for direct detection of organophosphates. Part I: immobilization, characterization and stabilization of acetylcholinesterase and organophosphate hydrolase on silica supports. *Biosensors and Bioelectronics* 14(8-9), pp. 703-713.

Stewart, A. J. et al. 2005. Role of Tyr84 in controlling the reactivity of Cys34 of human albumin. *FEBs journal* 272, pp. 353-362.
Stryer, L. 1999. *Biochemistry.* 4th ed. Freeman, p. 42.

Szeto, P. 2005. EDCI. In: Wipf ed. *Handbook of reagents for organic synthesis.* Wiley

Yang, A. et al. 2000. Large degree of racemization observed in the amide bond forming reaction on silica gel. *Journal of Chromatography A* 878(2), pp. 165-170.

Yarwood, R. J. et al. 1987. The influence of the ammonium ion on the stability of ethacrynic acid in aqueous solution. *Journal of Pharmaceutical and Biomedical Analysis* 5(4), pp. 369-378.

Chapter 5

Preparation and characterisation of aminosilanised silicon surfaces

5.1 Introduction

A fundamental aim for the development of a novel protein imprinting approach (Figure 1.12) was to control the distribution of functional groups on a flat substrate (Fig. 5.1). Gold-alkanethiol and silicon-silane surfaces were initially selected as potential attachment chemistries for protein immobilisation. However, functional molecules such as alkanethiols readily migrate together on gold forming packed self-assembled monolayers (SAMs) (Section 1.3.1, Mrksich and Whitesides 1996). This would be detrimental to the formation of a controlled dispersion of protein, required for the imprinting protocol (Section 1.5). The attachment chemistry of silane molecules onto silicon is much more stable than that of alkanethiol onto gold (Mrksich and Whitesides 1996). Silanes condense with the silica layer to form strong covalent bonds, whereas alkanethiols coordinate with metal surfaces. Silicon wafer was chosen as the flat, derivatisable surface with aminopropyltriethoxysilane (APS) as the functional molecule. The aim of this chapter was to develop a method for cleaning, activating and silanizing silicon surfaces and also to develop an approach for observing the APS layer indirectly using gold nanoparticles (AuNP). A published method was followed which used gas-phase deposition to derivatise silicon surfaces with APS (Bhat et al. 2002). The AuNP were detected by atomic force microscopy (AFM) and surface atomic composition was determined semi-quantitatively by X-ray photon spectroscopy (XPS). (Chapter 6 will describe the preparation of silane gradients using this approach).

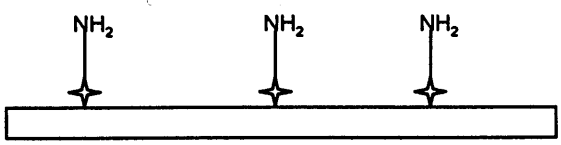


Fig. 5.1 Step one of a novel protein imprinting approach. A silicon surface derivatised with a controlled distribution of functional molecules.

5.1.1 The chemistry of silane deposition on silicon surfaces

5.1.1.1 The structure of silicon wafers

Silicon wafers are widely used in the microelectronics industry, due to the semiconducting nature of silicon (Zhang 2001). Round wafer discs are cut from a large, synthetically-grown silicon crystal, and have a highly ordered structure. Wafers can be purchased polished either on one or two sides and are commonly doped with other elements such as boron or phosphorous ([www] Bates 2000; [www] Kemi Silicon, Inc. 1999-2007). Silicon wafers have a bulk structure of tetravalent silicon and a surface layer of silicon dioxide (SiO_2). In dry conditions the thin silica layer is usually in the inactive 'siloxane' form but can be oxidised further to form reactive isolated silanol or geminal silanol groups (Fig. 5.2, Morrow et al. 1978 in Parida et al. 2006). In aqueous solutions, silanol groups are stablilised through H-bond interactions with H_2O (Wieringa 2000). Silanols can also H-bond with each other (Dugas and Chavalier 2003).

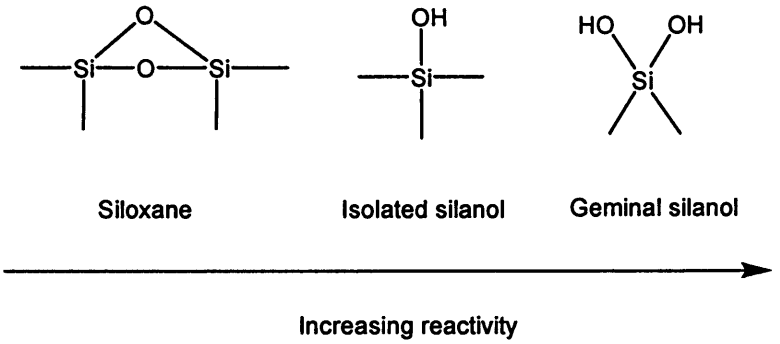


Fig. 5.2 Types of silica on the surface of silicon wafer substrates. *Adapted from Parida et al. 2006.*

5.1.1.2 Methods for activating the silica surface on silicon wafer surfaces

Before undergoing any chemical surface modification, a silicon wafer should be cleaned to remove fingerprints and other contaminants. A nitrogen stream is often used to remove loosely bound debris and dust and for drying surfaces after solvent rinsing. Wafers are often degreased by sonication in one or more solvents, such as acetone, alcohols, dimethyl formamide (DMF), de-ionised water (dH_2O) or a combination (Wei et al. 2000; Simon et al. 2002; Choi and Newby 2006).

biological molecules (Lin et al. 2004; Sorribas et al. 2002; Shim et al. 2004; Arroyo-Hernandez et al. 2003). APS has three ethoxy functional groups which hydrolyse in the presence of water. The resultant hydroxy-silanes hydrogen-bond (H-bond) with surface silanols and finally condense with the surface to form covalent siloxane bonds (Moon et al. 1996; Simon et al. 2002) (Fig 5.4).

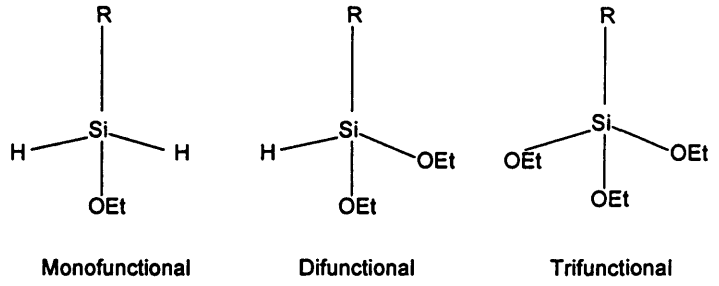


Fig. 5.3 Structure of silanes. The functional ethoxy (OEt)groups are given as examples. R = head group.

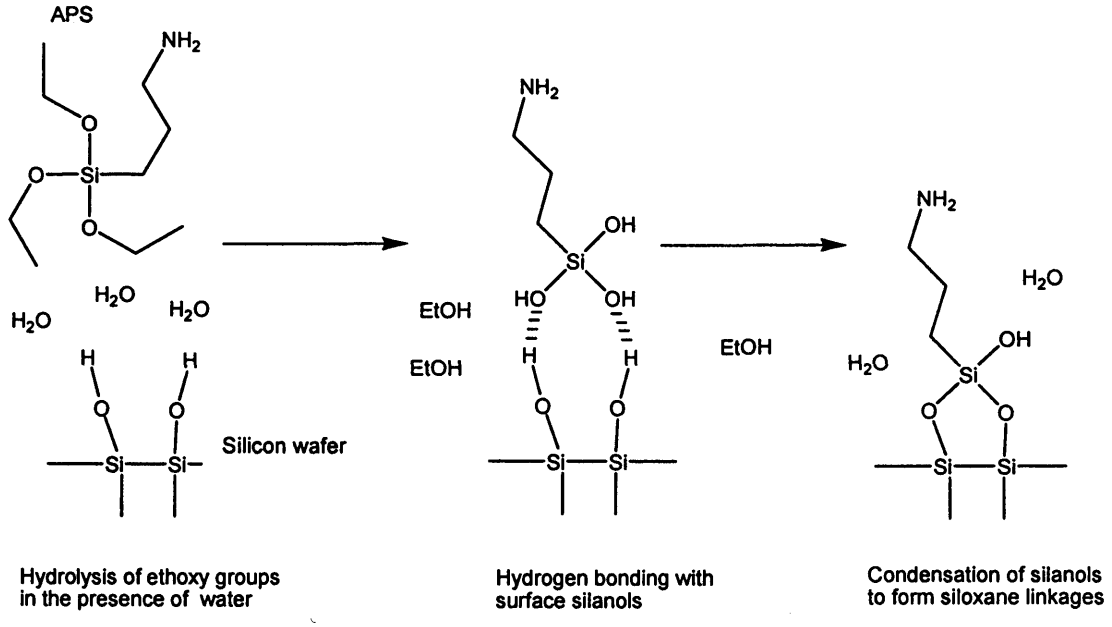


Fig. 5.4 The condensation of APS with activated silicon surface groups. Hydrolysis and condensation path *(Adapted from Simon et al. 2002)*

5.1.2 Derivatising silica with APS

As previously discussed (Section 5.1.1.3), APS is particularly susceptible to hydrolysis in the presence of water. APS will readily form networks in aqueous solution. It is thought that this process commences when amine groups of the APS hydrogen bond either with other APS molecules or with the silicon surface. This is followed by a condensation step, either between

To convert inactive siloxane groups into active silanols, more aggressive treatments are commonly used. Ultra-violet ozone (UVO) treatment can be used to etch a thin layer of the silica to leave surface silanol groups (Tabe 1984), but this requires specialist equipment. Silica activation can also be carried out using acid or alkaline solutions to hydrolyse the siloxane bonds. A standard treatment is the RCA procedure (Kern and Puotinen 1970 in Donose et al. 2006), which involves immersion of the wafer in alkaline (ammonium hydroxide (NH_4OH):hydrogen peroxide (H_2O_2):H_2O), followed by acid (HCl:H_2O_2:H_2O). Alternatively, a sulphuric acid (H_2SO_4):H_2O_2 solution (Piranha (PNA)) has been used to oxidise silicon surfaces and remove organic contamination. This method is cheap and effective and is commonly used for small-scale experiments ([www] Birch 2000). However, harsh acid or alkaline treatments cause increased surface roughness which can effect surface modification and subsequent analysis ([www] Birch 2000). Milder etches using concentrated sodium hydroxide (NaOH), or boiling H_2O have also be used ([www] Birch 2000), but these result in a slower conversion to silanol. Activated wafers can be stored in water to reduce contamination, but ideally should be used immediately (Sugimura et al. 2002). The density of activated silicon wafer hydroxyl groups has been reported as 4.5/nm^2 (Kruger 1988 in Junfu et al. 1998).

5.1.1.3 Silanes and their condensation with activated silicon surfaces

Silane (SiH_4) has been substituted with a range of groups (e.g. methoxy-, ethoxy- and chloro-) in order to give surface-reactive silanes. Many different mono-, di- or tri-functional silanes are available to carry out derivatisations of silicon (or other activated substrates) (Fig. 5.3). Silanes may hydrolyse and condense directly with the surface silanols (Dugas and Chavalier 2003). The silane will have a head-group that does not condense with the surface, and usually changes the chemistry of the surface. Large apolar head-groups e.g. methyl (CH_3) will render the surface inert. Amine head-groups are commonly used to functionalise surfaces for further chemical modification. The amine group can participate in a number of interactions including electrostatic bonding with negatively charged molecules or covalent coupling to carboxylic acid / aldehyde groups (Hermanson et al. 1992). APS has been commonly used as a basis of surface attachment for

adjacent APS molecules or with the silicon surface (Tredgold 1994 in Moon et al. 1996). This process tends to give rise to unordered, heterogeneous surfaces.

5.1.2.1 Solution-phase deposition

Solution-phase deposition of APS from extra-dry solvent such as toluene or hexane onto silicon is common (Wei et al. 2000; Moon et al. 1996; Hooper et al. 2001; Simon et al. 2002; Minard-Basquin et al 2005). The solvent should contain only a trace amount of water to prevent polymerisation networks of APS (Simon et al. 2002). Ellipsometry (Section 5.1.3.1) has been used to show film deposition of APS <0.6–0.7nm thick (Moon et al. 1996; Hooper et al. 2001). A uniform APS monolayer would be 0.55nm according to Simon et al (2002). Measurements of the layer thickness of an APS film (fused silica and silicon wafer) were irreproducible (Moon et al. 1996). XPS (Section 5.1.3.5) has been used to analyse the chemical state of nitrogen (N) in APS films. Basic amine (NH_2) and quaternary amine (NH_3^+) species were identified (Moses et al. 1978 in Hooper et al. 2001) and were shown to be dependent on solution pH exposure prior to XPS (Hooper et al 2001). Some APS was proposed to form a ring structure at the surface via electrostatic interactions between its hydroxyl and amine groups (Moses et al. 1978 in Hooper et al. 2001). Formation of the ring structure may lead to nucleophilic attack of the silane-silanol siloxane bond and release of the APS from the surface. This would be particularly true for long periods of incubation in neutral or basic pH (Etienne and Walcarius 2003). Differences in the activation state and cleanliness of the substrate as well as silanisation conditions will affect the APS film deposition (Hooper et al. 2001).

5.1.2.2 Gas-phase deposition

Chemical vapour deposition (CVD) of various silanes has been described using SiH_4 (Kajikawa et al. 2004), chlorosilanes and aminohexyl-APS (Hozumi et al. 2001). APS has a high vapour pressure (2 pascales (Pa) at 20°C, ([www] UNEP publications 2003) and can be evaporated into the gas-phase from solution at room temperature and pressure (Bhat et al. 2002). Gas-phase deposition of APS has been reported to produce a monolayer

~7Å thick with 5.3 silane molecules per nm^2 (Haller 1978). A single molecule of APS covers ~0.2nm^2 according to Jonas et al (2002). Extended periods of deposition will result in multilayer formation (Chu-jiang et al. 2006). Following silane deposition, substrates should be sonicated in an appropriate solvent to remove physisorbed silane from the surface (Vrancken et al. 1993). A curing step (incubation at high temperatures) encourages condensation of the chemisorbed silane with neighbouring silane molecules as well as with surface silanols to form a stable cross-linked layer (Vrancken et al. 1993).

5.1.3 Techniques for 2D surface chemistry analysis

Controlling and observing surface chemistry on flat, non-porous, two-dimensional (2D) surfaces at the nanometer scale is very challenging. The surface density of silanols in a 1μm^2 area of silicon wafer is lower than 3D porous silica due to its much lower surface area. The derivatisation of such silica gels with APS can be monitored using ultra-violet (UV), fourier-transform infra-red and nuclear magnetic resonance (NMR) spectroscopy (Vrancken et al. 1993), and by secondary chemical modification using dyes such as amine-reactive 4-nitrobenzaldehyde (Moon et al. 1996). Silanisation of non-porous glass beads with APS has been observed by reacting surface primary amines with ninhydrin (Merck 1974). However, flat 2D surfaces have too small a surface area to yield an observable colour change or give rise to measurable quantities of reaction products. Therefore alternative strategies have been developed to characterise step-wise changes in chemical composition, topology and distribution of molecules on a 2D surface. The most common techniques are described in Sections 5.1.3.1 – 5.1.3.5.

5.1.3.1 Ellipsometry

Ellipsometry can be used to study the thickness of molecular films deposited on flat surfaces by measuring the reflection of polarised light after refraction at the surface (Brennan et al. 1993). This technique has a resolution in the sub-nanometer range, however it is less accurate for sub-monolayer coverages (Chaudhury and Whitesides 1992) due to exposure of

the underlying substrate and is often used in conjunction with another technique.

5.1.3.2 Contact angle measurements

Contact angle measurements can be used to estimate the hydrophilicity of a surface. The contact angle of a sessile drop of dH_2O on a surface is measured using goniometry. A hydrophilic surface (e.g. silica with silanol groups) will attract the dH_2O molecules due to H-bonding and the droplets will spread on the surface, giving rise to low droplet-surface contact angles. A hydrophobic surface (e.g. silicon hydride) will be less attracted to the dH_2O molecules, reducing the contact area and resulting in a high contact angle (Fig 5.5). Therefore contact angles can be used as an indicator of change of surface chemistry.

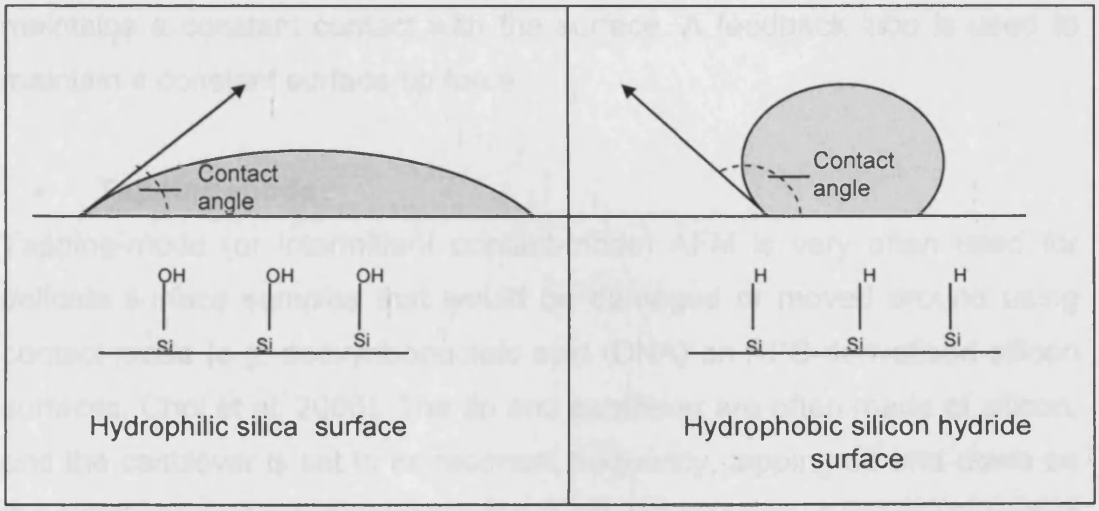


Fig. 5.5 Contact angle measurements used to determine the hydrophilicity of a surface. The contact angles are a rough representation of values for hydrophilic and hydrophobic surfaces.

5.1.3.3 Atomic force microscopy

Atomic force microscopy (AFM, Fig 5.6) is a scanning probe technique that can be used to produce a 3D image of surface topography. A detailed explanation of AFM is available (Veeco 2004). Briefly, AFM uses a cantilever with a sharp tip to track over surface features at the nanometer scale. A laser is positioned at the end of the cantilever and is used to monitor the change in height of the tip (z-axis) as it scans across a specified area (x vs y) on the substrate (e.g. $1\mu m^2$) in a specified number of lines. The

number of lines scanned determines the speed and resolution of the image. The tip scans rapidly in both directions for each line (x-axis), creating trace and retrace images and gradually moving down (or up) the y-axis. The tip extends (downwards) and retracts (upwards) during a scan as it moves over vertical surface features. The laser is reflected off the tip onto a photodiode array, which measures the voltage signal from the laser and the position of the tip. The signal is displayed as a sum (volts, V) and is used to position the laser. A feedback system ensures that the tip is maintained at a safe position from the surface to prevent damage on unpredictable surface features. AFM scans can be carried out in air, liquid, vacuum and at controlled temperatures and pressures. There are three principle modes:

- **Contact-mode**

The cantilever and tip are usually made of silicon nitride, and the tip maintains a constant contact with the surface. A feedback loop is used to maintain a constant surface-tip force.

- **Tapping-mode**

Tapping-mode (or intermittent contact-mode) AFM is very often used for delicate surface samples that would be damaged or moved around using contact-mode (e.g. deoxyribonucleic acid (DNA) on APS-derivatised silicon surfaces, Choi et al. 2006). The tip and cantilever are often made of silicon, and the cantilever is set to its resonant frequency, tapping up and down on the substrate as it moves along without any lateral force. A feedback loop is used to maintain the cantilever at constant amplitude. The amplitude is measured using a root-mean-squared (RMS) signal from the laser on the photodiode array and is a measure of the van der Waals (VdW) force between the tip and surface (Grabar et al. 1997). If the amplitude is set too low, the tip will scan too closely to the substrate and might break on raised surface features. If the amplitude is set too high, the tip will detach from the substrate completely.

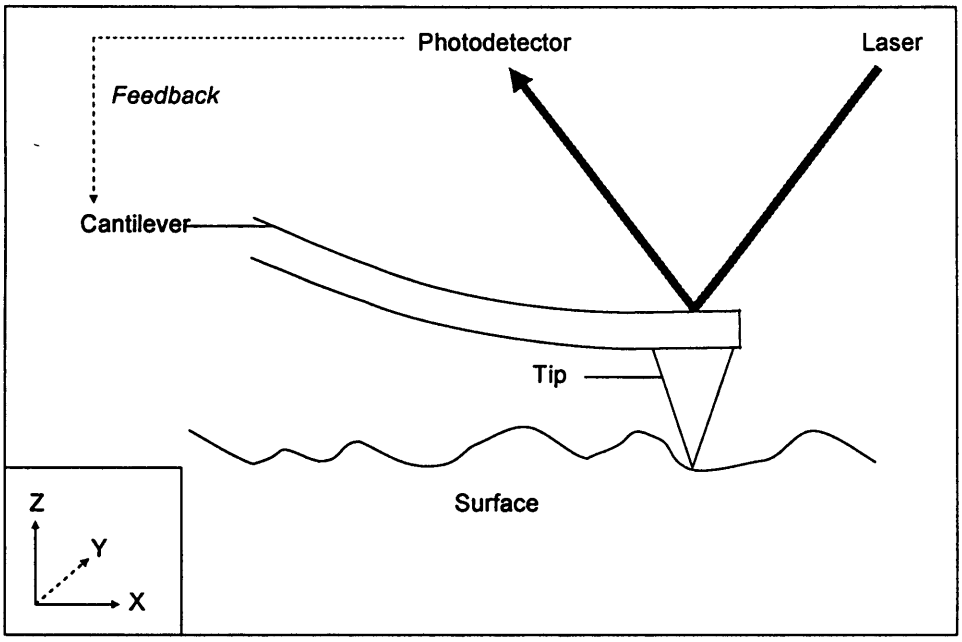


Fig. 5.6 Atomic force microscopy. A scanner moves the cantilever and tip rapidly across the x-axis of a surface in both directions (trace and retrace), gradually moving down the y-axis of a specified scan area. The deflection of a laser beam onto a photodetector monitors z-axis movement of the cantilever as the tip tracks along the surface. Feedback is used to maintain a constant tip position relative to the surface.

- **Non-contact-mode**

For extremely delicate samples, AFM can also be carried out without tip-surface contact. However in non-contact mode, the resolution in air is much lower than that of contact and tapping-mode AFM.

5.1.3.4 Electron microscopy

Although this technique has not been used in this study, scanning electron microscopy has been shown to be a very useful technique for analysing large surface areas (mm scale). Features down to 1nm – 20nm (depending on instrumentation) can be imaged (Grabar et al. 1997). Transmission electron microscopy can resolve surface features down to the atomic scale (0.1nm) (Grabar et al. 1997).

5.1.3.5 X-ray photon spectroscopy

X-ray photon spectroscopy (XPS) is an ultra-high vacuum technique for determining the atomic composition of a solid surface (Moulder et al. 1995). The substrate is irradiated with a beam of x-rays, set to contact the substrate at a shallow angle (grazing angle). The x-ray photons excite only the atoms in the upper surface of the material, which results in the emission

of electrons. The kinetic energies (KE, electron volts (eV)) of the emitted electrons are used to calculate the ground-state binding energy (BE, eV) of the photon from a certain surface atom (Equation 5.1). Each atom has its own charactistic BE(s). Aminosilane deposition on flat substrates has previously been analysed by XPS (Hooper et al 2001; Seitz et al. 2003; Sugimara et al. 2002; Chu-jiang et al. 2006)

Eq. 5.1 BE = X-ray photon energy - KE - Φ (work function of spectrometer)

The chemical state of a particular element can be identified (e.g. N could be present as amide (RNHR), RNH_2 or RNH_3^+), because compounds of different chemical potential and polarisability have different BEs (Moulder et al. 1995).

5.1.4 Characterization of silanised silicon wafer substrates using colloidal AuNP

5.1.4.1 AuNP synthesis

The method of Frens is commonly used to synthesise aqueous AuNP suspensions (Frens 1973 (modified from Turkevich 1951) in Kimling et al. 2006). AuNPs are precipitated from a solution of tetrachloroaurate ($HAuCl_4$) using a reducing agent, sodium citrate. The particles are stabilised by the negative sodium citrate ions which prevent aggregation. AuNPs of between 2nm and 120nm may be synthesised in this way (Grabar et al. 1996). AuNPs (5 ± 2, 10 ± 2 and 15 ± 3nm) produced by a modified tannic acid method of Slot and Geuze (1981 in Sigma-Aldrich 2006) are commercially available (Sigma-Aldrich, St Louis, MO, USA)). These have the advantage of high stability and monodispersity.

5.1.4.2 Electrostatic interaction between APS and AuNPs

AuNPs stabilised with negative citrate ions bind electrostatically to positively charged APS molecules and have widely been used to confirm the presence of APS on derivatised silicon wafers (Grabar et al. 1995; Park et al. 1999; Bhat et al. 2002). AuNPs do not bind to underivatised silicon

because the negative citrate and silanols repel each other (Bhat et al. 2002). The AuNP-APS interaction is stable for months in dH_2O (Nath et al 2004).

5.1.4.3 Analysis of AuNP binding on APS-derivatised silicon surfaces

A sub-monolayer of APS cannot be confidently distinguished from bare silicon using AFM. The tapping-mode AFM vertical detection limit is ~1nm in air. However, APS-derivatised silicon substrates can be readily visualised using 10nm AuNP as a 'developer' (Grabar et al. 1997). Other groups have used XPS to analyse AuNP binding to aminosilane surfaces (Cant et al. 2003; Seitz et al. 2003; Diegoli et al. 2007) XPS can also be used to analyse silane deposition without the need for AuNP derivatisation (Sugimura et al. 2002; Martin et al. 2007).

5.1.5 Chapter objectives

- To clean and activate silicon wafer surfaces for solution-phase and gas-phase silanisation with APS
- To optimise a gas-phase silanisation method.
- To develop an approach for observing the silane layer indirectly using AuNPs and directly using XPS.

5.2 Methods

This section describes the development of an optimal approach for the gas-phase deposition of APS on silicon surfaces based on work carried out by Bhat et al (2002).

5.2.1 Equipment and materials

Equipment: Pyrex petri dishes (Fisher, Waltham, MA, USA), IKAMAG Ret basic hot-plate (Sigma-Aldrich, St. Louis, MO, U.S.A) and shaker (Marius, Utrecht, Netherlands) were used.

Materials: Thermally oxidised silicon test wafers (polished one side, 600-700µm thickness, Boron and Phosphorous-doped were purchased from Compart Technologies (Peterborough, UK), AuNP solution (10nm diameter, 0.75A_{520} units/ml), APS solution (min 98%), H_2SO_4 (>97.5% wt solution, analytical reagent grade), H_2O_2 (25.7% wt solution in water) and hydrochloric acid (HCl, 37% wt in water, analytical reagent grade) were purchased from Sigma-Aldrich (St. Louis, MO, U.S.A). Eppendorf tubes, DECON, acetone (lab reagent grade), paraffin oil (PO) and toluene (lab reagent grade) were purchased from Fisher (Waltham, MA, USA). Isopropyl alcohol (IPA, analytical reagent grade), ethanol (EtOH, spectro. grade, 5% IPA and 5% methanol), dimethylformamide (DMF) and extra-dry toluene (with molecular sieve, < 50ppm water) were purchased from Acros. Organics (Geel, Belgium). De-ionised water (dH_2O) was used in-house.

5.2.2 Development of a method for the cleaning, activation and silanisation of silicon surfaces

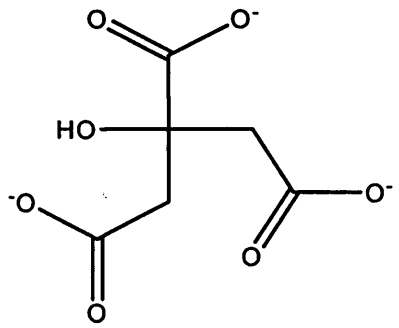
The silicon surfaces were cut into ~1cm^2 pieces and the glassware was pre-cleaned in ≈2% DECON. All experiments were carried out at room temperature (n = 4). At least four treatments were carried out for each silanisation method (Table 5.1). Surface treatments 1-3 acted as controls for the experimental treatment (surface treatment 4). Unless otherwise stated, surfaces were incubated in a 1/10 aqueous dilution of a stock AuNP solution

for 14-24 hours. Excess AuNP solution was subsequently removed by rinsing three times in dH_2O (4ml, 10mins).

Table 5.1 Four standard surface treatments carried out for each silicon derivatisation experiment. AuNP solutions were diluted 1/10 (aq).

Surface treatment	Cleaning / Activation	Silanisation With APS	Incubation with AuNP	Surfaces also denoted
1	Yes	No	No	PNA
2	Yes	No	Yes	PNA Au
3	Yes	Yes	No	APS
4	Yes	Yes	Yes	APS Au

AFM (Section 5.2.3.1) and contact angle measurements (Section 5.2.3.3) were used to characterise the surfaces. AFM was used to visualise changes in topography of the silicon surface before and after the various treatments. APS deposition on silicon was observed by XPS (Section 5.2.3.2) by monitoring changes in the surface atomic composition (nitrogen (N), carbon (C), silicon (Si) and oxygen (O)) compared to plain silicon surfaces. AuNP deposition was observed by monitoring C, O (AuNP were stabilised by citrate anions, Fig. 5.7) and gold (Au) compositions. Casa XPS (http://www.casaxps.com/berlin/) and electron spectroscopy for chemical analysis (ESCA, UWCC and Albert Carley 1996) software was used to analyse the XPS data (Section 5.2.3.2).



citrate

Fig. 5.7 Structure of the citrate anion that stabilises AuNPs

5.2.2.1 Solution-phase silanisation

a. Pre-cleaning silicon surfaces using a series of different solvents

Surfaces were pre-cleaned in a series of solvents; acetone, IPA, dH_2O, HCl (1M (aq)) and three times in dH_2O, each for 5 minutes. The surfaces were silanised in a static solution of APS (2% v/v in toluene) for 1hr, washed three times in EtOH and dried under a nitrogen stream (N_2). Surfaces were incubated in a 1/10 (aq) AuNP solution and imaged using contact-mode AFM (Section 5.2.3.1). The four standard surface treaments were carried out (Table 5.1).

b. Surfaces activated in PNA solution prior to silanisation

Debris was removed from the surfaces using N_2. Surfaces were activated in hot PNA etch solution (3:1 H_2SO_4:H_2O_2) for 20 minutes in a 5ml Petri dish (no pre-cleaning step). The PNA was left to cool for a further 10 mins before transferring the surfaces to dH_2O and thoroughly rinsing three times for 10 mins. The surfaces were silanised (Section 5.2.2.2 a), using 5% v/v APS in toluene and washing in acetone. The first acetone wash included an ultrasonication step. Surfaces were incubated in a 1/100, 1/1000 or 1/10000 dilution (aq) of the AuNP solution and imaged using contact-mode AFM. Surface treatments are listed in Table 5.2.

Table 5.2 Surface treatments for solution-phase APS silanisation on silicon wafers. Different AuNP dilutions were used.

Surface treatment	Cleaning / Activation	Silanisation With APS	Incubation with AuNP (dilution)
1	Yes	No	No
2	Yes	No	Yes
3	Yes	Yes	No
4	Yes	Yes	Yes (1/100)
5	Yes	Yes	Yes (1/1000)
6	Yes	Yes	Yes (1/10000)

c. Surfaces activated in hot PNA solution and silanised in extra-dry solvent

As 5.2.2.1b, except PNA solution was maintained at 60°C on a hot-plate during the 20 minute activation step. Extra-dry toluene was used as the

silanisation solvent. The surfaces were ultrasonicated and washed in toluene and DMF after silanisation. Surfaces were incubated in a 1/10 (aq) 10nm AuNP solution. Surfaces were imaged using contact-mode AFM and XPS. The four standard surface treatments were carried out (Table 5.1).

d. An optimised method for surface cleaning, activation and solution-phase silanisation

Surfaces were pre-cleaned by ultrasonication in EtOH and dimethylformamide (DMF) for 15 minutes each. PNA (7:3 H_2SO_4: H_2O_2) was maintained at 80-90°C on a hotplate during surface activation. Surfaces were silanised with APS (1%) in extra-dry toluene on a shaker for 20 minutes and incubated in a 1/10 (aq) AuNP solution. Surfaces were imaged using contact-mode AFM and XPS. Surface treatments are listed in Table 5.3.

5.2.2.2 Gas-phase silanisation

Silanisation was carried out on the bench-top and not in a fume-hood to prevent air-flow interfering with APS evaporation and deposition.

a. Evaporation of silane from a Petri dish lid

The experiment was carried out at the same time as the solution-phase silanisation (Section 5.2.2.1d) experiment, using the same pre-cleaning and activation procedures. For the silanisation step, APS (~66% in PO) was pipetted into a 5ml Petri dish, enclosed within a 10ml Petri dish in which the surfaces were placed. Subsequently, the surfaces were washed in acetone (x3) for 15 minutes and cured overnight at 110°C. The surfaces were then incubated in a 1/10 (aq) AuNP solution. Surface treatments are listed in Table 5.3.

Surfaces were imaged using contact-mode AFM and XPS. The XPS samples for gas- and solution-phase were analysed in parallel (Section 5.2.2.1d). A survey of the surface elements and a 'montage' of 'curvefit' spectra for each element were produced using Casa XPS. The binding energy and percentage chemical state of each element was also calculated. The molar % composition for each element was calculated using ESCA.

Table 5.3 Surface treatments for solution- and gas-phase APS silanisation on silicon wafers. All AuNP solutions were diluted 1/10 (aq).

	Surface treatment	AuNP incubation
1	Pre-clean and PNA incubation	Yes
2	1 plus 10min gas-phase silanisation	No
3	1 plus 10min gas-phase silanisation	Yes
4	1 plus 60min gas-phase silanisation	No
5	1 plus 60min gas-phase silanisation	Yes
6	1 plus 20 min solution-phase silanisation	No
7	1 plus 20 min solution-phase silanisation	Yes

b. Evaporation of silane from an Eppendorf tube lid

The procedure of Section 5.2.1.3a was followed except APS was evaporated from an Eppendorf tube lid enclosed within a Petri dish for 5, 15 or 20 minutes. Samples were imaged using contact-mode and tapping-mode AFM (Section 5.2.3.1). The four standard surface treaments were carried out (Table 5.1).

5.2.2.3 An optimised method of surface cleaning, activation and gas-phase silanisation

This method was used in all subsequent experiments (unless otherwise stated).

1. Cleaning

Surfaces were degreased by ultrasonication in EtOH and then DMF for 15 minutes each. The surfaces were dried in a N_2 stream using filter paper to absorb excess solvent.

2. Activation

PNA (7:3 H_2SO_4: H_2O_2) was pipetted onto the surfaces and maintained at 80-90°C on a hot-plate. The PNA solution was left to cool for 10 minutes before washing the surfaces three times in dH_2O for ten minutes, and drying with a nitrogen stream.

3. Silanisation

The surfaces were arranged around an Eppendorf tube lid, 0-4cm from the edge, and enclosed within a Petri dish (Fig. 5.8). APS and PO were pipetted into the Eppendorf lid, and APS was left to evaporate over the enclosed surfaces for 5 minutes at room temperature and pressure. The surfaces were ultrasonicated for 15 minutes in acetone, washed in acetone twice for 15 minutes, dried with a nitrogen stream and oven-cured overnight at 80°C or 110°C.

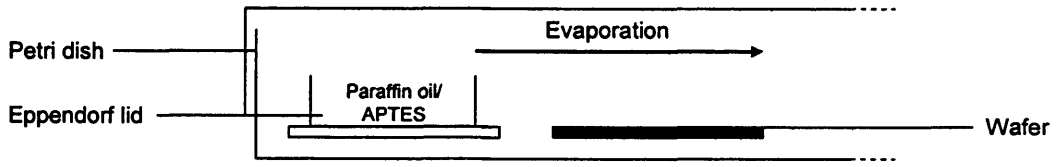


Fig. 5.8 Evaporation of APS onto PNA-activated silicon surface

5.2.2.4 Gas-phase silanisation of surfaces with an increasing exposure time to APS/PO, followed by a sonication step

Using the optimised gas-phase silanisation procedure (Section 5.2.2.3), the silicon surfaces were silanised with APS for 5, 10 and 15 minutes and analysed by XPS.

5.2.2.5 Contact angle measurements

Contact angles (Section 5.2.3.3) were measured for surfaces after treatments at various stages of cleaning, activating and silanisation (Table 5.4).

Table 5.4 Surface treatments measured by contact angle analysis.

Surface treatment (n = 3)	
1	Untreated
2	Acetone / DMF clean
3	2 and PNA treatment
4	3 and acetone ultrasonication
5	3, APS (evaporation deposition) and acetone ultrasonication
6	5 and oven cure (80°C)
7	3, APS (solution deposition) and acetone ultrasonication
Missing	PNA, acetone, oven cure

5.2.3 Analytical methods

5.2.3.1 Atomic Force Microscopy

An outline of the AFM technique is given in Section 5.1.3.3. A Veeco Scanning Probe Microscope (Veeco Instruments Inc., Woodbury, NY, USA) was used to obtain sub-micron resolution images of modified silicon surfaces. NP-20 non-conductive silicon nitride tips were used for contact mode AFM and RTESP 1-10 Ohm-cm phosphorous (n) doped silicon AFM tips were used for tapping mode AFM. The surfaces were mounted on 15mm AFM sample mounting disks using sample adhesive pads. All consumables were purchased from Veeco Instruments Inc.

The instrument was set up and used as recommended (Veeco 2004).

- **Scan settings**

All images were measured with 256 lines. The initial scan size was always set to 1μm^2. In air, with the likelihood of large pieces of surface debris, the z-limit (retraction) was set to the maximum (4.5μm) to prevent the AFM tip from breaking.

  - **Contact-mode AFM settings**

The laser was adjusted to give a sum of 4-6V (optimum voltage hitting the photodetector). The cantilever was set to a 'horizontal deflection' of 0 and 'vertical deflection' of -2 (to impart some force on the surface). The scan rate was 2Hz and the integral and proportional feedback gains were set to 1 and 1.5 respectively. The amplitude set-point (ASP) was set to 1V and adjusted during scanning to give an optimum surface force.

  - **Tapping-mode AFM settings**

The laser was adjusted to give a sum of 2-4V (optimum voltage hitting the photodetector). The cantilever was set to a horizontal deflection of 0 and vertical deflection of 0 and the integral and proportional gain scan parameters were set to 2 and 3 respectively. The cantilever was auto-tuned

to find its free-air resonance frequency (set to maximum amplitude of 2V). The amplitude set-point (ASP) was set as in contact mode.

- **Image processing**

All AFM pictures were processed using 'WSXM' image analysis, available as a free download (http://www.nanotec.es/wsxm_download.html).

Each scan of the surface produced three images (Fig. 5.9), a trace (forward scan, z axis = height (nm)), retrace (backward scan, z axis = height (nm)) and derivative (averaged signal of trace and retrace, z-axis = voltage).

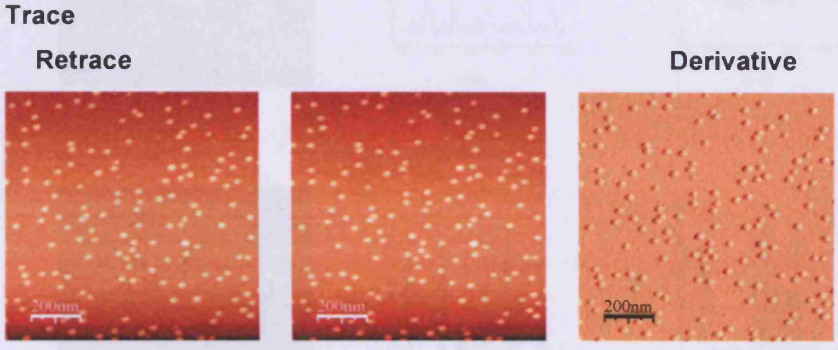


Fig. 5.9 Images produced from each AFM scan

- **Applying filters to remove image artefacts**

Images were automatically processed with a 'first-order planefit' (Veeco AFM software) which eliminated image tilt (Veeco 2004).

In the absence of processing, images were often 'bowed' (curvature away from an ideal plane, Veeco 2004). This is illustrated using height profiles of the x and y axes (Fig. 5.10a). 2nd order planefit was used to remove bow (arch-shaped) (Fig. 5.10b). The flatten tool was used to remove bow and also vertical offset (to bring all of the lines into the same plane) (Fig. 5.10c). Ideally filters should be used to a minimum to avoid changing the real surface topography (Veeco 2004). In order to count AuNPs precisely, 2nd order planefit and flatten offset tools were necessary.

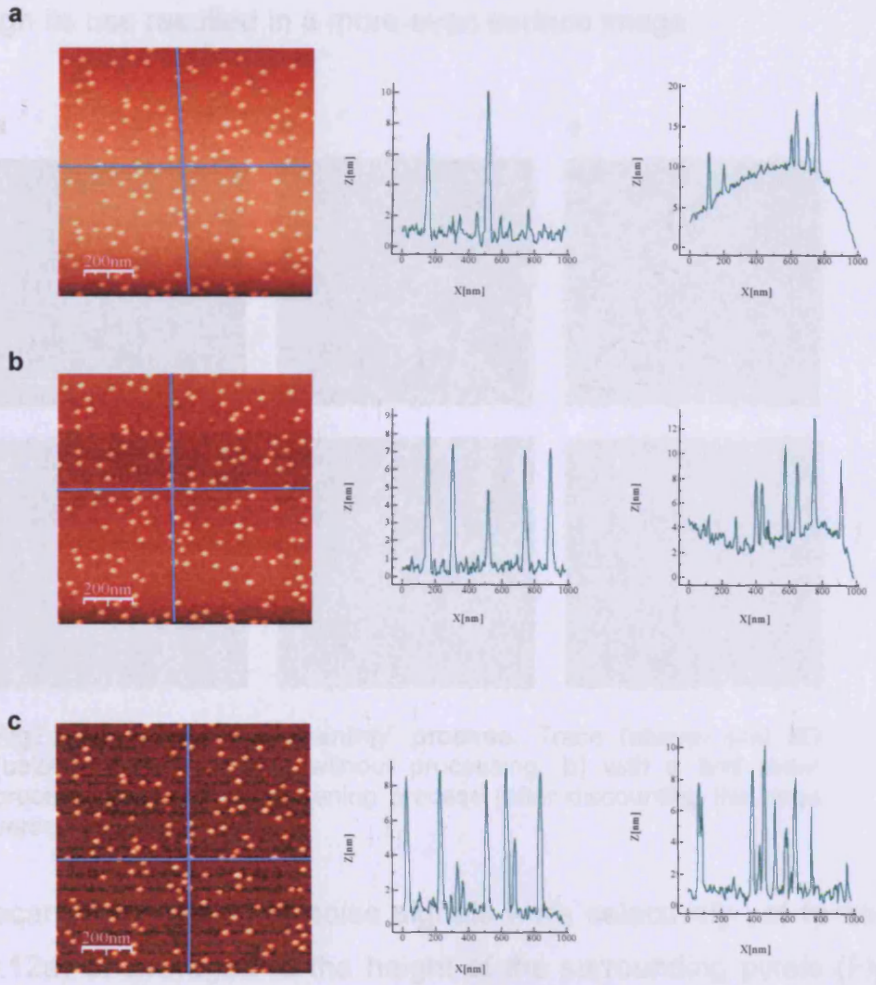


Fig. 5.10 Removal of 'bow' from AFM images using 2nd order and flattening processes. Horizontal and vertical cross-sections of each image (middle and right respectively) are shown for **a**) image with bow, **b**) image after 2nd order processing, **c)** image after flatten processing. Processes were carried out using WSXM.

Vertical offset was caused by a number of factors including bow, loud noises, poor surface-tip tracking and large surface debris (Veeco 2004). A scan with an artificial step is shown in Fig 5.11. The differences in the image before (Fig 5.11a) and after (Fig 5.11b) flattening, are shown as a 2D and 3D height images. Large vertical features were highlighted and discounted from the image before flattening (Fig 5.11c), to reduce additional image distortion. For AuNP images this was not important, as the number of AuNPs could still be counted accurately. Flattening does not remove or reduce surface features such as AuNPs (unlike the 'smoothing' process which was not used in these experiments). Flattening may not be

appropriate when measuring sub-nanometer-scale surface roughness, although its use resulted in a more even surface image.

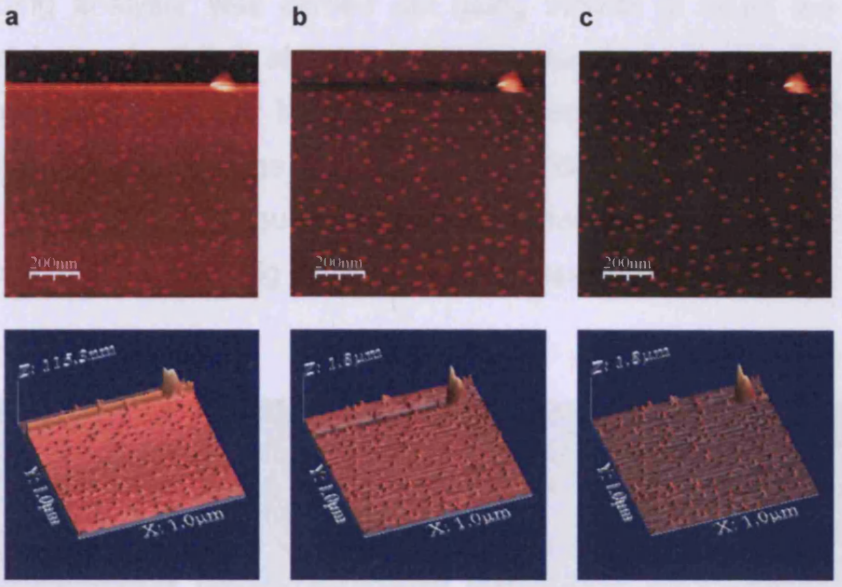


Fig. 5.11 The AFM 'flattening' process. Trace (above) and 3D (below) AFM images **a**) without processing, **b**) with a 2nd order process and c) with a flattening process (after discounting the large vertical feature).

AFM scan lines with large noise signals were selectively set to zero height (Fig 5.12a) or averaged to the height of the surrounding pixels (Fig 5.12b). However, this process tended to reduce image resolution.

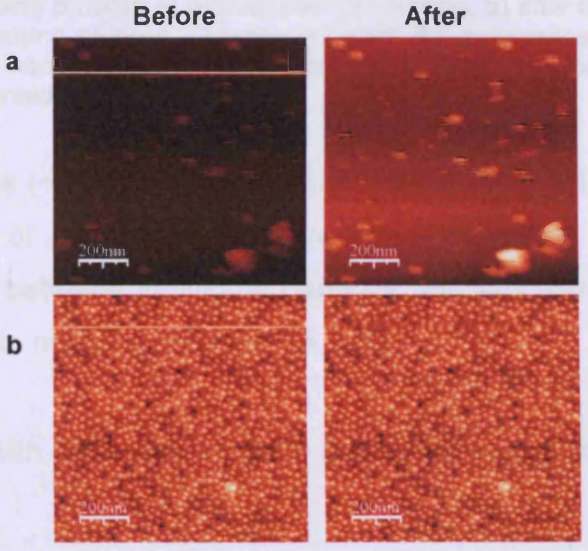


Fig. 5.12 Processing of selected AFM scan lines. Trace images with **a**) lines set to zero height and **b**) lines averaged to height of surrounding pixels.

- **Image analysis**

'Flooding analysis' was carried out using WSXM to count the number of raised features ('hills') above a specified height from a flat surface. The numbers of AuNPs per image were obtained in this way. Fig 5.13 shows flooding of a trace image with and without 'flatten' processing. The AuNPs were more easily distinguished from the surface with flatten processing (Fig 5.13c) than 2nd order (Fig 5.13b) or no processing (Fig 5.13a).

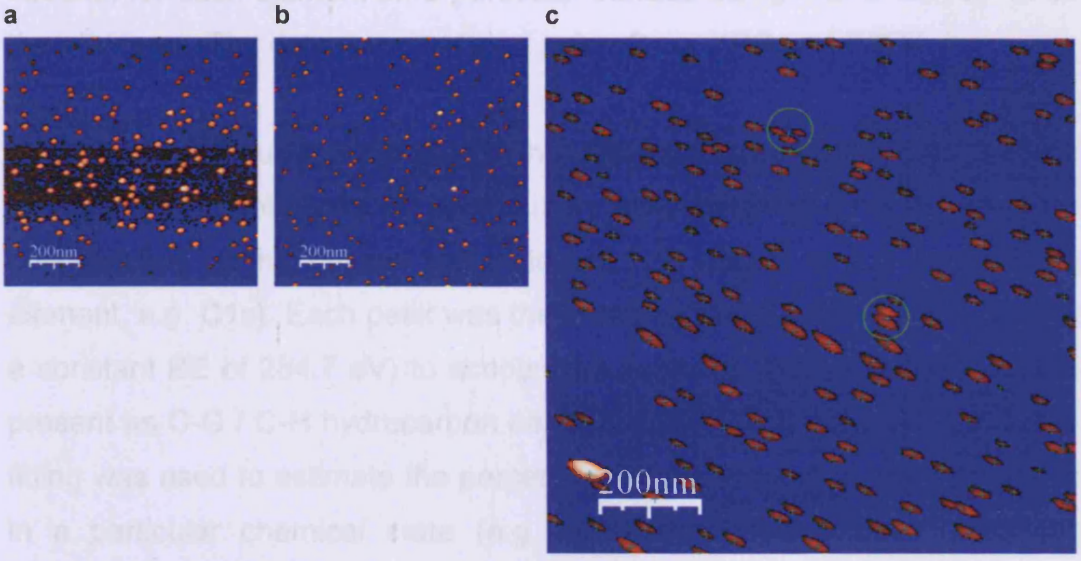


Fig. 5.13 Using WSXM flooding analysis to count AuNP number density. Trace image after the flooding process **a**) without prior processing, **b**) after the 2nd order process and **c**) after the flattening process. Crosses (+) mark the automatically counted AuNP. Two (or more) close nanoparticles were sometimes counted as one (circled) and had to be manually counted as two.

The crosses (+) show the centres of the hills (Fig 5.13c). In some instances, when two or more AuNPs were close together, the software failed to distinguish between individual particles (circled). When this occurred it was necessary to manually correct the data.

Problems with AFM scanning are described in Appendix V.

5.2.3.2 X-ray Photon Spectroscopy

An outline of the XPS technique is given in Section 5.1.3.5. X–ray photoelectron spectra were measured on a Kratos Axis Ultra DLD spectrometer (Kratos Analytical of Shimadzu, Kyoto, Japan) (Fig. 5.14) using a monochromatic AlK_{α} X-ray source (75 – 150 W) with an analyser pass energy of 160 eV (survey scans) or 40 eV (detailed scans). Photoelectrons were detected in a direction normal to the surface (i.e. 90° grazing angle). Surfaces were mounted using double-sided adhesive tape. Each XPS file contained a spectrum of photon energy (BE) vs counts per second, for each element on a particular surface along with a 'survey' of all the elements. The data was analysed using Casa XPS and ESCA.

Casa XPS was used to analyse the XPS spectra for a given surface treatment. Element peaks for each survey were identified (N.B. the electron configuration of the photon being detected is written to the right of the element, e.g. C1s). Each peak was then calibrated to the main C1s peak (at a constant BE of 284.7 eV) to account for variance. This peak was always present as C-C / C-H hydrocarbon contamination (Seitz et al. 2003). Curve fitting was used to estimate the percentage of the element that was present in a particular chemical state (e.g. APS nitrogen was basic (NH_2) or quaternary (NH_3^+)). Each curve was manually fitted with one or more peaks after defining a background (linear or Shirley), automatically adjusted by Casa XPS to a best-fit. The percentage of each peak and the BEs for each peak were given. A montage of the survey spectrum and each element for the different surface treatments was produced for visual comparison.

ESCA was used to accurately quantitate the data, by calculating elemental peak areas. Using MS-Excel the peak area of a particular element was divided by a specific sensitivity factor for that element, to obtain the relative molar composition. Wagner factors (Wagner 1981 and 1990 in [www] Walker and Morton 1998) were adjusted for the machine used (Kratos factors, Table 5.5). The total molar composition was then added up for each spectrum, and the molar percentage composition (mol%) of each element was calculated.

Table 5.5 XPS correction factors for a selection of elements.

Element	Electron configuration	Kratos correction
C	1s	0.28
N	1s	0.48
O	1s	0.78
Si	2p	0.33
Cl	2p	
Cl	2s	
Au	4f	6.25
Au	4d (5/2)	

The mol% of the background element, silicon (Si) was divided by that of another element (e.g. Si/N) to give a molar ratio. Other ratios were also calculated (e.g. C/O, C/N, Au/N).

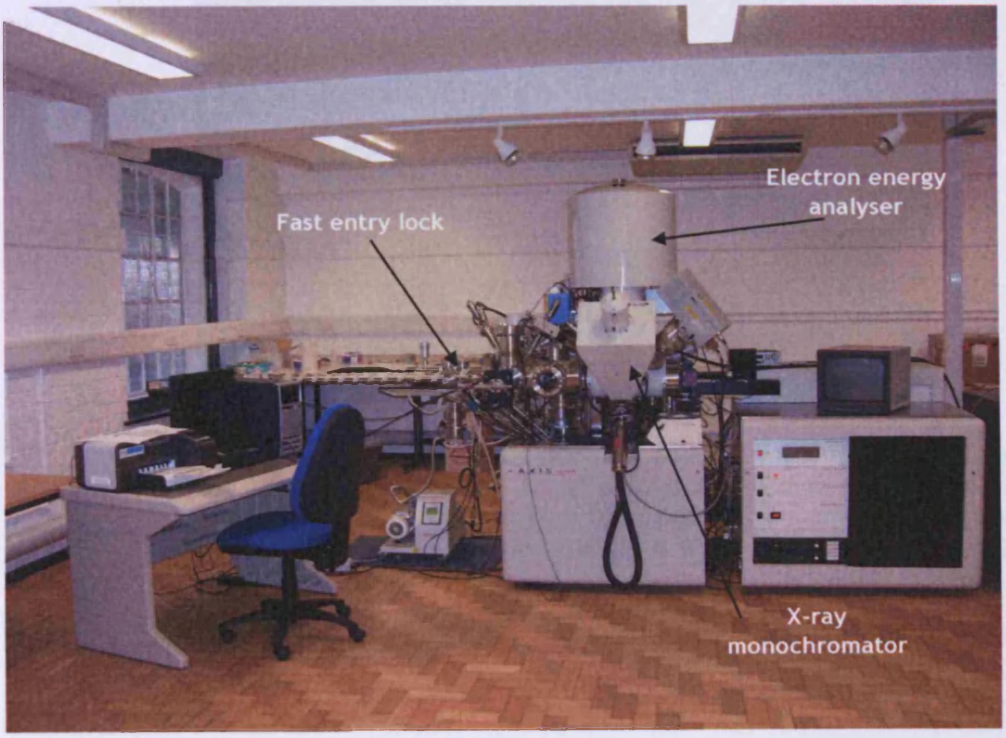


Fig. 5.14. Kratos Axis Ultra DLD x-ray photoelectron spectrometer

5.2.3.3 Contact angle measurements

An outline of the contact angle technique is given in Section 5.1.3.2. Contact angles were measured using the equipment set up illustrated in Fig. 5.15. The silicon surfaces were positioned on an adjustable stand and an Eppendorf pipette was clamped above. A 1µl drop of dH_2O was suspended above the surface from the pipette, and the surface gradually moved upward onto the droplet (Fig. 5.16). Images were obtained and analysed using a Sony DFW-X710 firewire camera (Sony Coorporation, Tokyo, Japan) and Labview 8.0 (http://www.ni.com/labview/) images were captured immediately after the dH_2O droplet was released from the pipette (Fig 5.17). Contact angles were measured between the horizontal and tangent arrows.



Fig. 5.15 Experimental set-up used for contact angle measurements. The silicon surfaces were placed on an adjustable stand to move them up onto the suspended dH_2O droplet from the pipette. The camera focus was kept constant and images were set against a white background for imaging in Labview 8.0.

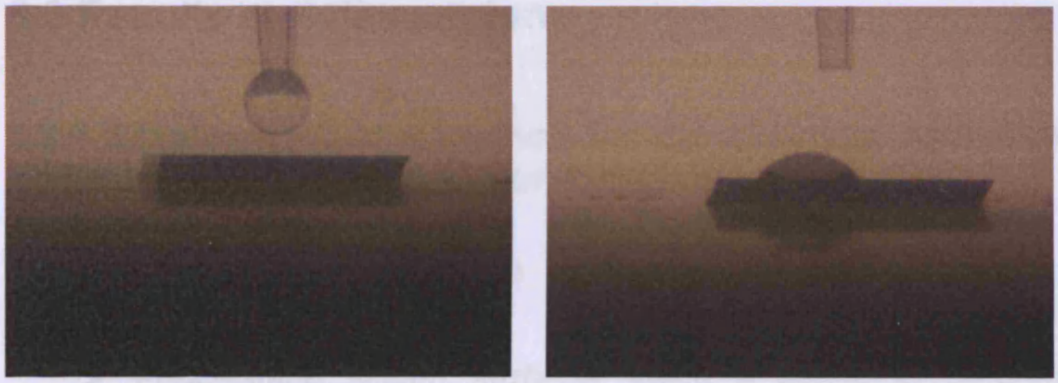


Fig. 5.16 Technique used to obtain contact angle measurements. A dH_2O droplet **a**) suspended from a pipette over a silicon surface and **b**) spread on the surface.

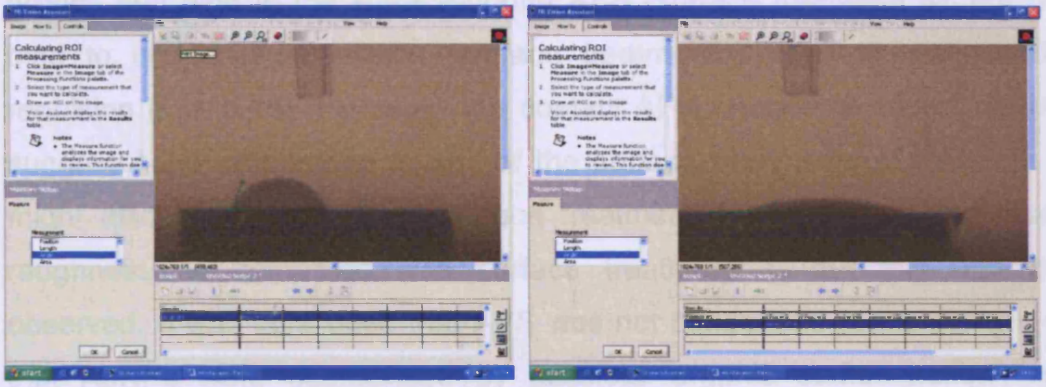


Fig. 5.17 Contact angle measurements on silicon surfaces with different hydrophilicities. Contact angles were viewed using Labview 8.0 software, and measured between the horizontal and tangent arrows.

5.3 Results and discussion

5.3.1 Development of a method for the cleaning, activation and silanisation of silicon surfaces

5.3.1.1 Solution-phase silanisation

a. Pre-cleaning silicon surfaces using a series of different solvents

It was expected that AuNPs would be electrostatically attracted to NH_3^+ groups and bind to the surface-bound APS (surface treatment 4), but not bind to underivatised silicon (surface treatment 2) due to electrostatic repulsion (Fig. 5.18). However, the contact AFM images of 10μm^2 did not suggest AuNP adherence to any of the surface treatments (Table 5.1). It might also be expected that surface treatment 3 would show increased roughness as compared with surface treatment 1, but this was not observed. It was concluded that APS was not condensed at the surface or that AuNPs were destabilised by possible 'organic contamination', not removed by the pre-cleaning solvents (however the surfaces were visibly cleaner). In future experiments, PNA solution was used to remove organic contamination and ensure activation of the surfaces for APS binding (Birch 2000). It is likely that imaging with contact-mode AFM was the real problem (see d).

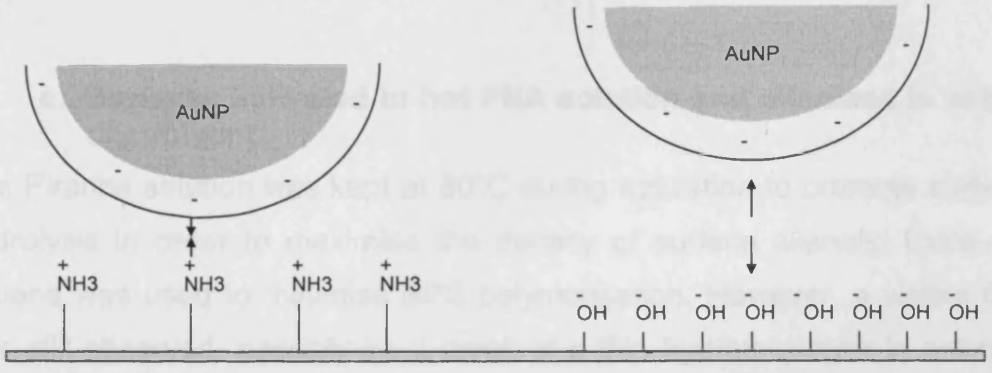


Fig. 5.18 The interaction of AuNPs with APS-derivatised (left) and underivatised (right) silicon surfaces (after pre-cleaning and activation steps).

b. Surfaces activated in piranha solution prior to silanisation

A visible film was observed on the APS-treated surfaces. This probably arose due to a range of solution and surface silanol condensation reactions

resulting in a 'thick' multilayered network of physi/chemisorbed polysilanes. (Tredgold 1994 in Moon et al. 1996). The film was visibly removed by sonication to prevent physisorbed silane from potentially interfering with AuNP binding (Vrancken et al. 1993).

Contact AFM images of 10μm^2 gave the same result as Section 5.3.1.2a for surface treatments 1-6 (Table 5.2). It is likely that PNA treatment resulted in surface activation; therefore, other reasons for lack of AuNP adherence were investigated. One conclusion was that solution-phase silane polymerisation occurred more rapidly than had surface condensation. This resulted in the complete loss of surface APS on sonication. Alternatively, it is possible that APS *did* condense with the surface but the resolution of the AFM images was insufficient to show the bound AuNPs (in future experiments it was decided to use smaller scan sizes (1μm^2)). Another possible conclusion was that the AuNP solutions were too dilute (1/100-1/1000) for surface treatment 4, and AuNP binding was highly dispersed (if at all). Future experiments used a 1/10 (aq) dilution.

XPS did not show the presence of gold but nitrogen was present on all of the surfaces (Surface treatments 1-6). This was surprising and suggests that for treatments 1 and 3 significant contamination was present. This also made it impossible to conclude that APS was present for treatments 2 and 4-6.

c. Surfaces activated in hot PNA solution and silanised in extra-dry solvent

The Piranha solution was kept at 80°C during activation to promote surface hydrolysis in order to maximise the density of surface silanols. Extra-dry toluene was used to minimise APS polymerisation. However, a visible film was still observed, possibly as a result of a thin hydrating layer in solution (Hooper et al. 2001). The percentage volume of APS in toluene (5% v/v) may have been too high, leading to self-condensation and network formation. Contact-mode AFM scans (1μm^2) of the surfaces were quite dirty/ streaky and gave the same result as Section 5.3.1.2a for surface treatments 1-4 (Table 5.1).

d. An optimised method for surface pre-cleaning, activation and solution-phase silanisation

The surfaces were pre-cleaned before PNA activation to reduce surface contamination and ensure an even etch (Birch 2000). Agitation of the surfaces during silanisation reduced 'visible' film formation (Sections 5.3.1.2a-c). After silanisation the surfaces were not sonicated. (Section 5.3.1.2c). However, during surface incubation in AuNP solution, the latter changed from red, to purple in colour. Loosely adsorbed, positively charged APS molecules may have desorbed and interfered with the negative citrate ions stabilising the AuNPs (Seitz et al. 2003).

Contact-mode AFM 3D and trace images of the silicon surfaces after different treatments are shown in Fig 5.19. Surface treatment 1 was completely flat as would be expected due to repulsion of the AuNP by an underivatised surface (Fig. 5.19a). Surface treatments 3 and 4 both showed cube-like features on the surface (Fig. 5.19b and c). A 1μm profile of the surface treatment 4 (Fig. 5.20a) shows a cross-section of a cube-like structure, having dimensions much larger than AuNPs. These probably correspond to loose material (silane layers and AuNP) being pushed along by the tip as it tracked the surface (Grabar et al. 1997). It was concluded that contact-mode AFM was exerting too much tip-sample force on the polysilane / AuNPs surface and tapping-mode AFM was used in future experiments.

Tapping-mode AFM was used as a less invasive approach than contact-mode for imaging soft or delicate samples. Tapping-mode AFM 3D and trace images of surface treatment 4 are shown in Fig 5.21 (surface treatments 1-3 were not scanned). The scan appears to show more detailed features compared to the contact-mode scan of surface treatment 4 (Fig. 5.19c). A 1μm length profile of surface treatment 4 (Fig. 5.20b) shows the unevenness of the surface, although some features (~10nm in height) were visible which may correspond to AuNPs. It is likely that the irregular base layer resulted due to uncontrolled solution-phase silanisation and polysilane networks (Section 5.3.1.1b). The larger features (Fig. 5.21) may correspond

to aggregated AuNPs, destabilised due to interaction with desorbed silane molecules. XPS experiments were also carried out and this data is presented in Section 5.3.1.2a.

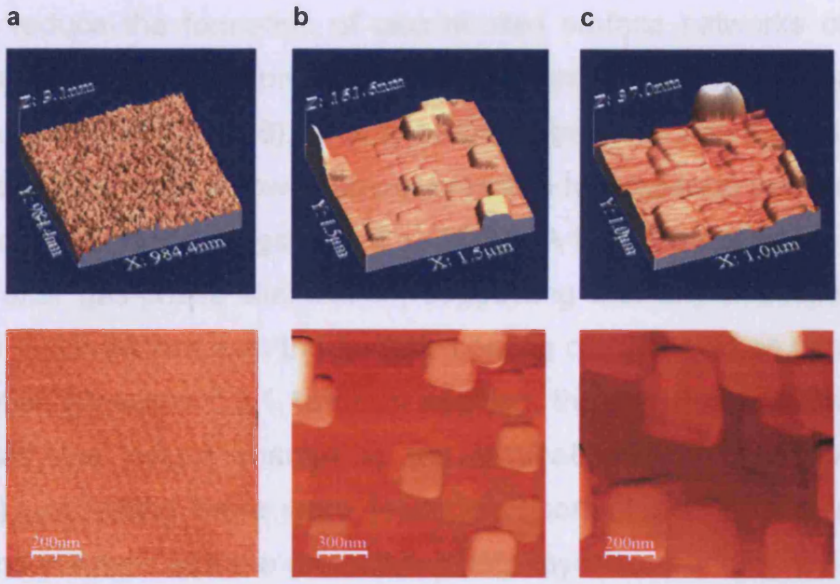


Fig. 5.19 Contact-mode AFM images of surfaces from solution-phase silanisation experiments. 3D (top) and trace (bottom) AFM images of surface treatments **a**) 1, **b**) 3 and **c**) 4 (Table 5.1) were obtained in WSXM. Surface treatments 3 and 4 were silanised in 1% APS in toluene. Scan size= 1µm^2.

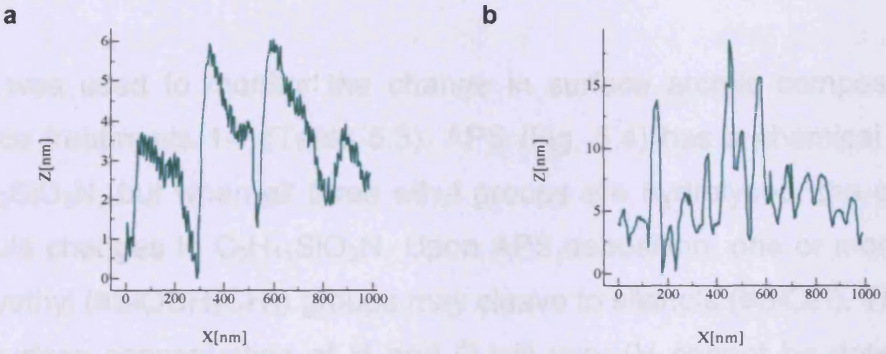


Fig. 5.20 AFM profiles of surfaces from solution-phase silanisation experiments. Profiles of surface treatment 4 (Table 5.1) were obtained using WSXM for **a**) contact-mode and **b**) tapping-mode AFM scans (1µm^2). Surface 4 was silanised in 1% APS in toluene. Scan size= 1µm^2.

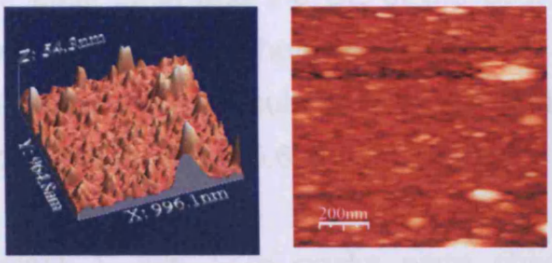


Fig. 5.21 Tapping-mode AFM scans of surfaces from solution-phase silanisation experiments. A 3D image (left) and trace image (right) of surface treatment 4 (Table 5.1) is shown. Scan size= 1µm^2. Surface 4 was silanised in 1% APS in toluene. Scan size= 1µm^2.

5.3.1.2 Gas-phase silanisation

a. Evaporation of silane from a Petri dish lid

The change from solution-phase silanisation to gas-phase silanisation aimed to reduce the formation of uncontrolled surface networks of APS. Gas-phase silanisation has previously been shown to improve the control of APS deposition (Haller 1978). This is probably because aggregated silane molecules would have too low a vapour pressure to evaporate and therefore deposit on the surfaces (Sugimara et al. 2002). A film was not visible on the surfaces after gas-phase silanisation, suggesting that any deposited APS layer was much thinner than the surface coating observed when depositing from solution (Sections 5.3.1.1b-d). In addition, the AuNP solution was not destabilised (no colour change in the incubating AuNP solution was observed) suggesting there were fewer physisorbed silane molecules to desorb and interfere with the protective citrate layer surrounding the AuNP. The low level of silanisation using gas-phase deposition is consistent with XPS data. Contact-mode AFM was used to image the surfaces, but as described in Section 5.3.1.1d this was invasive and lead to poor images.

XPS was used to monitor the change in surface atomic composition for surface treatments 1-7 (Table 5.3). APS (Fig. 5.4) has a chemical formula $C_9H_{23}SiO_3N$, but when all three ethyl groups are hydrolysed, the chemical formula changes to $C_3H_{11}SiO_3N$. Upon APS deposition, one or more of the siloxyethyl ($\equiv SiOCH_2CH_3$) groups may cleave to silanols ($\equiv SiOH$). Therefore the surface concentration of H and O will vary (H cannot be detected by XPS). Montages of the surveys and detailed spectra of each element for surface treatments 1-7 are shown in Fig. 5.22 (from bottom to top). The percentage area of each peak and the BE of the peaks were calculated after curve fitting using Casa XPS. The average BEs are quoted in the text. The mol% of each element was calculated in ESCA and used to calculate molar ratios for each surface (Table 5.6 and Fig. 5.23).

For surface treatment 1, two Si2p peaks were observed (98.82 and 102.76eV) corresponding to elemental silicon (SiE) and silicon oxide (SiO) respectively (Cant et al. 2003). Molar ratios of SiE/SiO were expected to

approach zero if the surface comprised SiO only (formula = repeating units of SiO_2). For underivatised wafers, the ratio was much higher (2.77) due to bulk SiE contribution (Table 5.6). The survey also shows O1s (532.28, corresponding to SiO_2 (Hooper et al. 2001)) and C1s (main peak 284.7eV, used to calibrate the spectra) peaks for surface treatment 1. Carbon contamination (284.7eV, corresponding to C-H/ C-C bonds) is often seen for surfaces prepared in air (Seitz et al. 2003). Contamination on APS surfaces is usually identified with a C/N molar ratio > 3 (Seitz et al. 2003) which was true for all the surfaces (Table 5.6). N1s (400.53eV, Fig. 5.24 (i)) and Au4f peaks (83.43 and 87.09eV, Fig. 5.3.7) were observed on surface treatment 1, due to contamination and non-specific AuNP binding respectively, but these were negligible.

All surfaces silanised with APS (surface treatments 2-7) showed a broad N1s curve (399-402eV) which was more prominent than that observed for surface treatment 1. This suggested that APS deposition had been successful (Fig. 5.22).

For surface treatments 2-5, the SiE/SiO ratio was ~ 2.0-2.4, suggesting SiE contribution. For surfaces 6 and 7, the Si curve was almost entirely SiO (the SiE/SiO ratio was ~0 (Table 5.6, Fig. 5.22), a silicon satellite peak (~116eV) was not visible (compared to surfaces 1-5) and the O1s signal was apparently reduced (Fig 5.22). X-ray surface penetration is dependent on the grazing angle of the x-ray beam (which was 90°). In this case, sampling depth was ~3-5nm; however most photons were detected 1-2nm from the surface. The actual value is dependent on elemental composition and structure (Albert). SiE and O1s peaks were attenuated (i.e. reduced in amplitude, Seitz et al 2003) probably due to a thick APS film deposited after solution-phase silanisation (Cant et al. 2003; Diegoli et al. 2006; Sugimara et al. 2002). Surface treatments 6 and 7 also showed much larger SiO, C1s and N1s peaks compared to surface treatments. Importantly Figure 5.23b (iv) shows little change in SiO signal for surface treatments 2 and 4 after gas-phase silanisation. It might be expected that the addition of APS to the surface would increase SiO (Figure 5.a treatments 2 and 4). However, the diluting contribution of other APS atoms (C, N), and their additional

attenuating effect, results in there being little change in the SiO signal. Greater attenuation was observed for SiE when APS exposure was increased from 10 mins (surface treatment 2) to 60 mins (surface treatment 4). As previously discussed, a much greater attenuating effect was observed for solution-phase silanisation (surface treatment 6). This directly indicated that solution-phase silanisation resulted in a much thicker APS surface layer than did gas-phase silanisation (without a sonication step) (Fig. 5.22).

Only surfaces that were incubated in AuNP solution (surface treatments 1, 3, 5 and 7) had additional Au4f peaks (83.43 and 87.09eV) (Fig. 5.22). This was comparable to published values (centred at 84eV, Seitz et al. 2003). Calculating molar ratios was complicated for surfaces derivatised with AuNP (10nm), due to attenuation of the background surface elements (Si2p, C1s and N1s) (previously reported for 40nm AuNP, Seitz et al. 2003). Surface treatment 7 had a smaller Au4f peak than the gas-phase silanised wafers (surface treatments 3 and 5). This may be due to the restricted number of free amine groups (on the film network surface) required for electrostatic binding (Fig. 5.22). Surface treatment 3 had a higher absolute Au4f signal than surface treatment 5. Although the N/Au molar ratio was lower for surface treatment 5, this may be the result of attenuation of the N1s signal by the AuNP, rather than an indication of a real increase in surface gold.

Si/N ratios were higher for surfaces 3, 5 and 7 than 2, 4 and 6 (Fig. 5.23). It might be expected that N1s and Si2p signals would both be attenuated by AuNP and the SiE more so, as it resides below the 1:1 N1s:SiO APS layer. Therefore Si/N would be expected to decrease with AuNP binding. The increase that was observed can be explained by considering the mol% compositions (Table 5.6). The surface treatment pairs 2 and 3, 4 and 5, and 6 and 7 all show decreasing N1s and Si2p signals upon AuNP binding. However, decrease of the N1s signal is greater; therefore the Si/N ratio appears to increase. There are two possible reasons for this. Firstly, the nitrogen containing layer could have been removed during the extended AuNP incubation/washing process. Secondly, the N1s signal could have been attenuated more than Si2p by the presence of the AuNPs. Figure

5.23b shows (ii) Si2p, (iii) SiE and (iv) SiO mol% compositions for each surface treatment. SiE was observed to decrease following silanisation and following AuNP binding. Since SiE concentration must remain constant, the observed decrease must have been due to attenuation. This attenuation was responsible for the observed decrease in the Si2p signal. Figure 5.23b (iv) also shows attenuation of SiO by AuNP binding and/or APS removal, for surface treatments 5 and 7

A montage of N1s curve fits was produced for the APS-derivatised (Fig 5.24 b (i)) and APS and gold-derivatised surfaces (Fig 5.24 c (i)). For surface treatments 2-5, two N1s peaks were fittted at 400 and 401eV, most likely corresponding to RNH_2 and RNH_3^+ respectively (Seitz et al. 2003; Sugimara et al. 2002; Hooper et al. 2001; Diegoli et al. 2006). Surface treatments 4 and 5 had an increased percentage of RNH_3^+ groups (70.76 and 48.91 respectively) compared to surface treatments 2 and 3 (35.01 and 30.48 respectively). This may reflect an increase in APS deposition between 10 and 60 minutes gas-phase silanisation, as the NH_3^+ peak also predominated for surface treatments 6 and 7 (with a thick APS film). IR studies have previously shown the % of NH_3^+ to increase upon film formation (Hooper et al. 2001). For surface treatment 6, two extra, small peaks were fitted at 399.00 and 406.62eV. For surface treatment 7, one extra peak was fitted, at 406.61eV. The latter was not formally identified but such high BEs usually correspond to nitrates (possibly formed within the APS film network) (Moulder et al 1995; Martin et al. 2007). The 399eV peak may be present at low levels in the N1s curves of other surface treatments. These may correspond to other NH_2 environments (e.g. H-bonded, likely for APS networks, Sugimara et al. 2002). Alternatively this may be an artefact of the curve-fitting process. AuNP incubation appeared to reduce the percentage of the NH_3^+ peak in each different silanisation method (Table 5.6). This may due to redistribution of the positive charge, giving rise to a different species, upon AuNP binding.

Three C1s peaks were fitted for surface treatment 1 with BEs of 284.7eV (contamination and other C-C/ C-H bonds), 286.2eV and 288.93eV (Fig. 5.24 a (ii)). The same three curves were fitted for all other surface treatment

(2-7) (Fig 5.24 b (ii) and c (ii)) with the 284.7 peak predominating for each. C1s peaks above 285eV usually correspond to 'functionalised' carbon (e.g. C-O, C-N, C=O, Seitz et al. 2003). APS would be expected to contribute to the C-C and C-H signal, but only uncleaved APS (containing siloxyethyl ($\equiv SiOCH_2CH_3$) groups) could have contributed to the increase in C1s peak areas >285eV. This was especially noticeable for surface 6, having a thick APS layer (Fig. 5.22). AuNPs were stabilised by citrate molecules (chemical formula $C_6O_7H_5$) and contributed to C1s and O1s signals as well as Au4f. Of the carbon atoms on citrate, there are three C=O, three C-O, five C-C and four C-H carbons (Fig. 5.7), which probably contributed to C1s signals >285eV.

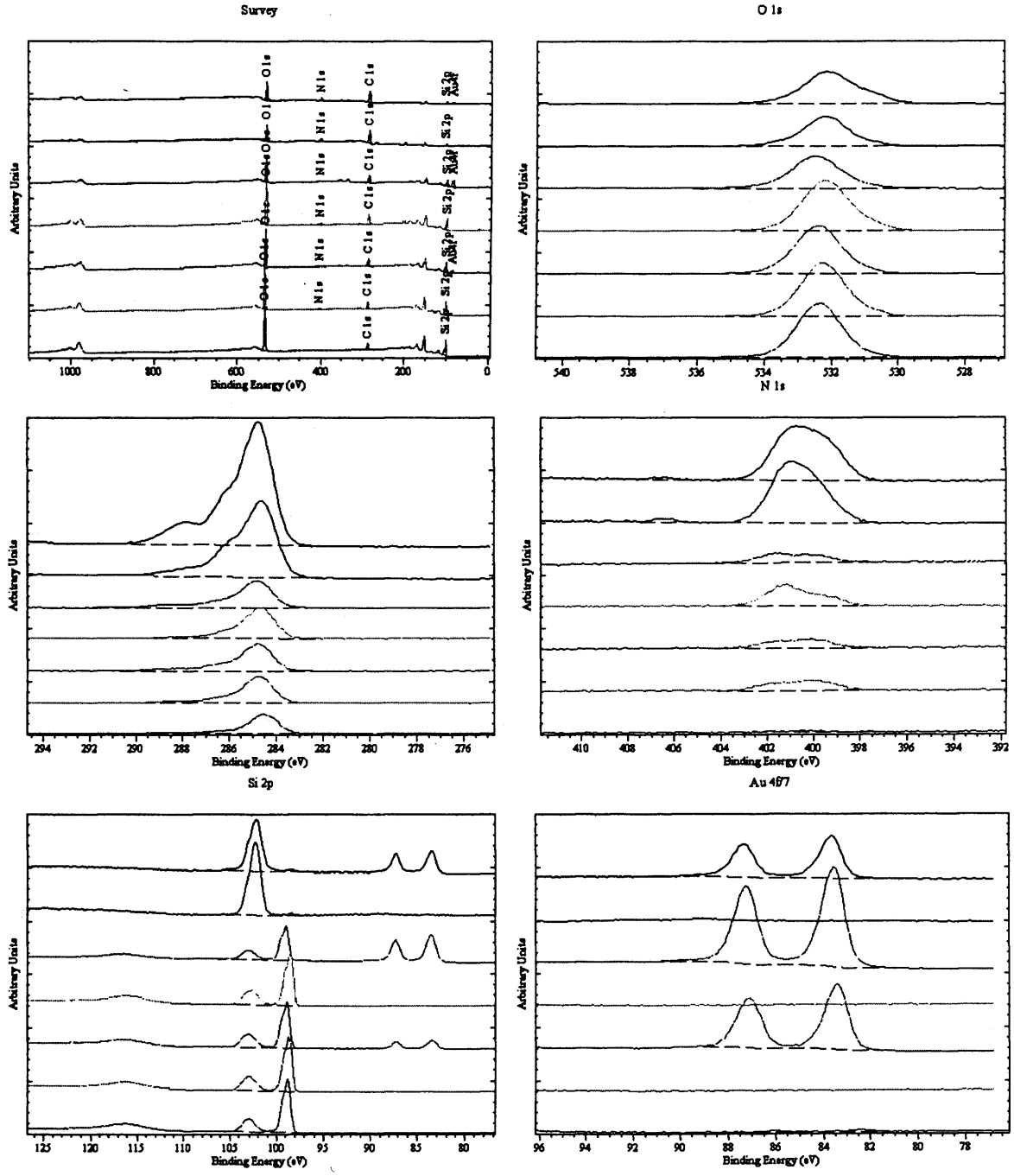


Fig. 5.22 XPS spectra of surfaces from gas-phase and solution-phase silanisation experiments. Montages of each element were created in CASA XPS for surface treatments 1-7 (**Table 5.3**) in the order: bottom-top.

Table 5.6 XPS surface atomic composition data for gas-phase and solution-phase silanisation experiments. Tables **a**) (i) mol% of whole curves and (ii) mol% of individual peaks and **b**) mol ratios of surface treatments 1-7 (Table 5.3) are shown, as calculated in ESCA.

a (i)

	Molar % Composition				
Surface treatment	**N1s**	**O1s**	**C1s**	**Si2p**	**Au4f**
1	0.23	33.85	13.62	36.39	0.01
2	1.19	32.82	18.81	31.73	0.00
3	1.04	32.43	21.58	29.30	0.40
4	2.10	32.57	22.15	28.07	0.00
5	1.73	29.83	27.36	24.68	1.55
6	7.08	21.27	51.21	7.70	0.00
7	6.03	23.83	50.27	6.89	0.18

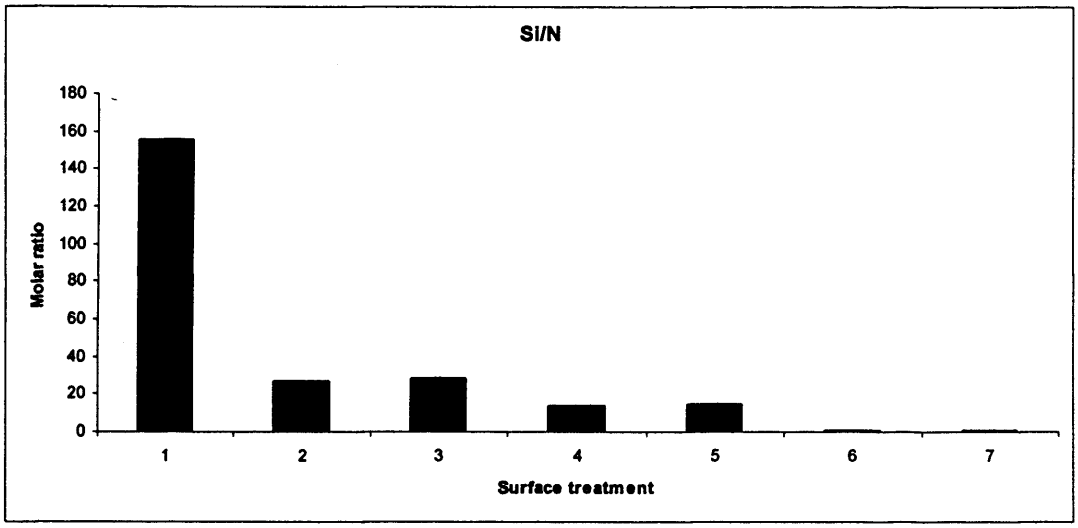
(ii)

	Molar % composition					
Surface treatment	**SiE (99eV)**	**SiO (103eV)**	**NH_2 (400eV)**	**NH_3^+ (401eV)**	**C (284.7eV)**	**C (>284.7eV)**
1	26.74	9.65	0.23	0.00	9.62	3.99
2	22.40	9.33	0.77	0.42	12.89	5.91
3	20.15	9.15	0.73	0.32	13.21	8.37
4	18.89	9.18	0.61	1.48	16.38	5.77
5	16.88	7.81	0.88	0.85	18.85	8.51
6	0.19	7.52	2.39	4.69	30.94	20.27
7	0.24	6.65	2.69	3.33	29.05	21.23

b

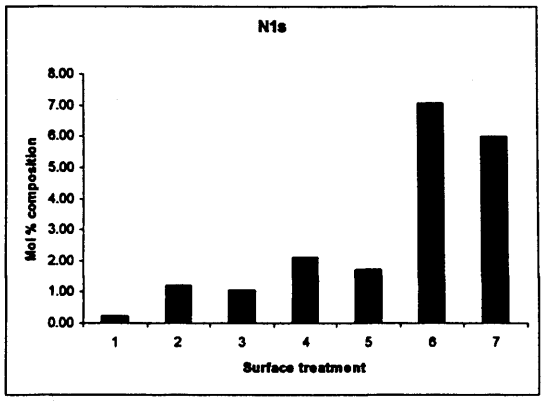
	Molar ratio									
Surface treatment	**Si/N**	**Si/C**	**C/N**	**Si/O**	**C/O**	**N/O**	**Si/Au**	**C/Au**	**N/Au**	**SiE/ SiO**
1	155.52	2:67	58.20	1.07	0.40	0.01			29.68	2.77
2	26.61	1.69	15.77	0.97	0.57	0.04				2.40
3	28.04	1.36	20.65	0.90	0.67	0.03	73.45	54.10	2.62	2.20
4	13.40	1.27	10.57	0.86	0.68	0.06				2.06
5	14.28	0.90	15.83	0.83	0.92	0.06	15.96	17.70	1.12	2.16
6	1.09	0.15	7.23	0.36	2.41	0.33				0.03
7	1.14	0.14	8.34	0.29	2.11	0.25	38.97	284.28	34.09	0.04

a

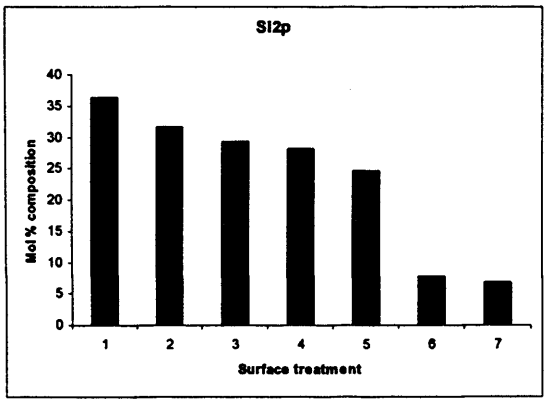


b

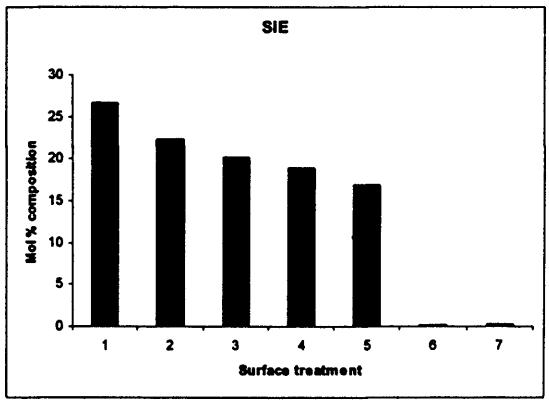
(i)



(ii)



(iii)



(iv)

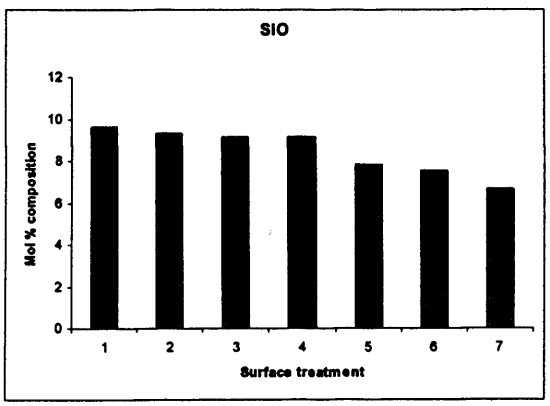


Fig. 5.23 Attenuation of Si2p and N1s XPS surface signals for gas-phase and solution-phase silanisation experiments. AuNPs and polysilane layers attenuated the XPS signal of underlying surface elements. Bar charts show **a**) Si/N molar ratios and **b**) molar % compositions of (i) N1s and (ii) Si2p (iii) SiE and (iv) SiO, for surface treatments 1-7 (Table 5.3).

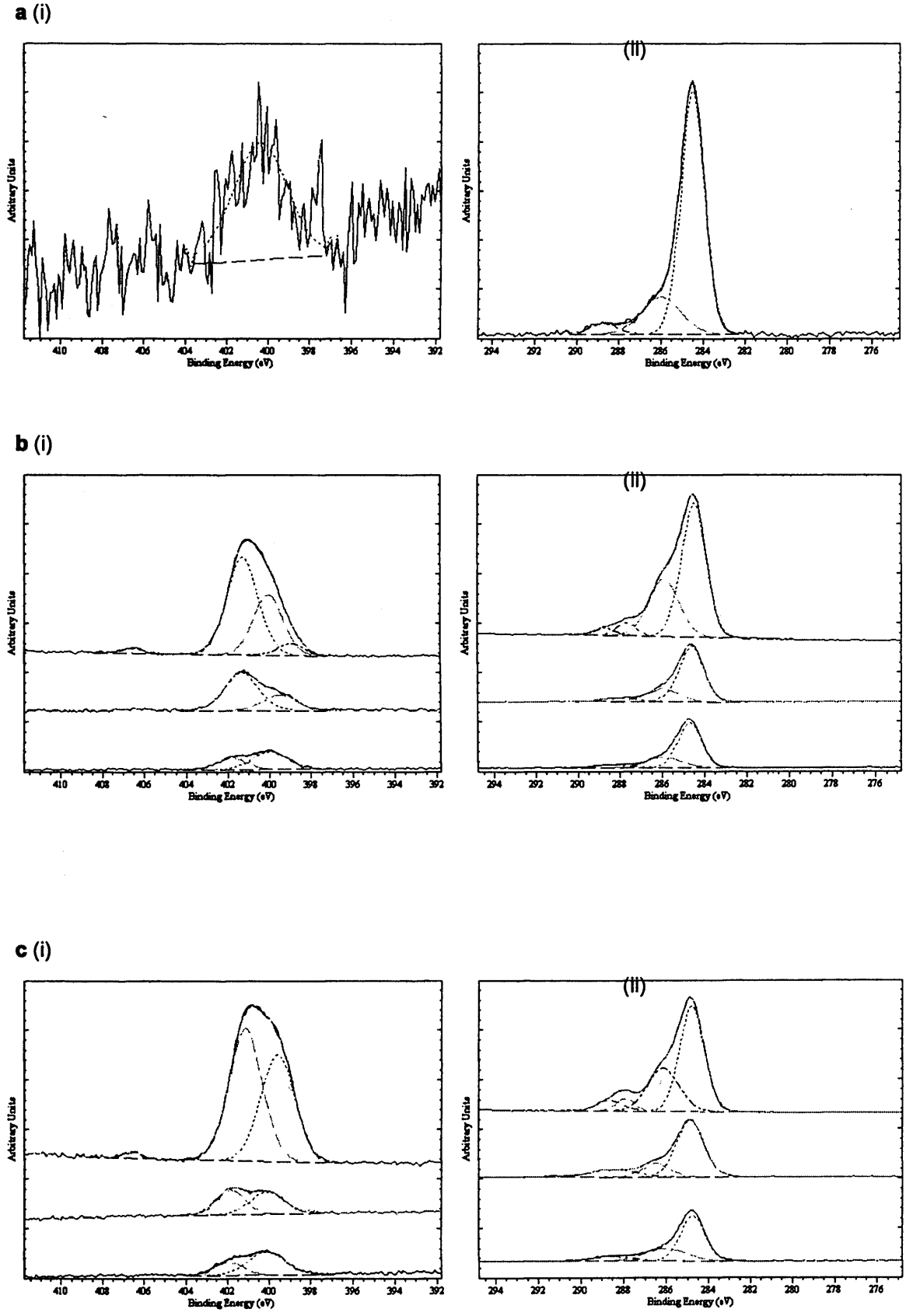


Fig. 5.24 XPS spectra with curve fits for gas-phase and solution-phase silanisation experiments. Curve fits are shown for **a**) wafer treatment 1 (i) N1s and (ii) C1s curves, **b)** surface treatments 2, 4 and 6 (bottom to top) (i) N1s and (ii) C1s curves and **c)** surface treatments 3, 5 and 7 (bottom to top) (i) N1s and (ii) C1s curves. Surface treatments are given in Table 5.3.

b. Evaporation of silane from an Eppendorf tube lid

A smaller container was used for the evaporation of APS to minimise waste. No visible film was observed after silanisation (Section 5.3.2.3a). There was no apparent difference in AuNP density after silanisation with APS for 5, 15 and 25 minutes. Images from the 5 minute evaporation were analysed.

Contact-mode AFM 3D and trace images of surface treatments 3 and 4 are shown in Fig 5.25. The absence of cube-like features in the gas-phase (Fig. 5.25b) suggested that for surface treatment 3, little loose material was moved around by the AFM tip suggesting that less APS had been deposited on the surface than for solution-phase silanisation (Fig. 5.19b). The cube-like features however, were observed for surface treatment 4 (Fig 5.25c) (similar to those observed for the solution-phase surface (Fig 5.19c)). Loose material, probably AuNPs, was being moved around and a 1μm length profile of surface treatment 4 (Fig.5.26a), shows a cross-section of the cube-like structure with a height of ~10nm (c.f. AuNPs) but a width of ~500nm.

Tapping-mode AFM 3D and trace images of surface treatments 1-4 are shown in Fig 5.27. Surface treatment 1 was fairly flat. Surface treatment 3 appeared to be 'dirtier' than the other treatments (Fig. 5.27). This could be due to the positively charged, underivatised amine attracting impurities from air (Siqueria et al. 1999 in Sugimara et al. 2002 (XPS)). Alternatively the large lumps may be APS islands (Chu-jiang et al. 2006), washed away from surface treatment 4 during AuNP incubation. It was apparent that the minimisation of contaminating debris in future experiments would be important. Tapping mode AFM of surface treatment 4 clearly shows the successful deposition of AuNP onto the gas-phase silanised surface (Fig. 5.27d). The well dispersed features are uniform in size and shape, and easily distinguishable from contaminating material. A 1μm length profile of the APS surface treatment 4 (Fig.5.26b (i)) shows a cross-section of the features on a flat surface. The AFM height profile of a single 10nm AuNP (Fig.5.26b (ii)), was more accurate in the vertical dimension (10nm) than the horizontal dimension (40nm). The lateral movement of the tip moving over surface features leads to a phenomenon called tip convolution, where the

tip may not appear to track up and down the sides of the AuNP correctly. This effect is due to the finite tip size and cannot be prevented (Grabar et al. 1997).

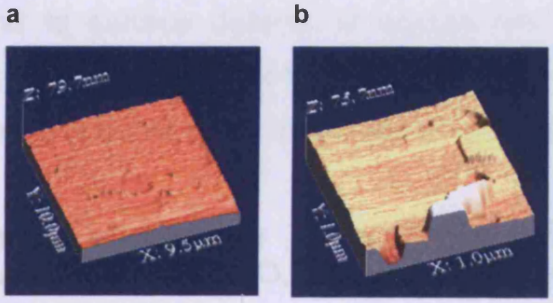


Fig. 5.25 Contact-mode AFM images of surfaces from solution-phase silanisation experiments. 3D AFM images of surface treatments **a**) 3 and **b**) 4 (**Table 5.1**) were obtained in WSXM. Surfaces were silanised with 50% w/w APS in PO, enclosed within a Petri dish. Scan size= 1μm^2. Surface preparation method is given in Section 5.2.2.2a.

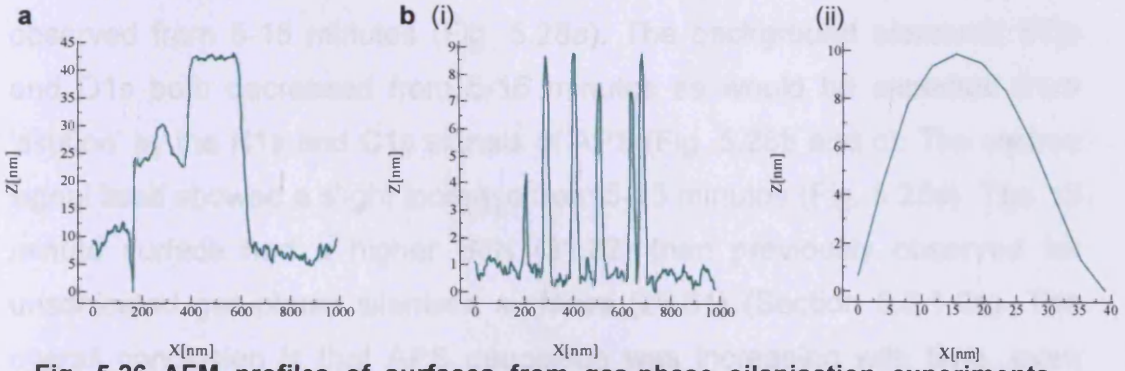


Fig. 5.26 AFM profiles of surfaces from gas-phase silanisation experiments. Profiles of surface treatment 4 (Table 5.1) were obtained using WSXM for **a**) contact-mode and **b**) tapping-mode AFM scans (1μm^2), (i) whole scan length (ii) single AuNP. Surface preparation method is given in **Section 5.2.2.2a.**

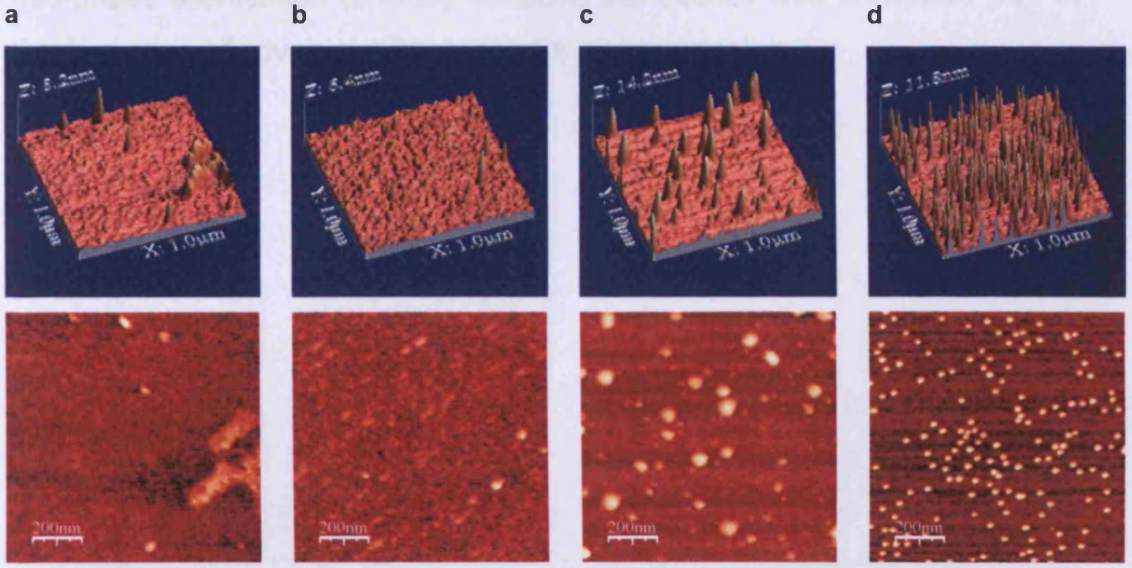


Fig. 5.27 Tapping-mode AFM images of surfaces from gas-phase silanisation experiments. 3D (top) and trace (bottom) AFM images of surface treatments **a**) 1, **b**) 2. **c**) 3 and **d**) 4 (Table 5.1) were obtained in WSXM. Scan size= 1μm^2. Surface preparation method is given in Section 5.2.2.2a.

A few non-specifically bound AuNP were visible on surface treatment 2 (Fig. 5.27b). This surface was underivatised and therefore there would be no electrostatic attraction between the plain silicon and the AuNPs (Fig. 5.18). AuNPs may bind to surface defects or contaminating material. Surface treatment 2 was also much cleaner than surface treatment 3, probably due to the absence of APS which binds impurities (Sugimara et al. 2002).

5.3.1.3 Gas-phase silanisation of surfaces with an increasing exposure time to APS/PO, followed by a sonication step

Section 5.3.1.2a XPS results showed that increasing APS deposition was observed for increasing gas-phase silanisation times (without a sonication step). The N1s signals were quite small relative to the strong O1s, Si2p and C1s signals, nevertheless a subtle increase in N1s mol% composition was observed from 5-15 minutes (Fig. 5.28a). The background elements Si2p and O1s both decreased from 5-15 minutes as would be expected from 'dilution' by the N1s and C1s signals of APS (Fig. 5.28b and c). The carbon signal itself showed a slight increase from 5-15 minutes (Fig. 5.28d). The 10 minute surface had a higher Si/N (31.82) than previously observed for unsonicated gas-phase silanised surfaces (26.61) (Section 5.3.1.2a). The overall conclusion is that APS deposition was increasing with time, even after a sonication step to remove the majority of excess physisorbed APS molecules. Either a monolayer of APS was not fully reached after 5 minutes gas-phase silanisation (unlikely because the excess was sonicated off), or the formation of covalent APS networks was increasing.

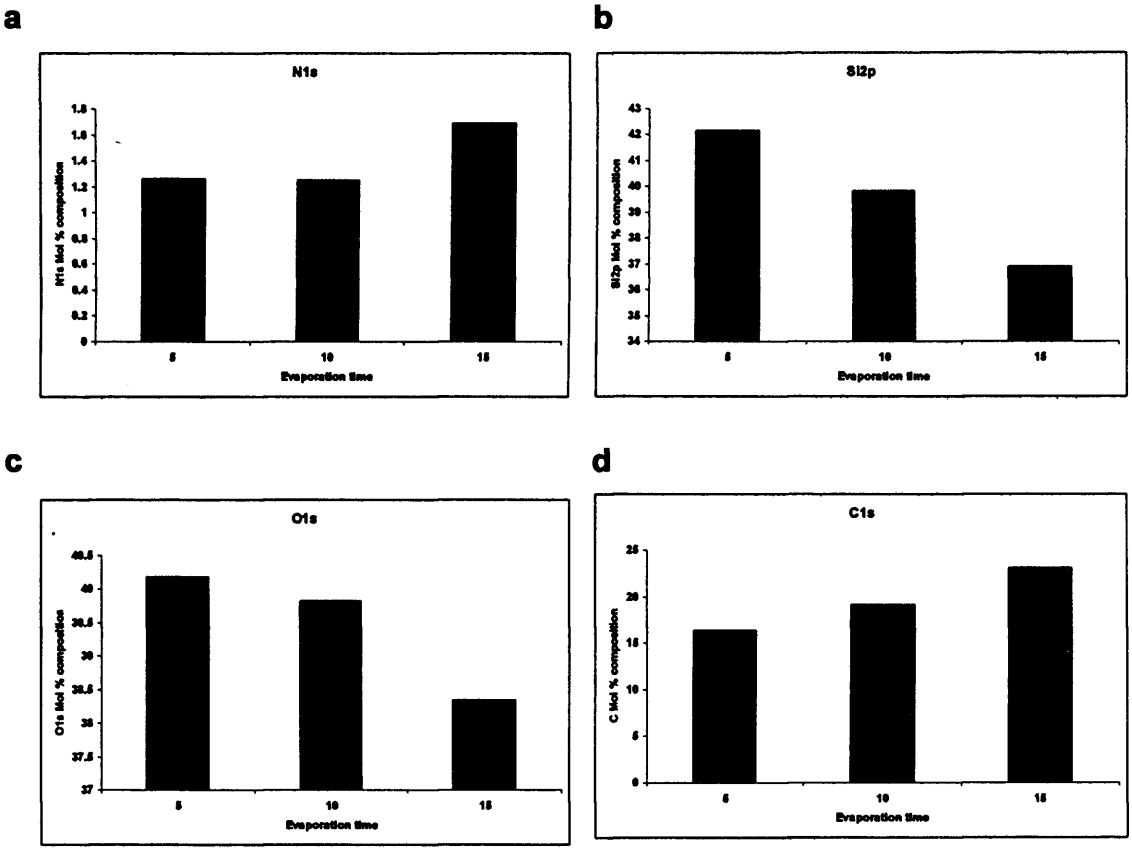


Fig. 5.28 Mol % composition of surface elements for increasing APS silanisation times. a) N1s. **b)** Si2p. **c)** O1s. **d)** C1s.

5.3.1.4 Contact angle measurements

Contact angles for the different surface treatments are shown in Table 5.7 and were used as an indication of surface modification (n=2-3). The untreated surfaces and pre-cleaned surfaces would have had a siloxane structure at the silica surface. The contact angle of surfaces pre-cleaned with acetone and DMF (62°) was not significantly different from the untreated surfaces (64°) (comparable to that previously reported by Sugimara et al. 2002 (60°)). After PNA treatment, the siloxane bonds were broken, forming active silanol groups (Birch 2000). The silanol covered surface was much more hydrophilic (16°), reducing the surface tension of the droplet (comparable to that reported using commercial goniometry: Simon et al. 2002 (16°), Diegoli et al. 2006 (<10°)). Surfaces were stored in air overnight before measuring contact angles, which may have allowed for the conversion of some of the silanols back to siloxane groups (Morrow et al. 1978 in Parida et al. 2006). Incubation and sonication in acetone did not significantly alter the surface contact angle (18°). A large increase in contact angle was observed for APS treated surfaces (54°) (although they were not

as hydrophobic as the untreated surfaces (63°)). After overnight oven-curing of APS-treated surfaces, the contact angle increased to that of untreated surfaces (62°, comparable to that reported using commercial goniometry by Minard-Basquin et al 2005 and Diegoli et al 2006 (57°)). This change may have resulted due to the conversion, at high temperature, of underivatised surface silanol groups back to siloxanes and/or complete condensation of APS. It is likely that solution-phase silanisation resulted in complete surface coverage (Section 5.3.1.1d). The contact angle for this surface was higher (71°) than for any of the other surfaces. This increase in hydrophobicity resulted from the reduction in surface silanol contribution due to the complete surface coverage and also to the resulting complex and unordered APS network. The surfaces were not cured and uncondensed silanols would also contribute to hydrophilicity.

Table 5.7 Contact angles of gas-phase and solution-phase silanised surfaces. Surface treatments are given in Table 5.5.

Surface treatment	Contact angle	n
1	62	3
2	64	3
3	16	3
4	19	2
5	55	3
6	63	2
7	71	3

5.3 Conclusions

Silicon surfaces were successfully activated using PNA solution.

Solution-phase silanisation resulted the formation of a thick visible multilayered APS film, which was removable by sonication. In the absence of sonication, desorption of loosely bound APS may have destabilised the AuNPs. The contact angle was higher than for wafers silanised in the gas-phase.

Contact-mode AFM exerted too much tip-sample force on the polysilane / AuNP surfaces and lead to images with streaks and cube-like structures. Tapping-mode AFM was sufficiently delicate to visualise AuNP binding. AuNPs selectively bound to surfaces silanised with APS, but not to underivatised surfaces. Surfaces silanised in the gas-phase were apparently much flatter than those silanised in solution.

XPS showed N1s and Au4f signals, corresponding to APS and AuNP deposition respectively. The Au4f signal was highest for gas-phase silanisation. Gas-phase silanisation resulted in much less APS deposition than solution-phase silanisation. Attenuation of the background surface element Si2p was observed, upon deposition of thick APS multilayers and AuNPs. The percentage of the NH_3^+ peak (of the N1s curve) decreased upon AuNP binding, probably due to redistribution of the positive charge, giving rise to a different species. Increasing APS deposition was observed with increasing gas-phase silanisation times. This effect was reduced by sonication.

A method for the pre-cleaning, activation and gas-phase silanisation of silicon wafer surfaces with APS was optimised. APS deposition was successfully visualised by AFM (using AuNPs) and XPS.

References

2003. *'3-aminopropyltriethoxysilane'* [WWW]. UNEP Publications. Available at: www.inchem.org/documents/sids/sids/919302 [Accessed: August 2007].

1974. Dyeing reagents for thin layer and paper chromatography. Merck. p. 64.

1999-2007. *Semiconductor ingots* [WWW]. Kemi Silicon Inc. Available at: http://www.kemisilicon.com/ [Accessed: August 2007].

2004. The Veeco Scanning Probe Microscope training handbook. Veeco.

Arroyo-Hernandez, M. et al. 2003. Biofunctionalization of surfaces of nanostructured porous silicon. *Materials Science and Engineering: C* 23(6-8), pp. 697-701.

Bates, S. P. 2000. *Silicon wafer processing* [Online]. Available at: http://www.iisme.org/etp/silicon_wafer_processing.pdf [Accessed: August 2007].

Bhat, R. R. et al. 2002. Fabricating planar nanoparticle assemblies with number density gradients. *Langmuir* 18(15), pp. 5640-5643.

Birch. W. R. 2000. *Coatings: an introduction to the cleaning procedures* [Online]. Available at: http://www.solgel.com/articles/June00/Birch/Cleaning4.htm [Accessed: 18th April 2006].

Brennan, J. D. et al. 1994. Ellipsometry, X-ray photoelectron spectrocopy ans surface plasmon resonance as techniques for the study of chemically modified surfaces. In: Pesek, J.J. and Leigh, I.E. eds. *Chemically modified surfaces.* The Royal Society of Chemistry, p. 73.

Cant, N. E. et al. 2003. Surface functionalisation for the self-assembly of nanoparticle/polymer multilayer films. *Thin Solid Films* 426(1-2), pp. 31-39.

Chaudhury, M. K. and Whitesides, G. M. 1992. How to Make Water Run Uphill. *Science* 256(5063), pp. 1539-1541.

Choi, S.-H. and Zhang Newby, B.-m. 2006. Suppress polystyrene thin film dewetting by modifying substrate surface with aminopropyltriethoxysilane. *Surface Science* 600(6), pp. 1391-1404.

Choi, S. S. et al. 2006. Analysis of force distance curve for biomolecule imaging. *Current Applied Physics* 6(Supplement 1), pp. 247-250.

Chu-jiang, C. et al. 2006. Surface topography and character of gamma-aminopropyltriethoxysilane and dodecyltrimethoxysilane films adsorbed on the silicon dioxide substrate via vapour phase deposition. *Journal of Physics D: Applied Physics* 39, pp. 4829-4837.

Diegoli, S. et al. 2006. pH-dependent gold nanoparticle self-organisation on functionalised Si/SiO_2 surfaces. *Journal of experimental nanoscience* 1(3), pp. 333-353.

Dugas, V. and Chevalier, Y. 2003. Surface hydroxylation and silane grafting on fumed and thermal silica. *Journal of Colloid and Interface Science* 264(2), pp. 354-361.

Etienne, M. and Walcarius, A. 2003. Analytical investigation of the chemical reactivity and stability of aminopropyl-grafted silica in aqueous medium. *Talanta* 59(6), pp. 1173-1188.

Frens, G. 1973. Controlled Nucleation for Regulation of Particle-Size in Monodisperse Gold Suspensions. Modified from Turkevich 1985. In: Kimling, J. et al. 2006. Turkevich method for gold nanoparticle synthesis revisited. *Journal of Physical Chemistry B* 110(32), pp. 15700-15707.

Grabar, K. C. et al. 1996. Two-dimensional arrays of colloidal gold particles: A flexible approach to macroscopic metal surfaces. *Langmuir* 12(10), pp. 2353-2361.

Grabar, K. C. et al. 1997. Nanoscale characterization of gold colloid monolayers: A comparison of four techniques. *Analytical Chemistry* 69(3), pp. 471-477.

Grabar, K. C. et al. 1995. Preparation and Characterization of Au Colloid Monolayers. *Analytical Chemistry* 67(4), pp. 735-743.

Haller, I. 1978. Covalently Attached Organic Monolayers on Semiconductor Surfaces. *Journal of the American Chemical Society* 100(26), pp. 8050-8055.

Hermanson, G. T. et al. 1992. *Immobilised affinity ligand techniques.* Academic Press, Inc., p. 53.

Hooper, A. E. et al. 2001. Evaluation of amine- and amide-terminated self-assembled monolayers as 'Molecular glues' for Au and SiO2 substrates. *Surface and Interface Analysis* 31(9), pp. 809-814.

Horcas, I. et al. 2007. WSXM. *Review of scientific instruments* 78, p. 013705.

Hozumi, A. et al. 2001. Amino-terminated self-assembled monolayer on a SiO2 surface formed by chemical vapor deposition. *Journal of Vacuum Science & Technology a-Vacuum Surfaces and Films* 19(4), pp. 1812-1816.

Jonas, U. et al. 2002. Colloidal assemblies on patterned silane layers. *Proceedings of the National Academy of Sciences of the United States of America* 99(8), pp. 5034-5039.

Kajikawa, Y. et al. 2004. Incubation time during the CVD of Si onto SiO2 from silane. *Chemical Vapor Deposition* 10(3), pp. 128-133.

Kern, W. and Puotinen, D. A. 1970. Cleaning Solutions Based on Hydrogen Peroxide for Use in Silicon Semiconductor Technology. In: Donose, B. C. et al. 2006. Effects of cleaning procedures of silica wafers on their friction characteristics. *Journal of Colloid and Interface Science* 299(1), pp. 233-237.

Kruger, A. A. 1988. *Surface and near-surface chemistry of oxide materials.* In: Junfu, L. et al. 1998. Micro-patterning of 3-aminopropyltrimethoxy-silane self-assembled monolayers with colloidal gold. *Supramolecular Science* 5(5-6), pp. 705-708.

Lin, T.-Y. et al. 2004. Determination of albumin concentration by MIP-QCM sensor. *Biosensors and Bioelectronics* 20(1), pp. 75-81.

Martin, H. J. et al. 2007. XPS study on the use of 3-aminopropyltriethoxysilane to bond chitosan to a titanium surface. *Langmuir* 23(12), pp. 6645-6651.

Minard-Basquin, C. et al. 2005. Gold-nanoparticle-assisted oligonucleotide immobilisation for improved DNA detection. *IEE Proceedings-Nanobiotechnology.* 152(2), pp. 97-103.

Moses, P. R. et al. 1978. Chemically Modified Electrodes .9. X-Ray Photoelectron-Spectroscopy of Alkylamine-Silanes Bound to Metal-Oxide Electrodes. In: Hooper, A. E. et al. 2001. Evaluation of amine- and amide-terminated self-assembled monolayers as 'Molecular glues' for Au and SiO2 substrates. *Surface and Interface Analysis* 31(9), pp. 809-814.

Moulder, J. F. et al. 1995. *Handbook of X-ray photoelectron spectroscopy.* Physical Electronics Inc.

Morrow, B. A. et al. 1978. *J. Phys. Chem.* In: Parida, S. K. et al. 2006. Adsorption of organic molecules on silica surface. *Advances in Colloid and Interface Science* 121(1-3), pp. 77-110.

Nath, N. and Chilkoti, A. 2004. Label-free biosensing by surface plasmon resonance of nanoparticles on glass: Optimization of nanoparticle size. *Analytical Chemistry* 76(18), pp. 5370-5378.

Parida, S. K. et al. 2006. Adsorption of organic molecules on silica surface. *Advances in Colloid and Interface Science* 121(1-3), pp. 77-110.

Park, S. H. et al. 1999. Adsorption kinetics of Au and Ag nanoparticles on functionalized glass surfaces. *Microchemical Journal* 63(1), pp. 71-91.

Shim, H. Y. et al. 2004. Micropatterning of diacetylenic liposomes on glass surfaces. *Materials Science and Engineering: C* 24(1-2), pp. 157-161.

Simon, A. et al. 2002. Study of Two Grafting Methods for Obtaining a 3-Aminopropyltriethoxysilane Monolayer on Silica Surface. *Journal of Colloid and Interface Science* 251(2), pp. 278-283.

Slot, J: W. and Geuze, H. J. 1985. A new method of preparing gold probes for multiple-labeling cytochemistry. *Eur J Cell Biol* 38(1), pp. 87-93. In Sigma product information for gold colloids and gold conjugates (Sigma-Aldrich, St Louis, MO, USA) 2006.

Sorribas, H. et al. 2002. Photolithographic generation of protein micropatterns for neuron culture applications. *Biomaterials* 23(3), pp. 893-900.

Sugimura, H. et al. 2002. Organosilane self-assembled monolayers formed at the vapour/solid interface. *Surface and Interface Analysis* 34(1), pp. 550-554.

Tabe, M. 1984. Uv Ozone Cleaning of Silicon Substrates in Silicon Molecular-Beam Epitaxy. *Applied Physics Letters* 45(10), pp. 1073-1075.

Tredgold, R. H. 1994. *Order in thin organic films.* Cambridge University. IN: Moon, J. H. et al. 1996. Formation of uniform aminosilane thin layers: An imine formation to measure relative surface density of the amine group. *Langmuir* 12(20), pp. 4621-4624.

Vrancken, K. C. et al. 1994. The physisorption and condensation of aminosilanes on silica gel. In: Pesek, J.J. and Leigh, I.E. eds. *Chemically modified surfaces.* The Royal Society of Chemistry, pp. 46-57.

Walker, C. and Morton, S. 1998. *Wagner sensitivity factors* [WWW]. UK surface analysis forum. Available at: http://www.uksaf.org/data/sfactors.html [Accessed: August 2007]. Reproduced from: Wagner, C. D. 1990. In: Wagner et al. 1981. *Surface and interface analysis* 3, p. 211.

Wei, Z. Q. et al. 2000. Study on single-bond interaction between amino-terminated organosilane self-assembled monolayers by atomic force microscopy. *Surface Science* 459(3), pp. 401-412.

Weiringa R. H. 2000. *Chapter 2: The aminosilane coupling layer.* PhD ('Thesis') University of Groningen. [WWW]. Available at: http://dissertations.ub.rug.nl/FILES/faculties/science/2000/r.h.wieringa/c2.pdf [Accessed: 2006]

Zhang, X. G. 2001. *Electrochemistry of silicon and its oxide.* Kluwer Academic, p. 45.

Chapter 6

Controlling APS deposition and the nanoscale patterning of AuNPs on silicon surfaces

6.1 Introduction

This chapter aims to develop an approach for preparing a controlled dispersion of aminopropyltriethoxysilane (APS) surface tethered molecules using an evaporative approach (Bhat et al. 2002). The binding of gold nanoparticles (AuNP) to the amino groups of the immobilised APS molecules was used to evaluate APS surface density. The effect of APS evaporation time and concentration and the concentration of AuNPs on *apparent* APS 'number density' gradients were systematically evaluated. Further investigations included the kinetics of AuNP binding and the stability of the APS layer.

6.1.1 Patterning of flat surfaces at the nanometer scale

Fabrication and manipulation of nano-sized features is a relatively new science, and is desirable for a number of applications in the electronics, materials and biotechnology industries (Rao and Cheetham 2001). Methods such as microcontact printing and photolithography are restricted to surface patterning at the micrometer scale (Section 1.3). While this is useful for many applications, controlling the position of single atoms and molecules at the nanometer scale is now also possible.

6.1.1.1 Scanning tunnelling microscopy

Scanning probe microscopy techniques have been used for such nano-patterning. A scanning tunnelling microscopy (STM) tip has been used to manipulate single atoms of xenon on a nickel surface (Eigler and Schweizer 1990 in [www] Moriarty 2006). In another study, fullerine molecules were pushed along a silicon wafer surface by a STM tip to create nanowires and arrays (Moriarty et al. 1998 in [www] Moriarty 2006). Lithography (Section 1.3) has also been demonstrated on the nanoscale using STM. A reactive surface (e.g. silicon wafer) was coated with an atomic layer of hydrogen which was then removed from pre-defined areas, using low energy electrons emitted from an STM tip (hydrogen depassivation, Shen et al. 1995 in [www] Moriarty 2006). This allows molecules to selectively bind to the exposed silicon, having a minimum line width of ~2nm ([www] Moriarty

2006). The technology to pattern single, stand-alone silanes and other small molecular weight molecules (<1nm) is yet to be developed. High-resolution transmission electron microscopy and STM are the only techniques currently able to image down to the atomic scale, but these techniques can be difficult and require lengthy sample preparation.

6.1.1.2 Patterning of AuNPs on flat surfaces

An extensive review of nanoparticle arrays was published by Shipway et al (2000). Since then, a number of methods have been developed for patterning nanoparticles on flat surfaces.

- **Atomic force microscope nanolithography**

Ordered arrays of single AuNPs have been demonstrated using an atomic force microscope (AFM) nanolithography technique (Li et al. 2003). In a process called anodic oxidation, areas of octadecyltrichlorosilane (ODS, ~70nm diameter) were removed from a silicon wafer using a programmed voltage pulse from an AFM tip. Remaining areas of bare, activated silicon were filled with APS. AuNPs selectively bound to the silanised oxide dots, although the efficiency was low (Fig. 6.1). A modified method has since been developed to improve the AuNP assembly on larger quantum dots, although in this case it was observed that several AuNPs bound to each dot (Liu et al. 2004). An alternative approach has since been developed using edge-spreading lithography to form single AuNP arrays on a mixed self-assembled monolayer (SAM) on a gold substrate (Zin et al 2006).

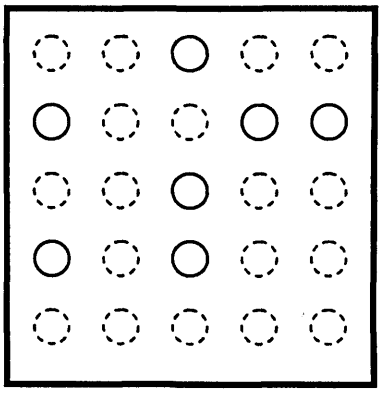


Fig. 6.1 Representation of an ordered array of single AuNPs developed using AFM nanolithography. The image depicts an AFM scan from Li et al (2003). Anodic oxidation of an ODS layer to give ordered quantum dots was followed by APS derivatisation of the dots and AuNP binding. Solid lines represent quantum dots with adsorbed AuNPs. The dashed lines represent 'empty' quantum dots.

- **Mixed SAMs**

A random distribution of APS clusters (microns wide) was formed from a mixed SAM with (2-cyanoethyl)triethoxysilane (Wayment and Harris 2006). Bottom-up surface chemistry was used to label the amine clusters with AuNP-labelled streptavidin.

- **Gravure printing**

Highly ordered arrays of single AuNPs on underivatised silicon have been achieved using gravure printing. Patterned nano-indentations on a polydimethylsiloxane surface are filled with single AuNP, by dragging the meniscus of an AuNP solution over the surface. The AuNPs are then transferred to the desired surface (e.g. silicon) creating a highly ordered and controlled pattern (Kraus et al. 2007).

6.1.2 Creating silane gradients on flat surfaces

Microcontact printing and lithographic techniques (Section 1.3) tend to produce sharp boundaries of surface functionality; however smooth gradients would be more useful in optoelectronic and microfluidic applications (Chaudhury and Whitesides 1992; Baker et al. 1996; Ruardy et al. 1997; Bhat et al. 2002; Ito et al. 2007).

A number of methods have been used to create molecular gradients on surfaces (Ruardy et al. 1997). Silane gradients can be achieved via diffusion through high and low density solvents (Ruardy et al. 1997; Elwing et al. in Chaudhury and Whitesides 1992), whilst Whitesides' group were first to describe the creation of silane gradients from the gas-phase (Chaudhury and Whitesides 1992). In this study, a piranha (PNA)-activated silicon wafer surface was placed at the edge of a solution of decylchlorosilane (DCS) in paraffin oil (PO). A DCS concentration gradient was proposed to form in the gas-phase which was reflected in the concentration deposited on silicon and contact angle measurements showed a smooth increase in hydrophilicity (ie decrease in hydrophobic DCS) away from the evaporating medium.

6.1.3 The preparation of AuNP density gradients using gas-phase deposition of APS on silicon surfaces

The method of Bhat et al. (2002) was developed based on the approach first reported by Whitesides (Chaudhury and Whitesides 1992). To create silane gradients, the evaporation medium (APS in PO) was positioned at one end of a 4cm length strip of ultra-violet/ozone (UVO)-activated silicon wafer. After evaporation, the wafers were incubated in AuNP solution (Frens 1973 (modified from Turkevich 1951) in Kimling et al. 2006). AuNP density and APS concentration was measured at different positions along the wafer and both showed a gradual decrease as the distance from the evaporation medium increased (Fig 6.2). In the image showing the 1.5 cm surface, the AuNPs appear to touch. This is highly unlikely since their surface charge would result in repulsion. The observed overlapping was probably due to AFM tip convolution (Section 5.3.1.2b). The APS gradient surfaces were characterised further using spectroscopic ellipsometry (Bhat and Genzer 2005). A number of parameters were investigated to control gradient formation including; evaporation time, APS concentration, temperature of APS and/or surface, immersion time in AuNP and the AuNP solution pH. In a previous publication, the density of active hydroxyl groups (and subsequently DCS) was varied using controlled UVO activation of polydimethylsiloxane (PDMS) surfaces (Efimenko and Genzer 2001). A smooth gradient of nanoparticles (NP) was first described on mercaptopropyltrimethoxysilane (MPTMS)-derivatised glass. This was achieved by varying solution-phase exposure time of the surfaces to AuNP solution (Baker et al. 1996). Following on from the group of Genzer, gas-phase diffusion of silane has been used to create step-wise or continuous gradients of silane, as viewed by fluorescent polystyrene nanoparticles (Song et al. 2006). A curved microcontact printing stamp was covered with APS, and the latter was allowed to evaporate onto a silicon surface. Silane gradients were controlled by varying contact time and stamp size/ shape.

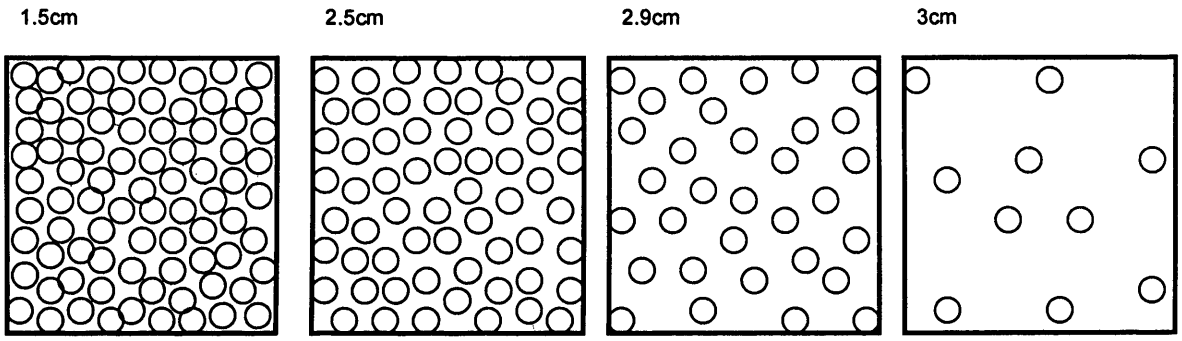


Fig. 6.2 A AuNP number density gradient generated along an APS gradient. Each picture represents an atomic force microscopy (AFM) image of a silicon wafer surface from Bhat et al (2002), at a distance (cm) from the evaporating medium (APS/PO).

6.1.4 Nanoparticles binding on functionalised silicon surfaces

6.1.4.1 The kinetics of AuNP binding to APS-derivatised silicon wafer

The rate of AuNP adsorption on a functionalised surface depends on parameters including AuNP size, AuNP concentration, solution viscosity and temperature (Park 1987 in Grabar et al. 1996). Initially, AuNP deposition increases linearly with time, when adsorption is diffusion-limited (Park et al. 1999). At later time-points, adsorption is limited by saturation and repulsive interactions between the citrate-stabilised AuNP (Grabar et al. 1996). A 'sticking probability' (ratio of AuNP bound/ AuNP reaching the surface) was used to describe the variable rate of adsorption due to saturation and repulsion. The equation for translational diffusion states that particle velocity increases with decreasing particle mass (Shaw 1992). Smaller colloids should therefore adsorb more quickly than larger colloids. Larger colloids have a greater tendency to aggregate (Shaw 1992) giving rise to clusters and strings of surface adsorbed AuNPs (Grabar et al. 1995).

6.1.4.2 The effect of solution concentration on AuNP binding to APS-derivatised silicon surfaces

Rough metal coated surfaces (i.e. dispersed AuNP on silicon) are desirable in the development of surface enhanced resonance scattering (SERS), which can greatly enhance analysis for biomedical and electrochemical applications (Chumanov et al. 1995 & 1996; Bright et al. 1995; Grabar et al. 1995 & 1996). At equilibrium, the concentration of adsorbed Au and silver (Ag) NPs on sulfhydryl (SH) and amino (NH_2)-silane-derivatised surfaces,

has been shown to depend on the starting concentration of the colloidal solution (Chumanov et al. 1995 & 1996; Bright et al. 1998; Minard-Basquin et al. 2005; Nath et al. 2004). A gradient of low to high density AuNP films with regularly spaced NPs was created. The regular spacing was attributed to repulsive electrostatic interactions between AuNPs (Chumanov et al. 1996). High-density AuNP films were described as having an average 'nearest neighbour distance' below the diameter of the NP and vice versa for low density films. The thermodynamics of Au/AgNP binding were described by the Natan group (Bright et al. 1998; Keating et al. 1999). The model of adsorption used was the Frumkin isotherm which states that adsorbed molecules interact and affect further adsorption by repulsion or attraction. An equilibrium binding constant of $1.7 \pm 0.3 \times 10^{8}$ M^{-1} was calculated.

6.1.4.3 The effect of the ionic strength on AuNP binding to APS-derivatised silicon surfaces

The stability of nano-colloidal solutions is based upon repulsion between individual nanoparticles. Likewise, on a surface, AuNP stabilised with negative citrate ions will not pack closely together and will maintain an inter-particle spacing dependent on particle size and ionic strength, (Doron et al. 1995). A well-developed model of 'random sequential adsorption' (RSA) (Feder 1980) describes a 'jamming' (i.e. fractional coverage) limit of 55% for the random, irreversible deposition of hard spheres (without overlapping) (Nath et al. 2004) (Fig. 6.3a). In aqueous solutions, negatively-charged citrate-stabilised AuNPs are surrounded by an electrical double layer of positive ions. Increasing thickness of the double layer directly increases the electrostatic repulsion and interparticle distance of colloids in solution (Deyagin-Landau and Verwy-Overbeek (DLVO) theory, Verwey et al. 1948 in Kooij et al. 2002). As ionic strength decreases the double layer thickness increases and so does inter-particle repulsion. A simplified diagram of electrostatic repulsion is shown in Fig. 6.3b and c. This does not include overlapping due to attractive Van der Waals (VdW) interactions (Shaw 1992). The binding density of AuNPs on APS surfaces has been shown to decrease with decreasing ionic strength (Kooij et al. 2002). Fractional coverages <20% were observed for a limited range of ionic strengths. Minard-Basquin et al. 2005 reported that the density of AuNPs (derivatised

with oligonucleotides) adsorbed on APS surfaces was the same for solutions diluted in water, 0.14M buffer (pH 6.9) and 1.14M buffer (pH 6.9).

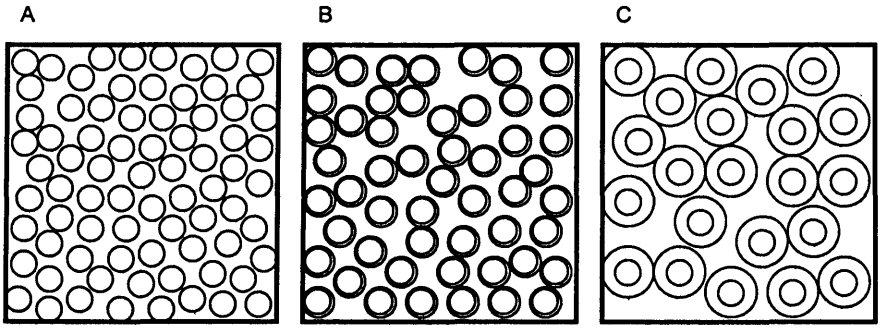


Fig. 6.3 The random deposition of AuNPs onto functionalised silicon surfaces from solution. A schematic of **a**) the 'jamming limit' (maximum area coverage = 55% for the random sequential adsorption of hard (non-overlapping) spheres), **b**) the high coverage of citrate-stabilised AuNPs in high ionic strength solutions and **c**) the low coverage of citrate-stabilised AuNPs in low ionic strength solutions. Inner circles represent the solid AuNP radius. Outer circles represent the effective radius due to an electrical double layer.

As described by the RSA model, irreversible random deposition will only allow an absolute maximum of 55% AuNP coverage. However, complete monolayer AuNP coverage is desirable in the microelectronics industry (Shipway et al 2000). The addition of thio-adsorbates to AuNP surfaces has been investigated to improve AuNP packing properties (Grabar et al. 1995; Fan and Lopez 1997; Liu et al. 2002) and even to reverse AuNP binding completely (Enders et al. 2006). Thiols form covalent bonds with the AuNPs, displacing the surface citrate anions in the process. This removes inter-particle repulsion (Fig. 6.4).

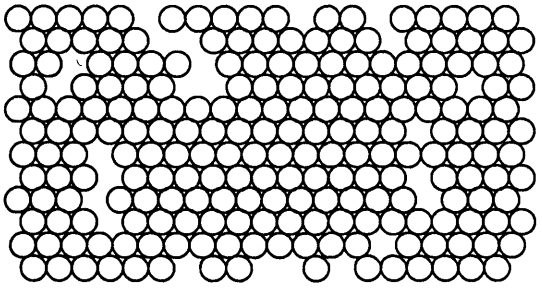


Fig. 6.4 A regular lattice of AuNP formed on a silicon surface. The image depicts part of a SEM image from Liu et al. (2002). Thioadsorbates were used to displace citrate anions from the AuNP surface, thus removing the electrostatic repulsion and so increasing packing density.

6.1.4.4 The effect of solution pH upon AuNP binding to APS-derivatised silicon wafer

Binding between aminosilanes and citrate-stabilised AuNP is electrostatic (Zhu et al. 1999). Solution pH affects the ionisation of APS molecules and therefore AuNP binding to derivatised surfaces (Zhu et al. 1999, Bhat et al. 2007). Using a constant NP concentration and ionic strength, the density of AuNPs adhered to aminothiophenol (pATP) surfaces was studied for solutions between pH 3 and 12 (Zhu et al. 1999). An extremely sharp drop in AuNP density was observed between pH5 and 6, attributed to a decrease in pATP ionisation. The inflection point of pH 5.8 was close to the pKa of pATP (5.3) (Zhang et al. 1998 in Zhu et al. 1999). In a later publication, AuNP gradients on APS-derivatised silicon wafers were controlled by modifying the AuNP solution pH (Bhat et al. 2007). The pKa of APS was estimated as 7.6 (Zhang et al. 1998 in Bhat et al. 2007), and was used to calculate a theoretical curve for the fraction of NH_3^+ groups between pH 4-12. AuNP solutions of between pH 4-12 were incubated with APS-derivatised wafers to give a similar S-shaped curve. However, the inflection point (pH 9.4) was much higher because AuNP adsorb across many APS molecules, and therefore, onto different coverages of APS with the same number density (Bhat et al. 2007). Similar pH effects have been observed for latex nanoparticle assembly on APS surfaces (Jonas et al. 2002). APS hydrolysis from the surface occurs at pH values higher than its pKa, due to nucleophilic attack of the siloxane bonds between the silane and surface (Zhu et al. 1999).

6.1.5 Chapter objectives

- To prepare a flat surface with a controlled dispersion of functional silane molecules.
- To indirectly monitor the dispersion of APS by measuring AuNP surface binding densities
- To investigate the factors that influence AuNP binding to APS derivatised surfaces.
- To keep the surrounding surface underivatised for a later bottom-up surface polymerisation (Fig. 1.12).

6.2 Methods

A method was developed to obtain an APS concentration gradient and AuNP 'number density gradient' on silicon surfaces based on work by Bhat et al. (2002).

6.2.1 Equipment and materials

As for Section 5.2.1.

6.2.2 Controlling the spatial distribution of molecules on silicon at the nanometer scale

The surfaces were prepared and analysed as described in Section 5.2.2 (Surface treatments 1-4, Table 5.2.1). AFM (Section 5.2.3.1) and X-ray photo-electron spectroscopy (XPS, Section 5.2.3.2) was used to measure the density of APS and AuNP binding to the surfaces (Section 5.2.2).

6.2.2.1 Creating AuNP number density gradients on silicon surfaces derivatised by evaporation and gradient deposition of APS

Distance gradient methods a-d were based on the standard protocol described in Section 5.2.2.2.

a. Distance gradient method 1, using diluted AuNP solution

For the silanisation step, surfaces were placed 0.5, 1, 1.5, 2, 2.5 and 3cm from the Eppendorf tube lid (Fig. 6.5a). The surfaces were placed directly on the Petri dish, below the height of the Eppendorf lid. APS was pipetted into the Eppendorf lid to ~2/3 full (173ul) and the lid was subsequently filled to 260ul with paraffin oil (PO), unmixed, to give ~66% w/w APS.

In this instance, following AuNP incubation, the standard washing protocol was emitted in favour of sonication for 2 minutes in de-ionised water (dH_2O) followed by two 10 minute rinses in dH_2O. AuNP densities were manually counted from tapping-mode AFM scans. Room temperature was 29°C.

b. Distance gradient method 2, using diluted AuNP solution

Surfaces were placed 0.5, 1.5, 2.5 and 3.5cm from the Eppendorf tube lid (Fig. 6.5b). The surfaces were placed level with the top of the eppendorf lid, by placing them on upturned Eppendorf lids. APS was pipetted into the Eppendorf lid to ~1/2 full (130µl) and the lid was subsequently filled to 260µl with paraffin oil (PO) and mixed to give an APS concentration of ~50% w/w. Room temperature was 25°C.

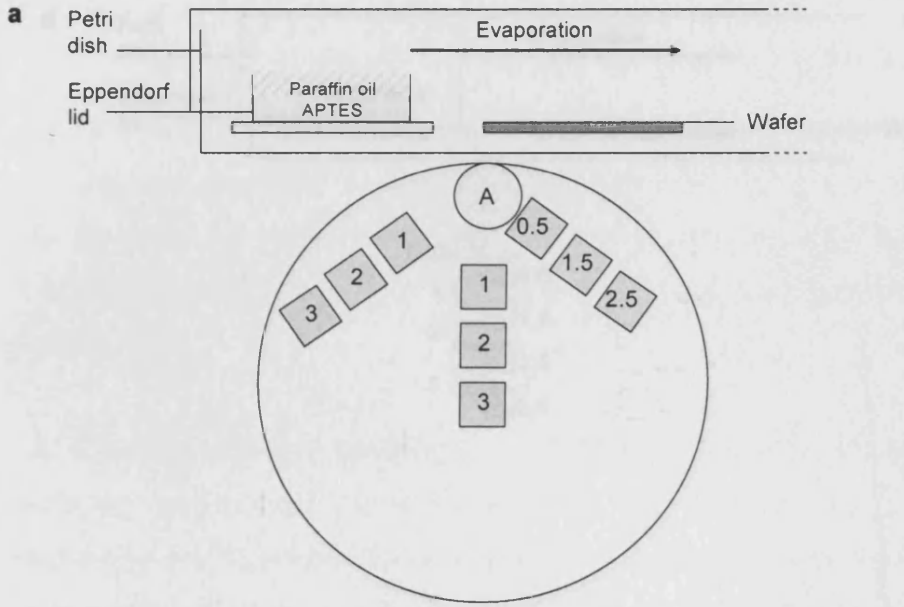
In addition to manual counting, WSXM flooding analysis (Section 5.2.3.1) was used to determine AuNP densities from tapping-mode AFM scans. Surfaces were also analysed by XPS.

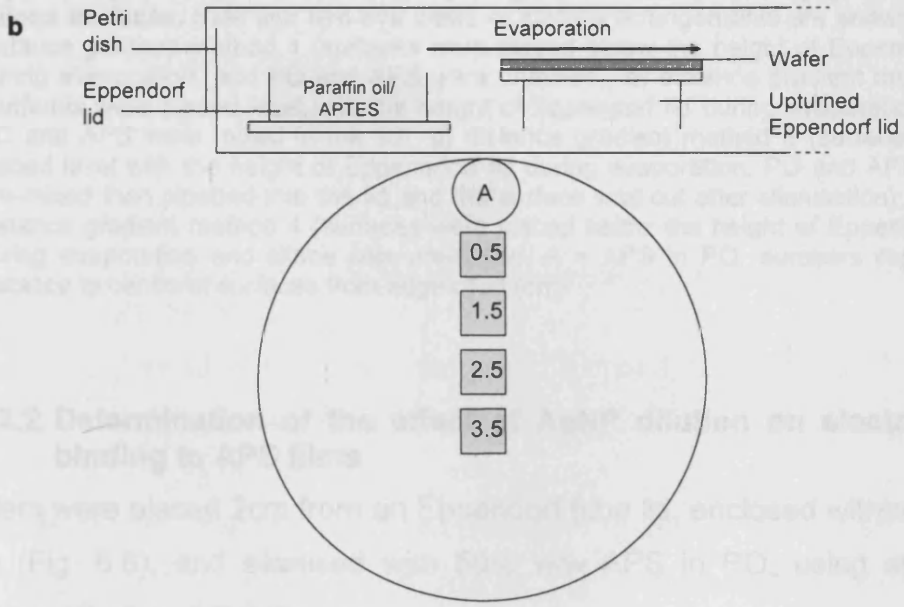
c. Distance gradient method 3, using diluted AuNP solution

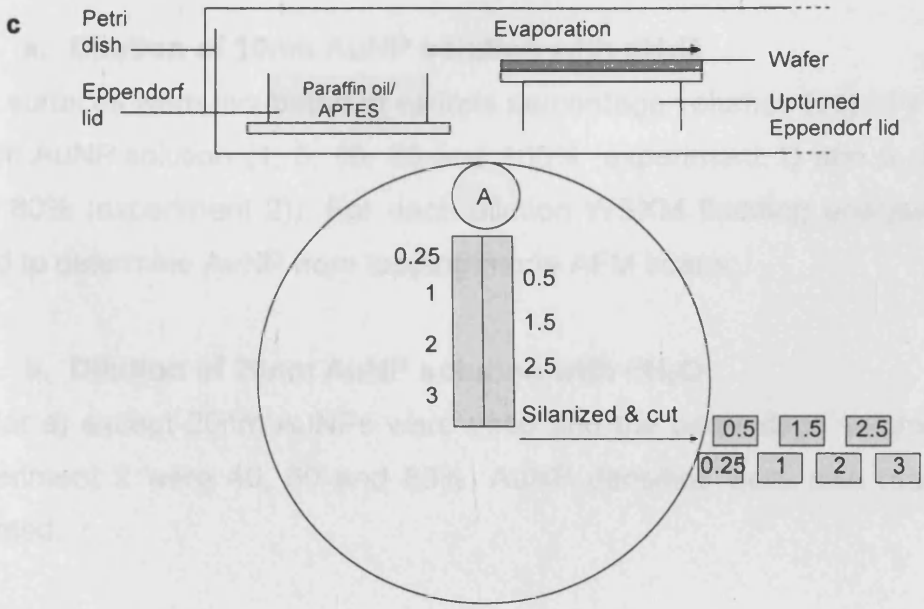
Two strips (~1 x 4cm) of silicon were placed adjacent to an Eppendorf tube lid (Fig. 6.5c). The surface was placed level with the top of the Eppendorf lid. 260µl APS (50% w/w in PO) was pipetted into the lid. Room temperature was 25°C. After silanization and curing, the silicon was cut into 1x1cm pieces. These were centred at 0.25, 0.5, 1, 1.5, 2, 2.5 and 3cm from the edge of the lid. In addition to manual counting, WSXM flooding analysis was used to determine AuNP densities from tapping-mode AFM scans. Room temperature was 27°C.

d. Distance gradient method 4, using undiluted AuNP solution

Surfaces were placed 0.2, 0.5, 1, 1.5, 2, 2.5 and 3cm from an Eppendorf tube lid (experiment 1) and 2.5, 3 and 3.5cm (experiment 2) (Fig. 6.5d). The surfaces were placed below the height of the lid. 260µl APS (50% w/w in PO) was pipetted into the lid. Surfaces were incubated in a 10nm AuNP solution (undiluted). The surfaces were rinsed twice in 500ml dH_2O water and three times in 4ml dH_2O, before analysing using AFM and XPS.


a
Petri dish
Eppendorf lid
Paraffin oil
APTES
Evaporation
Wafer
A
0.5
1.5
2.5
1
2
3
1
2
3


b
Petri dish
Eppendorf lid
Paraffin oil/
APTES
Evaporation
Wafer
Upturned
Eppendorf lid
A
0.5
1.5
2.5
3.5


c
Petri dish
Eppendorf lid
Paraffin oil/
APTES
Evaporation
Wafer
Upturned
Eppendorf lid
A
0.25
1
2
3
0.5
1.5
2.5
Silanized & cut
0.5
1.5
2.5
0.25
1
2
3

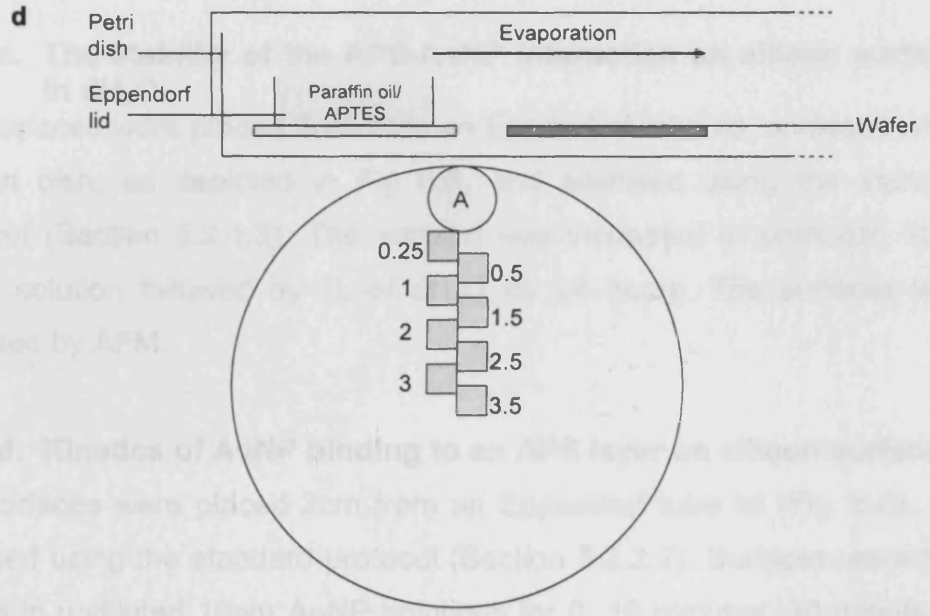


Fig. 6.5 Experimental set ups for preparing AuNP number density gradients on silicon surfaces. Side and bird-eye views of surface arrangements are shown for **a**) distance gradient method 1 (surfaces were placed below the height of Eppendorf lid during evaporation, and PO and APS were unmixed), **b**) distance gradient method 2 (surfaces were placed level with the height of Eppendorf lid during evaporation, and PO and APS were mixed in the lid), **c**) distance gradient method 3 (surfaces were placed level with the height of Eppenodorf lid during evaporation, PO and APS were pre-mixed then pipetted into the lid and the surface was cut after silanisation) and **d**) distance gradient method 4 (surfaces were placed below the height of Eppendorf lid during evaporation and silane was pre-mixed. A = APS in PO, numbers represent distance to centre of surfaces from edge of lid (cm).

6.2.2.2 Determination of the effect of AuNP dilution on electrostatic binding to APS films

Wafers were placed 2cm from an Eppendorf tube lid, enclosed within a Petri dish (Fig. 6.6), and silanised with 50% w/w APS in PO, using standard protocol (Section 5.2.2.2).

a. Dilution of 10nm AuNP solution with dH_2O

The surfaces were incubated in various percentage volumes (aq) of a stock 10nm AuNP.solution (1, 5, 10, 20 and 100% (experiment 1) and 5, 40, 60 and 80% (experiment 2)). For each dilution WSXM flooding analysis was used to determine AuNP from tapping-mode AFM scans.

b. Dilution of 20nm AuNP solution with dH_2O

As for a) except 20nm AuNPs were used and the percentage volumes for experiment 2 were 40, 60 and 80%. AuNP densities were also manually counted.

c. The stability of the APS-AuNP interaction on silicon surfaces in dH_2O

The surfaces were placed 2cm from an Eppendorf tube lid, enclosed within a Petri dish, as depicted in Fig 6.6, and silanised using the standard protocol (Section 5.2.1.3). The surface was incubated in undiluted 10nm AuNP solution followed by 1L of dH_2O for 24 hours. The surfaces were analysed by AFM.

d. Kinetics of AuNP binding to an APS layer on silicon surfaces

The surfaces were placed 2cm from an Eppendorf tube lid (Fig. 6.6), and silanised using the standard protocol (Section 5.2.2.2). Surfaces were then placed in undiluted 10nm AuNP solutions for 0, 10 minutes, 30 minutes, 1 hour, 2 hours, 4 hours, 6 hours, 8 hours, 16 hours or 24 hours. The surfaces were rinsed twice in 500ml dH_2O and three times in 4ml dH_2O. Manual counting was used to determine AuNP densities from tapping-mode AFM scans.

e. The stability of APS on silicon surfaces in dH_2O, as viewed by AuNP binding

The surfaces were placed 2cm from an Eppendorf tube lid (Fig. 6.6), and silanised using the standard protocol (Section 5.2.2.2).

After silanisation, the surfaces were placed in 4ml dH_2O in microwell plates for 0, 0.5, 1, 2, 4, 24 and 48 hours, followed by incubation in undiluted 10nm AuNP solution. The surfaces were rinsed as in Section 6.2.2.3. Manual counting was used to determine AuNP densities from tapping-mode AFM scans.

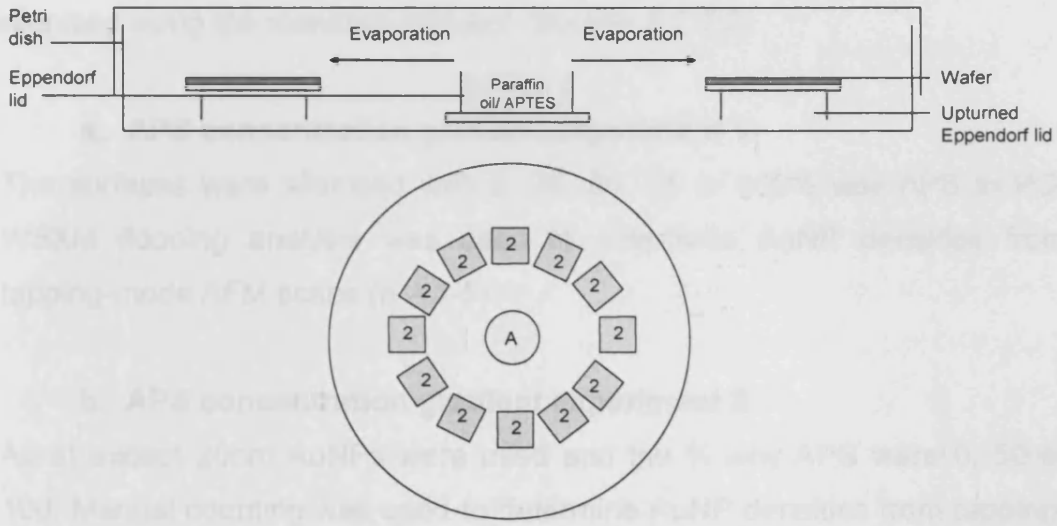


Fig. 6.6 Arrangement of surfaces around an Eppendorf lid during gas-phase silanization. Side-on and birds-eye view of the silicon surface arrangement. A = APS in PO, numbers represent distance of surface from lid (cm). The surfaces were kept level with the height of the evaporating Eppendorf lid by placing them on upturned Eppendorf lids.

6.2.2.3 Non-specific binding of undiluted AuNP solution to underivatised silicon surfaces

The underivatised silicon surfaces were placed 2cm from an Eppendorf tube lid as depicted in Fig. 6.6 (cleaned and activated using the standard protocol, Section 5.2.2.2).

Non-specific binding of 10nm AuNP to PNA surfaces (PNA Au) were compared for three incubation experiments: (a) 10% AuNP solution (aq) followed by three 10 minute washes in dH_2O (4ml) (Section 6.2.2.1c); (b) undiluted AuNP solution followed by three 10 minute washes in dH_2O (4ml) (Section 6.2.2.2d); (c) undiluted AuNP solution followed by a 30 second wash, agitating in dH_2O (1L) and three static 10 minute washes in dH_2O (4ml) (Section 6.2.2.2c).

6.2.2.4 Changing the concentration of APS in the evaporation medium

The surfaces were placed 2cm from an Eppendorf tube lid (Fig 6.6) and silanised using the standard protocol (Section 5.2.2.2).

a. APS concentration gradient experiment 1

The surfaces were silanised with 0, 25, 50, 75 or 100% w/w APS in PO. WSXM flooding analysis was used to determine AuNP densities from tapping-mode AFM scans (n = 1-5).

b. APS concentration gradient experiment 2

As a) except 20nm AuNPs were used and the % w/w APS were 0, 50 or 100. Manual counting was used to determine AuNP densities from tapping-mode AFM scans (n = 1-5).

c. APS concentration gradient experiment 3

As a) except the % w/w APS were 0, 4, 6, 8, 10, 25, 50 or 100 (experiment 1) or % w/w APS were 0, 2, 4, 6, 8 or 10 (experiment 2). For experiment 2, the APS/ PO mixtures were mixed for longer prior to evaporation (the solutions went completely clear). The lower the concentration of APS, the more mixing was required. XPS was also used to analyse surfaces (experiment 2) that were not incubated in AuNP solution.

d. APS concentration gradient experiment 4

As b) except the % w/w APS were 0, 2, 12, 17, 20, 30, 40, 75 or 100. Manual counting was used to determine AuNP densities from tapping-mode AFM scans (n = 2-4). XPS was also used to analyse surfaces not incubated in AuNP solution.

6.3 Results and discussion

6.3.1 Controlling the spatial distribution of molecules on silicon at the nanometer scale

Initially, it was assumed that at equilibrium the adsorbed concentration of AuNPs was dependant on the surface concentration of adsorbed APS but independent of the AuNP solution concentration. Therefore initial experiments were carried out using diluted solutions (in dH_2O) of the stock AuNP solution. 'Number density' is defined as the number of AuNPs counted in a $1\mu m^2$ AFM image ($AuNPs/\mu m^2$). All APS derivatisation was carried out in the gas-phase. All experiments were incubated for 24 hours in AuNPs solutions, initially to correlate with Bhat et al. (2002), and subsequently to keep all experiments the same. The n numbers refer to the number of images scanned for each treatment. The average number of AuNPs deposited within a $1\mu m^2$ scan area was counted for each surface treatment (± SEM).

6.3.1.1 Creating AuNP number density gradients on silicon surfaces derivatised by evaporation and gradient deposition of APS

For each method, tapping-mode AFM trace images of PNA, PNA Au and/or APS surfaces (Table 5.1) are shown. Images of APS Au surfaces centred at each evaporative distance are also shown. The average number density of AuNPs for each silicon surface (± SEM) was plotted against evaporative distance to give a 'AuNP distance gradient graph'.

a. Distance gradient method 1, using diluted AuNP solution

AFM images are shown in Fig. 6.7a, and a AuNP distance gradient graph was plotted (Fig. 6.7b). A small increase in the AuNP density was observed between 0.5 and 1cm, followed by a sharp decrease between 1 and 2cm. A similar negative gradient has previously been described for gas-phase chlorosilane and APS deposition onto silicon surfaces (Chaudhury and Whitesides, 1992; Bhat et al. 2002). The initial increase in AuNP concentration (reflecting silane density) may have arisen due to a 'shadowing' effect of the Eppendorf lid, since the surfaces were positioned below the lip of the Eppendorf lid during silanisation (Fig. 6.8). Shadow

mask evaporation techniques are often used to pattern nm-sized features using metal chemical vapour deposition (Han 2007). A number of the AFM images were streaky due to thermal drift of the AFM tip (Appendix VI).Therefore, AuNP dimensions were inconsistent at each evaporative distance (Fig. 6.7a), and this may have affected the apparent AuNP densities. At distances >2.5cm from the Eppendorf lid the numbers of deposited AuNPs were very low, and any AuNP binding was probably non-specific. Using a similar method, Bhat et al. (2002) reported a gradual negative AuNP gradient from 0.5 to 2.5cm followed by a sharp drop to ~3.2cm. The maximum AuNP number density was reported as 480/μm^2. In this study the maximum number density of AuNPs was ~200/μm^2 (Section 6.3.1.2).

b. Distance gradient method 2, using diluted AuNP solution

AFM images are shown in Fig. 6.9a and a AuNP density gradient graph was plotted (Fig. 6.9b). In these images the AuNPs were well defined. The AuNP number densities were not significantly different for APS Au surfaces centred at 0.5 and 1.5cm (158 ± 8 and 195 ± 41 AuNPs/μm^2 respectively Unlike 'distance gradient method 1', the surfaces were placed level with the lip of the Eppendorf lid, thus eliminating the 'shadow effect' (Fig. 6.8). There was a steep gradient between 1.5 and 2.5cm (as also observed for 'distance gradient method 1'). A few AuNPs were observed on the APS Au wafers centred at 2.5 and 3 cm (5 ± 3 and 1 AuNPs/μm^2 respectively). These are likely to be non-specifically adsorbed. The gradient was apparently shorter and the maximum number density of AuNPs (191/μm^2) was still lower than that reported (480/μm^2) by Bhat et al. (2002). There was no significant difference between AuNP densities when these were counted either manually or using WSXM flooding analysis (Fig. 6.9b). Since the latter approach was faster, it was, where possible, used for subsequent experiments.

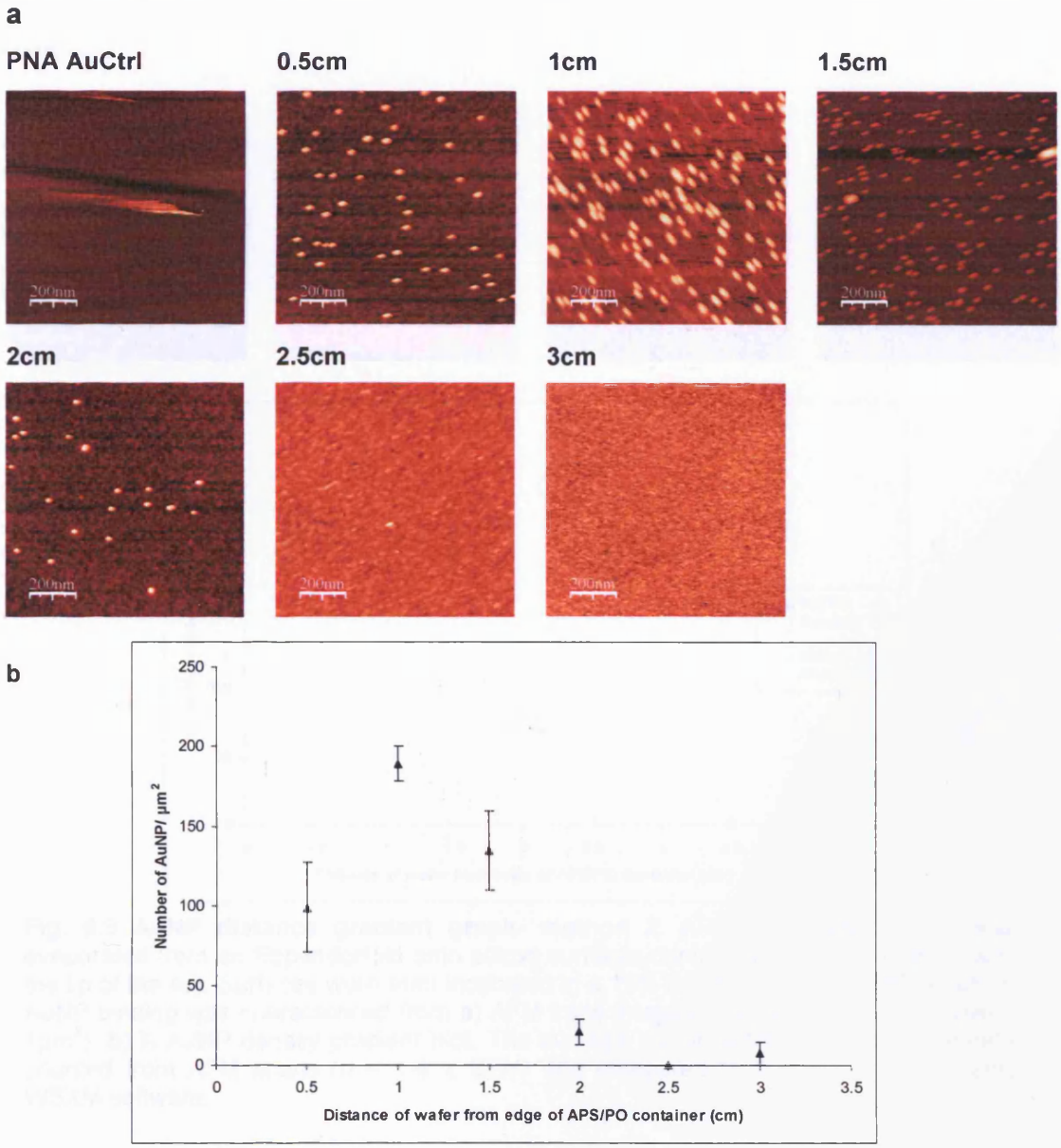


Fig. 6.7 AuNP distance gradient graph (method 1). APS (66% w/w in PO) was evaporated from an Eppendorf lid onto silicon surfaces centred at 0.5-3cm (below the lip of the lid). Surfaces were then incubated in a 10% (in dH_2O) 10nm AuNP solution. **a**) AFM trace images (z-axis = 20nm, scan size = 1µm^2). **b**) AuNP density gradient plot. The average no. of AuNPs/µm^2 were manually counted from AFM scans (n = 2-5 ± SEM).

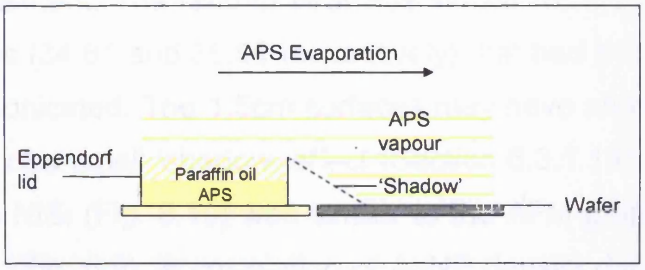


Fig. 6.8 A 'shadow effect' observed during APS silanisation. Silicon surfaces within the shadow of the Eppendorf lid are not exposed to APS vapour and therefore not silanised. AuNP binding is therefore not seen in these areas. This effect would not be expected for surfaces placed level with the lip of the lid.

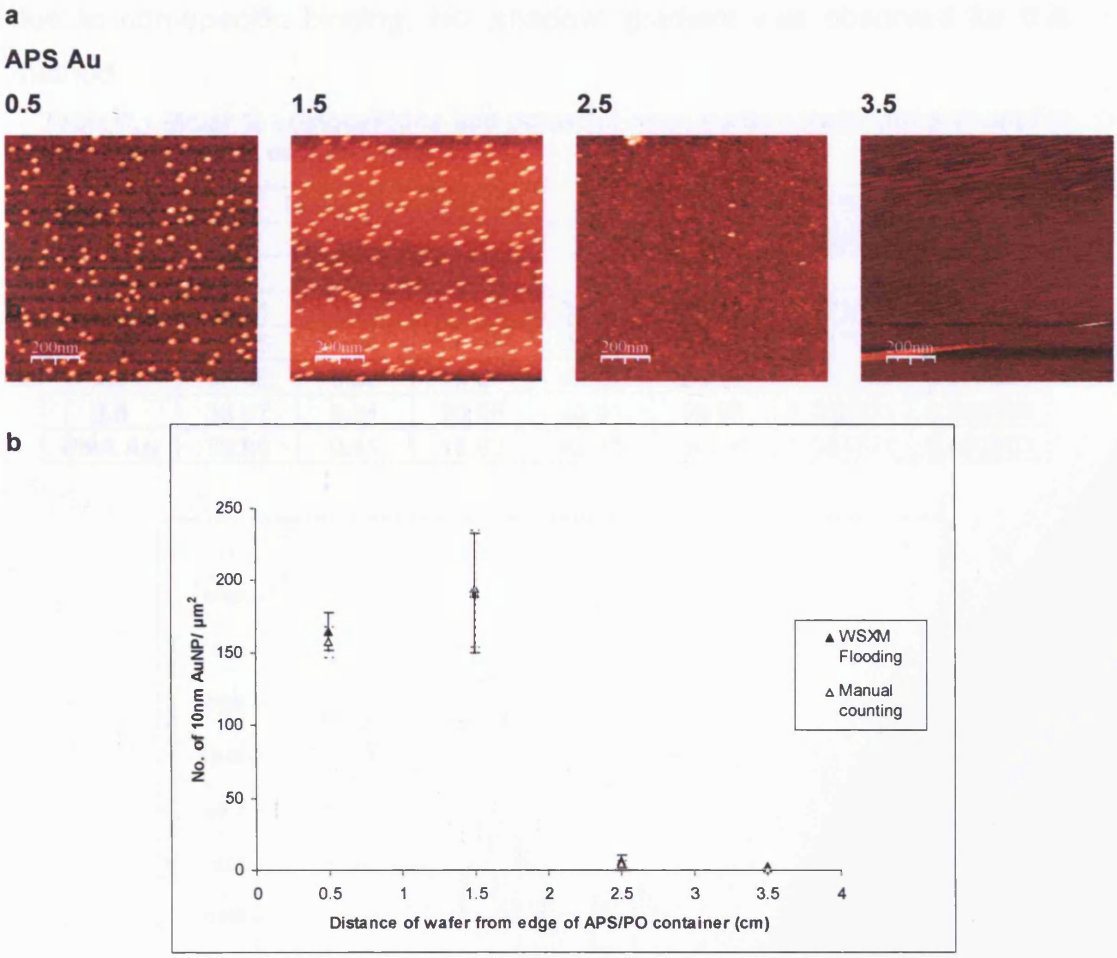


Fig. 6.9 AuNP distance gradient graph- method 2. APS (50% w/w in PO) was evaporated from an Eppendorf lid onto silicon surfaces centred at 0.5-3.5 cm (level with the lip of the lid). Surfaces were then incubated in a 10% (in dH_2O) 10nm AuNP solution. AuNP binding was characterised from **a**) AFM trace images (z-axis = 20nm, scan size = 1µm^2). **b**) A AuNP density gradient plot. The average no. of AuNPs/µm^2 were manually counted from AFM scans (n = 1-4 ± SEM) and compared to flooding analysis using WSXM software.

XPS data of APS gas-phase deposition onto PNA-activated silicon surfaces has been discussed previously (Section 5.3.1.2a). The mol % compositions and ratios are shown in Table 6.1. Very small levels of N1s were seen for surfaces 2.5 and 3.5, probably due to contamination. Si2p was used as the background element. The ratio of N/Si was similar for the APS Au 0.5 and 1.5cm surfaces (34.61 and 36.95 respectively) that had been silanised for 5 minutes and sonicated. The 1.5cm surfaces may have shown a higher N/Si ratio because of a small 'shadow' effect (Section 6.3.1.1a). The XPS graph of distance vs N/Si (Fig. 6.10) was similar to the AFM graph of distance vs AuNP density (Fig. 6.9). A correlation of AuNP density data from AFM and N/Si data from XPS is given in Fig. 6.11. The intercept was high probably

due to non-specific binding. No 'shadow' gradient was observed for this method.

Table 6.1 Molar % compositions and ratios for each surface treatment prepared in distance gradient experiment 2.

Distance (cm)	Molar % composition				Molar % ratios		
	O	N	C	Si	C/N	Si/O	N/Si
0.5	34.61	1.04	28.75	35.60	27.57	1.028539	0.029299
1.5	36.95	1.04	24.40	37.61	23.52	1.017887	0.027577
2.5	37.46	0.32	19.60	42.62	60.99	1.137602	0.007539
3.5	38.47	0.34	20.28	40.91	59.98	1.063471	0.008266
PNA Au	39.85	0.11	16.93	43.11	150.91	1.081721	0.002603

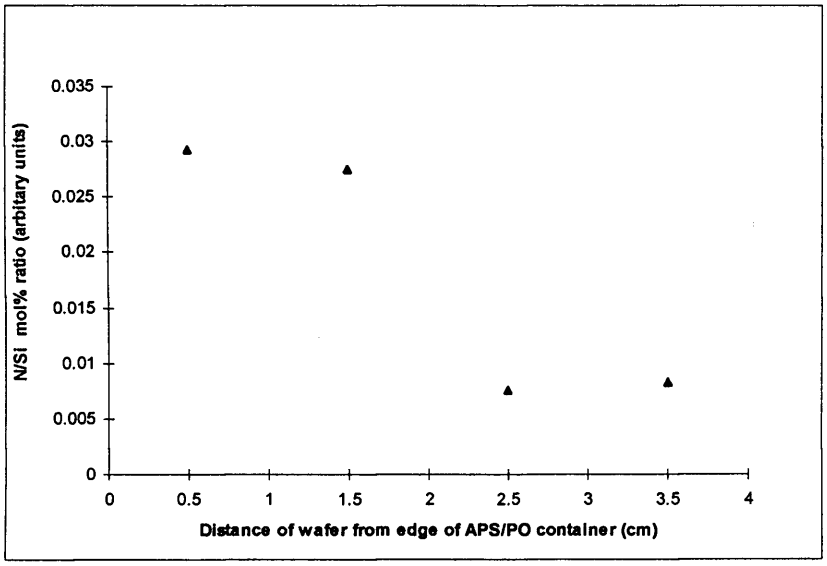


Fig. 6.10 APS concentration along a distance gradient (Method 2) measured by XPS. APS (50% w/w in PO) was evaporated from an Eppendorf lid onto silicon surfaces centred at 0.5-3.5 cm (level with the lip of the lid). The XPS N1s signal (corresponding to surface-deposited APS) was used to generate a ratio with the Si2p signal (corresponding to APS and the silicon surface) for each distance (n = 1).

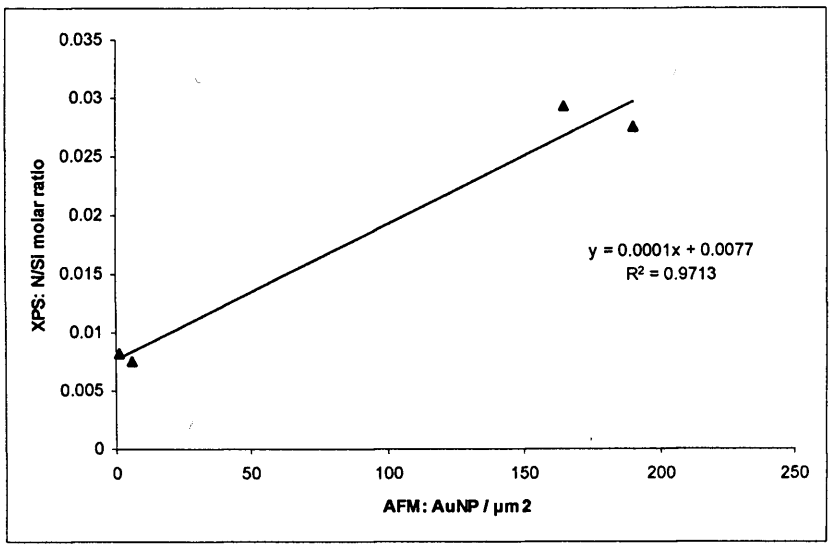


Fig. 6.11 Correlation between AFM and XPS data for distance gradient method 2. The number density of AuNPs (from AFM scans) was compared to the N/Si molar ratio of the surfaces (measured by XPS).

c. Distance gradient method 3, using diluted AuNP solution

AFM images are shown in Fig. 6.12a and a AuNP distance gradient graph was plotted (Fig. 6.12b). The AuNP dimensions were well defined. A general trend was observed where the AuNP number density gradually increased between 0.5 and 2cm and then rapidly decreased between 2 and 3cm. The slight drop observed at 1.5cm was attributed to experimental variability. In this instance the gradient was noted to extend for a greater distance than for distance gradient methods 1 and 2 (Figures 6.7 and 6.9). This was probably due to improved mixing of the APS / PO solution. The maximum number density of AuNPs was not significantly greater (242 ± 17 AuNPs/μm^2) than for distance gradient methods 1 and 2.

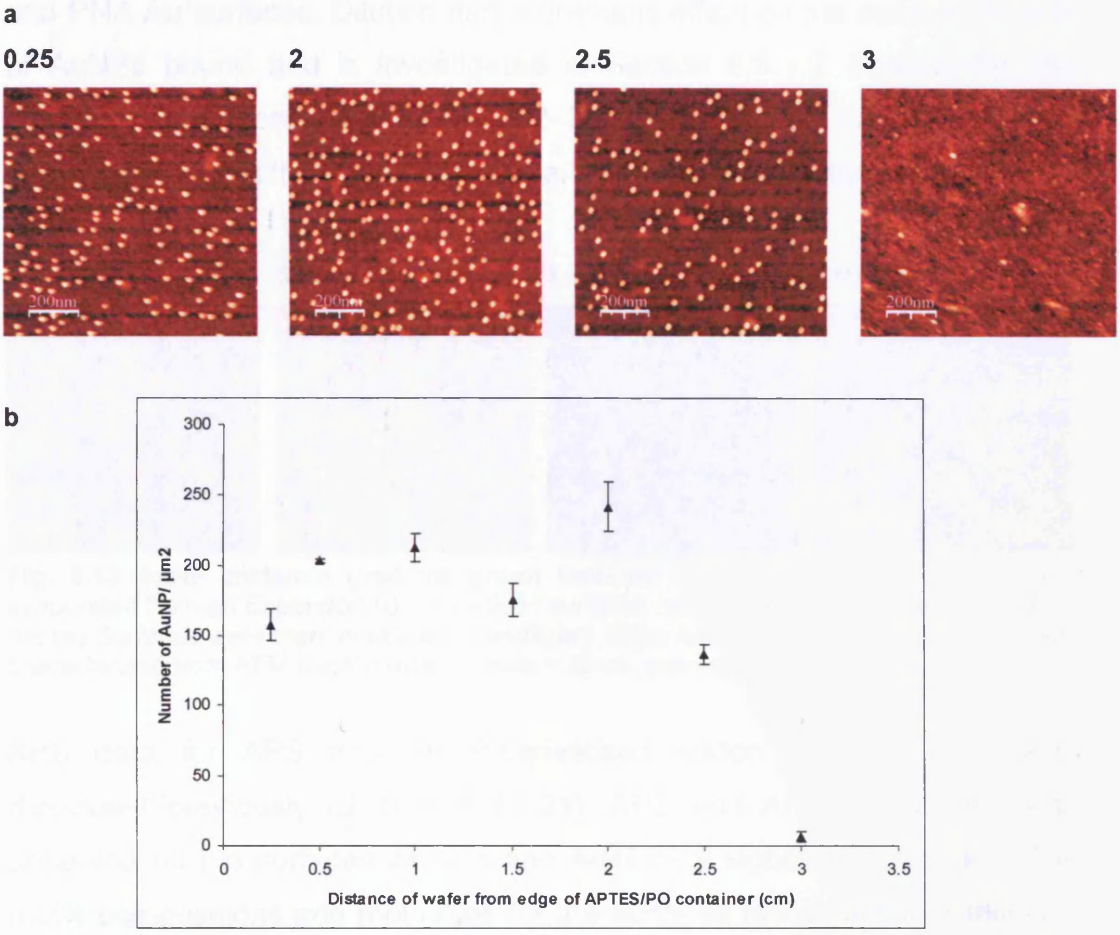


Fig. 6.12 AuNP distance gradient graph (method 3). APS (50% w/w in PO) was evaporated from an Eppendorf lid onto silicon surfaces centred at 0.2-3cm (level with the lip of the Eppendorf lid). This was followed by incubation in a 10nm AuNP solution **a**) AFM trace images are shown after WSXM software processing (z-axis = 20nm, scan size = 1μm^2). **b**) a AuNP density gradient plot. The average no. of AuNPs/μm^2 were counted using WSXM flooding analysis (n = 3 ± SEM).

d. Distance gradient method 4, using undiluted AuNP solution

Undiluted AuNP solution was used in order to more directly compare data with that described in the literature (Bhat et al. 2002). A selection of AFM trace images (Fig. 6.13) showed the AuNP number densities for distances between 0.2cm and 4cm. In these cases the AuNP dimensions were poorly defined, due to a damaged tip, and in some cases appear to overlap due to tip convolution (Section 5.3.1.2b). This is one of the main drawbacks of AFM (Grabar et al. 1997). For these reasons, the AuNP density was not determined for these images. APS Au surfaces incubated in undiluted AuNP solution appeared to have a complete coverage of AuNPs, up to 3cm along the surfaces, whereas very few bound to the APS Au 3.5 and 4cm surfaces and PNA Au surfaces. Dilution had a dramatic effect on the number density of AuNPs bound and is investigated in Section 6.3.1.2. Importantly, the complete AuNP coverage of the 0.2–3cm APS treated silicon surfaces, demonstrated that the underlying silane layer was near continuous.

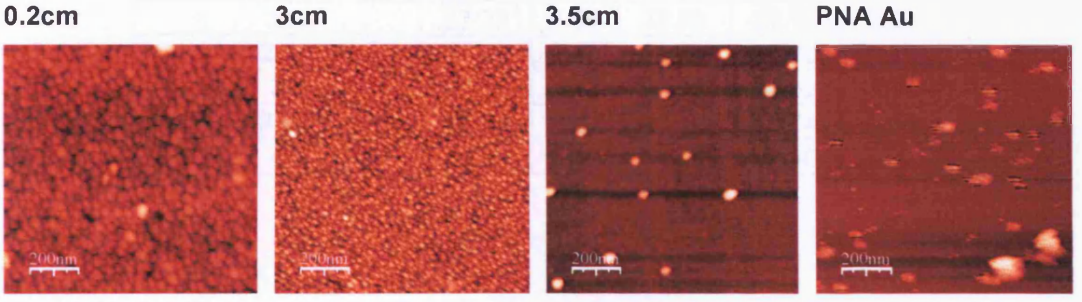


Fig. 6.13 AuNP distance gradient graph (method 4). APS (50% w/w in PO) was evaporated from an Eppendorf lid onto silicon surfaces centred at 0.2-4 cm (below the lip of the lid) Surfaces were then incubated in undiluted 10nm AuNP solution. AuNP binding was characterised from AFM trace images (z-axis = 20nm, scan size = 1μm^2).

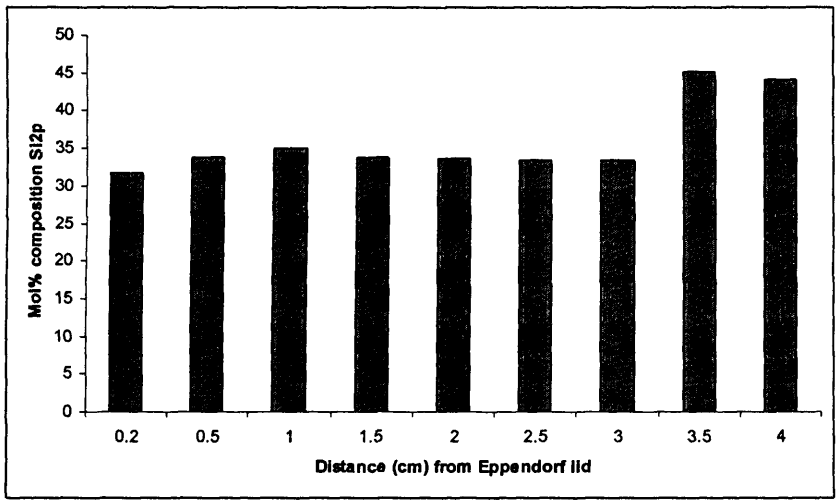
XPS data for APS and AuNP-derivatised silicon surfaces has been discussed previously (Section 5.3.1.2a). APS and AuNP deposition was observed on the surfaces as N1s and Au4f XPS signals respectively. The mol% compositions and mol ratios for the surfaces are shown in Table 6.2. AuNP attenuation of all the other atoms present on the surface (C1s, N1s, O1s, and Si2p) was observed as reported in Section 5.3.1.2a, and therefore it was difficult to apply a background for the mol ratios. The N1s mol% composition was <1 for all surfaces. This value is close to the detection limit of the equipment and as such it is possible that this data is unreliable. [A control (without AuNP binding) was not carried out]. Si2p (background

element) and Au4f mol% compositions are shown in Fig. 6.14. Si2p is attenuated for surfaces 0.2–3cm (with AuNP binding) and not attenuated for surfaces 3.5 and 4cm (without AuNP binding). A gradual increase in Au4f signal is observed for surfaces 0.2-2cm followed by a sharp increase at 2.5 and 3cm. This may reflect a 'shadow' gradient of APS (Fig. 6.8). The sharp increase was also observed by AFM measurements of AuNP surface density on the 2.5cm surface, when surfaces were placed level with the height of the Eppendorf lid (Fig. 6.12).

Table 6.2 Mol% compositions of each element for surfaces prepared in 'distance gradient method 4'. The elemental surface composition was calculated from XPS curves of each surface treatment using ESCA analysis. (n=1).

Molar % composition					
Distance (cm)	**C1s**	**N1s**	**Si2p**	**O1s**	**Au4f**
0.2	31.24	1.11	31.69	34.31	1.66
0.5	26.70	1.34	33.77	36.34	1.85
1	23.46	1.27	35.03	38.53	1.71
1.5	26.34	1.12	33.76	36.93	1.85
2	27.20	1.09	33.66	36.16	1.90
2.5	27.49	0.95	33.46	35.20	2.90
3	26.55	1.16	33.53	36.02	2.74
3.5	15.44	0.60	45.18	38.74	0.04
4	19.34	0.32	44.01	36.30	0.02

a



b

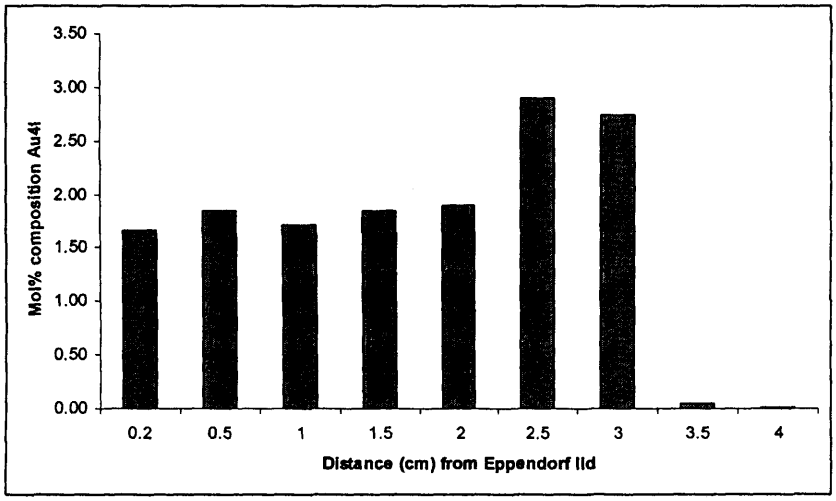


Fig. 6.14 Mol% compositions of elements for surfaces prepared in 'distance gradient method 4'. **a**) Si2p. **b**) Au4f. (n = 1)

6.3.1.2 Determination of the effect of AuNP dilution on electrostatic binding to APS films

In these experiments, APS was evaporated onto silicon surfaces level with the lip of the Eppendorf lid. A stock AuNP solution was diluted to between 0 and 100% v/v in dH_2O (100% was undiluted), unless otherwise stated. For each method, tapping-mode AFM trace images of PNA, PNA Au and/or APS surfaces (Table 5.1) are shown. Images of APS Au surfaces incubated in each percentage of the stock AuNP solution are also shown. The average number density of AuNPs for each silicon surface (± SEM) was plotted against percentage volume to give a 'AuNP dilution gradient graph'.

a. Dilution of 10nm AuNP solution with dH_2O

AFM images are shown in Fig. 6.15a and a AuNP dilution gradient graph was plotted (Fig. 6.15b). The AuNP dimensions appeared to be slightly distorted and this may have lowered the apparent number density (Section 6.3.1.1a). However, the dimensions were uniform across the two experiments and therefore, were comparable. A steady increase in AuNP density was observed (335 to 538 AuNPs/μm^2) on surfaces incubated in 40% - 100% AuNP solution (Fig. 6.15b). A sharp increase in AuNP density was also observed (97 to 335 AuNPs/μm^2) for surfaces incubated with AuNP dilutions between 1%. - 20%.

b. Dilution of 20nm AuNP solution with dH_2O

AFM trace images are shown in Fig. 6.16a. A profile plot of a 20nm AuNPs shows that height measurements were accurate (18-20nm from horizontal and vertical cross-sections (Fig. 6.16b) allowing for AuNP size dispersity. However, there was substantial tip convolution leading to inaccurate lateral measurements (80nm). AuNP dimensions were uniform across the two experiments and therefore were comparable. A dilution gradient graph was plotted Fig. 6.16c. A sharp increase in AuNP density was observed (48 to 141 AuNPs/μm^2) on surfaces incubated in 20-80% AuNP solutions. No further increase was seen for 100%. This suggests that AuNP binding reached a maximum saturation, at 80%. A sharp linear increase in AuNP density was observed (6 to 48 AuNPs/μm^2) on surfaces incubated in 1% to 20% AuNP solutions. This was very similar to that observed for the 10nm solutions.

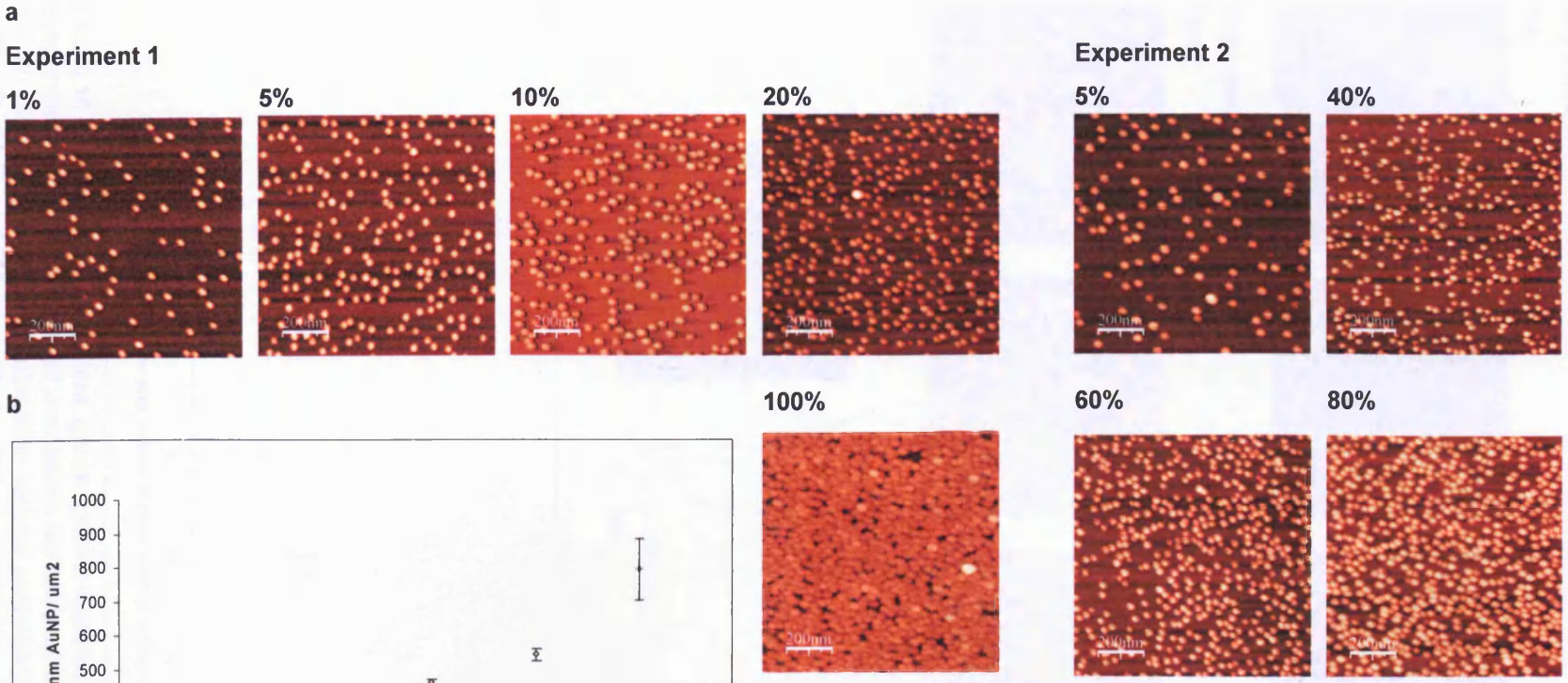


Fig. 6.15 AuNP dilution gradient graph (10nm AuNPs). APS (50% w/w in PO) was evaporated from an Eppendorf lid onto silicon surfaces centred at 2cm (level with the lip of the Eppendorf lid). Surfaces were then incubated in various percentage volumes of 10nm AuNPs (1-100%) in dH_2O. **a)** AFM trace images from two experiments are shown for each dilution after WSXM software processing. z-axis = 20nm. Scan size = $1\mu m^2$. **(b)** AuNP dilution graph: The average no. of AuNPs/μm^2 were counted manually or using WSXM flooding analysis from AFM scans (n = 3 ± SEM).

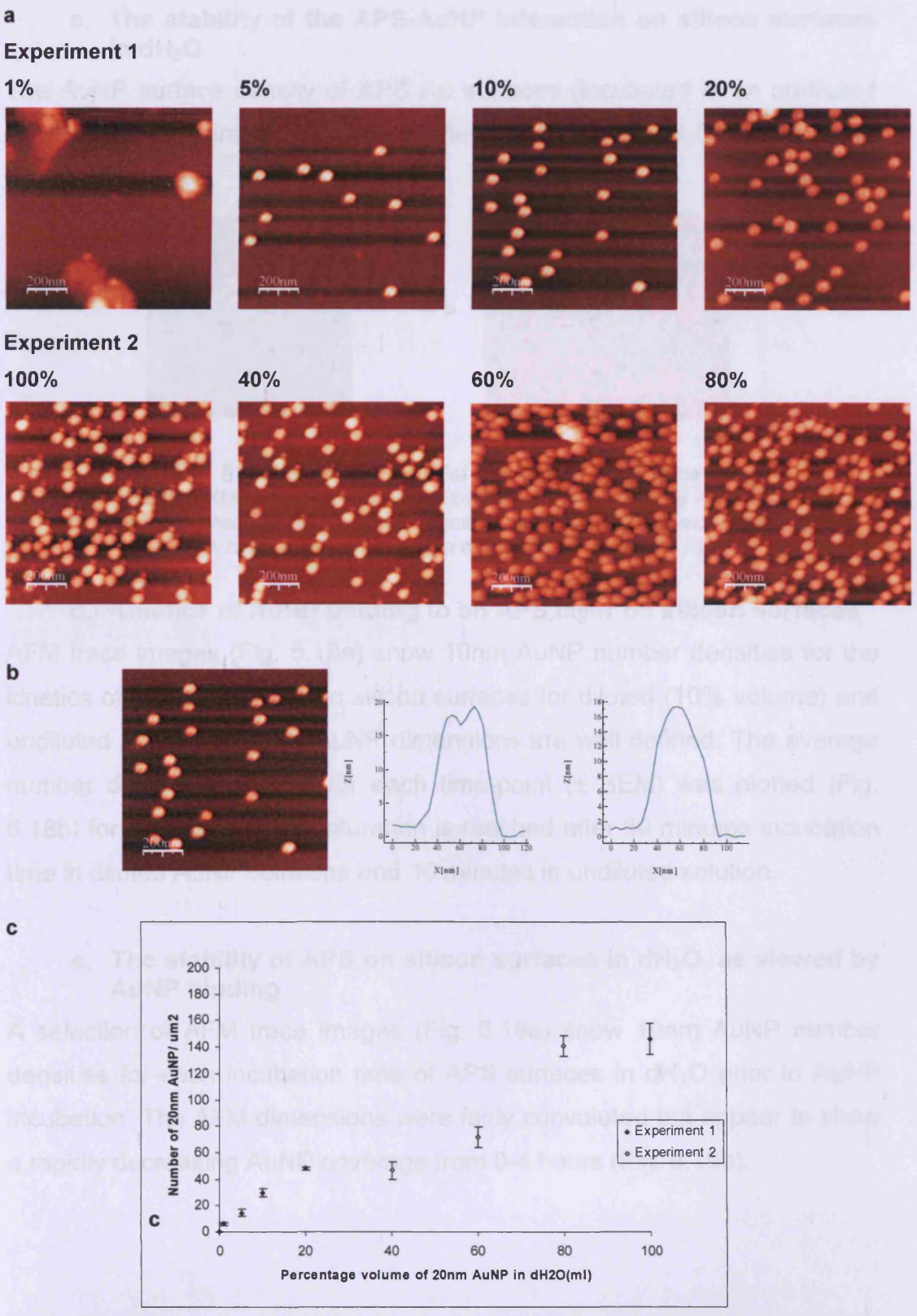


Fig. 6.16 AuNP dilution gradient graph (20nm AuNPs). APS (50% w/w in PO) was evaporated from an Eppendorf lid onto silicon surfaces centred at 2cm (level with the lip of the lid). Surfaces were then incubated in various percentage volumes of 20nm AuNPs (1-100%) in dH_2O. **a**) AFM trace images from two experiments are shown for each dilution after WSXM software processing. z-axis = 20nm. Scan size = 1μm^2. **b**) Dimensions of a 20nm AuNP on APS-derivatised silicon surfaces. Trace image (z = 20nm. Scan size = 1μm^2) of 20nm AuNPs (left). Profile images (centre and right) of the horizontal and vertical cross-sections of a single 20nm AuNP. **c**) AuNP dilution graph. The average no. of AuNPs/μm^2 were counted manually from AFM scans (n = 3 ± SEM).

c. The stability of the APS-AuNP interaction on silicon surfaces in dH_2O

The AuNP surface density of APS Au surfaces (incubated in an undiluted AuNP solution) remained constant after incubation in dH_2O for 24 hours (Fig. 6.17).

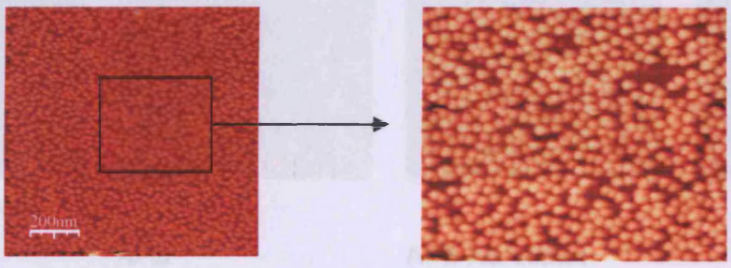


Fig. 6.17 Stability of the APS-Au interaction AFM trace image after WSXM software processing (z-axis = 20nm, scan size = 1μm^2. A saturated AuNP surface density was still observed after incubation of an APS Au surface in dH_2O for 24 hours (n = 1).

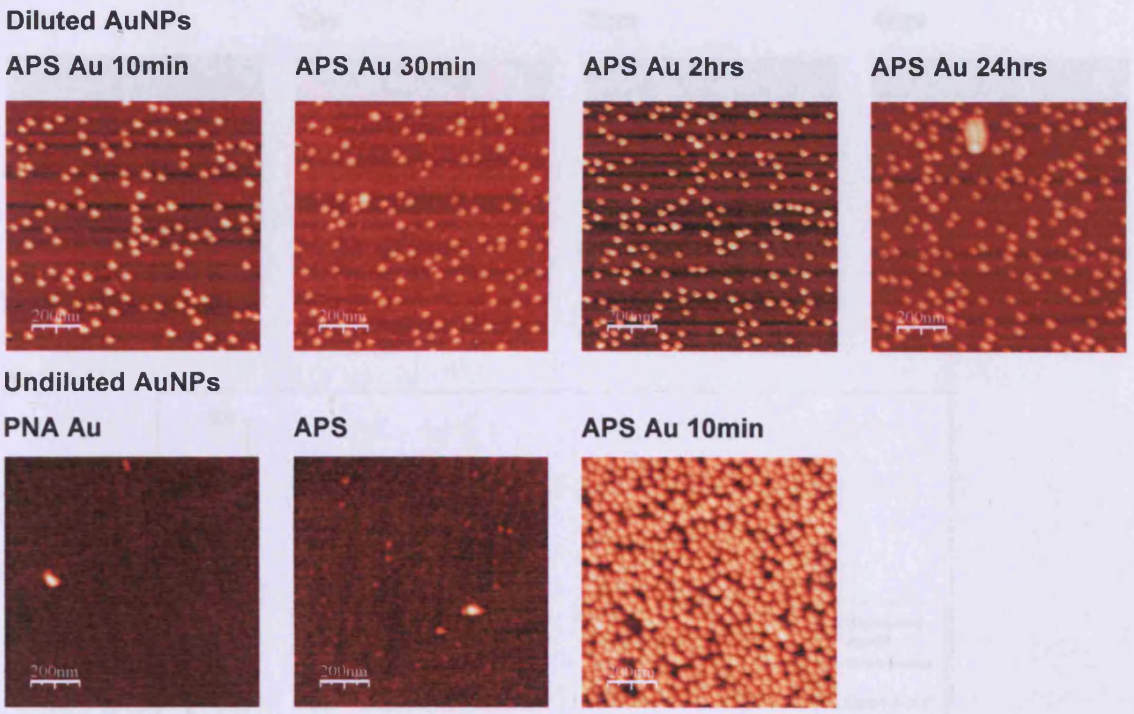
d. Kinetics of AuNP binding to an APS layer on silicon surfaces

AFM trace images (Fig. 6.18a) show 10nm AuNP number densities for the kinetics of binding to APS on silicon surfaces for diluted (10% volume) and undiluted AuNP solutions. AuNP dimensions are well defined. The average number density of AuNPs for each time-point (± SEM) was plotted (Fig. 6.18b) for diluted AuNPs. Saturation is reached after 30 minutes incubation time in diluted AuNP solutions and 10 minutes in undiluted solution.

e. The stability of APS on silicon surfaces in dH_2O, as viewed by AuNP binding

A selection of AFM trace images (Fig. 6.19a) show 10nm AuNP number densities for each incubation time of APS surfaces in dH_2O prior to AuNP incubation. The AFM dimensions were fairly convoluted but appear to show a rapidly decreasing AuNP coverage from 0-4 hours (Fig. 6.19b).

a



b

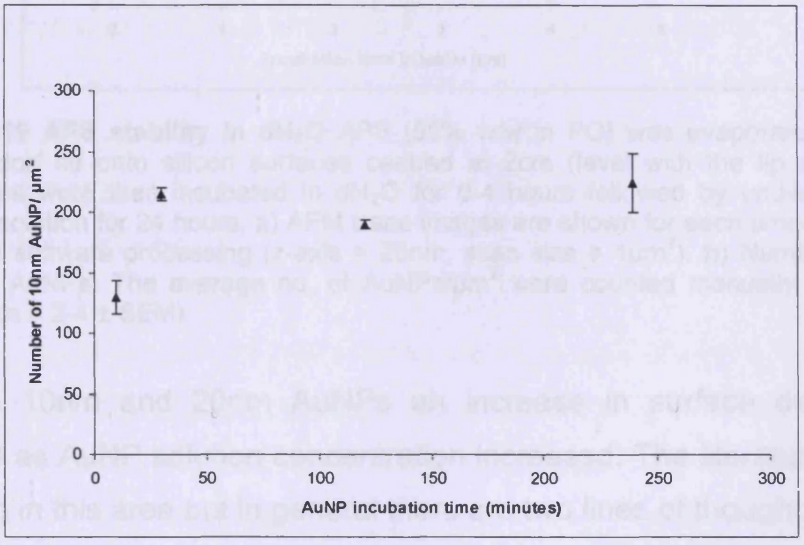


Fig. 6.18 Binding kinetics of diluted AuNPs. APS (50% w/w in PO) was evaporated from an Eppendorf lid onto silicon surfaces centred at 2cm (level with the lip of the lid). Surfaces were then incubated in diluted or undiluted 10nm AuNP solution for 0-24 hours. **a**) AFM trace images are shown for each time-point after WSXM software processing (z-axis = 20nm, scan size = 1µm^2). **b**) Number density plot of AuNP binding kinetics. The average no. of AuNPs/µm^2 were counted using WSXM flooding analysis (n = 3 ± SEM).

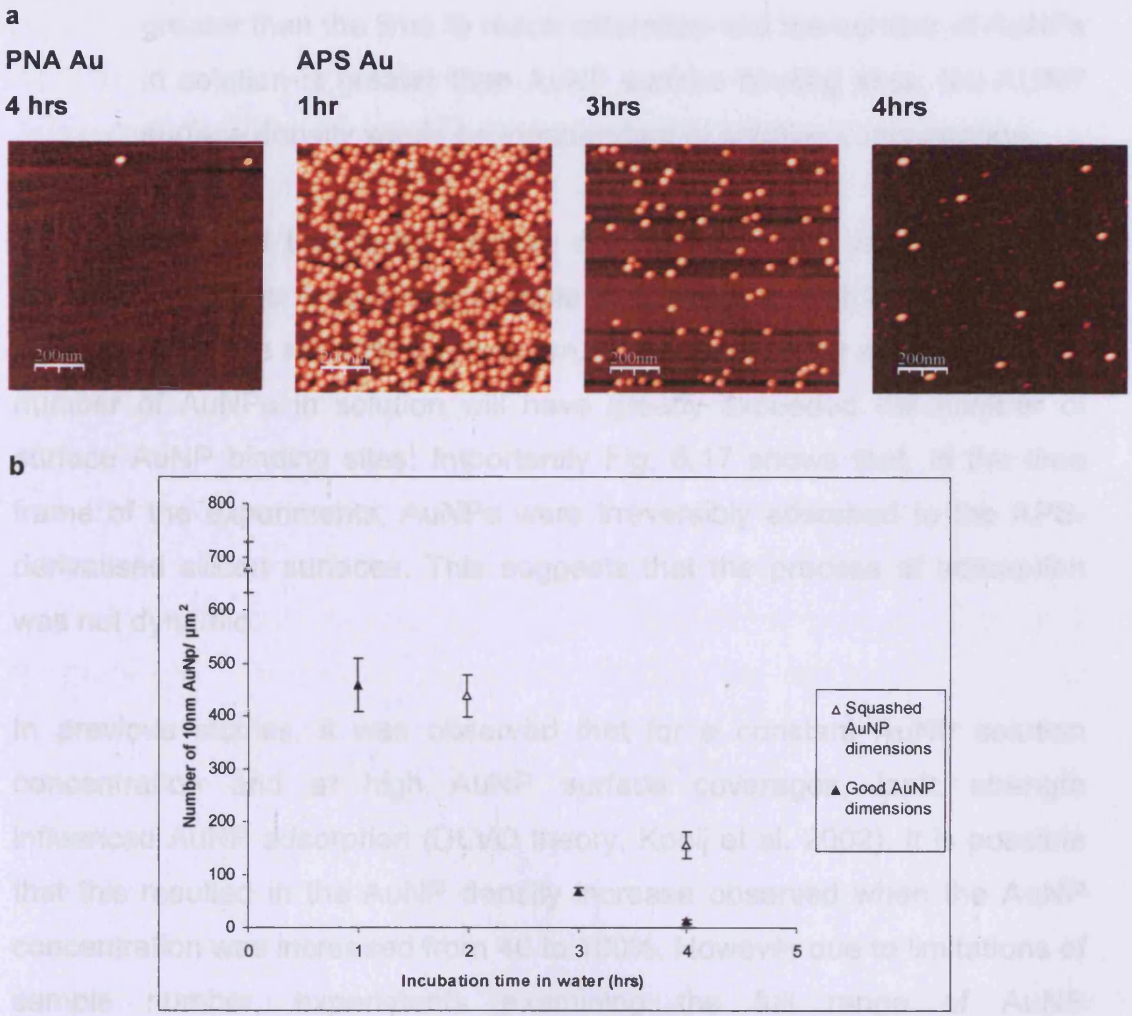


Fig. 6.19 APS stability in dH_2O APS (50% w/w in PO) was evaporated from an Eppendorf lid onto silicon surfaces centred at 2cm (level with the lip of the lid). Surfaces were then incubated in dH_2O for 0-4 hours followed by undiluted 10nm AuNP solution for 24 hours. **a**) AFM trace images are shown for each time-point after WSXM software processing (z-axis = 20nm, scan size = 1µm^2). **b**) Number density plot of AuNPs. The average no. of AuNPs/µm^2 were counted manually from AFM scans (n = 2-4 ± SEM).

For both 10nm and 20nm AuNPs an increase in surface density was observed as AuNP solution concentration increased. The literature is rather confusing in this area but in general there are two lines of thought:

i. AuNP binding to APS-derivatised surfaces is dynamic and as such it would be predicted that as the concentration of AuNPs in solution increased the surface density would increase. This relationship would be predicted to fit simple Langmuir type binding model (such as the Frumkin isotherm (Keating et al. 1999), Section 6.1.4.2)

ii. AuNP binding is irreversible (Kooij et al. 2003; Brouwer et al. 2005). In this case, for experiments where incubation times is

greater than the time to reach saturation and the number of AuNPs in solution is greater than AuNP surface binding sites, the AUNP surface density would be independent of solution concentration

Fig. 6.18 showed that AuNP surface density reached a maximum at 30 minutes. Therefore it would reasonable to suggest that at 24 hours AuNP densities will have reached a maximum. Additionally, in all experiments the number of AuNPs in solution will have greatly exceeded the number of surface AuNP binding sites. Importantly Fig. 6.17 shows that, in the time frame of the experiments, AuNPs were irreversibly adsorbed to the APS-derivatised silicon surfaces. This suggests that the process of adsorption was not dynamic.

In previous studies, it was observed that for a constant AuNP solution concentration and at high AuNP surface coverages, ionic strength influenced AuNP adsorption (DLVO theory, Kooij et al. 2002). It is possible that this resulted in the AuNP density increase observed when the AuNP concentration was increased from 40 to 100%. However due to limitations of sample number, experiments examining the full range of AuNP concentrations were not carried out at the same time. Therefore the increase observed from 40 to 100% AuNP solution, may be due to experimental variation.

In these studies the pH 6.5 stock AuNP solution was diluted with dH_2O. As previously reported (Zhu et al. 1999, Bhat et al. 2007), APS amine groups will be converted from ionised (NH_3^+) to unionised (NH_2) as pH increases (immobilised pKa 7.6, Bhat et al. 2007) and the former are required for electrostatic binding to AuNPs. Although no attempt was made to control pH in these experiments, all dilutions were shown to be between pH6.4 and 6.7 (When the pH was raised above the pKa of the silane with potassium carbonate (K_2CO_3), AuNP binding was not observed). Increasing solution pH also reduces the stability of the APS surface (Zhu et al. 1999). APS may self-hydrolyse from the surface upon extended periods of incubation in water (Etienne and Walcarius 2003).

APS surfaces were incubated for increasing time-points in water, followed by incubation in undiluted AuNP solution (Section 6.3.1.2e). A subsequent decrease in AuNP surface density was observed (Fig. 6.19), and may have reflected a decrease in NH_3+ density (pH effect) or total APS density (hydrolysis effect). In either case, incubation of APS surfaces in diluted AuNP solutions, for extended time-periods, would not be expected to give rise to an increase in surface AuNP density.

Although the results show that the observed trend in surface AuNP density was apparently a function of solution-phase concentration, the irreversible nature of AuNP adsorption (over a 24 hour time frame) suggested that a dynamic model was inappropriate. It is proposed that this trend resulted due to inter-AuNP electrostatic repulsion, whereby the interaction distances between AuNPs in solution is related to the resulting density of surface bound AuNPs. For a dilute solution, it is more favourable for the excess AuNPs to remain in solution than it is for them to increase the bound surface population. As the concentration of solution phase AuNPs increases the mean distance between particles decreases. This favours an increase in the surface bound population. Therefore the surface AuNP density is a function of solution concentration but it is not a function of the AuNP-surface bond energy.

Since the concentrations (number of particles per ml) of the purchased 20nm and 10nm AuNP solutions differed it was necessary to normalise their respective surface densities in order to directly compare results. For undiluted solutions of both 10nm and 20nm AuNPs the concentration of Au was ~0.01% (as tetrachloroaurate ($HAuCl_4$)). Since the volume of a 20nm AuNP (~4189nm^2) is eight times that of a 10nm AuNP (~524nm^2) the concentration of undiluted 20nm AuNPs would be eight times less than the 10nm solution. This would affect the relative densities of AuNPs adsorbed (Nath et al. 2004; Minard-Basquin et al. 2005). Also, a 20nm AuNP will cover an area four times greater than a 10nm AuNP (Fig. 6.20). Therefore, the theoretical maximum number of 10nm AuNPs that could be adsorbed in a 100nm^2 area would be ~100, whereas for 20nm AuNPs this number is ~25 (4-fold lower). Although this model is unrealistic for a random deposition of

spheres (Section 6.1.4.2; Feder 1980) it does serve as a simple illustration of the issue. As expected, the AuNP surface density for 20nm AuNPs (maximum 146/μm^2) was lower than 10nm AuNPs. The number density graphs are compared for 10 and 20nm AuNPs in Fig. 6.21 after a 12-fold adjustment of 20nm AuNP density, taking into account solution concentration and surface areas. At lower percentage volumes of AuNPs, i.e. when saturation of surface binding sites was not a limiting factor, the 10 and 20nm AuNP concentration gradient graphs appear to correlate.

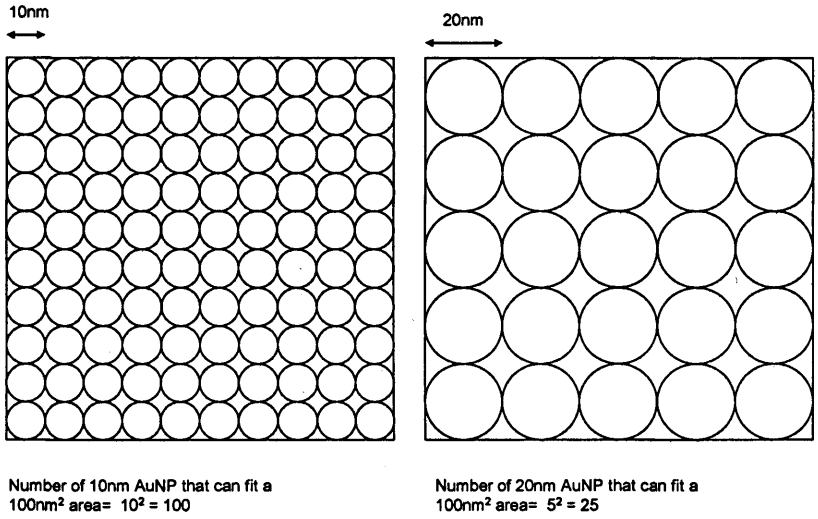


Fig. 6.20 A schematic showing surface areas occupied by closely packed 10nm and 20nm AuNPs.

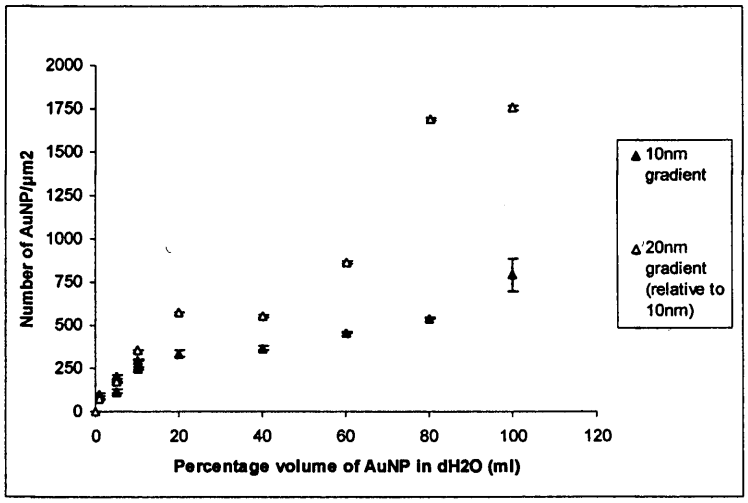


Fig. 6.21 A comparison between AuNP density gradient plots for AuNP dilution experiments a and b.

6.3.1.3 Non-specific binding of undiluted AuNP solution to underivatised silicon surfaces

When PNA Au surfaces were prepared using undiluted AuNP solution (rinsed three times in dH_2O (4ml)), greater non-specific AuNP binding, i.e. residual AuNP adherence to underivatised silicon, was observed than when PNA Au was prepared using 10% AuNP (in dH_2O) solution (Fig. 6.22). To reduce residual binding, the washing regime was subsequently modified by adding an additional 1L washing step (Fig. 6.22c).

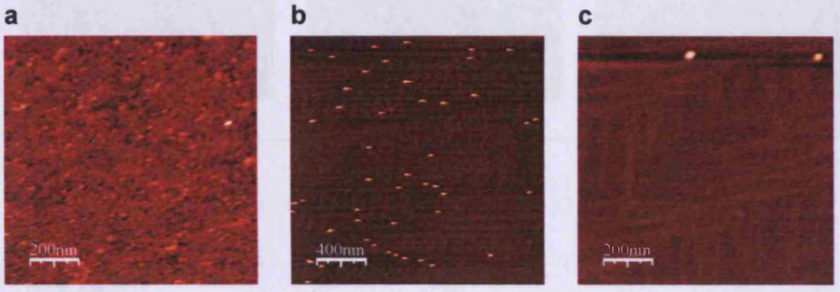


Fig. 6.22 Non-specific binding of 10nm AuNPs on PNA Au surfaces. a) Incubation with diluted AuNPs (10% in dH_2O) followed by three rinses in dH_2O (4ml). **b)** Incubation with undiluted AuNPs followed by three rinses in dH_2O (4ml). **c)** Incubation with diluted AuNPs followed by one rinse in dH_2O (1L, 30 seconds) and four rinses in dH_2O (4ml).

6.3.1.4 Changing the concentration of APS in the evaporation medium

For each method, AFM trace images of surfaces derivatised in the gas-phase with various APS concentrations (% w/w APS in PO) are shown. The average AuNP number densities (± SEM) for each silicon surface were plotted against APS concentration in an 'APS concentration gradient graph'.

a. APS concentration gradient experiments 1 and 2

AFM images (Figures 6.23a and 6.24a) show the dimensions of the 10nm and 20nm AuNPs to be accurate and uniform. The full range of AFM images are displayed in Appendix V. The APS concentration graphs were plotted (Figures 6.23b and 6.24b). Prior to establishing that the concentration of AuNPs in solution had an influence on the surface adsorbed AuNP concentration, stock AuNP solutions (10 or 20nm) were diluted to 10% volume in dH_2O and used to visualise the surface chemical modifications.

The average number densities for the 10nm and 20nm AuNPs were similar (Fig. 6.23b and 6.24b), with both reaching a maximum level at around 20% APS. In both cases a small increase from this maximal value appears to occur when the APS concentration reaches 100%.

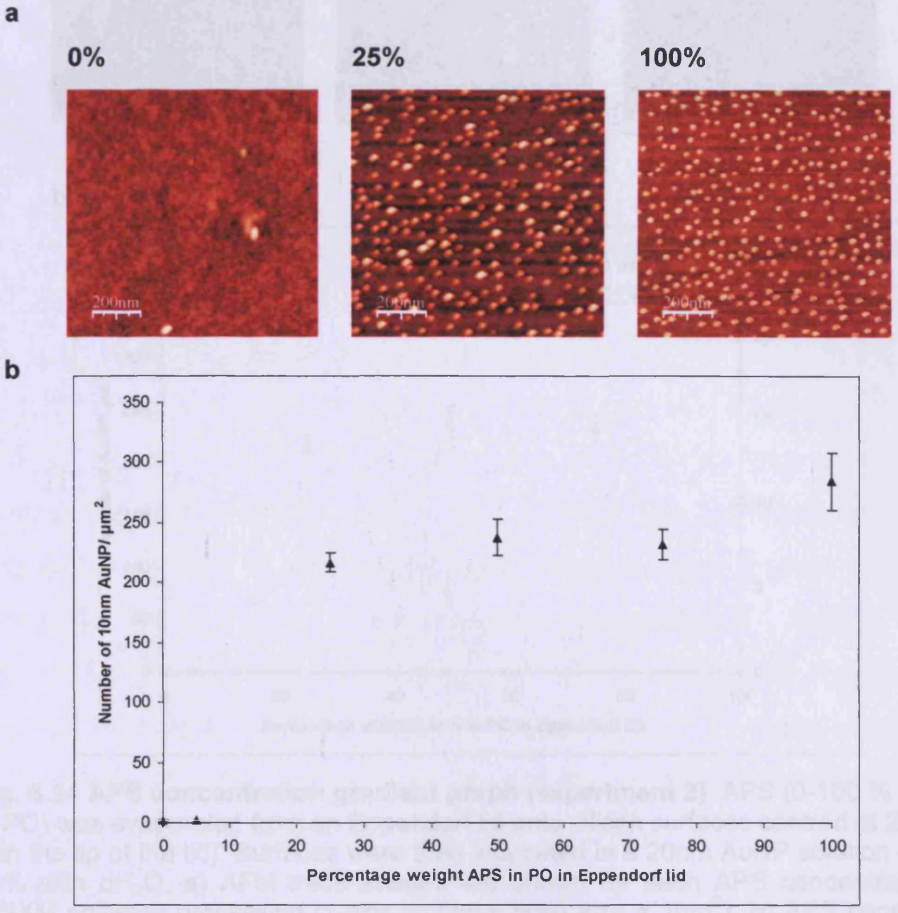


Fig. 6.23 APS concentration gradient graph (experiment 1). APS (0-100 % w/w APS in PO) was evaporated from an Eppendorf lid onto silicon surfaces centred at 2cm (level with the lip of the lid). Surfaces were then incubated in a 10nm AuNP solution diluted to 10% with dH_2O. **a)** A selection of AFM trace images are shown after WSXM software processing (z-axis = 20nm, scan size = 1µm^2). **b)** APS concentration gradient was plotted against AuNP density. The average no. of AuNPs/µm^2 were counted from AFM scans using WSXM flooding analysis (n = 1-5 ± SEM).

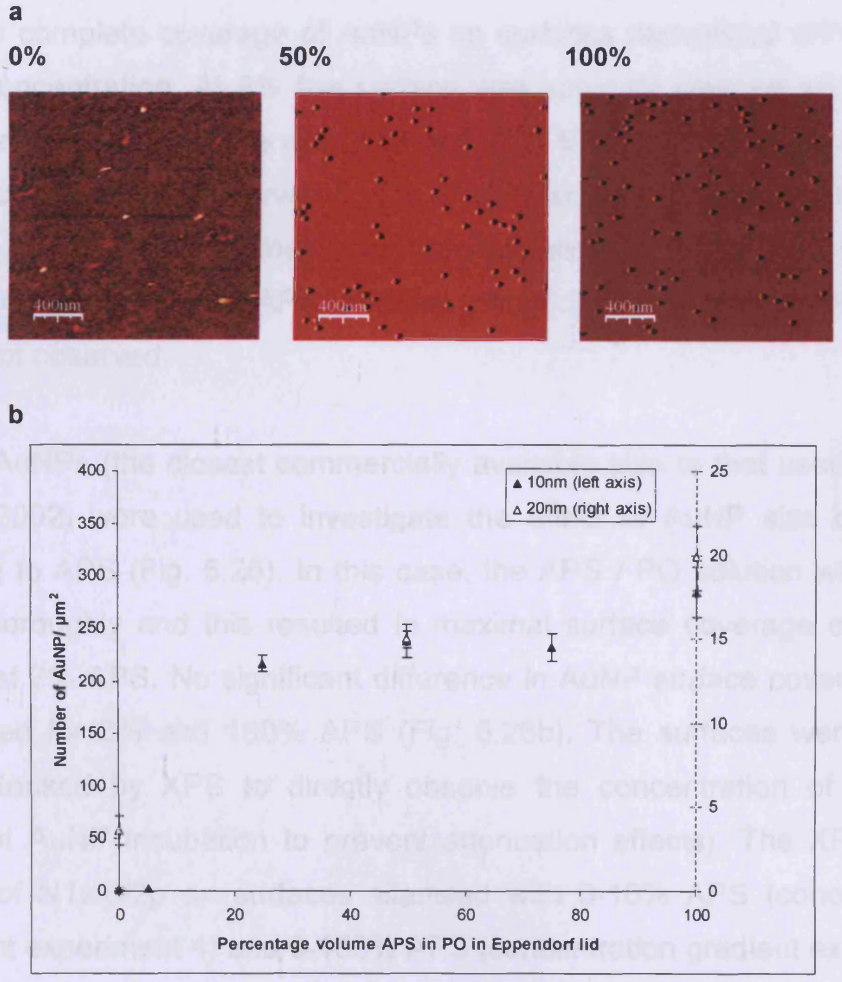


Fig. 6.24 APS concentration gradient graph (experiment 2). APS (0-100 % w/w APS in PO) was evaporated from an Eppendorf lid onto silicon surfaces centred at 2cm (level with the lip of the lid). Surfaces were then incubated in a 20nm AuNP solution diluted to 10% with dH_2O. **a**) AFM trace images are shown for each APS concentration after WSXM software processing (z-axis = 20nm, scan size = 1µm^2). **b**) APS concentration gradient was plotted against AuNP density t, comparing 10 and 20nm AuNP number densities. The average no. of AuNPs/µm^2 were counted from AFM scans using manual counting (n = 1-5 ± SEM).

b. APS concentration gradient experiment 3 and 4

Undiluted 10 and 20nm AuNP stock solutions were used to visualise surface chemical modifications. The full range of AFM images are shown in Appendix V. The 10 and 20nm AuNPs appeared to touch due to tip convolution, and the 20nm AuNPs appeared to cluster, possibly due to aggregation of the AuNPs in solution (Grabar et al. 1995). It has previously been observed that larger diameter AuNP solutions are usually less stable (Grabar et al. 1995).

For surfaces incubated with 10nm AuNPs (experiment 3a), there appeared to be a complete coverage of AuNPs on surfaces derivatised with 8-100% APS concentration. At 6% the surface was sparsely covered with AuNPs whilst at 4% AuNPs were not observed (Fig. 6.25). A high degree of non-specific binding was observed on the PNA Au surface. In experiment 3b, the longer APS/PO mixing times prior to silanisation gave rise to a complete AuNP coverage on 4% APS surfaces (Fig 6.25). At 2% and 0% AuNPs were not observed.

20nm AuNPs (the closest commercially available size to that used by Bhat et al. 2002) were used to investigate the effect of AuNP size on AuNP binding to APS (Fig. 6.26). In this case, the APS / PO solution was mixed very thoroughly and this resulted in maximal surface coverage of AuNPs with just 2% APS. No significant difference in AuNP surface coverage was observed for 2% and 100% APS (Fig. 6.26b). The surfaces were further characterised by XPS to directly observe the concentration of nitrogen (without AuNP incubation to prevent attenuation effects). The XPS molar ratios of N1s/Si2p on surfaces silanised with 0-10% APS (concentration gradient experiment 4) and 0-100% APS (concentration gradient experiment 5) is plotted in Fig. 6.27. There is a clear gradient of APS coverage from 0-10% which was not reflected in AuNP densities. It is probable that this anomaly was related to AuNP size and their ability to span a number of immobilised surface APS groups (Bhat et al. 2007). Therefore for a given solution concentration of AuNPs the resulting surface AuNP density will remain constant over a range of APS surface concentrations (Figure 6.28). This may also have been the reason that a AuNP density gradient was not observed for 'distance gradient' experiments in Section 6.3.1.1.

The lowest concentration of APS investigated for gas phase derivatisation was 2%. It is possible that lower concentrations would give rise to a more dispersed surface coverage. XPS results (Fig. 6.27) show that APS deposition reached a maximum when a 10% APS/PO solution was used. There was no increase in surface APS even when 100% APS was used. This suggests that at 10% APS the silicon surface was completely covered with an APS monolayer. There was no evidence for multilayer coverage

since there was no increase in surface nitrogen at APS concentrations >10 %.

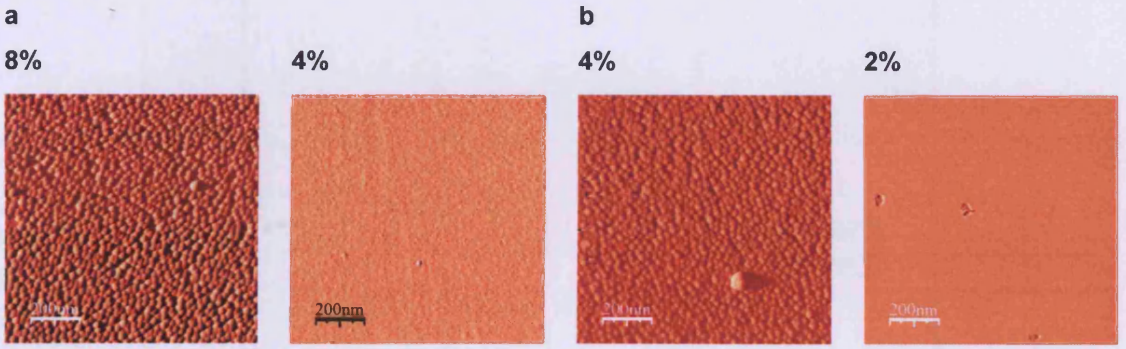


Fig. 6.25 AFM images of APS concentration gradient (experiment 3) surfaces. APS (0-100 % w/w APS in PO) was evaporated from an Eppendorf lid onto silicon surfaces centred at 2cm (level with the lip of the lid). Surfaces were then incubated in an undiluted 10nm AuNP solution. A selection of AFM trace images are shown after WSXM software processing (z-axis = 20nm, scan size = 1μm^2). **a**) Experiment 1. **b**) Experiment 2. (n = 1).

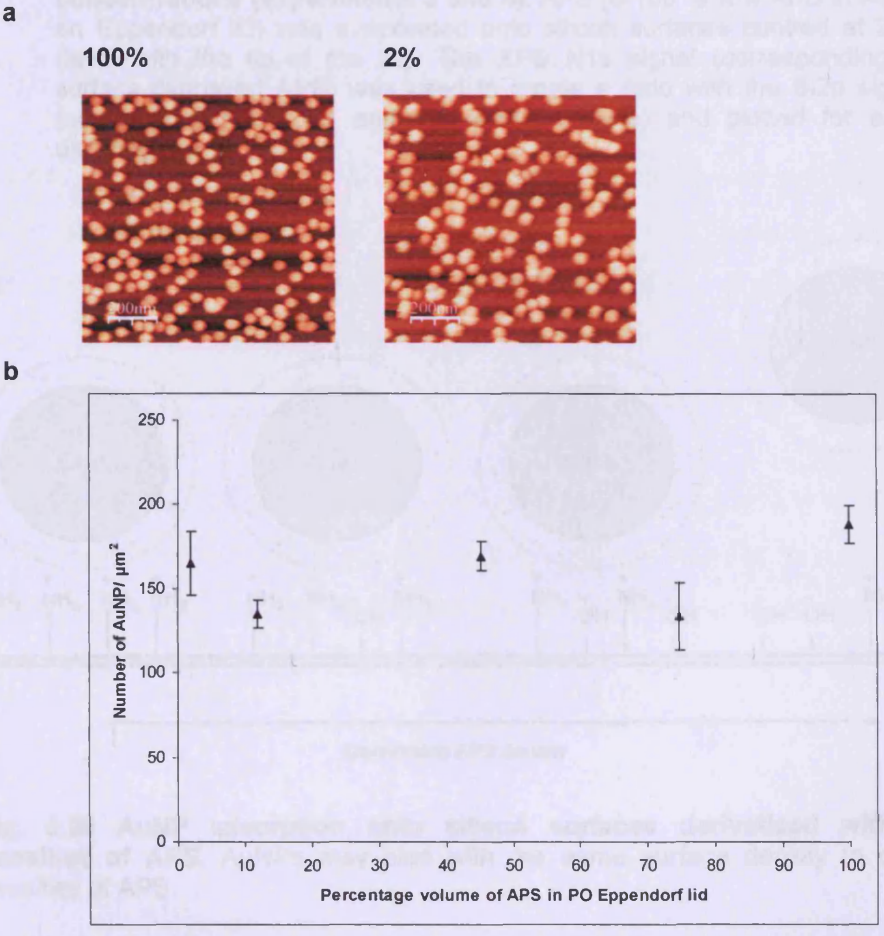


Fig. 6.26 APS concentration gradient graph (experiment 4). APS (2-100 % w/w APS in PO) was evaporated from an Eppendorf lid onto silicon surfaces centred at 2cm (level with the lip of the lid). Surfaces were then incubated in a undiluted 20nm AuNP solution. **a**) AFM trace images are shown for 2 and 100% after WSXM software processing (z-axis = 20nm, scan size = 1μm^2). **b**) APS concentration gradient was plotted against AuNP density. The average no. of AuNPs/μm^2 were counted manually AFM scans (n = 2-4 ± SEM).

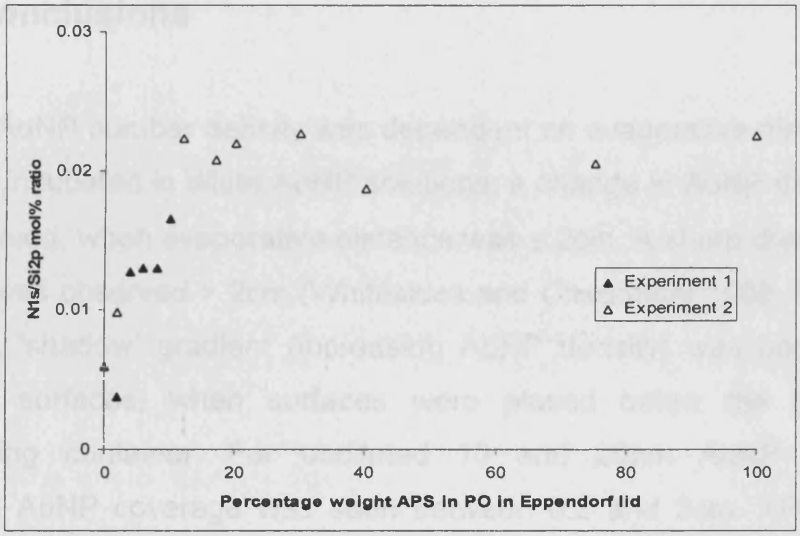


Fig. 6.27 XPS analysis of surfaces silanised with varying APS concentrations (experiments 3 and 4). APS (0-100 % w/w APS in PO in an Eppendorf lid) was evaporated onto silicon surfaces centred at 2cm (level with the lip of the lid). The XPS N1s signal (corresponding to surface-deposited APS) was used to create a ratio with the Si2p signal (corresponding to APS and the silicon surface) and plotted for each distance (n = 1).

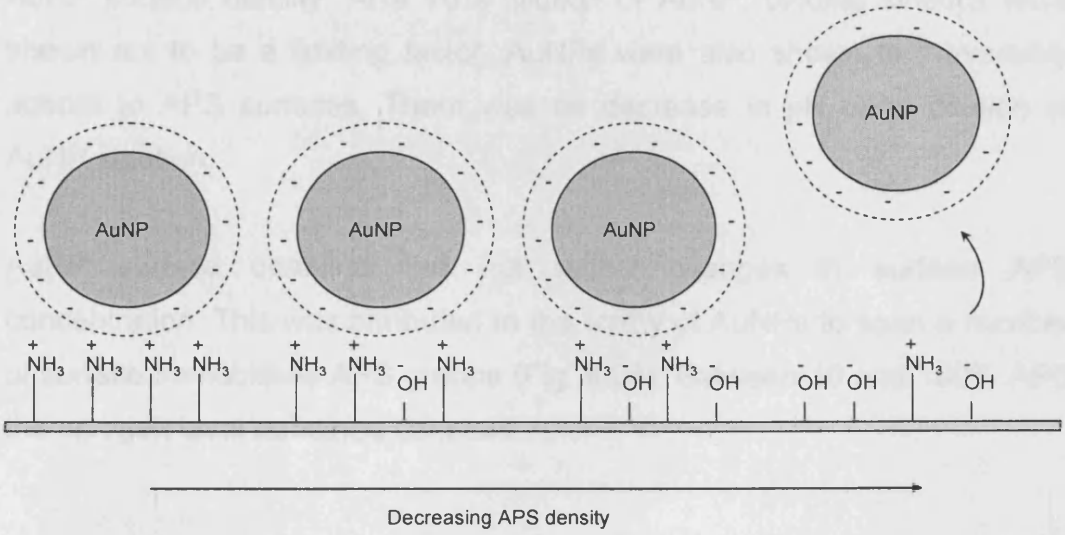


Fig. 6.28 AuNP adsorption onto silicon surfaces derivatised with various densities of APS. AuNPs may bind with the same surface density to decreasing densities of APS.

6.3.2 Conclusions

Surface AuNP number density was dependent on evaporative distance. For surfaces incubated in dilute AuNP solutions, a change in AuNP density was not observed, when evaporative distance was ≤ 2cm. A sharp drop in AuNP number was observed > 2cm (Whitesides and Chaudhury 1992; Bhat et al. 2002). A 'shadow' gradient (increasing AuNP density) was observed on 0.2–1cm surfaces, when surfaces were placed below the lip of the evaporating container. For undiluted 10 and 20nm AuNP solutions, complete AuNP coverage was seen between 0.2 and 3cm. XPS spectra were difficult to interpret due to attenuation of surface elements by AuNPs. A more thorough washing step was required to remove non-specifically bound AuNPs from surfaces after incubation with undiluted solutions.

Dilution of AuNPs (10nm or 20nm) was shown to reduce the adsorbed AuNP surface density. At a 10% dilution of AuNP, binding kinetics were shown not to be a limiting factor. AuNPs were also shown to irreversibly adsorb to APS surfaces. There was no decrease in pH upon dilution of AuNP solution.

AuNP surface densities did not reflect changes in surface APS concentration. This was attributed to the ability of AuNPs to span a number of surface-immobilised APS groups (Fig. 6.28). Between 10 and 100% APS the nitrogen level remained constant.

References

Baker, B. E. et al. 1996. Solution-based assembly of metal surfaces by combinatorial methods. *Journal of the American Chemical Society* 118(36), pp. 8721-8722.

Bhat, R. R. et al. 2002. Fabricating planar nanoparticle assemblies with number density gradients. *Langmuir* 18(15), pp. 5640-5643.

Bhat, R. R. and Genzer, J. 2005. Using spectroscopic ellipsometry for quick prediction of number density of nanoparticles bound to non-transparent solid surfaces. *Surface Science* 596(1-3), pp. 187-196.

Bhat, R. R. and Genzer, J. 2007. Tuning the number density of nanoparticles by multivariant tailoring of attachment points on flat substrates. *Nanotechnology* 18(2), pp. 1-6.

Bright, R. M. et al. 1998. Preparation and characterization of Ag colloid monolayers. *Langmuir* 14(20), pp. 5695-5701.

Brouwer, E. A. M. et al. 2005. Deposition kinetics of nanocolloidal gold particles. *Colloids and Surfaces A: Physicochemical and Engineering Aspects* 267(1-3), pp. 133-138.

Cant, N. E. et al. 2003. Surface functionalisation for the self-assembly of nanoparticle/polymer multilayer films. *Thin Solid Films* 426(1-2), pp. 31-39.

Chumanov, G. et al. 1996. Unusual extinction spectra of nanometer-sized silver particles arranged in two-dimensional arrays. *Journal of Physical Chemistry* 100(13), pp. 5166-5168.

Chumanov, G. et al. 1995. Colloidal Metal-Films as a Substrate for Surface-Enhanced Spectroscopy. *Journal of Physical Chemistry* 99(23), pp. 9466-9471.

Doron, A. et al. 1995. Organization of Au Colloids as Monolayer Films onto Ito Glass Surfaces - Application of the Metal Colloid Films as Base Interfaces to Construct Redox-Active Monolayers. *Langmuir* 11(4), pp. 1313-1317.

Efimenko, K. and Genzer, J. 2001. How to prepare tunable planar molecular chemical gradients. *Advanced Materials* 13(20), pp. 1560-1563.

Eigler, D. M. and Schweizer, E. K. 1990. Positioning Single Atoms with a Scanning Tunneling Microscope. In: Moriarty, P. 2006. *Molecular manipulation* [WWW]. Available at: http://www.nottingham.ac.uk/physics/research/nano/manipulation.htm [Accessed: 18th september 2006].

Elwing, H. et al. 1987. A wettability gradient method for studies of macromolecular interactions at the liquid/solid interface. In: Chaudhury, M. K. and Whitesides, G. M. 1992. How to Make Water Run Uphill. *Science* 256(5063), pp. 1539-1541.

Enders, D. et al. 2006. Reversible adsorption of Au nanoparticles on SiO2/Si: An in situ ATR-IR study. *Surface Science* 600(6), pp. 71-75.

Etienne, M. and Walcarius, A. 2003. Analytical investigation of the chemical reactivity and stability of aminopropyl-grafted silica in aqueous medium. *Talanta* 59(6), pp. 1173-1188.

Fan, H. Y. and Lopez, G. P. 1997. Adsorption of surface-modified colloidal gold particles onto self-assembled monolayers: A model system for the study of interactions of colloidal particles and organic surfaces. *Langmuir* 13(2), pp. 119-121.

Feder, J. 1980. Random sequential adsorption. *Journal of Theoretical Biology* 87(2), pp. 237-254.

Grabar, K. C. et al. 1996. Two-dimensional arrays of colloidal gold particles: A flexible approach to macroscopic metal surfaces. *Langmuir* 12(10), pp. 2353-2361.

Grabar, K. C. et al. 1997. Nanoscale characterization of gold colloid monolayers: A comparison of four techniques. *Analytical Chemistry* 69(3), pp. 471-477.

Grabar, K. C. et al. 1995. Preparation and Characterization of Au Colloid Monolayers. *Analytical Chemistry* 67(4), pp. 735-743.

Grabar, K. C. et al. 1996. Kinetic control of interparticle spacing in Au colloid-based surfaces: Rational nanometer-scale architecture. *Journal of the American Chemical Society* 118(5), pp. 1148-1153.

Han, M. et al. 2007. Controllable synthesis of two-dimensional metal nanoparticle arrays with oriented size and number density gradients. *Advanced Materials* 19(19), pp. 2979-2983.

Ito, Y. et al. 2007. The movement of a water droplet on a gradient surface prepared by photodegradation. *Langmuir* 23(4), pp. 1845-1850.

Jonas, U. et al. 2002. Colloidal assemblies on patterned silane layers. *Proceedings of the National Academy of Sciences of the United States of America* 99(8), pp. 5034-5039.

Keating, C. D. et al. 1999. Kinetics and thermodynamics of Au colloid monolayer self-assembly - Undergraduate experiments in surface and nanomaterials chemistry. *Journal of Chemical Education* 76(7), pp. 949-955.

Kooij, E. S. et al. 2002. Ionic strength mediated self-organization of gold nanocrystals: An AFM study. *Langmuir* 18(20), pp. 7677-7682.

Kraus, T. et al. 2007. Nanoparticle printing with single-particle resolution. *Nature Nanotechnology* 2(9), pp. 570-576.

Li, Q. G. et al. 2003. Site-selective assemblies of gold nanoparticles on an AFM tip-defined silicon template. *Langmuir* 19(1), pp. 166-171.

Liu, S. T. et al. 2004. Planned nanostructures of colloidal gold via self-assembly on hierarchically assembled organic bilayer template patterns with in-situ generated terminal amino functionality. *Nano Letters* 4(5), pp. 845-851.

Liu, S. T. et al. 2002. Evaporation-induced self-assembly of gold nanoparticles into a highly organized two-dimensional array. *Physical Chemistry Chemical Physics* 4(24), pp. 6059-6062.

Minard-Basquin, C. et al. 2005. Gold-nanoparticle-assisted oligonucleotide immobilisation for improved DNA detection. *IEE Proceedings-Nanobiotechnology.* 152(2), pp. 97-103.

Moriarty, P. 2006. *Molecular manipulation* [Online]. Available at: http://www.nottingham .ac.uk/physics/research/nano/manipulation.htm [Accessed: 18th september 2006].

Moriarty, P. et al. 1998. Translation, rotation and removal of C-60 on Si(100)-2x1 using anisotropic molecular manipulation. In: Moriarty, P. 2006. *Molecular manipulation* [WWW]. Available at: http://www.nottingham.ac.uk/physics/research/nano/ manipulation.htm [Accessed: 18th september 2006].

Nath, N. and Chilkoti, A. 2004. Label-free biosensing by surface plasmon resonance of nanoparticles on glass: Optimization of nanoparticle size. *Analytical Chemistry* 76(18), pp. 5370-5378.

Park, K. et al. 1987. Surface Characterization of Biomaterials by Immunogold Staining - Quantitative-Analysis. In Grabar, K. C. et al. 1996. Kinetic control of interparticle spacing in Au colloid-based surfaces: Rational nanometer-scale architecture. *Journal of the American Chemical Society* 118(5), pp. 1148-1153.

Park, S. H. et al. 1999. Adsorption kinetics of Au and Ag nanoparticles on functionalized glass surfaces. *Microchemical Journal* 63(1), pp. 71-91.

Rao, C. N. R. and Cheetham, A. K. 2001. Science and technology of nanomaterials: current status and future prospects. *Journal of Materials Chemistry* 11(12), pp. 2887-2894.

Ruardy, T. G. et al. 1997. Preparation and characterization of chemical gradient surfaces and their application for the study of cellular interaction phenomena. *Surface Science Reports* 29(1), pp. 3-30.

Shaw, D. J. 1992. *Introduction to colloid and surface chemistry.* Redwood books, pp. 26, 229, 810.

Shen, T. C. et al. 1995. Atomic-Scale Desorption through Electronic and Vibrational-Excitation Mechanisms. In: Moriarty, P. 2006. *Molecular manipulation* [WWW]. Available at: http://www.nottingham.ac.uk/physics/research/nano/manipulation.htm [Accessed: 18th Sep 2006].

Shipway, A. N. et al. 2000. Nanoparticle arrays on surfaces for electronic, optical, and sensor applications. *Chemphyschem* 1(1), pp. 18-52.

Song, F. et al. 2006. Fabricating tunable nanoparticle density gradients with the contact printing based approach. *Applied Surface Science* 253(5), pp. 2393-2398.

Verwey, E. J. W. and Overbeek, J. 1948. *Theory of the stability of lyophobic colloids.* Elselvier. In: Kooij, E. S. et al. 2002. Ionic strength mediated self-organization of gold nanocrystals: An AFM study. *Langmuir* 18(20), pp. 7677-7682.

Wayment, J. R. and Harris, J. M. 2006. Controlling binding site densities on glass surfaces. *Analytical Chemistry* 78(22), pp. 7841-7849.

Zhang, H. et al. 1998. Force titration of amino group-terminated self-assembled monolayers of 4-aminothiophenol on gold using chemical force microscopy. In Zhu, T. et al. 1999. pH-dependent adsorption of gold nanoparticles on p-aminothiophenol-modified gold substrates. *Langmuir* 15(16), pp. 5197-5199.

Zin, M. T. et al. 2006. Arrays of covalently bonded single gold nanoparticles on thiolated molecular assemblies. *Langmuir* 22(14), pp. 6346-6351.

Chapter 7

Chemical attachment of ETH to APS-derivatised silicon surfaces

7.1 Introduction

Step two (Fig. 7.1) of the protein imprinting schematic (Fig. 1.12) was to attach the high-affinity ligand of human serum albumin (HSA), ethacrynic acid (ETH), or its derivative ethacrynic acid-glycine (ETHGly, Fig. 4.18), to aminopropyltriethoxysilane (APS)-derivatised silicon surfaces. ETH deposition was monitored using XPS.

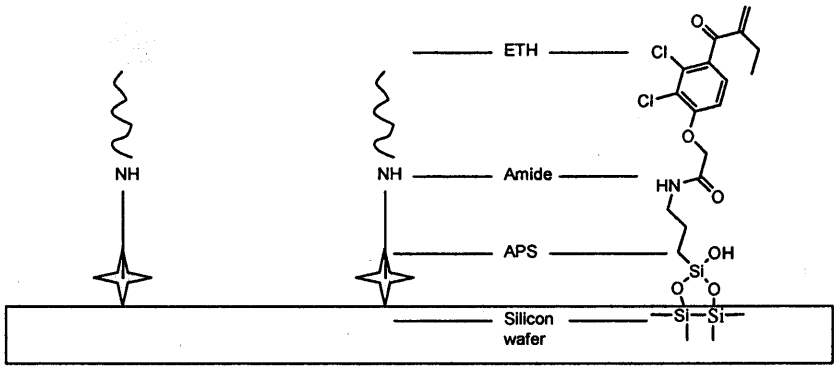


Fig. 7.1 Step two of a novel protein imprinting approach. ETH (a high-affinity ligand of HSA) attachment to an APS-derivatised silicon surface.

7.1.1 Amide coupling on surfaces

1-ethyl-3-(3-dimethylaminopropyl) carbodiimide (EDC) was chosen as the amide coupling reagent (previously used to couple ETH and Gly in solution (Section 4.2.4.3)). EDC is a useful water-soluble reagent often used to couple non-specific amine groups of proteins to carboxylated surfaces (Van der Merwe 2003). However, EDC has also been used for coupling carboxylic acids (fullerines (Patoslky et al. 1998), halyuronic acid (Stile et al. 2002) and Ferrichrome A hexapeptide (Melzak et al. 1995) to amine-derivatised surfaces. EDC coupling may behave differently on surfaces than in solution. Using various amide coupling reagents, Yang (Yang et al. 2000) reported lower yields and increased racemization of 3,5-dinitrobenzoyl-L-leucine (DNB-L-LEU) when coupling to APS silica gel than compared to APS in solution. This was attributed to a possible slowing of the product formation rate on surfaces, favouring by-product pathways.

7.1.2 Chapter objectives

- To covalently link a high-affinity ligand (or its derivative) to dispersed APS groups on a silicon surface using an amide coupling reagent.
- To characterise ligand immobilisation using AFM and/or XPS

7.2 Methods

Extra-dry DMF was used as the solvent unless otherwise stated (as used for solution-phase experiments, Section 4.2.1.3). APS surfaces were silanised using the standard protocol (Section 5.2.2.4) unless otherwise stated.

7.2.1 Equipment and materials

As for Sections 4.2.1 and 5.2.1.

7.2.2 XPS analysis of ETH-treated silicon surfaces

In a parallel experiment with Section 6.2.2.1b, each surface (0.5, 1.5, 2.5 and 3.5cm) was incubated in 0.3mM ETH in DMF and rinsed in DMF, acetone, MeOH, $CHCl_3$ (10 min each) and dH_2O (30 min). AFM scans were not carried out for these surfaces. XPS was used to detect surface chlorine (Cl2p and Cl2s electrons).

7.2.3 XPS analysis of APS-derivatised silicon surfaces incubated with ETH and EDC

Surfaces were silanised with APS for 15 minutes. APS surfaces were then incubated with different concentrations of ETH (1 or 5mM) and EDC (5 or 20mM) in extra-dry $CHCl_3$, DMF or DCM (Table 7.1).

Table 7.1 ETH / EDC surface treatments using different solvents

Surface	Extra-dry solvent	ETH concentration (mM)	EDC concentration (mM)
1	$CHCl_3$	1	5
2	$CHCl_3$	5	20
3	DMF	1	5
4	DMF	5	20
5	DCM	1	5
6	DCM	5	20

7.2.4 Deprotonation of surface amines using NaOH to improve amide coupling to ETH

PNA and APS-derivatised surfaces were treated according to Table 7.2. NaOH treatment involved incubation of surfaces in 0.1M NaOH (5 min). Surfaces were then washed in MeOH, one vigorous and two static (10 minutes). Surfaces were then re-cured at 80°C for one hour. DMF (extra-dry) treatment involved incubation (24 hrs) in DMF followed by two DMF washes (15 min) and one in dH_2O (15 min). All surfaces were then incubated in a solution of 10nm AuNPs (10% in dH_2O) for 24 hours and analysed by AFM.

Table 7.2 Control surface treatments

Surface	Surface treatment	NaOH incubation	DMF incubation
1	PNA	no	no
2	APS	no	no
3	APS	no	yes
4	APS	yes	yes

7.2.5 Amide coupling of ETH to APS surfaces

PNA and APS surfaces were incubated for 5 minutes in 0.1M NaOH as described in Section 7.2.3. PNA and APS surfaces were then incubated with or without ETH and/or EDC for 24 hours in dry DMF (Table 7.3). The surfaces were washed three times in DMF, dried and incubated in undiluted AuNP solution for 24 hrs. In a follow-up experiment, surfaces were sonicated in DMF after the incubation step.

Table 7.3 ETH / EDC surface treatments

Surface	Surface treatment	Solvent	ETH concentration (mM)	EDC concentration (mM)
1	PNA	DMF	-	-
2	PNA	DMF	1	-
3	PNA	DMF	-	5
4	PNA	DMF	1	5
5	APS	DMF	-	-
6	APS	DMF	1	-
7	APS	DMF	-	5
8	APS	DMF	1	5

7.3 Results and discussion

7.3.1 XPS analysis of ETH-treated silicon surfaces

APS-derivatised surfaces were incubated with ETH to determine whether the latter would bind non-specifically to the silicon surfaces. XPS montages were created using CASA XPS software (Section 5.3.2.2).

ETH has two chlorine atoms, which distinguish it from other surface molecules and atoms. Aromatic Cl2p peaks are usually seen at ~200eV (Moulder 1995). Fig. 7.2a shows a montage of Cl2p XPS spectra (bottom to top: PNA Au, 0.5cm, 1.5cm, 2.5cm and 3.5cm), showing signals (low) at ~200eV. XPS was previously used to analyse surfaces not incubated with ETH (Section 6.2.2.5c) and in these spectra a similar signal was observed at ~200eV (Fig. 7.2b). This was probably a 'satellite' signal of the silicon surface. Many satellites were observed between ~100-250eV (Fig. 7.3) for surfaces incubated with and without ETH. Satellites were probably caused by multiple reflections of the X-ray photoelectron beam (Ohtani et al. 2006). The Cl2s signal was not observed on any of the surfaces. The expanded region of the C1s spectrum where the Cl2s peak (~270eV) was expected is shown for the 0.5cm surface (Fig. 7.4). The Cl2s signal is not as strong the 2p signal and may be too weak to see, even with some ETH binding. However, without any obvious Cl2p or Cl2s signals it is unlikely that ETH was non-specifically bound on these surfaces. Variation in carbon contamination between the control and test surfaces made it impossible to estimate surface ETH from its C1s signal.

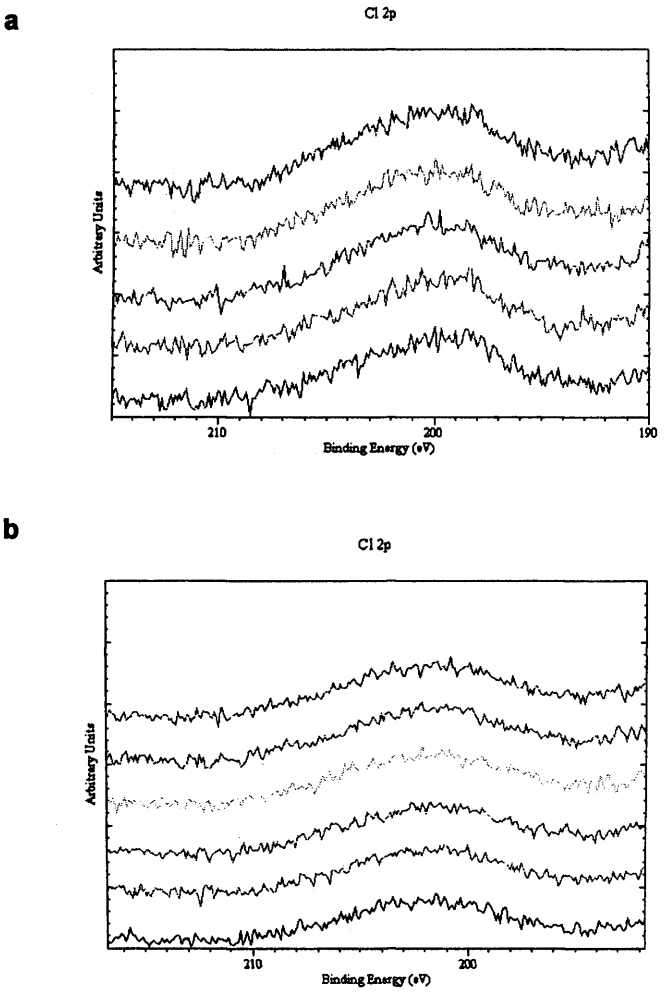


Fig. 7.2 Montage of XPS Cl2p spectra for the detection of non-specific ETH binding on PNA and APS surfaces. a) Surfaces incubated with 0.3mM ETH in DMF (from bottom-top: PNA; APS 0.5cm, 1.5cm, 2.5cm and 3.5cm,). b) APS surfaces not incubated in ETH (Section 6.2.2.5c). The montages were created in CASA XPS. (n = 1).

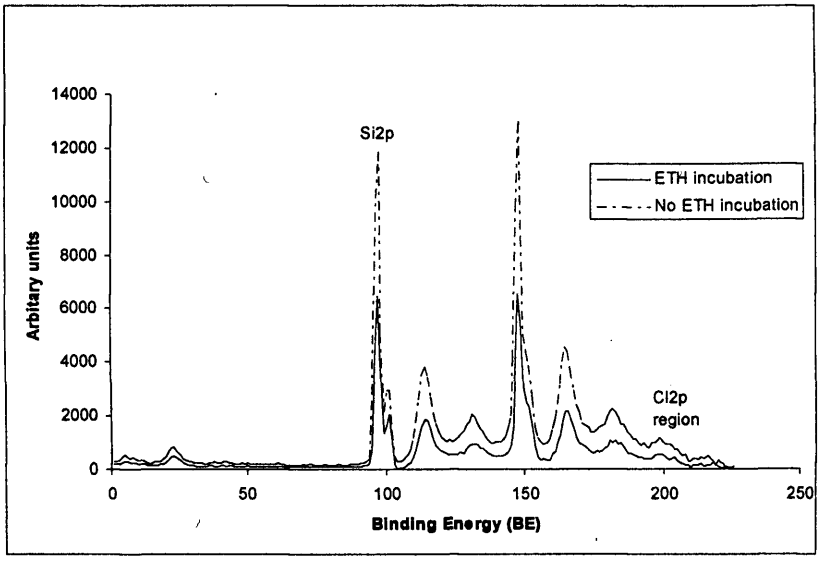
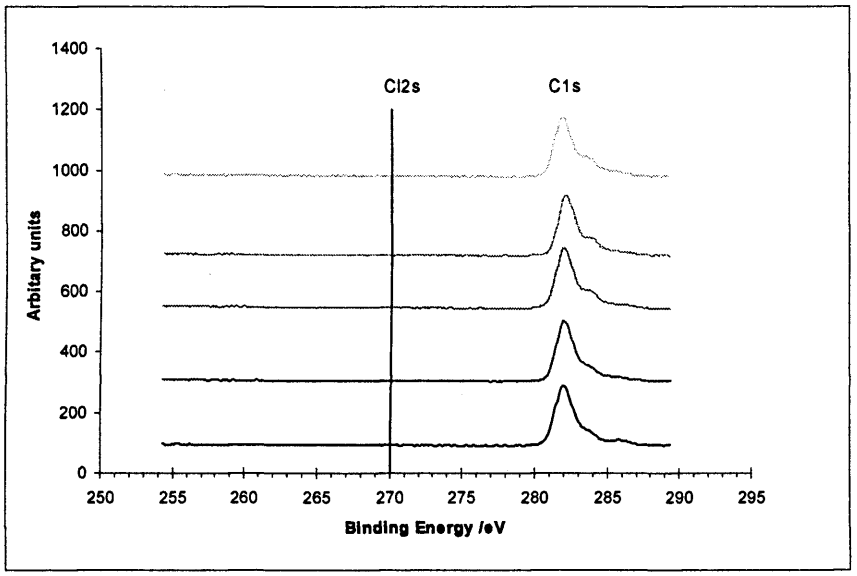


Fig. 7.3 Silicon satellite peaks for APS surfaces incubated with and without ETH. A section of the survey spectra (0-250eV) from surfaces incubated with (Section 7.2.1) or without (Section 6.2.2.5c) ETH. The background was normalized.

a



b

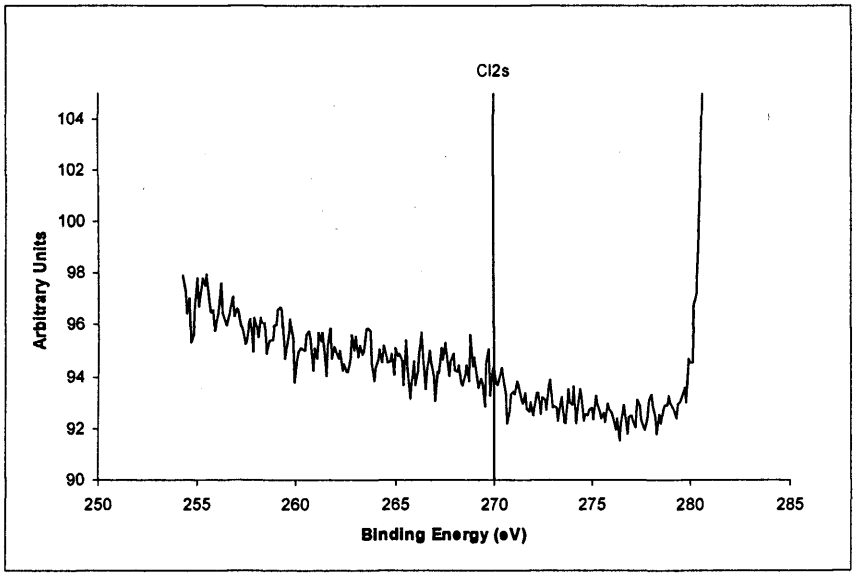


Fig. 7.4 XPS Cl2s spectra of ETH-incubated surfaces. Surfaces were incubated in 0.3mM ETH (Section 7.2.1), and analysed by XPS for a Cl2s signal. **a**) A montage of C1s spectra is shown for surfaces (bottom-top): PNA; APS 0.5cm, 1.5cm, 2.5cm and 3.5cm. (n = 1). The Cl2s peak is expected at 270eV (line). **b**) The Cl2s region was expanded for the 0.5cm surface.

7.3.2 XPS analysis of APS-derivatised silicon surfaces incubated with ETH and EDC

XPS montages were created using CASA XPS software and mol% compositions were calculated using ESCA software (Section 5.3.2.2).

Apolar, aprotic solvents ($CHCl_3$ and DCM) were used as well as DMF (polar aprotic) for the amide coupling reaction. $CHCl_3$ and DCM may reduce possible side-reactions of the EDC chemistry because they are apolar (Section 4.1.4.3). They were not used in solution-phase experiments (Section 4.2.1.3) because GlyOMe did not solubilise. In these experiments, the amine groups were attached to the silicon substrate.

A 5:1 ratio of EDC:ETH was maintained for all of the experiments (as used in Patolsky et al. 1998 for fullerene coupling to amine surfaces). Control surfaces were not analysed by XPS, and therefore definitive conclusions about ETH deposition could not be made. A montage of Cl2p XPS spectra (Fig. 7.5a) shows a repeating signal which is likely to be a satellite signal once more. However, the peaks do appear sharper and correspond with the expected binding energies for Cl2p (Fig. 7.5b). If the peaks were real Cl2p signals, they are relatively small compared to N1s (even though the signal should be just as strong), suggesting a low coupling efficiency. Once again, no Cl2s signal was observed for any of the surfaces. Without an excess of amine, the EDC reaction successfully demonstrated in solution between ETH and GlyOMe (Section 4.3.1.3) may not be as efficient between ETHGly and APS on silicon surface. The formation of the by-product may be favoured (in this case N-acylurea Fig. 4.4), as previously demonstrated for DNB-L-Leu (Yang et al. 2000, Section 7.1.1)).

The total mol % composition of N1s (1.19%) was similar to that measured previously (1.25%, Section 5.3.1.3), and was consistent for all of the surfaces (Fig. 7.6). This suggests that EDC adsorption (which would be characterised by an increased N1s signal (structure in Fig. 4.13a)) was absent or very low.

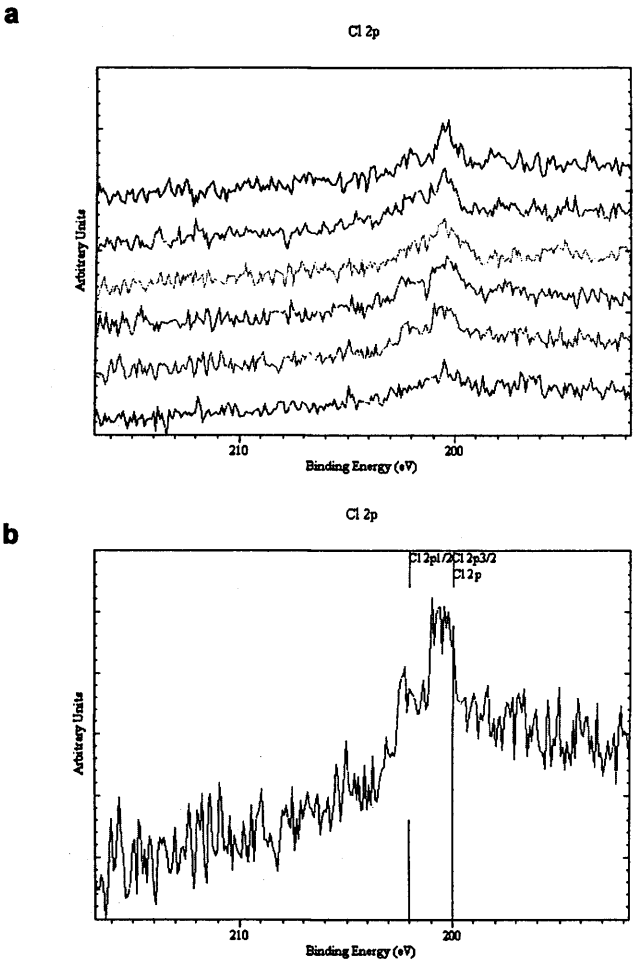


Fig. 7.5 XPS Cl2p spectra for the EDC-mediated coupling of ETH to APS surfaces. a) A montage of C1s spectra is shown for surfaces (top-bottom): 1, 2, 3, 4, 5, 6 (Table 7.2.1). **b**) A single spectrum for surface 5 showing the expected signals for Cl2p. (n = 1).

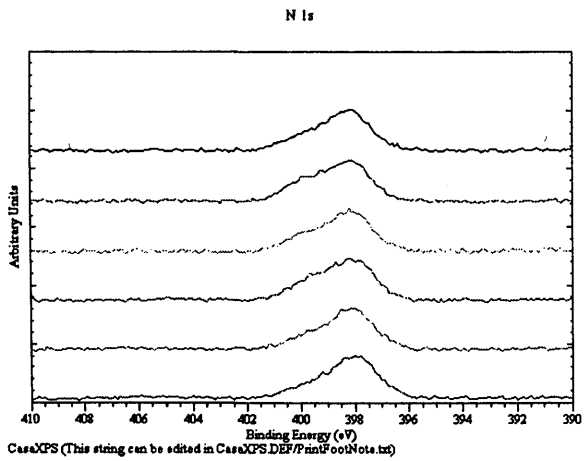


Fig. 7.6 XPS N1s spectra for the EDC-mediated coupling of ETH to APS surfaces. A montage of N1s spectra is shown for surfaces (bottom-top): 1, 2, 3, 4, 5 and 6 (Table 7.2.1). (n = 1).

7.3.3 Deprotonation of surface amines using NaOH to improve amide coupling to ETH

Uncharged amine (NH_2) was required for nucleophilic attack of the activated carboxyl group of ETH (Fig 4.4). In an attempt to improve the coupling efficiency of ETH to APS, NaOH incubation was used to favour amine conversion from NH_3^+ to NH_2 groups. The surfaces were agitated in the first wash to prevent possible surface precipitation of NaOH in MeOH. A DMF incubation step was included as a control for future coupling experiments.

AuNP binding was previously shown to be an inappropriate quantitative method for determining changes in APS surface density (Section 6.3.1.4b). However, it does give qualitative indication of APS density (Section 6.3.1.2e). The AuNP surface density was reduced for APS surface 2 compared to APS surface 1, suggesting a reduced APS density for surface 2 (Fig. 7.7). It is probable that the basic NaOH solution hydrolysed APS from surface 2 (Zhu et al. 1999) and it is likely that a milder base would be more appropriate. XPS data obtained by another researcher confirmed that significant hydrolysis of APS occurred under conditions comparable to surface treatment 2. Incubation in DMF (24 hrs) did not affect subsequent AuNP binding for surface 3 (Fig. 7.7). DMF therefore was deemed a suitable solvent for the surface coupling reaction.

7.3.4 Amide coupling of ETH to APS surfaces

Varying amounts of material (possibly AuNP clusters, precipitated reagents and contaminating debris) was noted on all surfaces and this made it difficult to draw any firm conclusions. However, a number of useful observations could be made. The greatest amount of material was observed on PNA surfaces 3 and 4, suggesting this was associated with EDC incubation. The material may have been EDC itself or other material adsorbed due to the presence of EDC. In a follow-up experiment, loosely bound or aggregated reagents were visibly removed from surface 3 after a sonication step (Fig. 7.8c). The APS surfaces (5-7) also showed varying amounts of surface coverage. The images suggested that a significant proportion of this material was AuNPs. Distinctive AuNP binding was

observed on surface 8 but not surface 4 (Fig. 7.8a and b), suggesting free amine groups remained available for AuNP binding. One anticipated outcome of this experiment was that ETH coupling to APS surfaces (after incubation with ETH and EDC) would prevent AuNPs binding to the surfaces (due to removal of free amine groups required for electrostatic interaction). However, this blocking effect was not observed. It is also possible that bound ETH could mimic the effect of the APS since a previous study had demonstrated that sodium acrylate, which has a similar unsaturated vinyl group to ETH, can stabilise AuNP suspensions (Hussain et al. 2003). However, another study suggested that the negatively charged acid group adsorbed to the gold and the acrylate moiety faced outwards (Diegoli et al 2006). In summary, it is more likely that the AuNPs were binding to APS rather than immobilised ETH.

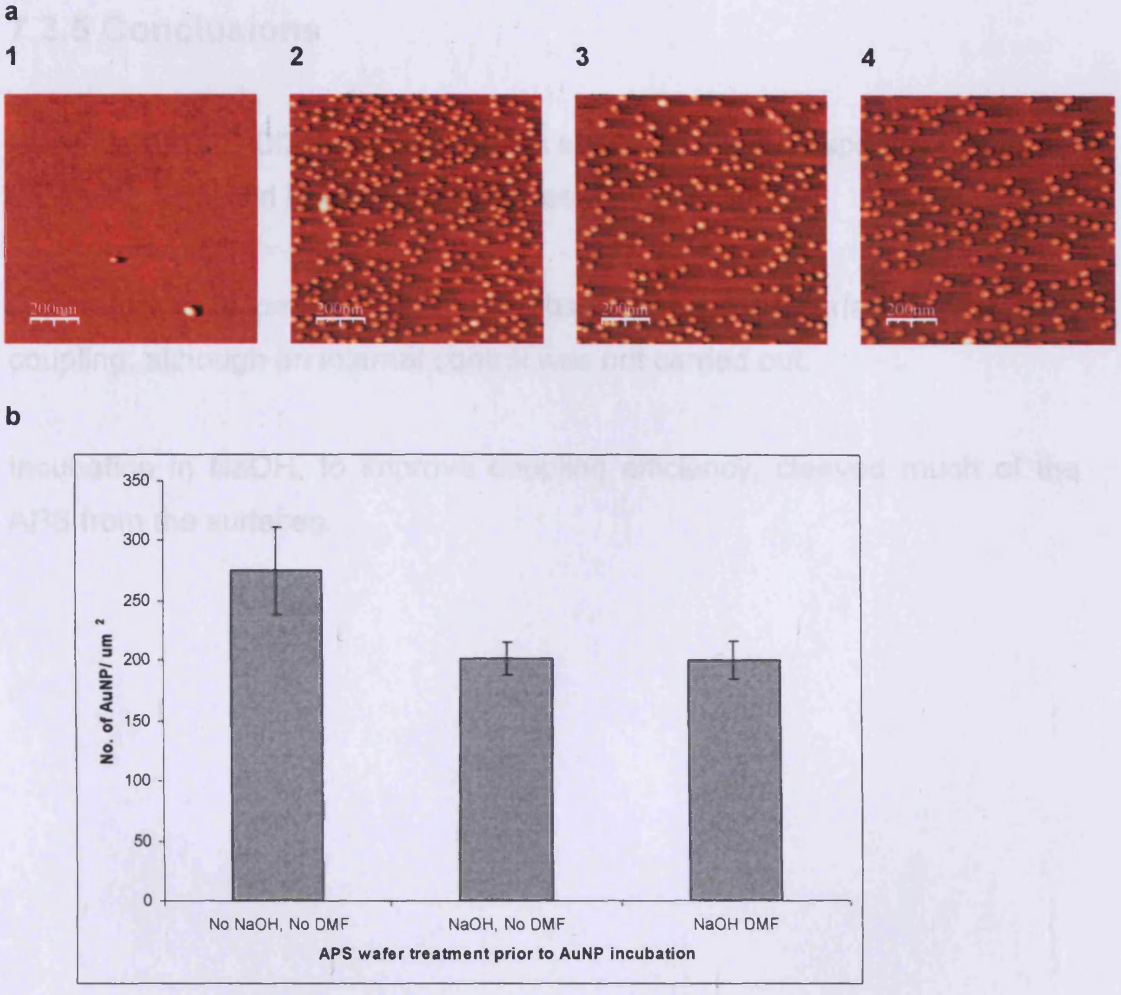


Fig. 7.7 The effect of NaOH and DMF incubation on the AuNP number density of APS Au surfaces. Surface treatments are numbered according to Table 2. **a**) AFM trace images are shown for each dilution after WSXM software processing. Z-axis = 20nm. Scan size = 1μm. **b**) AuNP density plot shows the average no. of AuNP/ μm^2 (n = 2-4 ± SEM), counted using WSXM flooding analysis from two to four scans of each surface.

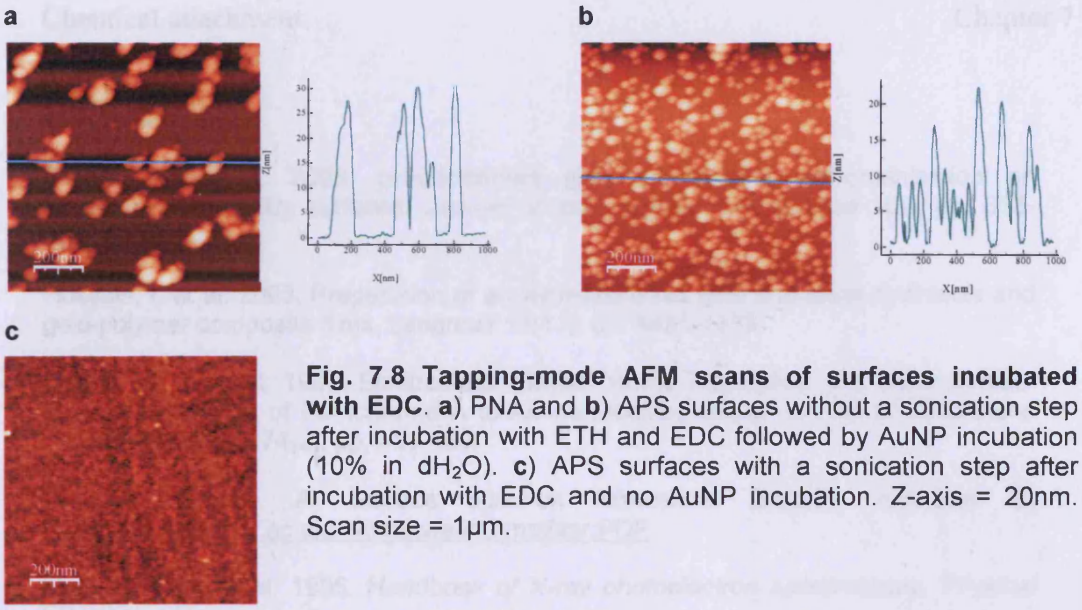


Fig. 7.8 Tapping-mode AFM scans of surfaces incubated with EDC. **a**) PNA and **b**) APS surfaces without a sonication step after incubation with ETH and EDC followed by AuNP incubation (10% in dH_2O). **c**) APS surfaces with a sonication step after incubation with EDC and no AuNP incubation. Z-axis = 20nm. Scan size = 1µm.

7.3.5 Conclusions

Absence of XPS Cl2p and Cl2s peaks suggests that non-specific binding of ETH onto APS and PNA silicon surfaces did not occur.

A possible Cl2p peak of ETH was observed on APS surfaces after EDC coupling, although an internal control was not carried out.

Incubation in NaOH, to improve coupling efficiency, cleaved much of the APS from the surfaces.

References

Diegoli, S. et al. 2006. pH-dependent gold nanoparticle self-organisation on functionalised Si/SiO_2 surfaces. *Journal of experimental nanoscience* 1(3), pp. 333-353.

Hussain, I. et al. 2003. Preparation of acrylate-stabilized gold and silver hydrosols and gold-polymer composite films. *Langmuir* 19(11), pp. 4831-4835.

Melzak, K. A. et al. 1995. Electrostatic Effects on the Adsorption and Carbodiimide-Mediated Coupling of Ferrichrome A to Amine-Modified Silica. *Journal of Colloid and Interface Science* 174(2), pp. 480-489.

Van der Merwe, A. Surface plasmon resonance. Biacore. Available at: http://users.path.ox.ac.uk/~vdmerwe/Internal/spr.PDF

Moulder, J. F. et al. 1995. *Handbook of X-ray photoelectron spectroscopy*. Physical Electronics Inc.

Ohtani, M. et al. 2006. Development of high-throughput combinatorial terahertz time-domain spectrometer and its application to ternary composition-spread film. *Applied Surface Science* 252(7), pp. 2622-2627.

Patolsky, F. et al. 1998. C60-mediated bioelectrocatalyzed oxidation of glucose with glucose oxidase. *Journal of Electroanalytical Chemistry* 454(1-2), pp. 9-13.

Stile, R. A. et al. 2002. Sequential robust design methodology and X-ray photoelectron spectroscopy to analyze the grafting of hyaluronic acid to glass substrates. *Journal of biomedical materials research* 61(3), pp. 391-398.

Zhu, T. et al. 1999. pH-dependent adsorption of gold nanoparticles on p-aminothiophenol-modified gold substrates. *Langmuir* 15(16), pp. 5197-5199.

Chapter 8

Adsorption and desorption of HSA and FITC-BSA on underivatised and APS-derivatised silicon surfaces

8.1 Introduction

Step three (Fig. 8.1) of a novel protein imprinting approach (Fig. 1.12) was to specifically bind a model protein (human serum albumin, HSA), with uniform orientation, to a high-affinity ligand (ethacrynic acid, ETH) dispersed on a silicon surface (Fig. 8.1a). Solution-phase incubation of HSA with the surfaces was required to achieve this. Therefore the prevention and / or removal of non-specifically-bound and denatured protein would be required (Fig. 8.1b). HSA and fluorescein isothiocyanate-bovine serum albumin (FITC-BSA) were adsorbed to underivatised hydrophilic silicon surfaces and aminopropyltriethoxysilane (APS)-derivatised surfaces. Adsorption and desorption were characterised using AFM and fluorescence microscopy.

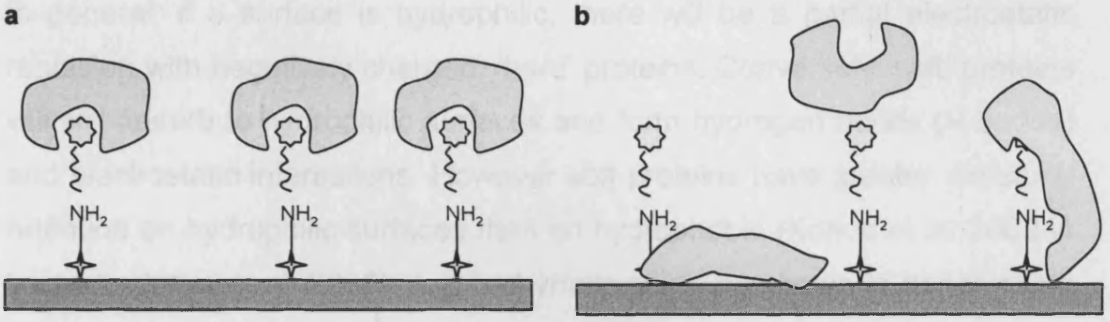


Fig. 8.1 Step three of a novel imprinting approach. a) Specific covalent attachment of protein template to ETH-derivatised silicon surfaces, giving uniform orientation of protein molecules. **b**) Non-specifically bound protein and denatured protein leading to non-uniform binding.

8.1.1 Protein adsorption on surfaces

Protein adsorption depends on the protein structure, the nature of the surface and the surrounding medium.

8.1.1.1 Protein structural stability upon surface adsorption

Proteins can be 'soft' or 'hard' depending on their secondary, tertiary and quaternary structures. Hard proteins with rigid beta sheets and extensive interlinking via dilsulfide bridges adsorb very little on hydrophilic surfaces but denature on hydrophobic surfaces (Bos et al. 1994 in Nakanishi et al. 2001). Soft, globular proteins with mainly alpha-helix structures are much more unstable and readily change conformation when dissolved in aqueous solutions and on surfaces (Nakanishi et al. 2001).

8.1.1.2 The effect of surface composition upon protein adsorption

- **Hydrophobic surfaces**

Most proteins bind with high affinity to hydrophobic surfaces. Generally, hydrophobic amino acid residues are tucked away inside the protein but upon adsorption these may become exposed and interact with the surface, causing irreversible conformational changes (Norde and Giacomelli 2000). The adsorption of plasma proteins has been shown to increase with increasing surface hydrophobicity (e.g. styrene > methylmethacrylate, Gessner et al. 2000).

- **Hydrophilic surfaces**

In general, if a surface is hydrophilic, there will be a partial electrostatic repulsion with negatively charged, 'hard' proteins. Conversely 'soft' proteins will still adsorb to hydrophilic surfaces and form hydrogen bonds (H-bonds) and electrostatic interactions. However soft proteins have greater structural retention on hydrophilic surfaces than on hydrophobic (Kondo et al. 2002 in Larsericsdotter et al. 2005), e.g. α-chymotrypsin was shown to denature on hydrophilic silica, but this did not lead to loss of activity (Zoungrans et al. 1997 in Nakanishi et al. 2001). It is entropically favourable for soft proteins to adsorb on any surface, irrespective of its nature due to the hydrophobic effect (Section 3.1.1.3) (Bos et al 1994 in Nakanishi et al. 2001).

- **Charged surfaces**

Protein molecules contain many ionisable groups on their surface in the form of acidic amino acids (aspartic acid (ASP) and glutamic acid (GLU)) and basic amino acids (lysine (LYS), argentine (ARG) and histidine (HIS)). Every protein has an isoelectric point (IEP), i.e. the pH at which the overall charge of the ionisable groups is zero. Below the IEP, the protein will be positively charged and above the IEP it will be negatively charged. At an oppositely charged surface (e.g. APS on silicon wafer), the protein will readily form electrostatic interactions and become irreversibly denatured (Rezwan et al. 2005).

8.1.1.3 Techniques for measuring protein adsorption

On surfaces with a low surface area (e.g. flat silicon wafer surfaces), conventional protein assays such as 'the Lowry method' (Chan 1984 in Nakanishi et al. 2001) cannot be used to quantify protein adsorption. Alternative methods include AFM (Section 5.1.3.3), fluorescence microscopy and ellipsometry (Section 5.1.3.1). The root mean squared roughness (RMSr) of AFM surface images can be calculated to compare the topology of plain and derivatised silicon wafer surfaces (Blasi et al. 2005; Ortega-Vinusa et al. 1998). Real-time protein adsorption can be monitored using QCM and AFM (Q-sense (Goteborg, Sweden) 2001; Numata et al. 2005). Single-molecule adsorption of ferritin to gold surfaces was observed using liquid tapping-mode AFM (Schon et al. 2007). Adsorption should be carried out with a small amount of shaking to keep the liquid moving (Ortega-Vinuesa et al. 1998; Gun'ko et al. 2003). BSA and HSA can be labelled with FITC (Fig. 8.2) via covalent attachment to free thiol (Cys-34) and / or amine groups. The ratio of FITC:BSA labelling can be controlled, but not the specific sites of attachment. FITC-labelled BSA was shown to bind APS-derivatised quartz with a fluorescence intensity of 19.8 ± 8, compared to 3 ± 2 for plain quartz (Vandenburgh et al. 1991). FITC-BSA was used in these experiments as a method of monitoring HSA adsorption and desorption.

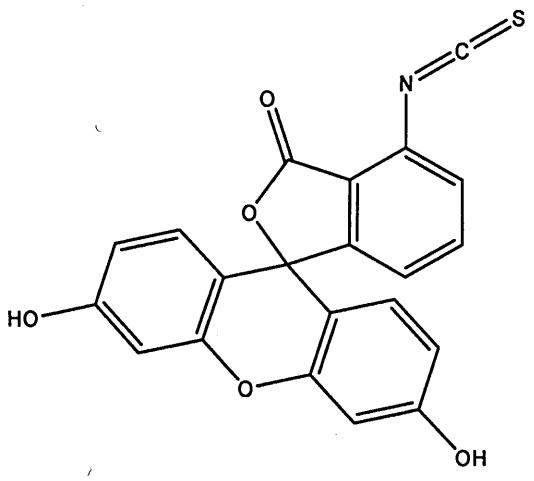


Fig. 8.2 Structure of FITC.

8.1.2 Serum albumin adsorption on silicon and glass surfaces

HSA (and BSA) is said to be a prolate ellipsoid with dimensions of 4 x 4 x 14nm or triangular / heart-shaped with dimensions of 8 x 8 x 3nm (Blomberg et al. 1994 in Sukhishvilli and Granick 1999) (Fig. 8.3). The flexibility (softness) of serum albumins allows them to take up different conformations in different environments (Peters 1996). As with most proteins, serum albumins contain many acidic amino acid surface groups and are negatively charged at physiological pH (7.4) (Peters 1996). The ionic strength, pH, protein concentration, type of buffer and type of surface affect serum albumin adsorption.

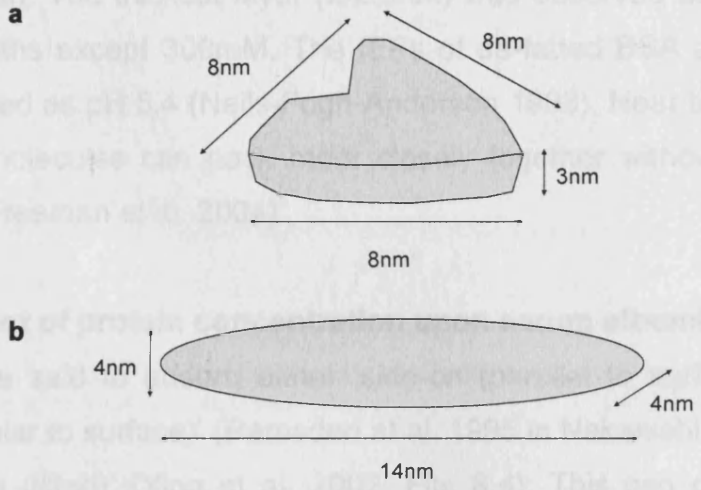


Fig. 8.3 Structures of HSA. a) Heart-shaped. **b**) Prolate ellipsoid.

8.1.2.1 The effect of solvent upon serum albumin adsorption

Plasma protein adsorption on hydrophilic surfaces has been widely studied for the development of blood-compatible materials for implants and drug delivery systems (Santin et al. 1997 & 2003; Gessner et al 2000). Proteins are colloidal, and therefore inter-protein and protein-surface interactions will depend on the nature of the surrounding medium (Shaw 1992). BSA was shown to retain the most structural stability when adsorbed to silica, using 10mM phosphate as buffer (Larsericsdotter et al. 2005). In this case differential scanning calorimetry was used to show that internal amino acid residues were not exposed to the solvent.

8.1.2.2 The effect of pH upon serum albumin adsorption

The structure of serum albumin adsorbed on a surface also depends on solution pH. BSA adsorption on silicon nitride chips was measured at pH 3, 5 and 7 using dual polarization interferometry (Freeman et al. 2004). Layer thickness (nm) was measured as <1, 3.9 and 1.1 along with saturation coverages of 80%, 76% and 59% respectively. Electrostatic repulsion between negatively charged proteins on the surface is likely at higher pH (Freeman et al. 2004). A similar effect was observed in this study with citrate-stabilised gold nanoparticles (Section 5.1.4.1). HSA adsorption to hydrophilic silicon wafer surfaces was followed at pH 4-9 with ionic strengths of 2-300mM using ellipsometry (Ortega-vinusa et al. 1998). At pH 7.4, the layer thicknesses were measured as less than 1nm, irrespective of ionic strength. The thickest layer (2-2.5nm) was observed at pH 4.7 for all ionic strengths except 300mM. The IEPs of de-fatted BSA and HSA have been reported as pH 5.4 (Neils-Fogh-Anderson 1993). Near to this pH, BSA and HSA molecules can pack more closely together without electrostatic repulsion (Freeman et al. 2004).

8.1.2.3 Effect of protein concentration upon serum albumin adsorption

Proteins are said to adsorb either 'side-on (parallel to surface)', 'end on (perpendicular to surface)' (Ramsden at al. 1995 in Nakanishi et al. 2001) or 'overlapping (tilted)' (Ying et al. 2002, Fig. 8.4). This can depend on the initial protein concentration e.g. BSA on titanium oxide (Giacomelli et al. 1999 in Nakanishi et al. 2001). The kinetics of protein adsorption is dependent on protein concentration, much like AuNPs (Larsericsdotter et al. 2005; Giacomelli and Norde 2000; Gun'ko et al. 2003). The random sequential adsorption model (Section 6.1.4.3) would predict that less than a monolayer of protein will adsorb for low concentrations and low ionic strengths (if adsorption is irreversible). At higher concentrations, proteins might crystallise and pack more closely at the surface (Ramsden at al. 1995 in Nakanishi et al. 2001).

Commonly, serum albumins are used to coat surfaces to prevent non-specific binding of other proteins. Typically, serum albumins are incubated with a surface for ~1 hour to ensure surface saturation, although overnight

incubations have also been used (Ombelli et al. 2005; Gun'ko et al. 2003; Santin et al. 2003). Predicting the behaviour of protein adsorption is more difficult than for uniform colloids (e.g. gold nanoparticles (AuNPs)) because of widely varying protein sizes and shapes and the different conformations that can occur upon adsorption (Shaw 1992).

8.1.2.4 The effect of the surface upon serum albumin adsorption

BSA was shown to adsorb to APS-derivatised silicon wafer surfaces with a higher density than underivatised surfaces (Ombelli et al. 2005). At pH 7, the serum albumin will be negatively charged and have high affinity to oppositely charged amines (vice versa for hydrophilic silica).

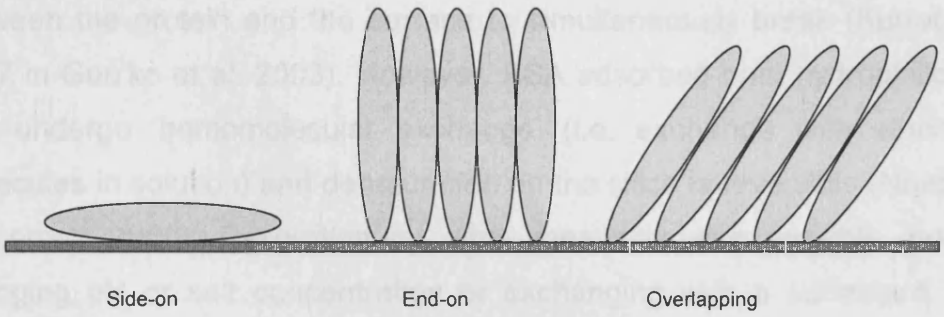


Fig. 8.4 Highly schematic representation of the possible orientation of protein molecules adsorbed to a surface. *Adapted from Ying et al. 2002.*

8.1.2.5 Specific orientation of serum albumins adsorbed to silica

Heating can cause protein disulfide bond interchange (Peters 1996). Aggregation of BSA adsorbed onto silica was not seen upon heating (Norde and Giacomelli 2000) and it was suggested that because Cys-34 is less accessible upon adsorption (Ingersoll et al. 1996 in Giacomelli and Norde 2001), disulfide bridge formation between molecules was prevented. It was suggested that the Cys-34 residue would therefore be facing the surface rather than the solution. However, in another study a limited tryptic digest of BSA adsorbed onto silica suggested that domain 2 faced the surface, and that domains 1 (with Cys-34) and 3 were more exposed (Laricsdotter et al. 2005).

Acrylodan is a fluorescent probe, specific for free thiol groups (Viappiani 1994) and has been used to follow BSA adsorption to a fused silica optical

fibre (Wang et al. 1995). Time-resolved fluorescence suggested that the local environment of the Cys-34 pocket had become more relaxed. Structural information of protein conformation and orientation is still much more difficult to obtain for proteins adsorbed on a surface than free in solution (Mrksich and Whitesides 1996).

8.1.3 Protein desorption from surfaces

Non-specific protein adsorption is a large problem in the development of biocompatible materials, biosensors and immunoassays (Section 1.1.3.6). Adsorption is very often irreversible, in the fact that proteins do not exchange with solvent molecules. It is unfavourable for the many bonds formed between the protein and the surface to simultaneously break (Kurrat et al. 1997 in Gun'ko et al. 2003). However, BSA adsorbed onto hydrophilic silica can undergo 'homomolecular exchange' (i.e. exchange with other BSA molecules in solution) and denaturation on the silica is reversible (Norde and Giacomelli 2000). Desorption by other means is also possible, such as changing pH or salt concentration or exchanging with a surfactant. Many surfactants required to remove proteins cause irreversible denaturation e.g. DECON. For this thesis, protein molecules would ideally be fixed on the surface in their natural conformation, so that molecularly imprinted polymer recognition sites are complementary to naturally occurring protein (Fig. 1.12). Strong urea or guanidinium hydrochloride solutions are sometimes used to remove physically adsorbed proteins (Blasi et al. 2005). Complete refolding of BSA in solution, after urea treatment occurred after 24 hours (Peters 1992). The extreme pH required may disturb the underlying APS layer required to bind proteins to a surface (Section 6.1.4.4). Strong acid (2M HCl) has also been used but would irreversibly denature the protein (Rezwan et al. 2005). A zwitterionic, non-denaturing detergent, 3-[3-cholamidopropyl)dimethylammonio]-1-propanesulfonate) (CHAPS) has been used to displace BSA adsorbed to silica surfaces (Ombelli et al. 2005). Isopropanol (IPA) was also investigated to desorb various proteins from polymer surfaces (Santin et al. 1997; Santin et al. 2003). IPA was proposed to disrupt H-bonding and hydrophobic protein-surface interactions, favouring water-protein interactions and even IPA-protein interactions with a detergent-

like effect. The IPA would be denaturing and a protein refolding step would be required. For some applications, non-specific protein adsorption can be prevented by coating a surface with 'biologically inert' molecules (Mrksich and Whitesides 1996, Section 1.1.3.6). However a plain silicon background is required for polymerisation around the final protein-bound surfaces (Fig. 1.12).

8.1.4 Chapter objectives

- To characterise the non-specific adsorption and desorption of the model protein on piranha (PNA) and aminopropyltriethoxysilane (APS)-treated silicon surfaces.
- To selectively immobilise and orientate the model protein onto silicon surfaces derivatised with the dispersed high-affinity ligand.

8.2 Methods

The RMSr (Section 8.1.1.3) of AFM (Section 5.2.3.1) scans was measured to distinguish between silicon wafer and glass coverslip surfaces with or without HSA / FITC-BSA adsorbed. The average RMSr was measured for three cross-sections along the x-axis (Section 5.1.3.3) of each image (without raised features- possibly debris) using Veeco AFM software (Fig. 8.5). Fluorescence microscopy (Section 8.2.2) was used to monitor adsorption of FITC-BSA on glass coverslip surfaces. To measure protein removal quantitatively, a calibration curve of surface-adsorbed FITC-BSA fluorescence was required. Initially, it was assumed that FITC-BSA would behave as reported for HSA adsorption on silicon (Ortega-Vinusa et al. 1998; Giacomelli and Norde 2000).

PNA and APS surfaces (Table 5.2.1) were prepared using a standard protocol (Section 5.2.2.4). Both sides of the glass surfaces (which could not be distinguished) and the polished sides only of the silicon surfaces were derivatised with APS. Sodium phosphate buffer (NaPB) was filtered before use. Incubation of surfaces in protein solution was carried out at room temperature for 24hours and surfaces were dried using a nitrogen (N_2) stream.

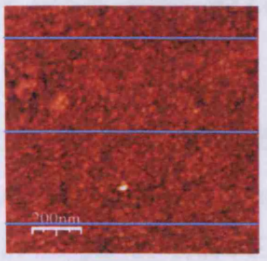


Fig. 8.5 Measurement of RMSr. The average RMSr of three x-axis cross-sections of a 1μM^2 AFM scan was calculated.

8.2.1 Equipment and materials

As for Sections 2.2.1 and 5.2.1. Additional equipment and materials were also used.

Equipment: Leica DMIRB fluorescence microscope (Leica Microsystems, Wetzlar, Germany) with a Q-imaging Retiga cooled 12-bit mono camera (Q-imaging, Surrey, BC, Canada).

Materials: Glass microscope slides and glass coverslips were purchased from Fisher Scientific (Waltham, MA, USA). FITC-BSA was purchased from Sigma-Aldrich (St. Louis, MO, U.S.A). Sodium phosphate buffer (NaPB, 67mM, pH 7.4) was used (Section 2.2.1). Glycine buffer (pH 2.7, 0.1M) was prepared using glycine.hydrochloric acid (HCl) salt in de-ionised water (dH_2O), adjusted to pH using 1M HCl ([www] Invitrogen).

8.2.2 Fluorescence microscopy for analysis of FITC-BSA adsorption onto silicon surfaces

Glass coverslips were fixed to glass slides using nail varnish. A Leica fluorescence microscope was used to observe FITC-BSA adsorbed to PNA and APS glass surfaces, under blue light (450-490nm). The exposure time (1s), exposure setting (3) and magnification (x40) were kept constant for all experiments. Images of each surface were captured using a Q-imaging camera. The fluorescence of the captured images was measured using Adobe Photoshop 6.0. The detection limit was calculated as three times the average blank value.

8.2.3 The adsorption of HSA and FITC-BSA on silicon and glass surfaces

8.2.3.1 HSA (30μM) adsorption on silicon surfaces in water

PNA surfaces were incubated in glass vials with static solutions (5ml) of water (dH_2O), HSA (30μM) in dH_2O or HSA-ETH (30μM), as prepared in Section 3.2.3.3b) in dH_2O (Surface treatments 1-4, Table 8.1). One surface was incubated in each vial. The surfaces were dried either immediately after the incubation, or after one 30 minutes dH_2O wash (5ml). Surfaces were analysed by AFM.

Table 8.1 Surfaces prepared in experiment 8.2.2.1.

Surface treatment	Surface	Treatment	Incubation: Protein (Solvent)	Wash
1	Silicon	PNA	No protein (dH_20)	dH_2O x1
2	"	"	30μM HSA (dH_2O)	None
3	"	"	30μM HSA (dH_2O)	dH_2O x1
4	"	"	30μM HSA-ETH (dH_2O)	dH_2O x1

8.2.3.2 HSA (20μM) adsorption on silicon surfaces in NaPB

PNA and APS surfaces were incubated as described in Section 8.2.3.1, except in solutions (10ml) of NaPB (10mM, pH 7.4) or HSA (20μM) in NaPB (10mM) (Surface treatments 1-12, Table 8.2). The surfaces were dried either (1) without a washing step, (2) after an acid wash (0.1M GlyHCl pH 2.7, (Invitrogen 2006) or (3) after a NaPB (10mM, pH 7.4) wash for 2 hours, followed by one dH_2O wash (5ml) for 30 minutes. One surface was incubated in each vial. Surfaces were analysed by AFM.

Table 8.2 Surfaces prepared in experiment 8.2.3.2.

Surface treatment	Surface	Treatment	Incubation: Protein (Solvent)	Wash
1	Silicon	PNA	No protein (NaPB only)	none
2	"	APS		
3	"	PNA	No protein (dH_2O only)	none
4	"	APS		
5	"	PNA	20μM HSA (NaPB)	none
6	"	APS		
7	"	PNA	"	NaPB x1, dH_2O x1
8	"	APS		
9	"	PNA	"	GlyHCl (pH 2.7) x1, dH_2O x1
10	"	APS		
11	"	PNA	20μM HSA (dH_2O)	none
12	"	APS		

8.2.3.3 Calibration of FITC-BSA (1nM-10^4nM) adsorption from NaPB on glass surfaces using AFM and fluorescence microscopy

FITC-BSA (10:1 mol ratio of FITC:BSA) was used to monitor protein adsorption by fluorescence microscopy (glass surfaces) and AFM (silicon surfaces). For the former, glass surfaces were used for transparency and the luminescence was measured for each FITC-BSA surface as an average of the whole image. PNA and APS, glass and silicon surfaces were incubated in solutions (2ml) of 0, 1, 10, 10^2, 10^3 and 10^4nM FITC-BSA in NaPB (67mM, pH 7.4) in glass vials covered with aluminium foil and agitated on a shaker-incubator (Surface treatments 1-12, Table 8.3). One glass surface or two silicon surfaces were incubated in each vial. The surfaces were rinsed thoroughly four times with dH_2O.

Table 8.3 Surfaces prepared in experiment 8.2.3.3. * Not analysed by AFM.

Surface treatment	Surface	Treatment	Incubation: Protein (Solvent)	Wash
1	Glass	PNA	No protein (NaPB)	dH_2O x4
2*	"	"	1nM FITC-BSA (NaPB)	"
3*	"	"	10nM FITC-BSA (NaPB)	"
4*	"	"	10^2nM FITC-BSA (NaPB)	"
5*	"	"	10^3nM FITC-BSA (NaPB)	"
6	"	"	10^4nM FITC-BSA (NaPB)	"
7	"	APS	No protein (NaPB)	"
8	"	"	1nM FITC-BSA (NaPB)	"
9	"	"	10nM FITC-BSA (NaPB)	"
10	"	"	10^2nM FITC-BSA (NaPB)	"
11	"	"	10^3nM FITC-BSA (NaPB)	"
12*	"	"	10^4nM FITC-BSA (NaPB)	"

8.2.3.4 FITC-BSA (0.1-10^2nM) adsorption on glass surfaces in NaPB

PNA and APS, glass and silicon surfaces were prepared and analysed as described in Section 8.2.3.3, except they were incubated in solutions (2ml) of 0, 0.1, 0.5, 1, 1.5, 2.5, 5, 10, 50 and 10^2nM FITC-BSA (Surface treatments 1-17, Table 8.4). Surfaces were analysed by AFM (silicon) and fluorescence microscopy (glass) (n = 1). The luminescence of fluorescence microscope images was measured for each FITC-BSA surface as an average of three areas of each image.

Table 8.4 Surfaces prepared in experiment 8.2.3.4. * Not analysed by AFM.

Surface treatment	Surface	Treatment	Incubation: Protein (Solvent)	Wash
1	Glass and silicon	PNA	No protein (NaPB)	dH_2O x4
2	"	"	0.1nM FITC-BSA (NaPB)	"
3*	"	"	1nM FITC-BSA (NaPB)	"
4*	"	"	5nM FITC-BSA (NaPB)	"
5*	"	"	10nM FITC-BSA (NaPB)	"
6*	"	"	50nM FITC-BSA (NaPB)	"
7	"	"	10^2nM FITC-BSA (NaPB)	"
8	"	APS	No protein (NaPB)	"
9	"	"	0.1nM FITC-BSA (NaPB)	"
10	"	"	0.5nM FITC-BSA (NaPB)	"
11	"	"	1nM FITC-BSA (NaPB)	"
12	"	"	1.5nM FITC-BSA (NaPB)	"
13	"	"	2.5nM FITC-BSA (NaPB)	"
14	"	"	5nM FITC-BSA (NaPB)	"
15	"	"	10nM FITC-BSA (NaPB)	"
16	"	"	50nM FITC-BSA (NaPB)	"
17	"	"	10^2nM FITC-BSA (NaPB)	"

8.2.3.5 FITC-BSA (10nM) desorption from glass and silicon surfaces

APS and PNA silicon surfaces and glass cover slips were derivatised as described in Section 8.2.3.3 except with 10nM FITC-BSA. Different methods of protein removal were used, including sonication in NaPB (67mM, pH 7.4) for 10 or 60 minutes, incubation in isopropyl alcohol (IPA) (0.1, 1 or 10% volume in dH_2O) or sodium chloride (NaCl, 0.1 or 1M in dH_2O) incubation for 10 minutes. All surfaces were washed thoroughly twice in dH_2O, before and after the 'protein removal' steps. Surfaces were analysed by AFM and fluorescence microscopy, although the latter were not included in the results due to fluorescence quenching problems (Section 8.3.2.5) (n = 1). Surfaces that were analysed by AFM are shown in Table 8.5.

Table 8. 5 Surfaces prepared in experiment 8.2.3.5.

Surface treatment	Surface	Treatment	Incubation: Protein (solvent)	Protein removal step
1	Silicon	APS	10nM FITC-BSA (NaPB)	dH_2O
2	"	APS	"	Sonication in NaPB (10 minutes)
3	"	APS	"	Sonication in NaPB (60 minutes)
4	"	APS	"	IPA (0.1% v/v in water)
5	"	APS	"	NaCl (0.1M)
6	"	APS	"	NaCl (1M)

8.2.3.6 A comparison between AuNP, FITC-BSA (10nM) and HSA (10nM) adsorption on glass and silicon surfaces

APS and PNA silicon surfaces and glass cover slips were incubated in FITC-BSA solution as described in Section 8.2.3.3 except with solutions (2ml) of 10nm AuNP (10% in dH_2O), 10nM FITC-BSA in NaPB (67mM, pH 7.4) or HSA in NaPB (67mM, pH 7.4) (n = 1) (Surface treatments 1-16, Table 8.6).

Table 8.6 Surfaces prepared in experiment 8.2.3.6.

Surface treatment	Surface	Treatment	Incubation: Protein / AuNP (Solvent)	Wash
1	Glass	PNA	No protein / AuNP (NaPB)	dH_2O
2	"	APS	"	"
3	"	PNA	10nm AuNP (dH_2O)	"
4	"	APS	"	"
5	"	PNA	10nM HSA (NaPB)	"
6	"	APS	"	"
7	"	PNA	10nM FITC-BSA (NaPB)	"
8	"	APS	"	"
9	Silicon	PNA	No protein / colloid (NaPB)	"
10	"	APS	"	"
11	"	PNA	10nm AuNP (dH_2O)	"
12	"	APS	"	"
13	"	PNA	10nM HSA (NaPB)	"
14	"	APS	"	"
15	"	PNA	10nM FITC-BSA (NaPB)	"
16	"	APS	"	"

8.2.3.7 HSA (10^2nM) adsorption on a silicon surface in NaPB

One PNA silicon surface was incubated with a solution (6ml) of 10^2nM HSA in NaPB (67mM, pH 7.4) for 24 hours. The surface was washed once in dH_2O, dried and analysed by AFM (n = 1).

8.3 Results and discussion

8.3.1 Fluorescence microscopy for analysis of FITC-BSA adsorption onto silicon surfaces

A number of important considerations were taken into account when imaging the surfaces. Fluorescence microscope images are included in Appendix VII. Images were captured in areas away from the varnish mount since it had been observed that this gave rise to an increased level of fluorescence. Scratches and imperfections in the fluorescent layer were also avoided since these also resulted in error. In addition, surface contamination could also be a problem since it resulted in localised areas of high or low fluorescence. Fluorescence quenching was another source of error and was shown to occur rapidly when FITC was exposed to blue light (λ = 450-490nm). Another important consideration was that the glass cover-slip surfaces were APS-derivatised on both sides and therefore the measured surface fluorescence was a sum of the two sides. Surface imperfections were used to focus the images. The n number refers to the number of images captured for a particular surface treatment. The fluorescence was measured for 3-5 areas of each image (± SEM).

8.3.2 The adsorption of HSA and FITC-BSA on silicon and glass surfaces

AFM cannot easily image individual HSA molecules on the surface because they are soft and can have variable dimensions upon surface adsorption (Ortega-Vinusa et al. 1998). This makes them difficult to distinguish from dirt and debris, unlike AuNPs which have relatively hard, uniform structures upon adsorption (Chapters 5 and 6). The RMSr of the surfaces was plotted as an RMSr graph for each experiment. Trace images and profiles (created in WSXM, Section 5.2.2.1) of the selected surface are also shown. The n number refers to the number of images scanned for a particular surface treatment. The RMSr was measured for 3 areas of each image (± SEM).

8.3.2.1 HSA (30μM) adsorption on silicon surfaces in water

The RMSr graph (Fig. 8.6) and AFM images (Fig. 8.7) are shown. Surface treatments are given in Table 8.1. There was no significant difference in RMSr between surface treatments 3 and 2 (0.52 ± 0.08nm and 0.55 ± 0.12nm respectively), indicating that HSA adsorption to hydrophilic silicon surfaces is irreversible in water. This correlates with the literature (Kurrat et al. 1997 in Gun'ko et al. 2003). Both had a significantly higher RMSr than surface treatment 1 (0.26 ± 0.07nm). Surface 4 had a higher average RMSr than HSA after one wash (1.19 ± 0.39nm). The addition of the Cys-34 HSA-binding ligand (ETH) appears to have brought about a conformational change giving rise to a rougher protein surface. Modification of the Cys-34 group leads to conformational changes in different HSA domains (allosteric effect, Stewart et al. 2004). This result suggests that ETH may have modified HSA at Cys-34 (as desired, Section 3.1.2). However, excess ETH and buffer salts were also present and may have affected the HSA surface adsorption conformations.

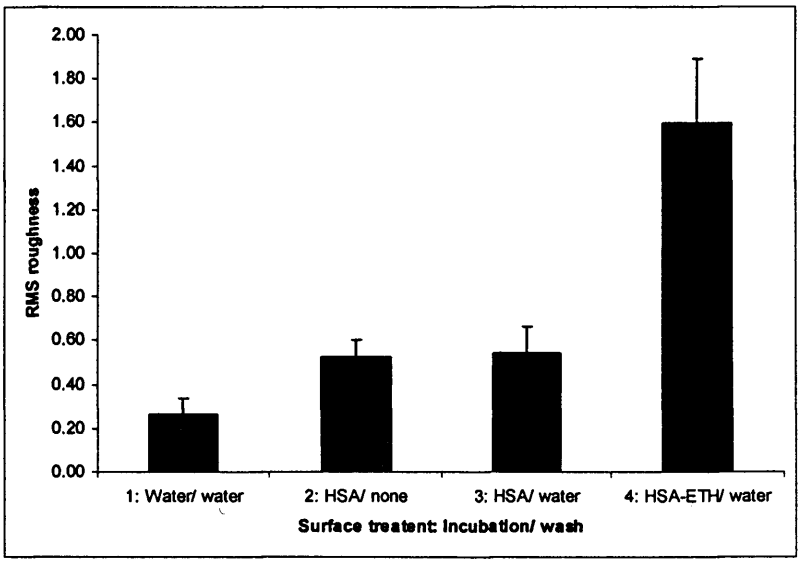


Fig. 8.6 AFM RMSr measurements of PNA silicon surfaces incubated with various HSA solutions in water. Surfaces were incubated for 24 hours without agitation. Error bars are SEM of different areas of the surfaces (n = 1). Surfaces treatments are given in Table 8.1.

Individual protein molecules may have been visible from AFM images (Fig. 8.7). In high magnification images, raised features appear better defined for surface treatment 2 than for surface treatment 1 (Fig. 8.7c). On surface 2, these features have a height of ~3nm (Fig. 8.7b), but it was not possible to determine the depth of the HSA films and whether the HSA was present as

a monolayer or a multilayer. Other techniques such as ellipsometry (Section 5.1.3.1) would be useful to measure film thickness (Ortega-Vinusa et al. 1998). The apparent area of each raised feature (~40 x 20 nm, Fig. 8.7b) was larger than would be predicted for an HSA molecule (dimensions for prolate ellipsoid are 14 x 4 x 4nm, Fig. 8.3). However this could be due to tip convolution effects (Section 5.3.1.2a).

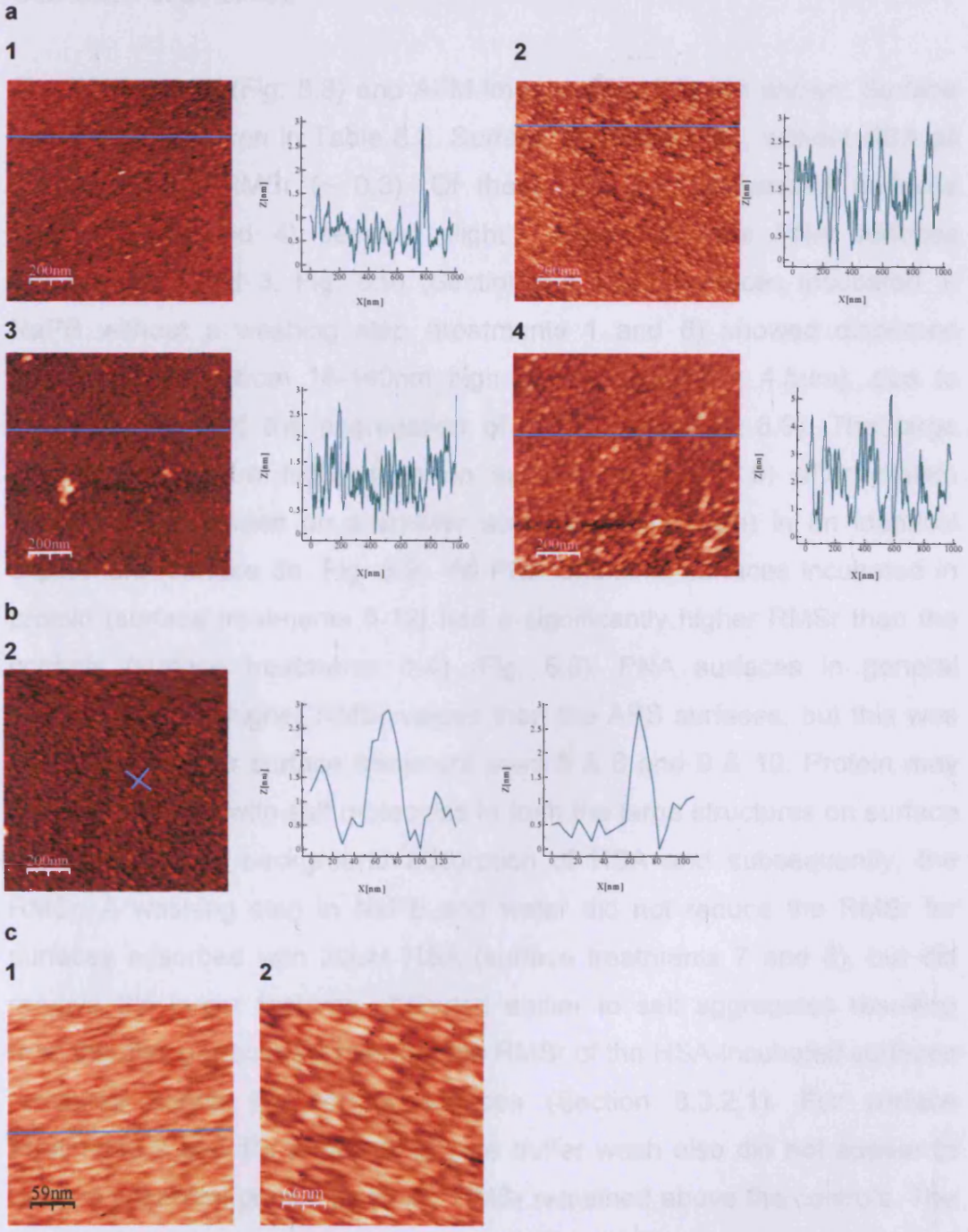


Fig. 8.7 AFM scans of HSA adsorbed to PNA silicon surfaces in water. a) AFM height images and profiles for each surface (1um^2). **b**) Profile of an individual 'raised feature' (possibly a protein molecule) from Surface 2. **c**) Zoomed-in AFM height images of surfaces 1 and 2 (300nm^2). Surface treatments (1-4) are given in Table 8.1. Profile Y-axes are 3nm for easy comparison.

8.3.2.2 HSA (20μM) adsorption on silicon surfaces in NaPB

Protein solutions were dissolved in NaPB (as used for HSA-ETH solution binding experiments) (Section 3.2.3.2) so that results would be directly relevant to subsequent HSA-ETH surface binding experiments. In addition, several groups have previously used NaPB as a solvent for studying serum albumin binding to surfaces (Wang et al. 1995; Larsericsdotter et al. 2005; Giacomelli et al. 2000).

The RMSr graph (Fig. 8.8) and AFM images (Fig. 8.9) are shown. Surface treatments are given in Table 8.2. Surface treatments 1-4, without HSA all have a similar RMSr (~ 0.3). Of these, the APS-derivatised surfaces (treatments 2 and 4) seemed slightly dirtier than the PNA surfaces (treatments 1 and 3, Fig. 8.9) (Section 5.3.1.2b). Surfaces incubated in NaPB without a washing step (treatments 1 and 6) showed dispersed features ranging from 18-140nm high (z-limit of AFM = 4.5μm), due to drying affects and the aggregation of buffer salts (Fig. 8.9). The large structures (~140nm high) seen on surface 6a (Fig. 8.9) after protein incubation were seen on a smaller scale (25-50nm high) in an identical experiment (surface 6b, Fig. 8.9). All PNA and APS surfaces incubated in protein (surface treatments 5-12) had a significantly higher RMSr than the controls (surface treatments 1-4) (Fig. 8.8). PNA surfaces in general seemed to have higher RMSr values than the APS surfaces, but this was only significant for surface treatment pairs 5 & 6 and 9 & 10. Protein may have aggregated with salt molecules to form the large structures on surface 6a, reducing the background adsorption of HSA and subsequently, the RMSr. A washing step in NaPB and water did not reduce the RMSr for surfaces adsorbed with 20uM HSA (surface treatments 7 and 8), but did remove the larger features attributed earlier to salt aggregates resulting from the drying process. Therefore the RMSr of the HSA-incubated surfaces remained above the control surfaces (Section 8.3.2.1). For surface treatments 9 and 10, a low pH glycine buffer wash also did not appear to remove adsorbed protein since the RMSr remained above the controls. The PNA surface (treatment 9) had a much higher RMSr compared to the APS surface (treatment 10) and all other surfaces incubated with protein. Table 8.7 summarises the HSA adsorption process for PNA and APS surfaces at

pH 7.4 and 2.7. The isoelectric point of HSA is pH 5.4 (Neils-Fogh-Anderson et al. 1993), and therefore, at pH 7.4 the protein is negatively charged. The process of HSA adsorption to PNA and APS surfaces was quite different. At pH 7.4 the PNA surface was neutral, whilst the APS surface was positively charged. Adsorption on the hydrophilic, yet neutral PNA surface is driven by entropic effects (hydrophobic) and H-bonding (Kondo et al. 2002 in Larsericsdotter et al. 2005). On similar silica surfaces, previous studies have suggested that HSA denatures to take up a flat conformation (Table 8.7b), but that this is reversible with homomolecular exchange between surface adsorbed and solution-phase molecules (Norde and Giacomelli 2000). The ionic attraction between HSA and the charged APS surface resulted in irreversible denaturation of the flattened protein (Rezwan et al. 2005) (Table 8.7b). Changing the pH to 2.7 (glycine buffer) has the effect of changing the overall charge of HSA from negative to positive. It also has the effect of disrupting H-bonding interactions between the protein and PNA surfaces. At pH 2.9, on the hydrophilic PNA surfaces, albumin would be expected to be in an expanded form (phosphate buffer), lying very flat on the hydrophilic surface (Peters 1996; Freeman et al. 2000). However, an upwards expansion was observed as shown by the increase in RMSr roughness for surface treatment 9. This is likely to be due to reversible denaturation and possibly the presence of glycine. However, the protein-surface interactions were collectively too strong to completely desorb the protein. For HSA adsorbed on APS surfaces, the conformation of HSA did not change, due to the effects of irreversible denaturation.

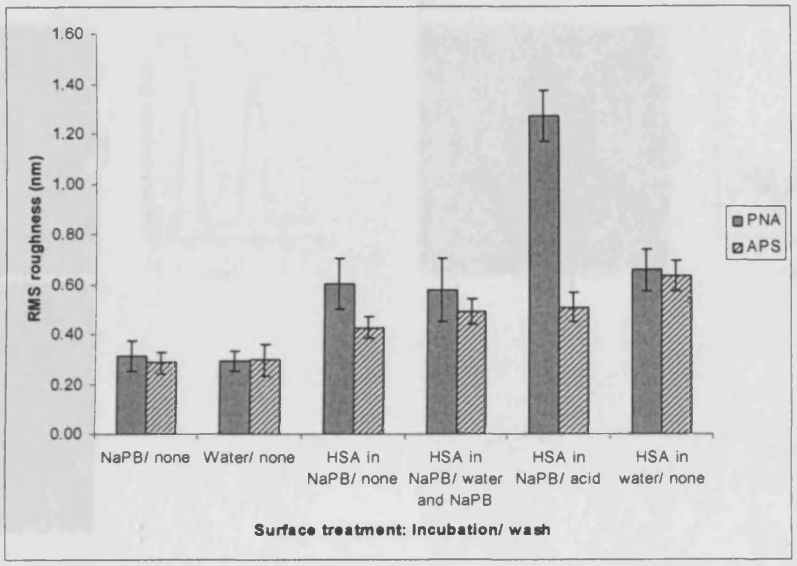
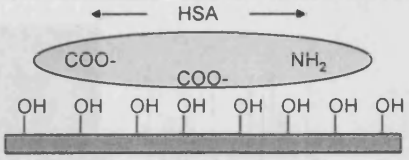
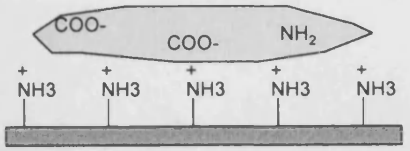
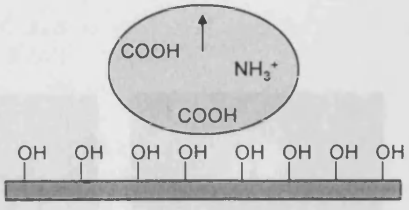
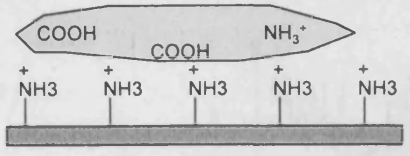
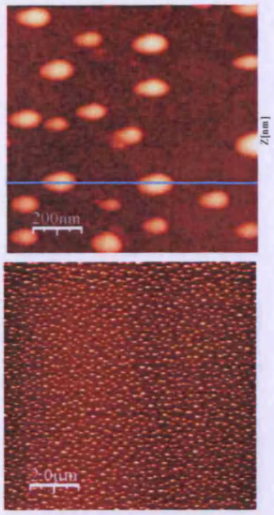


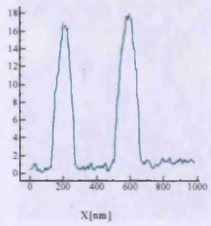
Fig. 8.8 AFM RMSr measurements of PNA and APS silicon surfaces incubated with various HSA solutions in NaPB or water. Surfaces were incubated for 24 hours without agitation. Error bars are SEM of different areas of the surfaces (n = 1-2). Surface treatments are given in Table 8.2.

Table 8.7 HSA adsorption processes on PNA and APS surfaces at pH 7.4 and 2.7

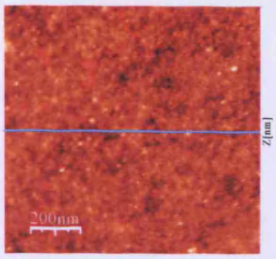
	PNA silicon surface	APS silicon surface
NaPB pH 7.4	 Negatively charged albumin binds to hydrophilic silicon due to entropic effects and H-bonding. HSA takes up a flat conformation but is reversibly denatured.	 Negatively charged HSA binds to the positively charged surface by ionic bonding, leading to irreverisble structural denaturation. Protein takes up a flat conformation.
Glycine buffer pH 2.7	 Albumin is positively charged and H-bonding is disrupted between HSA and the surface. The low pH also disrupts H-bonding within the HSA molecule leading to an expanded conformation. Although surface denaturation is reversible, HSA-surface interactions are collectively too strong for desorption.	 The HSA is irreversibly denatured and adsorbed, and the removal of ionic boning has little effect upon the HSA conformation.

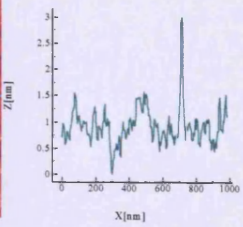
1


200nm
2.0μm

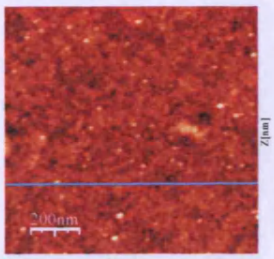

Z[nm]
X[nm]

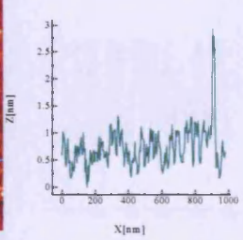
2


200nm

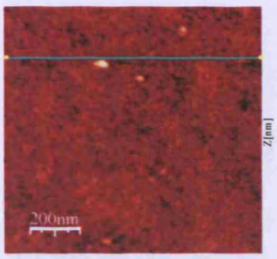

Z[nm]
X[nm]

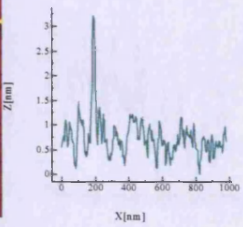
3


200nm

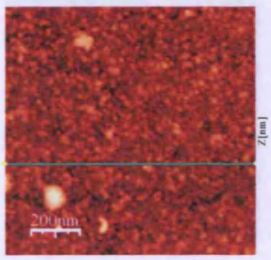

Z[nm]
X[nm]

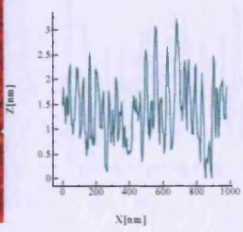
4


200nm

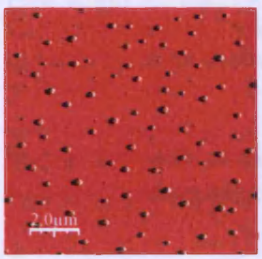

Z[nm]
X[nm]

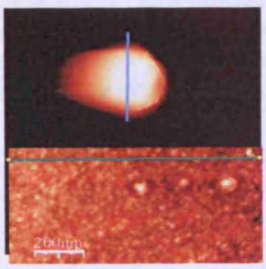
5

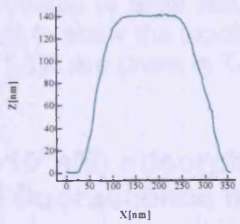

200nm

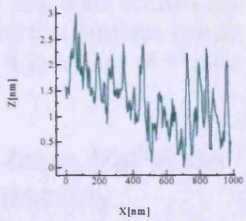

Z[nm]
X[nm]

6a


2.0μm


200nm


Z[nm]
X[nm]


Z[nm]
X[nm]

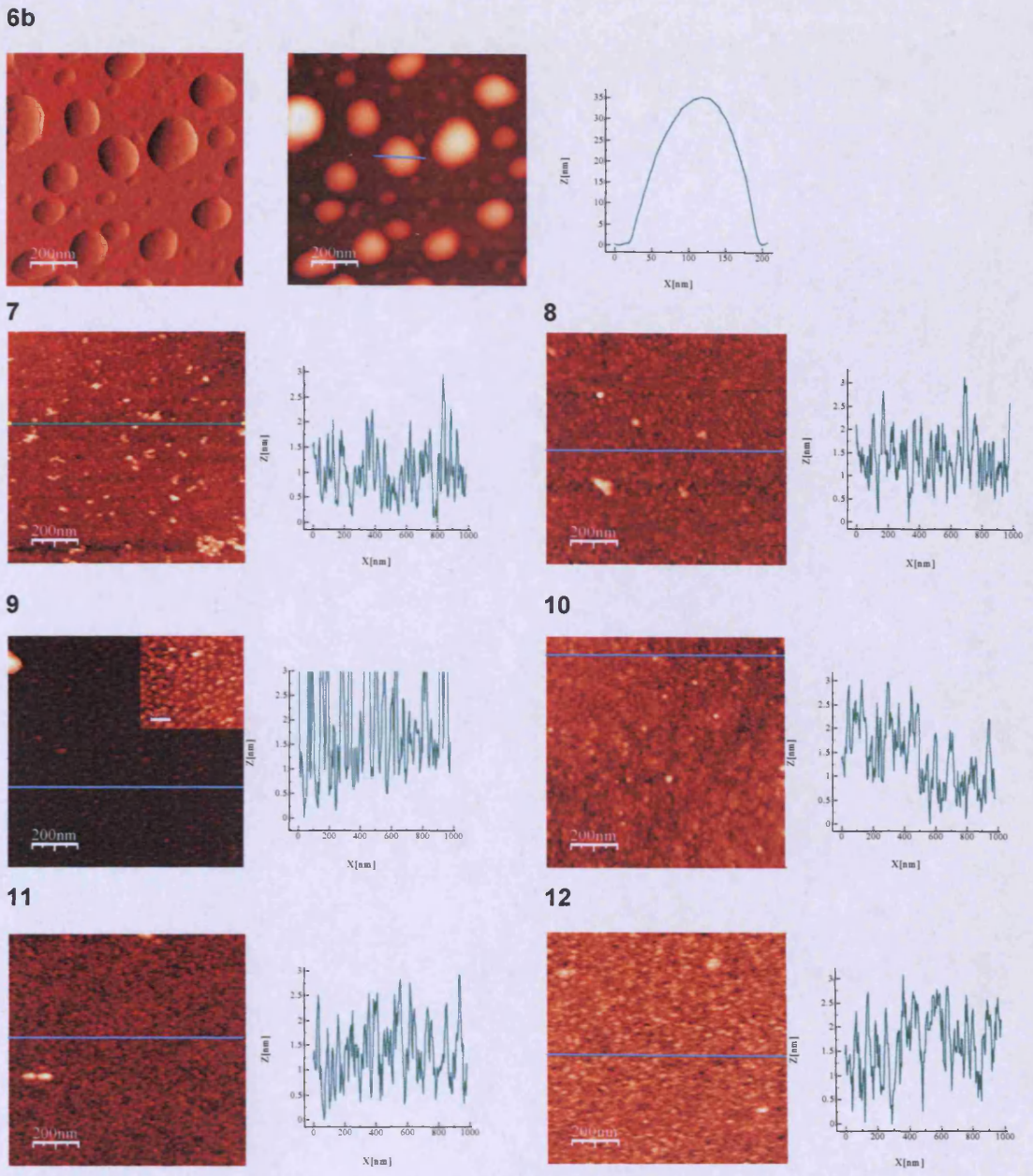


Fig. 8.9 AFM scans of PNA and APS silicon surfaces incubated with various HSA solutions in NaPB or water. AFM height images (1um^2 or 10um^2) and profiles (along the blue lines) for each surface (1-12) are shown. Profiles of large features are also shown for surfaces 1 and 6. Insets on surfaces 6a and 9 are to show the topology of the surface made unclear by large features. Surfaces treatments (1-12) are given in Table 8.2. Value of Y axis is 3nm for easy comparison of all profiles.

8.3.2.3 Calibration of FITC-BSA (1nM-10^{4}nM) adsorption from NaPB on glass surfaces using AFM and fluorescence microscopy

a. Theoretical HSA or FITC-BSA concentration required for monolayer coverage of glass or silicon surfaces in glass vials

The total area of glass vials and the silicon / glass surfaces covered by the HSA / FITC-BSA solutions during 24hr incubation steps was roughly

calculated. This was used to estimate the minimum concentration of protein from solution that would result in monolayer coverage.

The area of the base of the vial was calculated (a_b, Equation 8.1). The height of the vial wall covered by the protein solution (h) and the circumference of the vial (c) (Equation 8.2) were used to calculate the area of the glass vial wall (a_w, Equation 8.3). The total area of the glass vials (a_v) was then calculated (Equation 8.4).

Eq. 8.1	a_b	$= \pi r^2$	$= 4.15 \times 10^{14}\ nm^2$
Eq. 8.2	c	$= \pi d$	$= 7.2 \times 10^{7}\ nm$
	h	$\approx 1cm$	$= 1 \times 10^{7}\ nm$
Eq. 8.3	a_w	$= h \times c$	$= 7.2 \times 10^{14}\ nm^2$
Eq. 8.4	a_v	$= a_b + a_w$	$= 1.14 \times 10^{15}\ nm^2$

Glass and silicon surfaces were cut to sizes of between 0.5cm^2 and 1cm^2. The following calculations use 1cm^2 surfaces as an example. HSA was assumed to adsorb to both sides of each glass and silicon surface. Single 1cm^2 glass coverslips would have a total surface area (a_s) of $2 \times 10^{14} nm^2$. With two surfaces in each vial, the total area (a_t) that protein could adsorb onto was calculated as $1.54 \times 10^{15}\ nm^2$ (Equation 8.5).

Eq. 8.5	a_t	$= a_v + 2(a_s)$	$= 1.54 \times 10^{15}\ nm^2$.

HSA and BSA can have different dimensions in solution and when adsorbed on surfaces (Bloomberg et al. 1994; Sukhishvilli and Granick 1999). With dimensions of 4 x 4 x 14nm, the area predicted to be taken up by a single protein molecule (a_p, assuming a rectangular adsorption area) would lie in the approximate range 16 (4 x 4) – 56 (14 x 4) nm^2. At pH ~7.4, HSA film thickness was measured ~1nm (Ortega-Vinusa et al. 1998), which suggests flattening of the protein molecules upon adsorption. Inter-molecular repulsion may also prevent close packing (Freeman et al. 2000).

Therefore, it is likely that HSA / FITC-BSA would adsorb with an area greater than 56nm^2 and equations 8.6 – 8.8 may overestimate the concentration required.

The number of protein molecules (n_p, Equation 8.6) and subsequently moles (mol_p, Equation 8.7) that could adsorb in a monolayer with an area of 56nm was calculated for two 1cm^2 glass surfaces:

Eq. 8.6 $n_p = a_t/a_p$ = 2.75 x 10^{13} molecules.

Eq. 8.7 mol_p =n_p/Avogadros constant (6×10^{23})
= 4.58 x 10^{-11} moles

The concentration of protein (C) required for monolayer coverage was calculated from the known volume (V, 0.002L) and predicted number of moles (Equation 8.8).

Eq. 8.8 C =mol_p/V =2.29 x 10^{-8} M
= ~22.9nM for two 1cm^2 glass surfaces in each vial.
= ~18.5nM for one

Both AFM and fluorescence microscopy suggested that FITC-BSA did not adsorb onto PNA surfaces but did bind to APS surfaces (This Section and Section 8.3.2.4). Therefore FITC-BSA was assumed not to bind to glass vials and the calculation for monolayer protein coverage was adjusted. HSA was shown to bind PNA surfaces (Section 8.3.2.1) and the calculation should hold true for these surfaces. For two 1cm^2 glass surfaces in each vial, the total area that FITC-BSA could adsorb onto (a_t) was 2(a_s) = 4 x10^{14} nm^2. Using Equations 8.6–8.8, the concentration of FITC-BSA required for a monolayer was therefore ~6nM. For one glass surface this would be ~3nM, and for one silicon surface this would be ~1.5nM (because only one side was derivatised with APS). Table 8.8 shows the predicted concentrations required for monolayer coverages of HSA and FITC-BSA on one or two, 0.5 - 1cm^2 glass or silicon surfaces.

Table 8.8 Predicted concentration of HSA or FITC-BSA required for monolayer coverage of APS glass and silicon surfaces. HSA calculations assume that HSA did bind to the glass vials. FITC-BSA calculations assume that FITC-BSA did not bind to glass vials (or any surfaces not derivatised with APS, Section 8.7). Silicon surfaces were only derivatised with APS on one side, while both sides of the glass surfaces were derivatised with APS. The calculations for HSA also apply to PNA surfaces. FITC-BSA did not appear to bind PNA surfaces. Range of concentration values is shown to account for the range of surface sizes ($0.5cm^2$ - $1cm^2$). Other calculations are shown for $1cm^2$ only.

Surface	Protein	Area that protein will bind (nm^2)			Predicted protein (area = $56nm^2$) adsorption (from 2ml)		
		Vial	Surface	Total	Molecules	Moles	Concentration (nM)
Glass x1	HSA	1.14×10^{15}	2×10^{14}	1.34×10^{15}	2.39×10^{13}	3.98×10^{-11}	17.17 - 19.91
Glass x1	FITC-BSA	0	2×10^{14}	2×10^{14}	3.57×10^{12}	6.25×10^{-11}	0.39 - 3.13
Glass x2	HSA	1.14×10^{15}	4×10^{14}	1.54×10^{15}	2.75×10^{13}	4.58×10^{-11}	17.71 - 22.92
Glass x2	FITC-BSA	0	4×10^{14}	4×10^{14}	7.14×10^{12}	1.19×10^{-11}	0.74 - 5.95
Silicon x1	HSA	1.14×10^{15}	2×10^{14}	1.34×10^{15}	2.39×10^{13}	3.98×10^{-11}	17.17-19.91
Silicon x1	FITC-BSA	0	1×10^{14}	1×10^{14}	1.79×10^{12}	2.98×10^{-11}	0.18 - 1.49
Silicon x2	HSA	1.14×10^{15}	4×10^{14}	1.54×10^{15}	2.75×10^{13}	4.58×10^{-11}	17.71 - 22.92
Silicon x2	FITC-BSA	0	2×10^{14}	2×10^{14}	3.57×10^{12}	5.95×10^{-11}	0.37 - 2.98

b. Experimental results for FITC-BSA binding to surfaces

The RMSr graph (Fig. 8.10) is shown. AFM images are shown in Appendix VII. Surface treatments are given in Table 8.3.The AFM tip tracked badly on the surface, as shown by artificial pucks and lines on the images for surface treatments 3 and 5. The glass surfaces were also quite dirty. FITC-BSA incubation did not increase the RMSr for surfaces 1 and 6. This suggests the FITC-BSA behaved differently from HSA (Section 8.3.2.1) on hydrophilic PNA surfaces (Vandenburgh et al. 1991). For surface 6 there was a high enough FITC-BSA solution concentration (10^4nM) for theoretical monolayer coverage (3nM, Table 8.7). Since previous studies have shown that unmodified BSA will bind to hydrophilic silicon, the high FITC:protein conjugation ratio (10:1) must have significantly changed the surface characteristics. This can be explained by the fact that on average, 10 free surface-available amines have been modified with large, multi-functional, aromatic groups (Fig. 8.2). At pH 7.4 this means that the overall charge of the FITC-BSA would be more negative than for just BSA.

FITC-BSA adsorption was observed on APS surface treatments 10 and 11 (10^2 and 10^3nM FITC-BSA respectively) with RMSr values significantly different from the control (Fig. 8.10). One glass surface or two silicon surfaces were incubated in each vial and therefore the theoretical concentration of FITC-BSA required for a monolayer was 0.39 - 3nM for all APS surfaces (Table 8.7). For surfaces incubated in 10nM FITC-BSA or below, the RMSr was not significantly different from the control (Fig. 8.10). The results correlated with fluorescence microscopy measurements. This shows good correlation with predicted concentrations. Profiles of an area where the protein film appears to be absent (Fig. 8.11) suggest a film thickness of 3nm. Individual HSA molecules were previously shown to have a height of ~ 3nm (Section 8.3.1).

The fluorescence of each surface was plotted in Fig. 8.12 (Images in Appendix VII). The fluorescence of PNA surfaces 2-6 did not significantly differ from the control (surface 1). This was attributed to auto-fluorescence. In general, for APS surfaces (8-12). This correlated with AFM results

(Section 8.3.2.3). Surface treatment 12 (10^4nM, not analysed by AFM) showed a lower level of fluorescence than surface treatments 10 and 11. This was attributed to fluorescence quenching (Section 8.3.1). This technique was extremely useful in that it allowed visualisation of FITC-BSA surface binding. In Section 8.3.2.4, the technique was improved by focussing the concentration range between 1nM-10^4nM. Fluorescence microscopy was predicted to allow the detection of sub-monolayer FITC-BSA coverage.

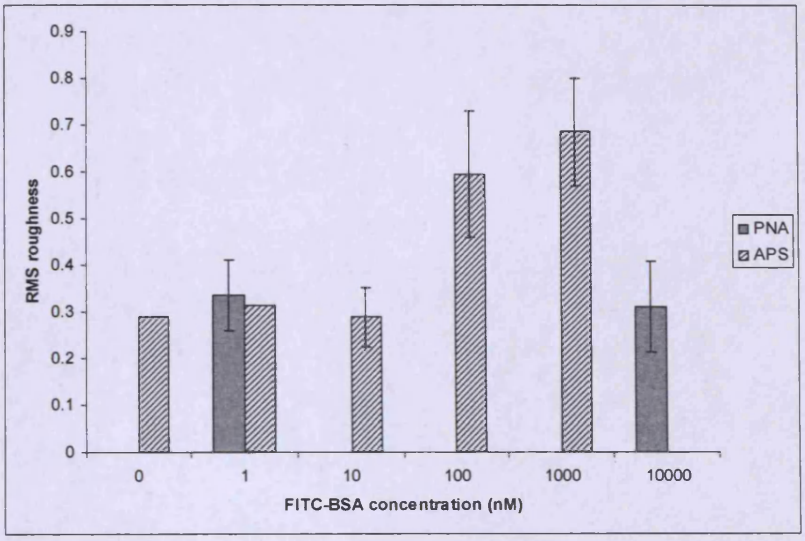


Fig. 8.10 AFM RMSr measurements of PNA and APS glass surfaces incubated with an increasing FITC-BSA concentration in NaPB. Surfaces were incubated for 24 hours with agitation. SEM are measured from one area of each surface (n = 3). Surface treatments are given in Table 8.3.

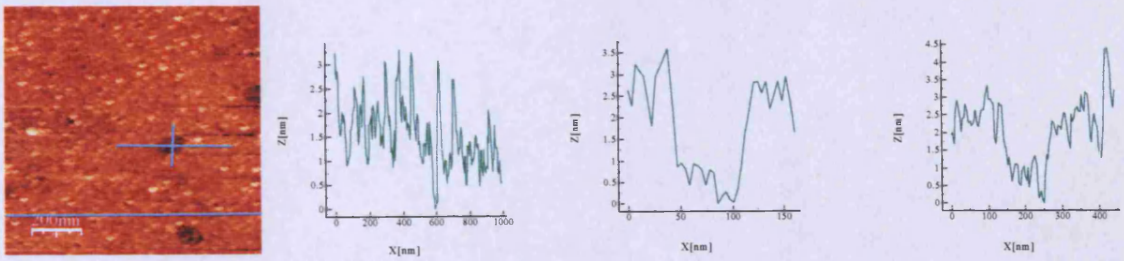


Fig. 8.11 AFM image of apparent 'holes' in a surface FITC-BSA film. The AFM trace image (1um^2) and profiles (along the blue lines) for surface 10 is shown (Table 8.3).

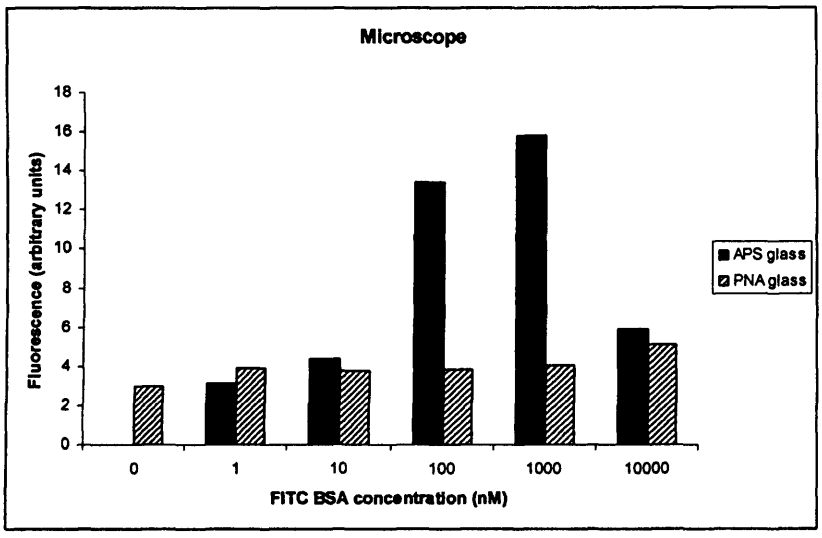


Fig 8.12 Fluorescence microscopy of PNA and APS glass surfaces incubated with an increasing FITC-BSA concentration in NaPB. Experimental surfaces were incubated in FITC-BSA in NaPB. Control surfaces (0nM) were incubated in NaPB only (n = 1). The relative fluorescence of each microscope image was measured using Adobe Photoshop 6.0.

8.3.2.4 FITC-BSA (0.1-10^2nM) adsorption on glass surfaces in NaPB

Fig. 8.13 shows the AFM RMSr values for PNA and APS surfaces treated with a range of FITC-BSA solutions (Table 8.4). The RMSr of PNA surface treatment 7 and APS surface treatments 9-12, incubated in 0.1-1.5nM FITC-BSA, did not significantly differ from the APS control (surface treatment 8). This result correlates well with observations made in Section 8.3.2.3b where FITC-BSA was shown to bind poorly to PNA surfaces. For APS surfaces incubated in FITC-BSA solutions >2.5nM (treatments 13-17), RMSr was greater than for the control. A step increase in RMSr occurred between 1.5 and 2.5nM FITC-BSA; a gradual increase was not observed. This step increase in RMSr may have resulted from a surface concentration induced protein conformational change. At low concentrations surface immobilised BSA is present in a flattened form that does not increase RMSr above the control value (Ortega-Vinusa et al. 1998). As the bound concentration increases, protein molecules get closer together and increasing inter-molecular repulsive forces result in a change to a raised conformational form resulting in the sharp increase in RMSr. The concentration of FITC-BSA required to give rise to monolayer coverage on a single 0.5 – 1cm^2 APS silicon surface was previously estimated as 0.18 - 1.5nM (Table 8.7) and therefore it is proposed that maximum RMSr may have correlated with the completion of a FITC-BSA monolayer. RMSr may look the same

whether FITC-BSA is adsorbed in a monolayer or a multilayer. It is likely that multilayer formation was prevented due to electrostatic repulsion between surface bound and solution protein. HSA was shown to adsorb in multilayers only at extreme pH (9) and ionic strength (300mM) (Ortega-Vinusa et al. 1997).

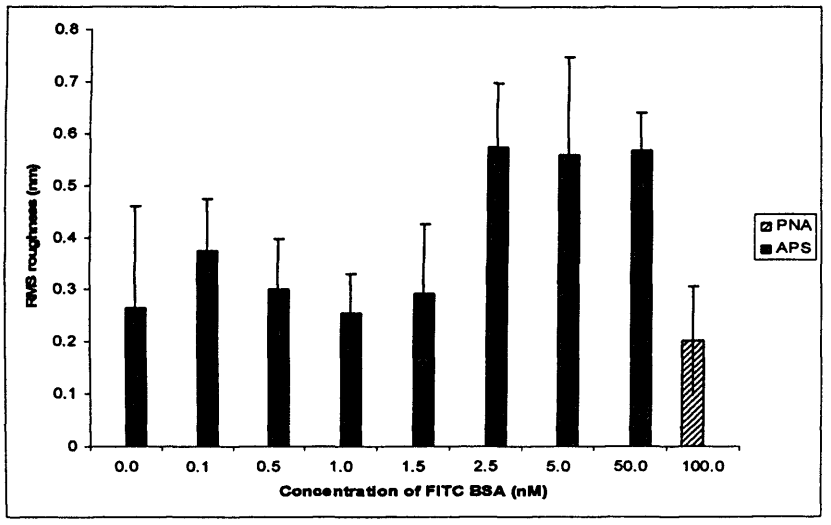


Fig. 8.13 AFM RMSr measurements of PNA and APS silicon surfaces incubated with an increasing FITC-BSA concentration in NaPB. Surfaces were incubated for 24 hours with agitation. Error bars are SEM of different areas of the surfaces (n = 1). Results were from two experiments. Surfaces treatments are listed in Table 8.4.

Fig. 8.14 shows the surface fluorescence of each surface (examples of the images obtained are given in Appendix VII). As was anticipated the PNA surface treatments 1-7 (Table 8.4) showed fluorescence similar to that observed for the control (Table 8.4, treatment 1) (Fig. 8.14). This correlates well with the AFM-RMSr data and with previous results (Section 8.3.2.3). The concentration of FITC-BSA required for a monolayer on a single APS glass surface was estimated as 0.39 - 3nM (Table 8.7). A step increase in fluorescence occurred between 2.5 and 5nM, in good agreement with the RMSr study. However it is surprising that the fluorescence data contains this step change. It is likely that fluorescence quenching affected the results by exaggerating the changes in fluorescence observed between 2.5nM and 5nM. Fluorescence quenching was noted for some of the surfaces (including 2.5nM) and a gradual change to monolayer coverage was not observed. A difference in fluorescence between the control (surface treatment 1) and APS surface treatments 10 and 11 (0.5nM and 1nM) was observed (Fig. 8.14). The absence of RMSr / FITC-BSA concentration

dependence beyond 2.5nM was evidence for the presence of a monolayer. It would be expected that for a limited number of FITC-BSA layers, fluorescence output would be proportional to the number of layers.

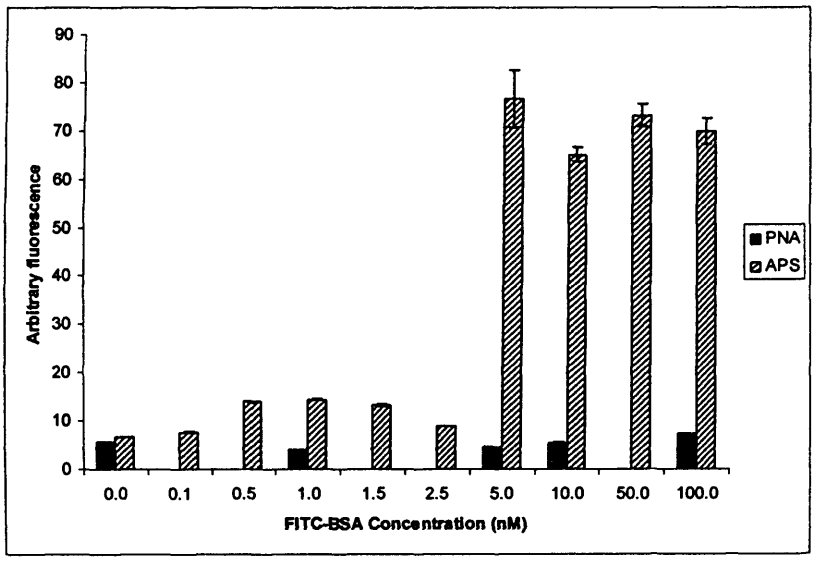


Fig. 8.14 Fluorescence measurements of PNA and APS glass surfaces incubated with an increasing FITC-BSA concentration in NaPB. Results were from two experiments. Surfaces were incubated for 24 hours with agitation. Error bars are SEM of different areas of the surfaces (n = 1). Surfaces treatments are listed in Table 8.4.

8.3.2.5 FITC-BSA (10nM) desorption from glass and silicon surfaces

In the protein-imprinting scheme proposed in this thesis, the imprinted surface is silicon that is coated with a dispersed layer of an immobilised HSA ligand. During the process of binding the target protein, HSA, to the ligand it is inevitable that a proportion of HSA will also become non-specifically bound to the silicon substrate. It is important that such non-specifically bound protein can be removed from the silicon substrate prior to polymerisation (Fig. 1.12). Ideally, HSA removal from PNA surfaces should be able to be monitored, although sub-monolayers are difficult to identify by AFM (Section 8.3.2.6) (Ortega-Vinusa et al. 1998). In this section, APS surfaces, coated with FITC-BSA, were studied in order to investigate the effectiveness of a range of protocols for removing non-specifically adsorbed protein. AFM was used to monitor protein removal. Fluorescence imaging was attempted but serious fluorescence quenching problems made the data unreliable.

It was anticipated that significant protein removal would lead to a substantial decrease in RMSr. Fig. 8.15 shows the RMSr for each surface as measured from AFM scans. None of the surfaces (Table 8.5) showed a decrease in RMSr corresponding to protein removal. RMSr appeared to increase for some surface treatments which is likely to correspond to FITC-BSA conformational changes after the different 'protein removal' steps. An interesting pattern was observed on surface treatment 5 (0.1M NaCl). This may have arisen due to aggregation of the protein molecules at high ionic strength (Fig. 8.16).

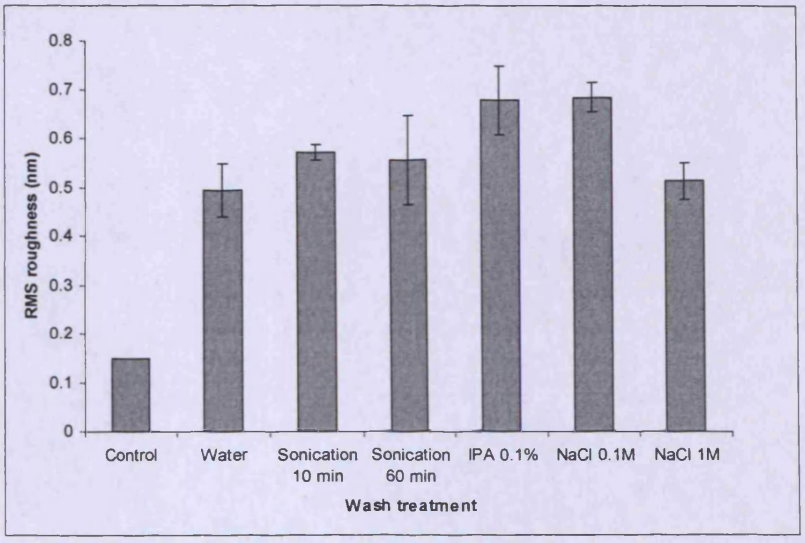


Fig. 8.15 Various washing treatments to remove FITC-BSA adsorbed to APS surfaces. Surfaces were incubated for 24 hours with agitation. Error bars are SEM of different areas of the surfaces (n = 1). Surfaces treatments are listed in Table 8.5.

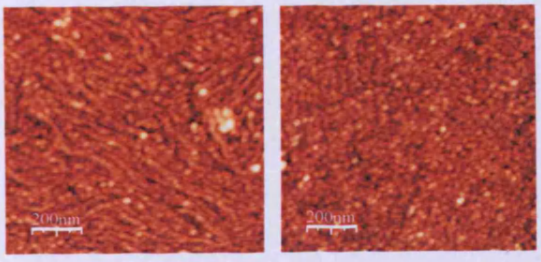


Fig. 8.16 Two images of an APS FITC-BSA surface washed in NaCl (0.1M) and dH_2O

8.3.2.6 A comparison between AuNP, FITC-BSA (10nM) and HSA (10nM) adsorption on glass and silicon surfaces

The AuNPs bound with the same density on APS-glass and APS-silicon surfaces (~520/μm^2) (Fig. 8.17), showing that glass surfaces were comparable to silicon.

Fig. 8.18 shows the RMSr for each protein surface as measured from AFM scans. The only surface with a significantly higher RMSr than the control (surface treatments 2 and 10), was APS FITC-BSA for both silicon and glass surfaces (treatments 8 and 16). However it is probable that this is due to the absence of FITC-BSA binding to the surface of the glass vial (Section 8.3.1.3a shows that HSA binds to both non-treated glass and APS-glass whilst FITC-BSA binds only to APS-glass). Since the surface area of the vials used to carry out the experiments was ~10-fold larger than that of the silicon/glass substrate, absence of FITC-BSA binding to the vial walls would have resulted in a FITC-BSA concentration of ~10nM, which is greater than the estimated concentration required to achieve monolayer coverage (0.39 - 1.5nM, Table 8.7)). This would then give rise to an increase in FITC-BSA binding to APS/glass and APS/silicon resulting in an increase in RMSr.

None of the HSA surfaces (5, 6, 13 and 14) were significantly different from the controls. The estimated HSA concentration required for monolayer coverage was 17.17 - 9.91nM (Table 8.7) as it bound to underivatised glass vials (unlike FITC-BSA) (Section 8.3.2.3a). Therefore, HSA from a solution of 10nM was probably binding in a sub-monolayer (50%) to the silicon surfaces which may have caused it to flatten more (Section 8.3.2.4) than when it was adsorbed from a concentrated solution (Section 8.3.2.1).

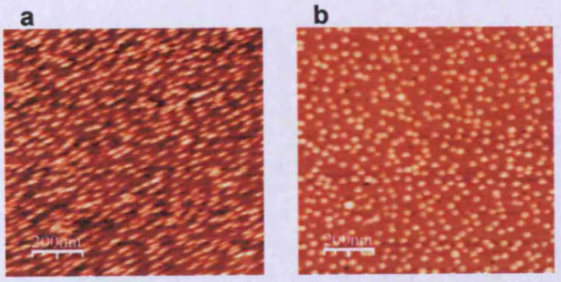


Fig. 8.17 A comparison of AuNP binding to glass and silicon APS surfaces. a) Silicon surface. **b**) Glass surface.

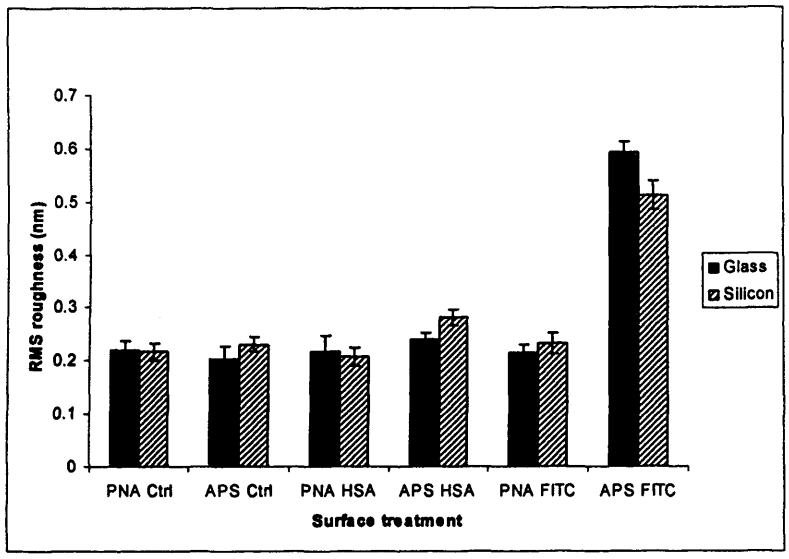


Fig. 8.18 AFM RMSr measurements of HSA and FITC-BSA (0.01uM) adsorbed on APS / PNA, glass / silicon surfaces. Surfaces were incubated for 24 hours with agitation. Error bars are SEM of different areas of the surfaces (n = 3). Surfaces treatments are listed in Table 8.6.

8.3.2.7 HSA (10^2nM) adsorption on a silicon surface in NaPB

The concentration of HSA (10^2nM) was increased above that estimated to be required for a monolayer of protein (17.17 -19.91nM, Table 8.7). This would be expected to show an increase in RMSr, as seen for FITC-BSA surfaces (Section 8.3.2.4). After exposure to the protein the surface was washed once in dH_2O prior to AFM imaging (comparison with Section 8.3.2.2 which showed an increased RMSr for surfaces incubated in 20μM HSA). A new AFM tip was used to improve resolution.

Figure 8.19 shows AFM images of a PNA surface incubated in 10^2nM HSA along with a PNA control surface and a surface incubated in 20μM HSA. The RMSr of the 10^2nM surface was not significantly different to the control but the trace image suggests that the two surfaces differed. RMSr differences may only detect HSA adsorbed in a monolayer deposited from concentrated solutions of protein (Section 8.3.2.2). HSA has been reported to bind in a layer thickness <1nm, below the AFM z-axis resolution (Ortega-Vinusa et al. 1998). FITC-BSA did not flatten on surfaces until concentrations were used below that required for monolayer coverage (Sections 8.3.2.4 – 8.3.2.6). It would appear that FITC modification has significantly changed the protein conformation (Section 8.3.2.3b). Experimental differences between this and the surface incubated in 20μM HSA (Section 8.3.2.2) include agitation during

incubation and the ionic strength of the buffer, although the latter has been reported not to dramatically affect HSA adsorption on silicon (Ortega-Vinusa et al. 1998). Agitation did not affect FITC-BSA adsorption in previous experiments (Sections 8.3.2.3 to 8.3.2.6).

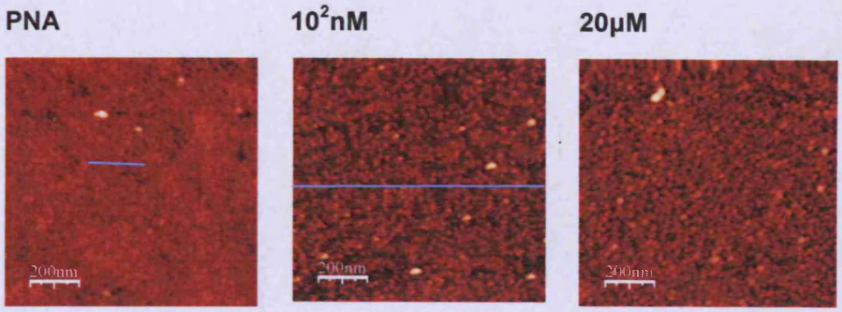


Fig. 8.19 HSA binding to APS silicon surfaces from different solution concentrations. Trace AFM images are shown for each surface.

8.3.3 Conclusions

The RMSr of AFM images was used to evaluate PNA surface adsorption of HSA from concentrated solutions (>20μM). Adsorbed HSA had a height of ~3nm. When a washing step was omitted, large salt structures / islands were observed on surfaces after HSA adsorption from NaPB. HSA adsorption to PNA silicon surfaces was irreversible in water, buffer and glycine buffer. The latter increased the RMSr.

FITC-BSA did not adsorb to PNA surfaces. For theoretical monolayers of FITC-BSA, coverage on APS surfaces was shown to occur independently of concentration, except where fluorescence quenching was observed.

The lowest concentration for which a significant fluorescence was observed (FITC-BSA APS surfaces) was 0.5nM, however, some fluorescence quenching occurred and a gradual increase to monolayer coverage was not observed. The RMSr values were not significantly different than the controls. HSA adsorption from dilute solutions (10^2nM), sufficient for (theoretical) monolayer coverage, gave a similar RMSr.

References

Glycine buffer [WWW]. Invitrogen. Available at: http://www.invitrogen.com/contentcfm?pageid=10699 [Accessed: 31st May 2006].

2001. QCM-D Applications. Biosurfaces in depth. $q_{®}$sense.

Blasi, L. et al. 2005. Characterization of glutamate dehydrogenase immobilization on silica surface by atomic force microscopy and kinetic analyses. *Enzyme and Microbial Technology* 36(5-6), pp. 818-823.

Blomberg, E. et al. 1994. In: Sukhishvili, S. A. and Granick, S. 1999. Adsorption of human serum albumin: Dependence on molecular architecture of the oppositely charged surface. *Journal of Chemical Physics* 110(20), pp. 10153-10161.

Bos, M. A. et al. 1994. Influence of the electrical potential of the interface on the adsorption of proteins. In: Nakanishi, K. et al. 2001. On the adsorption of proteins on solid surfaces, a common but very complicated phenomenon. *Journal of Bioscience and Bioengineering* 91(3), pp. 233-244.

Chan, B. M. C. and Brash, J. L. 1984. Adsorption of fibrinogen on glass: reversibility aspects. In: Nakanishi, K. et al. 2001. On the adsorption of proteins on solid surfaces, a common but very complicated phenomenon. *Journal of Bioscience and Bioengineering* 91(3), pp. 233-244.

Fogh-andersen, N. et al. 1993. Ionic binding, net charge, and donnan effect of human serum albumin as a function of pH. *Clinical chemistry* 39(1), pp. 48-52.

Gessner, A. et al. 2000. Nanoparticles with decreasing surface hydrophobicities: influence on plasma protein adsorption. *International Journal of Pharmaceutics* 196(2), pp. 245-249.

Giacomelli, C. E. et al. 1999. ATR-FTIR study of IgG adsorbed on different silica surfaces. In: Nakanishi, K. et al. 2001. On the adsorption of proteins on solid surfaces, a common but very complicated phenomenon. *Journal of Bioscience and Bioengineering* 91(3), pp. 233-244.

Giacomelli, C. E. and Norde, W. 2001. The Adsorption-Desorption Cycle. Reversibility of the BSA-Silica System. *Journal of Colloid and Interface Science* 233(2), pp. 234-240.

Gun'ko, V. M. et al. 2003. Study of interaction of proteins with fumed silica in aqueous suspensions by adsorption and photon correlation spectroscopy methods. *Journal of Colloid and Interface Science* 260(1), pp. 56-69.

Ingersoll, C. M. et al. 1996. In: Norde, W. and Giacomelli, C. E. 2000. BSA structural changes during homomolecular exchange between the adsorbed and the dissolved states. *Journal of Biotechnology* 79(3), pp. 259-268.

Kondo, A. et al. 1991. In: Larsericsdotter, H. et al. 2005. Structure, stability, and orientation of BSA adsorbed to silica. *Journal of Colloid and Interface Science* 289(1), pp. 26-35.

Kurrat, R. et al. 1997. In: Gun'ko, V. M. et al. 2003. Study of interaction of proteins with fumed silica in aqueous suspensions by adsorption and photon correlation spectroscopy methods. *Journal of Colloid and Interface Science* 260(1), pp. 56-69.

Larsericsdotter, H. et al. 2005. Structure, stability, and orientation of BSA adsorbed to silica. *Journal of Colloid and Interface Science* 289(1), pp. 26-35.

Mrksich, M. and Whitesides, G. M. 1996. Using self-assembled monolayers to understand the interactions of man-made surfaces with proteins and cells. *Annual review of biophysics and biomolecular structure* 25, pp. 55-78.

Nakanishi, K. et al. 2001. On the adsorption of proteins on solid surfaces, a common but very complicated phenomenon. *Journal of Bioscience and Bioengineering* 91(3), pp. 233-244.

Norde, W. and Giacomelli, C. E. 2000. BSA structural changes during homomolecular exchange between the adsorbed and the dissolved states. *Journal of Biotechnology* 79(3), pp. 259-268.

Numata, K. et al. 2006. Adsorption of biopolyester depolymerase on silicon wafer and poly[(R)-3-hydroxybutyric acid] single crystal revealed by real-time AFM. *Macromolecular Bioscience* 6(1), pp. 41-50.

Ombelli, M. et al. 2005. Biomimetic dextran coatings on silicon wafers: thin film properties and wetting. *Materials research society symposium proceedings* [WWW] 845. Available at.http://repository.upenn.edu/cgi/viewcontent.cgi?article=1002&context=mse_papers.

Ortega-Vinuesa, J. L. et al. 1998. Molecular packing of HSA, IgG, and fibrinogen adsorbed on silicon by AFM imaging. *Thin Solid Films* 324(1-2), pp. 257-273.

Peters, T. 1996. *All about albumin: Biochemistry, genetics and medical applications.* Academic press, pp. 15, 26-17, 70, 74.

Ramsden, J. J. 1995. Puzzles and paradoxies in protein adsorption. In: Nakanishi, K. et al. 2001. On the adsorption of proteins on solid surfaces, a common but very complicated phenomenon. *Journal of Bioscience and Bioengineering* 91(3), pp. 233-244.

Rezwan, K. et al. 2005. Lysozyme and bovine serum albumin adsorption on uncoated silica and AlOOH-coated silica particles: the influence of positively and negatively charged oxide surface coatings. *Biomaterials* 26(21), pp. 4351-4357.

Ruardy, T. G. et al. 1997. Preparation and characterization of chemical gradient surfaces and their application for the study of cellular interaction phenomena. *Surface Science Reports* 29(1), pp. 3-30.

Santin, M. et al. 2003. Hydrothane® interactions with biological components: a comparison with chromoflex®. *Journal of applied biomaterials and biomechanics* 1, pp. 67-75.

Santin, M. et al. 1997. Adsorption of [alpha]-1-microglobulin from biological fluids onto polymer surfaces. *Biomaterials* 18(11), pp. 823-827.

Schon, P. et al. 2007. Nonspecific protein adsorption at the single molecule level studied by atomic force microscopy. *Langmuir* 23(20), pp. 9921-9923.

Shaw, D. J. 1992. *Introduction to colloid and surface chemistry.* Redwood books, pp. 110, 235.

Stewart, A. J. et al. 2005. Role of Tyr84 in controlling the reactivity of Cys34 of human albumin. *Febs Journal* 272(2), pp. 353-362.

Vandenberg, E. T. and Krull, U. J. 1991. The Prevention of Adsorption of Interferents to Radiolabeled Protein by Tween-20. *Journal of Biochemical and Biophysical Methods* 22(4), pp. 269-277.

Viappiani, C. 1994. Use of nonradiative decays of extrinsic fluorophores as structural and dynamical probes in protein environments: Fluorescence quenching. *Biophysical Chemistry* 50(3), pp. 293-304.

Wang, R. et al. 1995. Dynamics Surrounding Cys-34 in Native, Chemically Denatured, and Silica-Adsorbed Bovine Serum-Albumin. *Analytical Chemistry* 67(1), pp. 149-159.

Ying, P. et al. 2003. Competitive protein adsorption studied with atomic force microscopy and imaging ellipsometry. *Colloids and Surfaces B: Biointerfaces* 32(1), pp. 1-10.

Zoungrans, T. et al. 1997. Structure, stability and activity of adsorbed enzyme. In: Nakanishi, K. et al. 2001. On the adsorption of proteins on solid surfaces, a common but very complicated phenomenon. *Journal of Bioscience and Bioengineering* 91(3), pp. 233-244.

Chapter 9

General discussion and future work

9.1 Discussion

It would be desirable to synthesise a molecularly imprinted polymer (MIP) with specific high-affinity protein recognition sites as a durable, cost-effective replacement for antibodies (Ab) in biotechnology (Chapter 1). A novel protein imprinting approach was proposed as an outline for these investigations (Section 1.5). Proteins would be bound specifically to ligands that were covalently immobilised to a flat-surface and a controlled polymerisation approach used to build the polymer layer step-by-step (Ruckert, Hall and Sellergren 2002). Individual protein molecules should be sufficiently distributed to allow for subsequent polymer growth (Fig 1.12). A high-affinity protein-ligand interaction would be used as a recognition element within the protein-imprinted polymer site. The resulting binding affinity would be governed by this interaction, in addition to multi-point weak non-covalent, and complementary shape interactions between the template protein and polymer.

The aim of this project was to consider fundamental aspects of surface nanometer-scale patterning and protein-surface interactions, with the aim of preparing an ordered array of surface-immobilised protein. This was in part achieved during the course of the work.

A key early focus of the project, was to identify and characterise a suitable high-affinity protein-ligand interaction. A diffusion cell equilibrium dialysis method was initially used, but abandoned in favour of a small volume approach that used Eppendorf tubes (Chapter 2). Although this approach was time consuming and required considerable dexterity there was no real alternative

available and the technique was shown to produce data compliant with that reported in the literature (Ozer and Tacal 2002; Appendix II). Techniques such as CD spectroscopy, MS and SPR, perhaps more suitable for high throughput ligand screening, would have produced the same information as that obtained using dialysis.

It was initially anticipated that a wide range of ligands would be screened using the Eppendorf dialysis approach. However, it soon became obvious that such an undertaking would be extremely time consuming. Therefore, to shorten this process, a number of high-affinity ligand-protein interactions were identified from the literature (Chapter 3). This process resulted in the selection of human serum albumin (HSA) and ethacrynic acid (ETH). Importantly, one mode of interaction between HSA and ETH was via a covalent binding site (Cys-34) (Bertucci et al. 1998 & 1999). It was anticipated that a covalent interaction could be used to bring about stable and orientated protein immobilisation. However this would complicate the interpretation of dialysis data and ultimately it would also make template removal more difficult. Molecular modelling of the covalent site appeared to show the carboxylate end of ETH free in solution (Appendix III). In order to confirm that derivatisation of the ETH carboxyl group, for subsequent surface immobilisation, would not block binding to HSA (Fig. 9.1), ETH was modified with glycine (Gly) (Chapter 4). A very high purity of ETHGly was required for use in equilibrium dialysis studies. Therefore extensive purification of the ETHGly product was undertaken. Unfortunately the desired level of purity was difficult to attain and resulted in a very low yield.

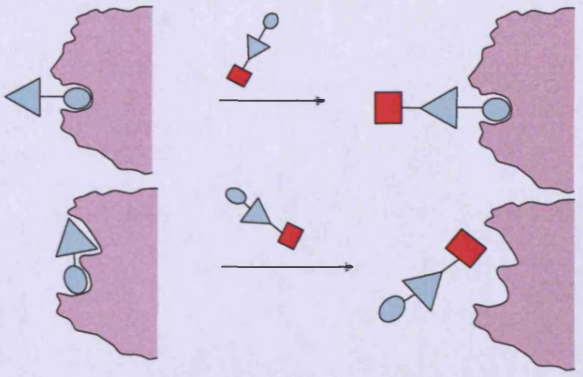


Fig. 9.1 The effect of derivatisation of ETH on the binding of HSA. Derivatisation of ETH (blue) at the carboxyl end (red) may or may not prevent the covalent interaction of Cys-34 (HSA) with the β-unsaturated ketone group (ETH).

A number of dialysis experiments were outlined to characterise covalent and non-covalent binding of HSA with ETH and ETHGly (Table 9.1). A two-site, non-covalent binding curve was fitted to the data using Scatchard analysis, however the detection limit of UV spectroscopy was insufficient to precisely determine the high-affinity binding parameters. Covalent binding may have affected the parameters for high [ETH]:[HSA] ratios.

Table 9.1 Equilibrium dialysis experiments outlined to characterise covalent and non-covalent binding of HSA with ETH.

Experiment	Protein	Pre-saturation of Covalent sites (Cys-34) with	Dialysed with
1	HSA	-	ETH
2	HSA	-	ETHGly
3	HSA	ETH	ETH
4	HSA	ETHGly	ETH
5	HSA	ETH	ETHGly

Considerable effort was made to isolate and purify the covalent HSA-ETH complex so that non-covalent ETH binding could be studied (this would also have been true for the ETHGly ligand). In order to compare the binding of ETH and ETHGly to the covalent site it was necessary to compare the binding parameters of ETH

for the non-covalent sites when the covalent site was fully saturated with either ETH or ETHGly. Unfortunately, isolation of the *pure* HSA-ETH complex (the removal of *free* ETH following covalent site saturation) was not achieved (Chapter 3) and residual ETH would have invalidated subsequent dialysis data. As previously discussed, insufficient ETHGly was synthesised (Chapter 4) to carry out these experiments.

The protein-imprinting concept (Section 1.5), to which this study contributes, requires that a ligand-protein construct is immobilised to a surface. The approach adopted in this study was to surface immobilise the ligand prior to the formation of this complex. Silicon was chosen as an appropriate surface since it is atomically flat, chemically modifiable and readily available. Ligand attachment was to be achieved using amine modification of activated silicon surfaces with aminopropyltriethoxysilane (APS). Subsequently amide linking chemistry would be used to attach the carboxyl group-containing ligand, ETH (Chapter 5). In order to achieve an appropriate degree of protein dispersion, it was essential to control the APS deposition. This was monitored indirectly using gold nanoparticles (AuNPs) and directly using X-ray photoelectron spectroscopy (XPS). A number of different strategies have been described that achieve molecular dispersion and nanoscale patterning on flat surfaces (Section 6.1.1). For this project it was important that APS dispersion was carried out on *unmodified* silicon since subsequent steps in the imprinting process would necessitate further surface modification around the site of ligand immobilisation (Fig. 1.12). This was attempted using a gas-phase evaporation method (from an APS / paraffin oil mixture) based on that reported by Bhat et al. (2002) (Chapter 6). When an undiluted solution of AuNPs were used to visualise the APS gradients it was observed

that AuNP surface coverage was complete when APS was evaporated onto surfaces placed less than 3cm from the evaporating container. At distances in excess of 3cm, AuNP binding was not observed. Interestingly, when the concentration of APS in paraffin oil was varied, XPS showed an APS gradient (between 0-10% APS in paraffin oil). However, this was not reflected in AuNP density since this remained at full coverage down to 2%. This conveys the difficulty in preparing surfaces with a range of AuNP coverages.

Initially, and perhaps naively, it was anticipated that a 1:1 ratio existed between surface adsorbed APS and AuNP. It is clear from the observations that this is not the case and that a key parameter is the APS:AuNP binding ratio.

Another, perhaps surprising observation, was that the AuNP surface densities, for a given APS derivatised surface, was dependent on the extent of dilution of the AuNP solution. Superficially this might imply that AuNP adsorption was concentration-dependent with a kinetically defined end-point. This could not have been possible since it was shown that the interaction between AuNPs and APS was, within the timeframe and conditions of these experiments, irreversible. Therefore the resulting AuNP density represented a thermodynamically stable end-point. Careful consideration was given to the effects of AuNP dilution (with dH_2O) on factors other than AuNP concentration such as changes in ionic strength and pH and their resultant effect on AuNP stability. A decrease in the ionic strength of the AuNP solution upon dilution, may have increased repulsive double layer interactions between AuNPs, which at higher AuNP surface coverages (40-100% v/v dilution) would affect packing densities (Kooij et al 2002).

Additionally, for solutions diluted to <10% (v/v) the stability of the AuNPs may have decreased, this leading to lower binding densities. A change in pH was not observed upon dilution. A concentration-dependence on AuNP adsorption has been previously reported (Chumanov et al. 1995 & 1996; Bright et al. 1998; Minard-Basquin et al. 2005; Nath et al. 2004). It is therefore proposed that AuNPs adsorbed with lower surface densities from more dilute solutions, in order to maintain the repulsive interaction distances between individual AuNPs.

ETH coupling to 'monolayer' APS surfaces films was attempted using EDC / amide chemistry (Chapter 7). This method would subsequently be used to couple ETHGly to APS surfaces. XPS was used to measure the Cl2p group of ETH, however any signal may have been masked by silicon satellite peaks. It was therefore not possible to conclude whether ETH had been successfully coupled to the surface. It was hypothesised that charged APS groups were lowering the amide coupling efficiency. Therefore, APS surfaces were incubated in NaOH to deprotonate the amine groups. Unfortunately, AFM and XPS demonstrated that this step hydrolysed many of the APS groups from the surface.

In order to couple HSA to ETH, the surfaces needed to be incubated with HSA solutions. It was anticipated that HSA would also adsorb non-specifically to the silicon surfaces (Blomberg et al. 1994 in Sukhishvilli and Granick 1999; Giacomelli and Norde 2000) in addition to the specific binding to the high-affinity ligand. Therefore a method of non-specific HSA removal was required. AFM was not able to detect small concentrations of HSA adsorbed to the surface, probably due to protein flattening and denaturation. Instead, adsorption of FITC-BSA was monitored using fluorescence

microscopy and AFM (Chapter 8). Interestingly, the surface roughness of FITC-BSA monolayers on APS surfaces was higher than that observed for HSA, suggesting that modification with bulky FITC groups significantly changed the albumin conformation. In addition, unlike HSA, FITC-BSA did not bind to underivatised PNA silicon surfaces. The fluorescence of FITC-BSA on APS surfaces could be detected after adsorption of proteins from 0.5nM solutions. However significant surface roughness (AFM) was observed only for coverage of protein adsorbed from 2.5nM and above. This was possibly due to the flattening of less closely packed proteins approaching sub-monolayer coverage. Several methods of protein removal including sonication, acid treatment and addition of apolar solvents were investigated, but none demonstrated significant efficiency.

9.2 Future work

9.2.1 Specific immobilisation and orientation of HSA on ETH-derivatised silicon surfaces

A number of experiments are still required to fully characterise the HSA-ETH interaction and achieve a controlled distribution of HSA specifically bound to surface ETH groups.

Isolation of the HSA-ETH complex after saturation of the Cys-34 covalent binding site is required. A chromatography method could be used, with an organic solvent as the mobile phase to provide a more favourable environment for elution of free ETH. Dialysis of HSA-ETH with ETH would then be used to determine non-covalent binding parameters. This would be compared to the HSA and ETH binding curve.

A scaled-up synthesis of ETHGly is required. A HPLC method may be required instead of SPE (limited volumes) to concentrate the purified product after preparative HPLC. ETHGly would subsequently be used in binding experiments with HSA (Table 9.1).

Better control of the distribution of free APS groups on silicon surfaces would be desirable. Since HSA has comparable dimensions (4 x 4 x 14nm) to AuNPs (10nm), the successful control of AuNP dispersion, through controlled APS deposition, would indicate that the controlled dispersion of HSA is possible. In this study neither the distance gradient nor concentration gradient methods gave sufficient control over APS deposition. However, control of AuNP density was shown to be possible by varying the dilution of the commercial AuNP solution. A key observation was that APS was unstable when exposed to water for extended periods whilst it was also observed that AuNPs remained adhered to the surface under the same conditions. This suggests that loss of APS from the surface, due to hydrolysis, was prevented when APS was attached to AuNPs. This process provides an alternative route for patterning the surface (Fig. 9.2). The AuNPs could be selectively removed by physical (Keating et al. 1999) or chemical (Enders et al. 2006) methods. The dispersed APS 'clusters' could subsequently be detected by re-incubating the surfaces in AuNP solution. Coupling of the ETH to APS and subsequent binding of HSA could lead to a dispersion of specifically bound HSA. The issue of steric hindrance upon HSA binding to closely packed immobilised ETH groups, may need to be addressed.

An efficient protocol for ETH coupling to APS surface groups is also required. Due to time constraints, the choice of solvent was limited to that used for ETHGly coupling (DMF) and was not optimised.

Additives such as 1-hydroxybenzotriazole (HOBt) could be used to try and favour the O-acylurea product. Aqueous protocols, using N-hydroxysuccinimide (NHS) to stabilise the activate carboxylate, may be more efficient than DMF. However, neither ETH nor ETHGly were water-soluble. The latter was more polar (dissolved better in MeOH than $CHCl_3$) and may be more soluble in a buffer.

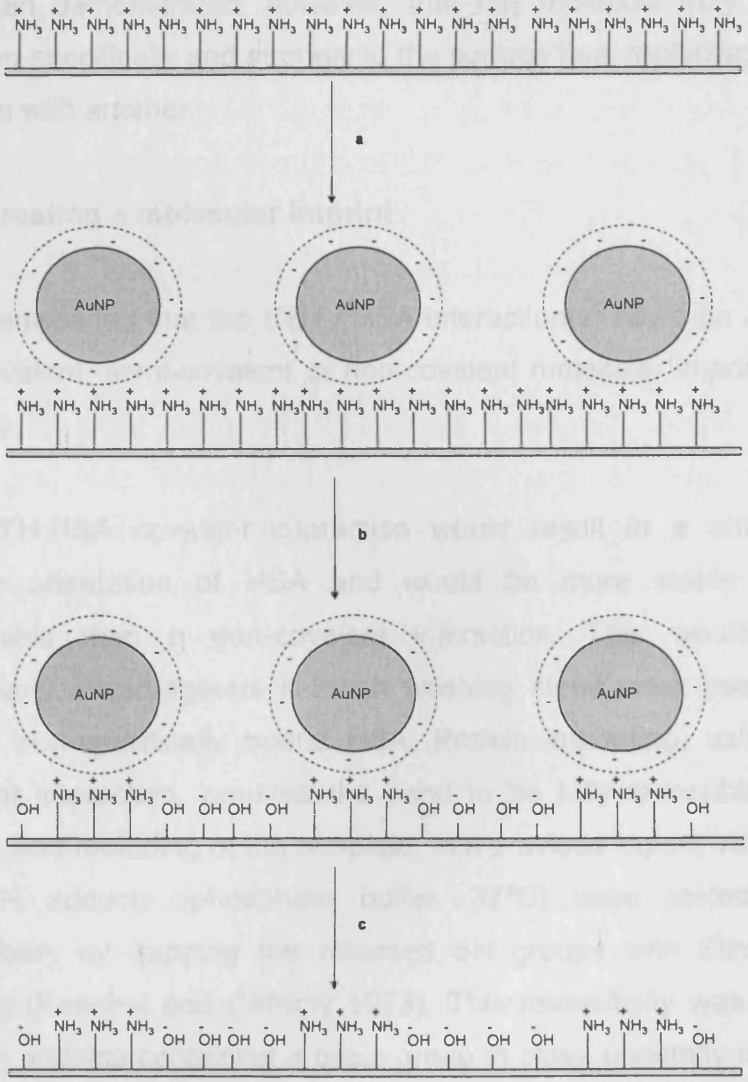


Fig. 9.2 Schematic for creating nanometer-scale patterned APS groups on silicon surfaces. a) Incubation of an APS monolayer surface in dilute AuNP solution. **b**) A controlled surface density of 10nm AuNPs adsorbed to the APS surface. After 24 hrs incubation in aqueous solution, underivatised APS molecules hydrolyse from the surface. **c**) Removal of AuNPs to leave patterned APS clusters. ETH would then be coupled to the surface amines, followed by specific binding of HSA to ETH.

It would also be important to develop a method for desorption of non-specifically adsorbed HSA from PNA-treated silicon surfaces. A combination of sonication and basic solvents (e.g. urea) may yield better results although it is likely that the APS attachment may not be stable in such conditions. Alternatively a non-ionic detergent such as CHAPs could be used (Ombelli et al. 2005). It has been demonstrated, however, that this molecule may also bind non-specifically and strongly to the surface thus replacing one problem with another.

9.2.2 Creating a molecular imprint

It was envisaged that the ETH / HSA interaction(s) could be used in a covalent, semi-covalent or non-covalent molecular imprinting strategy.

The ETH-HSA covalent interaction would result in a uniform surface orientation of HSA and would be more stable and predictable than a non-covalent interaction. This would be particularly advantageous if harsh washing steps were used to desorb non-specifically bound HSA. Protein imprinting, using a covalent interaction, requires the bond to be fully reversible for binding and rebinding of the template. In a previous report, various ETH-SH adducts (phosphate buffer, 37°C) were tested for reversibility by trapping the released SH groups with Ellman's reagent (Koechel and Cafruny 1973). This reversibility was only seen in adducts containing a basic group in close proximity to the labile bond (e.g. ETH-Cys). Digestion of the protein following polymerisation (Fig. 1.12) could favour this process, leaving the high-affinity ETH ligand in the imprinted site. However, the original ETH vinyl recognition element may not be available for covalent

rebinding due to incomplete digestion, irreversibility of the covalent bond and / or instability of the vinyl group. Furthermore, using a covalent interaction is a disadvantage in biosensor applications due to slow rebinding kinetics. The covalent MIP would only be suitable as a single-use biosensor.

As an alternative to the covalent HSA-ETH interaction, the two high-affinity, non-covalent sites could be exploited. Non-covalent MIP recognition is more suitable for multiple use biosensors. However, the binding orientation of ETH in the non-covalent sites is unknown, and this strategy would not allow controlled surface orientation of HSA. Also the non-covalent interaction may not be stable in vigorous protein desorption steps.

A 'semi-covalent' approach could be used to combine the advantages of covalent immobilisation, with the advantages of non-covalent rebinding. If the original ETH vinyl group was not regenerated in the MIP site, multiple weak non-covalent interactions and a complementary shape would still contribute to specific rebinding of the template protein. The covalent imprinting step should result in a homogenous and easily accessible population of binding sites.

Cross-reactivity of the MIP would have to be considered. Proteins such as β-lactoglobulin also have free SH groups that could potentially react. However shape complementarity and multi-point weak interactions are also very important. A further consideration is that the underlying APS-silicon bond anchoring the affinity ligand to the surface may be unstable in the harsh conditions required to digest protein from the MIP sites. Alternatively, the polymer may confer protection to the bond.

9.3 Conclusions

- An equilibrium dialysis method was successfully validated for the characterisation of ligand-protein binding parameters.
- HSA and ETH were identified as an appropriate ligand-protein pairing for use in a novel approach to protein imprinting.
- ETHGly, was synthesised to a very high purity as a means of investigating the role of the carboxyl group during ligand binding.
- Controlled gas-phase deposition of APS could not be used to directly facilitate dispersed ligand attachment.
- AuNPs were patterned onto APS-modified surfaces by varying the dilution of a stock AuNP solution.
- AuNP patterning can potentially be used as an indirect method for controlling surface dispersion of immobilised ligand.

References

Bertucci, C. et al. 1998. Chemical modification of human albumin at Cys-34 by ethacrynic acid: structural characterisation and binding properties. *Journal of Pharmaceutical and Biomedical Analysis* 18(1-2), pp. 127-136.

Bertucci, C. et al. 1999. Reversible binding of ethacrynic acid to human serum albumin: Difference circular dichroism study. *Chirality* 11, pp. 33-38.

Bhat, R. R. et al. 2002. Fabricating planar nanoparticle assemblies with number density gradients. *Langmuir* 18(15), pp. 5640-5643.

Blomberg, E. et al. 1994. In: Sukhishvili, S. A. and Granick, S. 1999. Adsorption of human serum albumin: Dependence on molecular architecture of the oppositely charged surface. *Journal of Chemical Physics* 110(20), pp. 10153-10161.

Bright, R. M. et al. 1998. Preparation and characterization of Ag colloid monolayers. *Langmuir* 14(20), pp. 5695-5701.

Chumanov, G. et al. 1996. Unusual extinction spectra of nanometer-sized silver particles arranged in two-dimensional arrays. *Journal of Physical Chemistry* 100(13), pp. 5166-5168.

Chumanov, G. et al. 1995. Colloidal Metal-Films as a Substrate for Surface-Enhanced Spectroscopy. *Journal of Physical Chemistry* 99(23), pp. 9466-9471.

Enders, D. et al. 2006. Reversible adsorption of Au nanoparticles on SiO2/Si: An in situ ATR-IR study. *Surface Science* 600(6), pp. 71-75.

Giacomelli, C. E. and Norde, W. 2001. The Adsorption-Desorption Cycle. Reversibility of the BSA-Silica System. *Journal of Colloid and Interface Science* 233(2), pp. 234-240.

Keating, C. D. et al. 1999. Kinetics and thermodynamics of Au colloid monolayer self-assembly - Undergraduate experiments in surface and nanomaterials chemistry. *Journal of Chemical Education* 76(7), pp. 949-955.

Koechel, D. A. and Cafruny, E. J. 1973. Synthesis ans structure-activity relationship of some thiol adducts of ethacrynic acid. *Journal of medicinal chemistry* 16(10), pp. 1147-1152.

Kooij, E. S. et al. 2002. Ionic strength mediated self-organization of gold nanocrystals: An AFM study. *Langmuir* 18(20), pp. 7677-7682.

Minard-Basquin, C. et al. 2005. Gold-nanoparticle-assisted oligonucleotide immobilisation for improved DNA detection. *IEE Proc.-Nanobiotechnol.* 152(2), pp. 97-103.

Nath, N. and Chilkoti, A. 2004. Label-free biosensing by surface plasmon resonance of nanoparticles on glass: Optimization of nanoparticle size. *Analytical Chemistry* 76(18), pp. 5370-5378.

Ombelli, M. et al. 2002. Biomimetic dextran coatings on silicon wafers: thin film properties and wetting. *Materials research symposium proceedings* [WWW] 374. Available at: http://repository.upenn.edu/cgi/viewcontent.cgi?article=1002&

context=mse_papers.

Ozer, I. and Tacal, O. 2001. Method dependence of apparent stoichiometry in the binding of salicylate ion to human serum albumin: A comparison between equilibrium dialysis and flourescence titration. *Analytical biochemistry* 294, pp. 1-6.

Ruckert, B. et al. 2002. Molecularly imprinted composite materials via iniferter-modified supports. *Journal Of Materials Chemistry* 12(8), pp. 2275-2280.

Appendices

Appendix I	Chapter 2	Calculations
Appendix II	Chapter 2	HSA and SAL interaction research
Appendix III	Chapter 3	Ligand information, UV and fluorescence scans and molecular modelling
Appendix IV	Chapter 4	NMR chemical shifts
Appendix V	Chapter 5	Problems with AFM scanning
Appendix VI	Chapter 6	AFM images
Appendix VII	Chapter 8	Fluorescence microscope images and AFM images

Appendix I

Preparation of solutions prior to equilibrium dialysis

SAL stock solution (1mM)

Mr = 160.11g

- 1mM
  - 0.016g in 100ml

HSA solution (30µM)

Mr = 66,500 (approx.)

- 30µM
  - 0.1g in 500ml

NaPB pH 7.4

$NaH_2PO_4.2H_2O$ Mr = 156.01

$Na_2HPO_4.12H_2O$ Mr = 358.14

- 67mM
  - 2.1g $Na_2HPO_4,12H_2O$ in 1000ml
  - 19.1g $NaH_2PO_4,2H_2O$ in 1000ml

This was calculated using a website by [WWW] Beynon 1996 by entering the required parameters; pH7.4, phosphate pKa2 = 7.2, 67mM and 25°C.

The NaPB concentration was increased to 100mM, pH7.4, 25°C (as used by Ozer and Tacal, 2001), calculated by [WWW] Beynon 1996:

- 100mM
  - 15.6g $Na_2HPO_4,12H_2O$ in 1000ml
  - 35.814g $NaH_2PO_4,2H_2O$ in 1000ml

Equilibrium dialysis of HSA with SAL

A number of values must be calculated to analyse protein-ligand binding:

Starting [SAL]	= [SAL] added to L compartment
Free [SAL]	= free [SAL] after dialysis (adjusted for non-specific binding)
Bound [SAL]	= bound [SAL] after dialysis

Bound [SAL]	= starting [SAL] – free [SAL]
Y	= bound [SAL] / total [HSA] in P compartment

In the paper 'Ozer et al' complex non-linear regression mathematics was used to calculate binding parameters. An alternative graphical method was used.

A non-linear binding curve (free [SAL] vs Y) was plotted using a trial version of GraphPad prism 4. A step by step example of 'Saturation Binding Curves and Scatchard plots' was downloaded from the website, together with the trial from GraphPad Software ([WWW] 1995-2004) . The parameters for the curve were set as 'Non-linear regression; one-site or two-site binding hyperbola'. This graph calculates two parameters, B_{max} and K_d:

B_{max} = Maximum no. of binding sites

K_d = Equilibrium dissociation constant
= Concentration of free [L] when half of the binding sites are occupied.

K_a = Association constant
= $1/K_d$

The K_d value is a measure of the binding affinity of the ligand to the protein. The higher the value of K_d, the less tightly the ligand binds.

The non-linear curve was transformed into a linear Scatchard plot (Y vs ([L]/Y) using GraphPad Prism. The x-intercept was equal to B_{max} and the Y-intercept equal B_{max}/Kd. The slope is equal to $-1/K_d$ or $-K_a$.

Volume adjustments for ligand control and protein-ligand binding experiments

Adjustment of free [L], measured in the L compartments, to take the volume of the whole dialysis cell into account:

$$\text{Free [L]} = \frac{\text{Starting [L]}}{(\text{L compartment V} + \text{P compartment V})/\text{L compartment V}}$$

Diffusion cell dialysis: e.g. (3.5 ml + 3.4 ml)/3.5ml (= 2)
Eppendorf tube dialysis: e.g. (520ul + 260ul)/520ul (=1.5)

Therefore starting [L] were divided by 2 or 1.5 for the respective experiments.

Adjustment of Y to take into account smaller volume in the P compartments:

$$\text{Y (adjusted)} = \text{Y} \times \frac{(\text{L compartment V} + \text{P compartment V})}{\text{P compartment V}}$$

Diffusion cell dialysis: e.g. (3.4 ml + 3.5 ml)/3.4ml (= 2.03, always 2)
Eppendorf tube dialysis: e.g. (260ul + 520µl)/260µl (always =3)

Therefore, Y was multiplied by 2 or 3 for the respective experiments.

Volume adjustment for diffusion cell equilibrium control experiment

A buffer replacement of 200µl was required for each diffusion cell compartment at each time-point during the equilibrium control experiment. This was necessary to maintain a constant volume within the compartments.

To calculate a mass balance the [SAL] measured were adjusted:

$$\text{Dilution factor for each dialysis cell at each time-point} = \frac{\text{the total volume replaced at each time-point (400ul)}}{\text{the average total volume of the dialysis cells (6012ul)}}$$

$$= 6.66\%$$

The L and P compartment [SAL]s were each adjusted using this dilution factor.

Appendix II

a

Paper	HSA preparation(source)	SAL preparation (source)	Experimental conditions	Method
Brown & Crooks 1975	Crystalline, Fraction V (Sigma-Aldrich)	Recrystallised (not specified)	pH7.4 67mM PB 37°C	Equilibrium Dialysis (bag)
Otagiri & Perrin 1976	Fraction V (Sigma-Aldrich) [14.5 - 58μM]	Sigma-Aldrich	pH7.4 100mM NaPB 22°C	CD spectroscopy
Aarons et al. 1980	Not FA free (Kabi AB) batch variation	Radiolabelled (Amersham)	pH 7.4 50mM PB 37°C	Ultracentrifugation
Zaroslinski et al. 1973	Crystalline HSA (Pentex)-with FA, Cl, bilirubin	Radiolabelled and non-RL (Amersham-Searle corp)	pH7.4 67mM PB 25°C (and a range)	Gel filtration frontal analysis
Sjoholm 1975	Blood bank plasma, charcoal and gel filtrated	Radiolabelled (not specified)	pH7.4 Isotonic PB 37°C	CD spectroscopy
Ozer and Tacal 2001	FA and globulin free lyophilised (Sigma)	(Sigma-Aldrich)	pH7.4 100mM KPB 25°C+/- 2°C	Equilibrium dialysis (Eppendorf tubes) and fluorescent spectroscopy and ultracentrifugation & sephadex chromatography
Honore and Brodersen 1983	Defatted with charcoal and lyophilised (AB Kabi).	Radioligand (not specified)	pH 7.4 66mM NaPB 37°C	Equilibrium dialysis (cellophane membrane)
This research	FA and globulin free lyophilised (Sigma)	(Sigma-Aldrich)	pH7.4 67mM NaPB Ambient room temperature	Equilibrium dialysis (Eppendorf tubes)

b

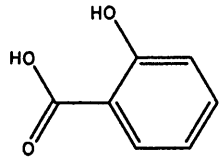
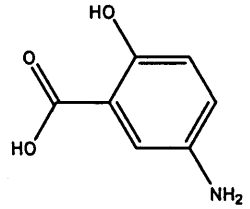
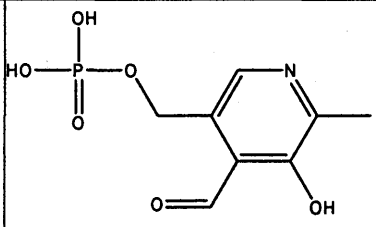
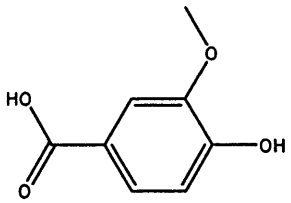
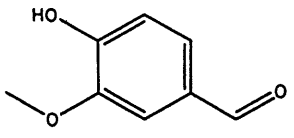
Publication	Method	Analysis	Binding constants Ka (M^{-1}) Kd (μM)	Comparison to this research
Brown & Crooks 1975	Equilibrium dialysis bag	Scatchard (two-site)	K_a1 222,600 $B_{max}1$ 1.07 Kd1 = 4.5 K_a2 1567 $B_{max}2$ 5.24 K_d2 = 638	Lower K_ds observed at *higher* temperatures. K_d1 lower than this research.
Otagiri & Perrin 1976	CD spectroscopy	Scatchard (two-site)	K_a1 120,000 $B_{max}1$ 1.38 Kd1 = 8.3 K_a2 5100 $B_{max}2$ 3.73 K_d2 = 196	K_d of SAL (hydrophilic) < ASN (hydrophobic) Lower K_ds observed at *lower* temperatures. K_d1 comparable to this research.
References from Motagiere & Perrin			K_c1 = 120,00, K_d1 = 8.3 K_c1 = 70,00, K_d1 = 14.3 K_c1 = 200,000, K_d1 = 5 K_c1 = 30,000, K_d1 = 33.3	K_d1 values comparable to this research.
Aarons et al. 1980	Ultracentrifugation	Scatchard (two-site) --- Stoichiometric (three sites) using NONLIN computer program (Gay and Welsch 1981)	K_a1 13000, $B_{max}1$ 1.3, Kd1 76.9 K_a2, $B_{max}2$ 30, K_d2 12500 --- K_c1 19,500, K_d1 51.82 K_c2 2800, K_d2 357.14 K_c3 1900, K_d3 526.32	K_d1 values much higher than this research.

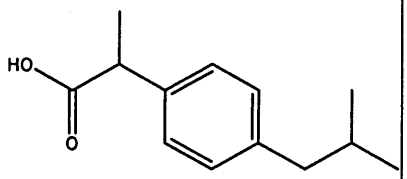
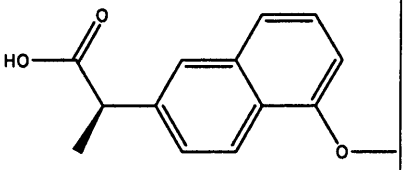
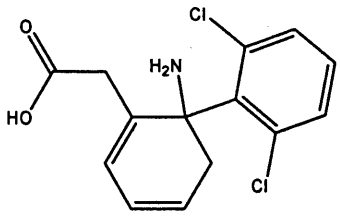
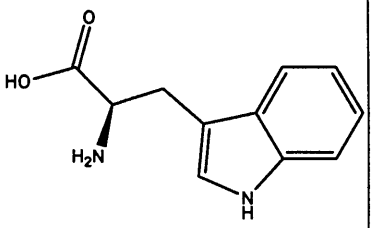
Zaroslinski et al. 1973	Gel filtration frontal analysis	Scatchard (two-site)	K_a1 53900, $B_{max}1$ 1.46 K_d1 18.55 K_a2 5100, n2 4.10 K_d 196.1	K_d1 values comparable to this research.
Sjoholm 1975	CD spectroscopy, Equilibrium dialysis	Scatchard (one-site)	K_a 18,000, B_{max} 2.7 K_d 55.6	Higher K_d than this research using higher temperature. B_{max} is comparable.
Ozer and Tacal 2001	Equilibrium dialysis, fluorescence spectroscopy, ultracentrifugation & sephadex chromatography	Scatchard (one-site, multiple binding)	K_d 25+/- 2.4 B_{max} 3.2 +/- 1.6	Identical protein and methods, best comparison available. Kd and B_{max} values comparable to this research.
Honore and Brodersen 1983	Equilibrium dialysis using cellophane membrane	Stoichiometric	K_c1 48000, K_d1 20.8 K_c2 12000, K_d2 83.3 K_c3 1400, K_d3 714 K_c4 470, K_d4 2127.66 K_c5 150, K_d5 6666.67	Higher K_d1 than this research using a *higher* temperature.
This research	Equilibrium dialysis (Eppendorf tube method, UV spectroscopy)	Scatchard	One-site K_d 30.33 +/- 4.50 B_{max} 3.153 +/- 0.14 Two-site K_d1 9.224+/- 2.92 $B_{max}1$ 1.753+/- 0.27 K_d2 360.6+/- 216.50 B_{max} 2.842 =/- 0.42	-

A comparison of dialysis results (Section 2.3.4.4b) with published data for the HSA-SAL interaction. a) Experimental details. Varying parameters used in the published results include the HSA preparation, temperature and method. All experiments were carried out at pH7.4 in 50-100mM phosphate buffer (PB). **b)** Binding constants and comparison with this research. Association constant = K_a. Equilibrium constant = K_c (combination of K_as). Dissociation constant = K_d. Maximum number of binding sites = B_{max}. Scatchard analysis was used for this research (Appendix I).

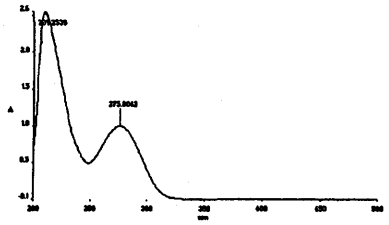
Appendix III

Potential HSA ligands

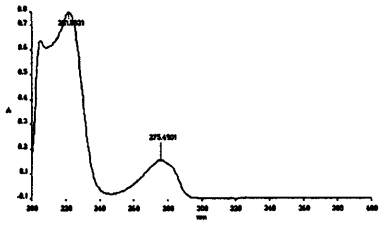
Potential Ligand	Structure of Ligand	Reported Binding to Albumin	Primary binding site
SAL		See Chapter 2	Site I
ASA		K_d = 202.39μM (at 26°C) Cui et al (2004)	Site I
P5P		Bohney et al (1992)	Covalent to Lys-190 (Schiff base).
VAC		-	-
VAN		-	-

Potential Ligand	Structure of Ligand	Reported Binding to Albumin	Primary binding site
IBU		Ka = 2.7 x10^6 M^{-1} Kd = 3.7µM (Kragh-Hansen in AAA, 1981) Ka = 4.8 x 10^5 M^{-1} Kd = 20.8µM (at 25°C, Cheruvallath et al, 1997)	Site II
NAP		Ka = 1.2 x 10^6 M^{-1} Kd = 8.3µM (Honore and Brodersen, 1984 in AAA) Ka = 1.6 x 10^6 M^{-1} Kd = 6.25µM (Cheruvallath et al, 1997 at 25°C) Kd = 0.11 and 41.67µM BMax = 0.83 and 4.1µM (at 37°C, Mortensen et al., 1978) Kd = 10.65µM, BMax = 5.3 (at 25 °C, this research)	Site II
DIF		No binding parameters given. (Martinus et al, 1992)	Site II
TRP		Ka = 4.4x10^4 M^{-1} at 20°C Kd = 22.73µM (McMenamy and Oncly, 1958 in AAA)	-

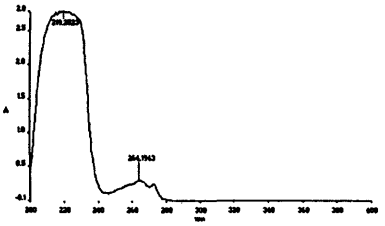
UV Spectroscopy



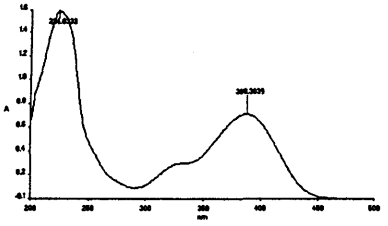
DIF



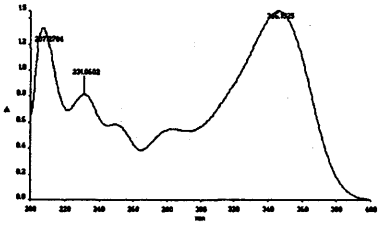
HPA



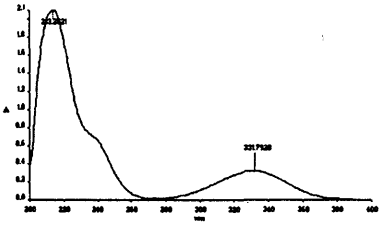
IBU



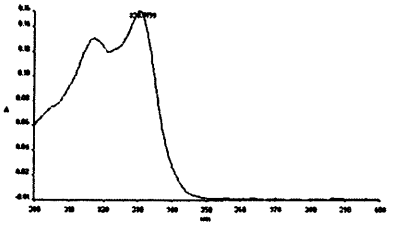
P5P



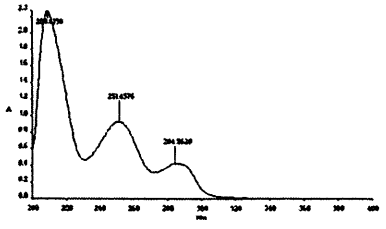
VAN



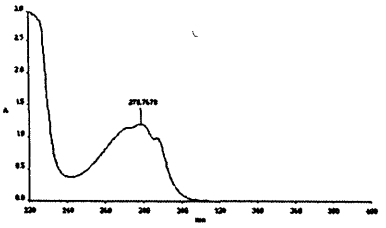
ASA



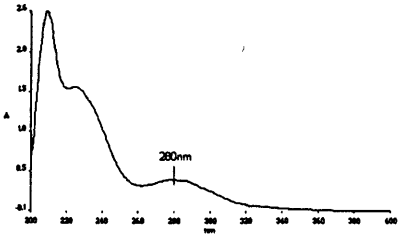
NAP



VAC



TRP

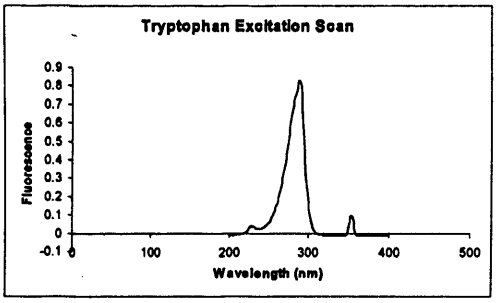


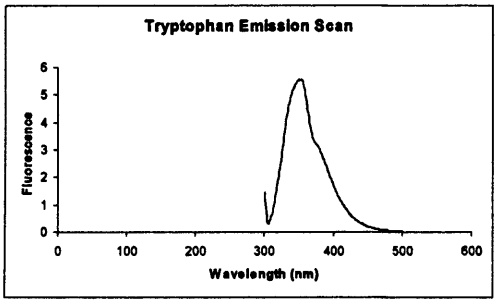
ETH

UV scans of various potential HSA ligands UV scans for TRP (50μM), P5P (200μM) and DIF, HPA, IBU, VAN, ASA, NXN, VAN and ETH (all 100μM). All scans were read at room temperature.

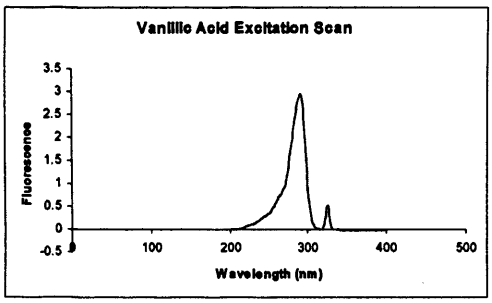
Fluorescence Spectroscopy

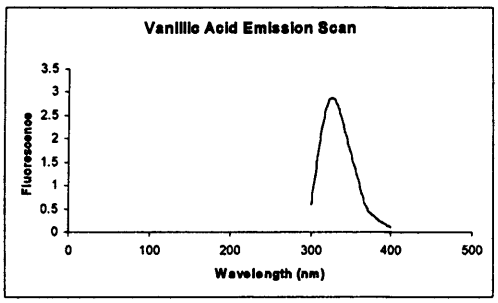
TRP



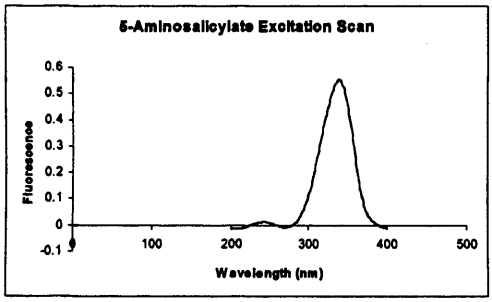


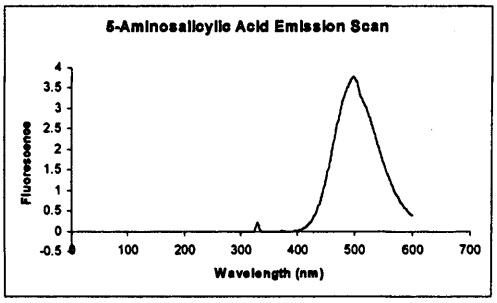
VAC



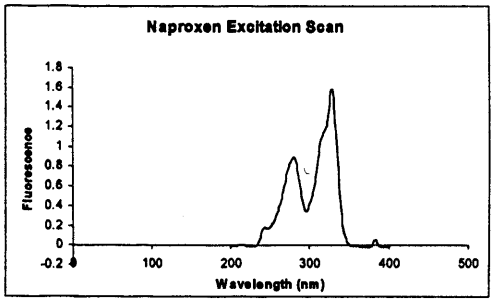


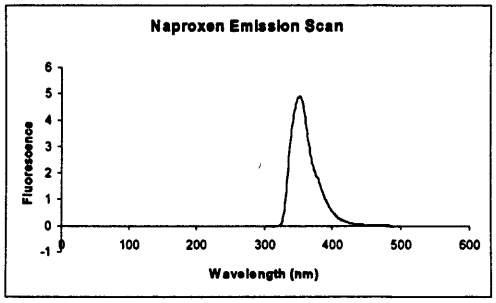
ASA





NAP





Fluorescence scans of various potential HSA ligands Fluorescence excitation (left) and emission (right) scans for TRP (50µM) and VAC, ASA and NAP (all 100µM). All scans were read at 25 +/- 5°C.

Molecular modelling of HSA and ETH

Method

A crystal structure of HSA at 2.5Å (PDB ID: 1A06) with deleted water was used in this procedure. The PDB structure was shown as a dimer, so one protein monomer was deleted, to clarify the monomeric structure of HSA. The modifying group, ETH was constructed in the Molecular Operating Environment (MOE) modeling program and manually attached to the sulfur of Cys-34 (as in ETH-Gly, Fig. 3.4). Chimera was used to locate and visualize the Cys-34 atom of HSA which binds covalently to ETH.

The model of interaction was performed by MOE. The program ran a number of experiments to minimize the energy of each bond of the ligand. In the first run, all sidechains and α-carbon atoms (including Cys-34) in the protein were fixed in position to speed up the modeling interaction. The ligand only was minimized using the built-in MMFF94 force field. During the second run, the ligand and all atoms within a 20Å radius of Cys-34 were minimized.

A large exaggerated bond was first made between the C (ethacrynate) and S (cysteine) atoms, and then the ligand was 'dragged' in towards the protein as the bond shortened to minimize energy. The energy of conformation of each experiment was measured. The root mean squared gradient (RMSG) was calculated for each experiment as the difference between the RMS of one conformation and the next. This value starts off very large and gradually falls as energies are minimized. Once the RMSG is below 1, there are very little changes between the conformations of subsequent experiments. After 10 experiments with an RMSG below 1 the run will automatically stop.

Images were captured using built-in Apple Mackintosh image technology. MOE was then used to put a Connolly surface over the protein. This gave a correct visual picture of the protein and the space that its atoms fill. Hydrophobic (green), hydrophilic (blue) and exposed areas (red) were highlighted.

Results and Discussion

The aromatic ring in ETH is quite rigid, and two points of interaction other than the covalent bond were visible between ETH and HSA. Normally the unsaturated ketone group is quite flexible, but the ethyl group seems to position itself away from a nearby Valine and into a small pocket giving it a specific orientation. Also, the chlorines may fit into a small hydrophobic cleft (Cl is hydrophobic and has similar properties to the methyl group). ETH appears to be solvent accessible. The first run was not ideal, because the Cl atom has some overlap with the protein and this is not physically possible. However, with the rigidity of ETH and its apparent non-covalent interactions with HSA, a good confidence of the binding orientation was assumed. During the second run a similar but noticeably different binding orientation was observed. ETH still seems to protrude about the same distance from HSA. The distances were measured as between 8-10 Å which would be sufficient for derivatisation.

Minimisation of the whole protein with the ligand was not carried out. Fixing the protein in place was not the most accurate measurement of the HSA-ETH conformation. Fixing Cys-34 probably did not change its rigidity much because only one CH_2 group links the sulphur (S) to the α-carbon. The procedure must be repeated without fixing any of the atoms of the ligand or the protein, which will take longer but give a more accurate reflection of the relative positions of the ligand atoms to the protein. Being a crystal structure the protein was not in the same conformation as it would be in solution (i.e. flexible, constantly changing).

Molecular modelling was used in conjunction with equilibrium dialysis experiments.

Appendix IV

NMR spectra

The chemical shifts are quoted as parts per million (ppm). NMR signals are abbreviated as: s (singlet), d (doublet), t (triplet), q (quartet), m (multiplet), dd (doublet of doublets).

Starting materials

ETH

δ_H ($CDCl_3$): 1.16 (3H, t, J= 7.54 Hz $CH_2\underline{CH_3}$), 2.47 (4H, q, J= 7.52 Hz, $\underline{CH_2}CH_3$), 4.85 (2H, s, OCH_2), 5.63 (1H, s, $\underline{CH_2}$=C), 6.05 (1H, d, J = 1.24 Hz, $\underline{CH_2}$=C), 6.85 (1H, d J= 8.50 Hz, Ar), 7.19 (1H, d J= 8.52 Hz, Ar).

GLY

δ_H (CD_3OD): 3.86 (3H, s, OCH_3), 3.88 (2H, s, NCH_2).

CDI synthesis

ETH(Iz)GLYOMe

δ_H ($CDCl_3$): 0.881 (3H, t, J= 7.49 Hz $CH_2\underline{CH_3}$), 1.49 (1H, m, $\underline{CH_2}CH_3$), 1.68 (1H, m, $\underline{CH_2}CH_3$), 3.59 (1H, m, CH_2-$\underline{CH}$) 3.79 (3H, s, OCH_3), 4.09 (2H, d J= 5.39 Hz, NCH_2), 4.54 (2H, s, OCH_2), 4.20 (2H, dd, J = 14.03Hz, J = 14.00Hz, $\underline{CH_2}$-CH), 6.75 (1H, d J= 8.65 Hz, Ar), 7.02 (1H, d J= 8.62 Hz, Ar).

EDC synthesis

ETHGLYOMe

δ_H ($CDCl_3$): 1.08 (3H, t, J= 7.41 Hz $CH_2\underline{CH_3}$), 2.40 (2H, q J= 7.45 Hz, $\underline{CH_2}CH_3$), 3.73 (3H, s, OCH_3), 4.10 (2H, d J= 5.37 Hz, NCH_2), 4.56 (2H, s, OCH_2), 5.52 (1H, s, $\underline{CH_2}$=C), 5.89 (1H, t J = 1.41 Hz, $\underline{CH_2}$=C), 6.81 (1H, d J= 8.46 Hz, Ar), 7.12 (1H, d J= 8.43 Hz, Ar), 7.23 (1H, s, NH).

δ_H (CD_3OD): 1.04 (3H, t, J= 7.54 Hz $CH_2\underline{CH_3}$), 2.35 (2H, q J= 7.47 Hz, $\underline{CH_2}CH_3$), 3.64 (3H, s, OCH_3), 3.96 (2H, s, NCH_2), 4.67 (2H, s, OCH_2), 5.50 (1H, s, $\underline{CH_2}$=C), 5.94 (1H, t J = 1.26 Hz, $\underline{CH_2}$=C), 7.02 (1H, d J= 8.49 Hz, Ar), 7.15 (1H, d J= 8.49 Hz, Ar).

Four ester hydrolysis products after HPLC and SPE purification

ETHGLY

δ_H (CD_3OD): 1.05 (3H, t, J= 7.58 Hz $CH_2\underline{CH_3}$), 2.35 (2H, q J= 7.35 Hz, $\underline{CH_2}CH_3$), 3.93 (2H, s, NCH_2), 4.66 (2H, s, OCH_2), 5.51 (1H, s, $\underline{CH_2}$=C), 5.93 (1H, t, J= 1.40 Hz, $\underline{CH_2}$=C), 7.03 (1H, d J= 8.63 Hz, Ar), 7.14 (1H, d J= 8.63 Hz, Ar), 8.11 (1H, s, NH).

ETHGLY (hydroxylated)

δ_H (CD_3OD): 0.84 (3H, t, J= 7.55 Hz $CH_2\underline{CH_3}$), 1.45 (1H, m, $\underline{CH_2}CH_3$), 1.67 (1H, m, $\underline{CH_2}CH_3$), 3.34 (1H, m, CH_2-$\underline{CH}$), 3.39 (1H, dd J = 9.11, J = 9.42, $\underline{CH_2}$-CH), 3.53 (1H, dd J = 9.11, J = 9.42, $\underline{CH_2}$-CH), 3.92 (2H, s, NCH_2), 4.67 (2H, s, OCH_2), 7.04 (1H, d J = 8.61 Hz, Ar), 7.44 (1H, d J = 8.61 Hz, Ar), 7.23 (1H, s, NH).

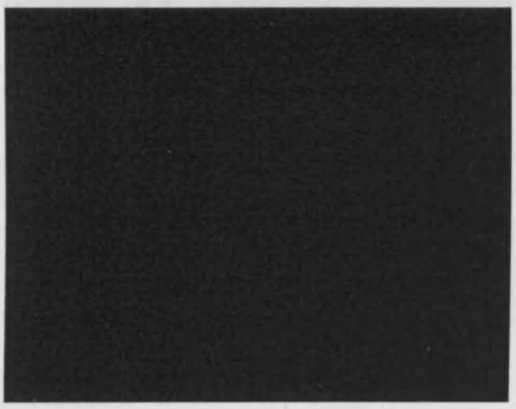
ETH

δ_H (CD_3OD): 1.02 (3H, t J = 7.42 Hz $CH_2\underline{CH_3}$), 2.32 (2H, q J = 7.55 Hz, $\underline{CH_2}CH_3$), 4.60 (2H, s, OCH_2), 5.48 (1H, s, $\underline{CH_2}$=C), 5.89 (1H, t J =1.48Hz, $\underline{CH_2}$=C), 6.86 (1H, d J= 8.66 Hz, Ar), 7.07 (1H, d J= 8.66 Hz, Ar).

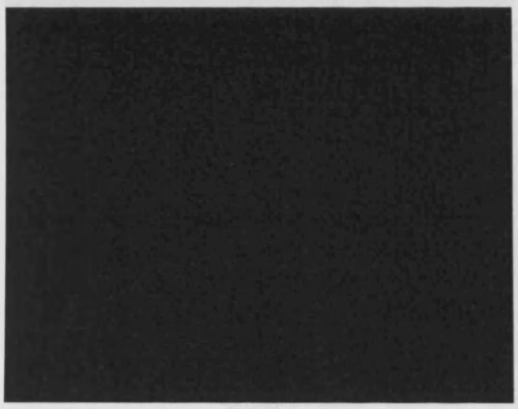
ETH (hydroxylated)

δ_H (CD_3OD): 0.95 (3H, t, J= 7.49 Hz $CH_2\underline{CH_3}$), 1.57 (1H, m, $\underline{CH_2}CH_3$), 1.79 (1H, m, $\underline{CH_2}CH_3$), 3.47 (1H, m, CH_2-$\underline{CH}$), 3.51 (1H, dd J = 8.82, J = 9.13, $\underline{CH_2}$-CH), 3.65 (1H, dd J = 8.82, J = 9.13, $\underline{CH_2}$-CH), 4.74 (2H, s, OCH_2), 7.01 (1H, d, J = 8.77 Hz, Ar), 7.53 (1H, d, J = 8.77 Hz, Ar).

PNA 10^4nM



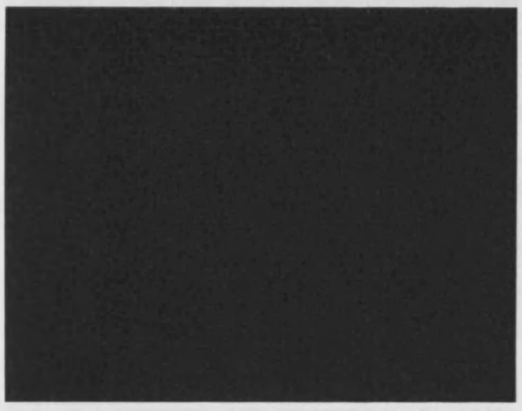
1nM



10nM



10^2nM



10^3nM



10^4nM



Microscope images of APS glass surfaces incubated in increasing concentrations of FITC-BSA (Section 8.3.2.2a).